

# **Supramolecular Chemosensor and Assay Development in Aqueous Media**

Zur Erlangung des akademischen Grades einer

**DOKTORIN DER NATURWISSENSCHAFTEN**

(Dr. rer. nat.)

von der KIT-Fakultät für Chemie und Biowissenschaften

des Karlsruher Instituts für Technologie (KIT)

genehmigte

**DISSERTATION**

von

**M. Sc. Joana Krämer**

1. Referent: Prof. Dr. Stefan Bräse

2. Referent: Prof. Dr. Pavel Levkin

Tag der mündlichen Prüfung: 26. April 2023



This document is licensed under a Creative Commons Attribution-ShareAlike 4.0 International License (CC BY-SA 4.0): <https://creativecommons.org/licenses/by-sa/4.0/deed.en>





## **Deklaration**

Hiermit erkläre ich, Joana Krämer, dass ich die vorliegende Arbeit mit dem Titel „Supramolecular Chemosensor and Assay Development in Aqueous Media” selbstständig verfasst und keine anderen als die angegebenen Quellen und Hilfsmittel verwendet habe, sowie die wörtlich und inhaltlich übernommenen Stellen als solche kenntlich gemacht habe. Weiterhin erkläre ich, dass ich die Satzung des Karlsruhe Instituts für Technologie (KIT), zur Sicherung der guten wissenschaftlichen Praxis in der gültigen Fassung beachtet habe. Die Dissertation wurde bisher an keiner anderen Hochschule oder Universität eingereicht.

Unterschrift: **Joana Krämer** .....

Datum: **02.10.2023** .....



Die vorliegende Arbeit wurde in der Zeit von 01. August 2019 bis 13. März 2023 am Institut für Nanotechnologie (INT) am Campus Nord des Karlsruher Instituts für Technologie (KIT) unter der Leitung von Dr. Frank Biedermann (Emmy Noether-Nachwuchsgruppenleiter) und Prof. Dr. Stefan Bräse (Professor für Organische Chemie) angefertigt. Die Arbeit wurde von der Evonik Stiftung über das Werner Schwarze Stipendium sowie dem Globalink Award von MITACS gefördert.

*The present work was realized between August 1<sup>st</sup>, 2019, and March 13<sup>th</sup>, 2023, at the Institute of Nanotechnology (INT) on the Campus North of the Karlsruhe Institute of Technology (KIT) under the supervision of Dr. Frank Biedermann (Emmy Noether junior research group leader) and Prof. Dr. Stefan Bräse (Professor of Organic Chemistry). The work was funded by the Evonik Foundation with the Werner Schwarze Stipendium and by MITACS with the Globalink Award.*



## Table of contents

1.	Kurzzusammenfassung / Abstract in German .....	1
2.	Abstract.....	3
3.	Introduction.....	5
3.1.	(Supra)Molecular recognition.....	7
3.2.	Artificial chemosensors for biomarker detection.....	9
3.2.1.	Molecular probes based on covalent interactions .....	9
3.2.2.	Non-covalent interaction-based chemosensors .....	13
3.2.3.	Artificial macrocyclic hosts suitable for chemosensor design.....	16
3.2.3.1.	Cucurbit[ <i>n</i> ]urils as promising host molecules for chemosensor design.....	16
3.2.3.2.	Other artificial macrocyclic hosts suitable for chemosensor design .....	20
3.2.4.	Determination of binding affinities ( $K_a$ ) of supramolecular host•guest complexes .....	22
3.2.4.1.	Types of binding assays for emission-based sensing.....	25
3.2.5.	Sensing of biorelevant molecules in aqueous media and biofluids.....	29
4.	Aim .....	32
5.	Results and discussion .....	35
5.1.	Fundamental studies and assay development for insoluble guests .....	35
5.1.1.	Investigation of existing types of binding assays for insoluble guests .....	36
5.1.2.	Guest displacement assay - a new method to solve current assay limitations	37
5.1.2.1.	Determination of binding affinities for selected host•guest complexes.....	39
5.1.2.2.	Performance window .....	49
5.1.2.3.	Limitations of GDA .....	52
5.2.	Conceptual study of a new sensing system for (illicit) drug detection.....	54
5.2.1.	Design concept.....	54
5.2.2.	Evaluation of complex formation and analyte binding.....	57
5.2.3.	Drug sensing experiments .....	62

5.3.	Salt-stable rotaxane chemosensor .....	69
5.3.1.	Design concept for a salt-stable chemosensor .....	70
5.3.2.	Preparation of a rotaxane-based chemosensor .....	73
5.3.2.1.	Synthesis of DAP dyes.....	73
5.3.2.2.	Synthesis of the chemosensing rotaxane.....	75
5.3.2.3.	Characterization of rotaxane .....	79
5.3.3.	Emission-based binding studies of the rotaxane-based chemosensor for indole-type analytes .....	81
5.3.3.1.	Emission-based binding affinities and selectivity of rotaxane chemosensor for biorelevant analytes.....	83
5.3.4.	Tryptophan sensing in biofluids.....	90
5.3.4.1.	Tryptophan sensing in blood serum .....	93
5.3.4.2.	Tryptophan sensing in urine samples.....	97
5.3.4.3.	Comparison of the rotaxane chemosensor to a selection of commonly used non-covalent supramolecular chemosensors .....	99
5.3.5.	Rotaxane microarrays for analyte detection.....	102
5.3.6.	Label-free enzymatic reaction monitoring.....	105
5.3.7.	Chirality sensing with rotaxane chemosensor.....	107
6.	Conclusion and outlook .....	109
6.1.	Fundamental binding studies and assay development for insoluble and weakly binding guest molecules .....	109
6.2.	Conceptual study of a new sensing system for analyte discrimination .....	111
6.3.	Development of a salt-stable rotaxane chemosensor .....	113
7.	Experimental Section.....	116
7.1.	Miscellaneous .....	116
7.1.1.	Materials and equipment.....	116
7.2.	Preparative work.....	120
7.2.1.	General procedures and information.....	120
7.3.	Synthetic procedures.....	130

8.	Additional data.....	139
8.1.	Additional data for chapter 5.1 .....	139
8.2.	Additional data for chapter 5.2 .....	140
8.3.	Additional data for chapter 5.3 .....	144
9.	List of abbreviations .....	146
10.	References.....	151
11.	Appendix.....	170
11.1.	Publications and conference contributions .....	170
11.2.	Acknowledgements.....	171



## 1. Kurzzusammenfassung / Abstract in German

Die molekulare Diagnostik hat in den letzten Jahrzehnten durch die Möglichkeit der Früherkennung von Krankheiten und möglichen Risikofaktoren zunehmend an Bedeutung gewonnen. Da Krankheiten häufig in direktem Zusammenhang mit einem gestörten Stoffwechsel stehen, liegt der Schwerpunkt dabei auf dem selektiven Nachweis und der Quantifizierung von Metaboliten (sog. Biomarkern) in physiologisch relevanten Konzentrationsbereichen. Aktuell basiert der Nachweis von Biomarkern meist auf zeit- und kostenintensiven instrumentellen Detektionsmethoden (HPLC-MS oder NMR). Eine vielversprechende Alternative dazu sind schnell ansprechende und einfach zu handhabende Chemosensoren, die auf dem Prinzip der molekularen Erkennung von Wirt•Gast Komplexen basieren. Die Entwicklung von robusten Chemosensoren, die eine sensitive und selektive Detektion von Analyten in einem komplexen Medium wie beispielsweise Urin ermöglichen, stellt bisher jedoch eine Herausforderung dar.

Im Rahmen der vorliegenden Arbeit wurde die Entwicklung neuer, robuster Chemosensorsysteme, die für den selektiven Nachweis biologisch relevanter Moleküle in wässrigen salzhaltigen Puffern und Biomedien verwendet werden können, vorangetrieben. Dabei wurden hauptsächlich die makrozyklischen Cucurbit[*n*]urile eingesetzt. Durch die Entwicklung eines neuen Assaytyps (Guest Displacement Assay) zur Bestimmung der Bindungsaffinität von unlöslichen und schwach bindenden Gastmolekülen wurde ein tieferes Verständnis von der Wirt•Gast Wechselwirkung erlangt. Weiterhin wurde im Rahmen einer Konzept-Studie ein Array-basierter Sensor-Assay für den Nachweis kationischer und neutraler Analyten in wässrigen Lösungen entwickelt. In diesem kombinatorischen Ansatz wurden Chemosensoren mit unterschiedlichen Erkennungseinheiten eingesetzt, um verschiedene Wirkstoffe wie beispielsweise Narkotika voneinander zu unterscheiden. Die gewonnenen Erkenntnisse über die Wirt-Gast-Chemie wurden im letzten Teil der Arbeit genutzt, um die Selektivität und Affinität von selbstassemblierten Chemosensoren zu verbessern. Durch das Design eines Rotaxan-basierten CB8•Farbstoff-Chemosensors konnte eine hohe Salzstabilität und eine damit verbundene Funktionalität des Chemosensors zur Detektion von Biomarkern in komplexen Medien erreicht werden. Der entwickelte Chemosensor ermöglichte die emissionsbasierte Detektion des Biomarkers Tryptophan im Hochdurchsatz-Screening-Format in Blutserum und Urin, sowie die Überwachung enzymatischer Reaktionen und die chiralitätsbasierte Untersuchung von Enantiomeren. Darüber hinaus konnten gedruckte Sensorchips mit oberflächenimmobilisierten Rotaxan-Microarrays für die fluoreszenzmikroskopische Tryptophan-Detektion hergestellt werden.



## 2. Abstract

In recent decades, molecular diagnostics has become increasingly important for the early detection of diseases and possible risk factors. Here the focus is on the selective detection and quantification of metabolites (so-called biomarkers) in physiologically relevant concentrations since diseases are often directly related to a disturbed metabolism. Currently, biomarker detection is mainly based on time- and cost-intensive instrumental detection methods (HPLC-MS or NMR). Therefore, fast-responding and easy-to-use chemosensors based on the principle of molecular recognition of host•guest complexes are a promising alternative. However, the development of robust chemosensors that allow for sensitive and selective detection of target analytes in a complex medium such as urine is so far challenging.

In this work, the development of new, robust chemosensor systems that can be used for the selective detection of biologically relevant molecules in saline buffers and biomedica was pursued. For this purpose, the macrocyclic cucurbit[*n*]urils were mainly used. First, a deeper understanding of the host•guest interaction was gained by developing a new type of assay ('guest displacement assay') to determine the binding affinity of insoluble and weakly binding guest molecules. Furthermore, an array-based chemosensor assay for the detection of cationic and neutral analytes in aqueous solution was developed as part of a concept study. In this combinatorial approach, several chemosensors with different recognition units were assembled to discriminate between various drugs, such as anesthetics, by cross-reactive detection. Using the gained more profound understanding of host-guest chemistry, the final part of the work aimed to overcome the reduced selectivity and affinity of previous self-assembled chemosensors. By designing a rotaxane-based CB8•dye chemosensor, the chemosensor's high salt stability and concomitant functionality for biomarker detection in complex media were achieved. The developed chemosensor enabled the emission-based detection of the biomarker tryptophan in high-throughput screening format in blood serum and urine, as well as the monitoring of enzymatic reactions and the chirality-based investigation of enantiomers. Furthermore, printed sensor chips with surface-immobilized rotaxane microarrays were prepared for fluorescence-based microscopic detection of tryptophan.



### 3. Introduction

Diagnosis and treatment of diseases are the core pillars of a functioning health care system and are indispensable for maintaining human health. In this context, molecular diagnostics is a constantly growing and increasingly important field of work. Especially the improvement and development of new analytical technologies and methods are of great relevance for clinical diagnostics and point-of-care testing (POCT).<sup>1</sup> Early detection of diseases and associated risk factors can help prevent or delay the onset of severe health conditions and is vital in improving health care. Many diseases are only discovered after the onset of (severe) symptoms, which often occur only at an advanced stage of a disease, making it more difficult to cure, if it is still possible at all.<sup>2</sup> Early detection, *i.e.*, ideally prior to the occurrence of (severe) symptoms, would simplify subsequent treatment and increase the chances of success. A possible approach for early-stage diagnostics is the monitoring of alterations in the individual metabolic profile.<sup>3,4</sup>

Genetic disorders or diseases often lead to an altered metabolism, which results in increased or decreased concentrations of specific small molecules (*i.e.*, metabolites) in the body. Therefore, these molecules, further called biomarkers, can serve as indicators in a biological system or pathogenic processes. Biomarkers are present in various biofluids, such as urine, saliva, and blood serum.<sup>5,6</sup> By (frequent) monitoring of such biomarkers, diseases and associated risk factors can be detected sooner, allowing an earlier follow-up treatment of a condition.<sup>6,7</sup> The following paragraph briefly summarizes selected biomarkers (see **Figure 1**) and their altered biofluidic concentrations associated with diseases and disorders. Note that most of the presented biomarkers are not necessarily the only indicator for one specific disease but that an interplay of several factors must be considered to draw a complete clinical picture.

For example, altered concentrations of amino acids and their derivatives are linked to various medical conditions.<sup>8,9</sup> In biofluids such as urine or blood serum, typical concentrations of amino acids are in the micro- to millimolar concentration ranges.<sup>7</sup> The most commonly known disorder connected to a disrupted amino acid metabolism is phenylketonuria (PKU), where phenylalanine (Phe, **1**) cannot be metabolized into tyrosine, leading to abnormally high Phe concentrations in the body.<sup>10</sup> This condition causes, amongst others, seizures, physiological disorders, and intellectual disabilities. Besides, variations in the tryptophan (Trp, **2**) metabolism lead to abnormal concentrations of Trp and kynurenine (**3**) in the human body, which is associated with inflammations as well as neurological and psychiatric disorders.<sup>11-13</sup> Altered concentration levels of the prominent neurotransmitters dopamine (**4**) and serotonin (**5**) are linked to neurological disorders such as anxiety,<sup>14</sup> depression,<sup>15</sup> and bipolar disorders,<sup>16</sup> as well as Parkinson's disease.<sup>17</sup>

Amines and polyamines are a biomarker class associated with dysfunctions in the body. For example, mild cognitive impairment and Alzheimer's disease are connected to an abnormal polyamine level<sup>18</sup> of spermidine (**7**) and arginine (**8**), whereas cadaverine (**9**) is an indicator of food spoilage.<sup>19</sup> Glucose (**10**) is another excellent example of a disease-associated biomarker, as elevated blood glucose levels are the hallmark of diabetes mellitus, a well-known and widespread endocrine disease.<sup>20,21</sup> Carbohydrates, in general, are connected to various diseases such as kidney disease, obesity, and hypertension.<sup>20,22</sup> Aside from detecting body-inherent biomarkers, detecting substances supplied to the body, such as drugs, is essential. For example, steroids such as estradiol (**11**) and progesterone (**12**) are administered in menopausal hormone replacement therapy to treat vasomotor symptoms.<sup>23,24</sup> Equally important is the detection of prescription drugs such as benzodiazepines, which, however, are also frequently abused. Diazepam (**13**) is a commonly administered benzodiazepine for the emergency treatment of epileptic seizures and insomnia or panic disorder. However, long-term use of these drugs causes serious health risks and addictions.<sup>25,26</sup>

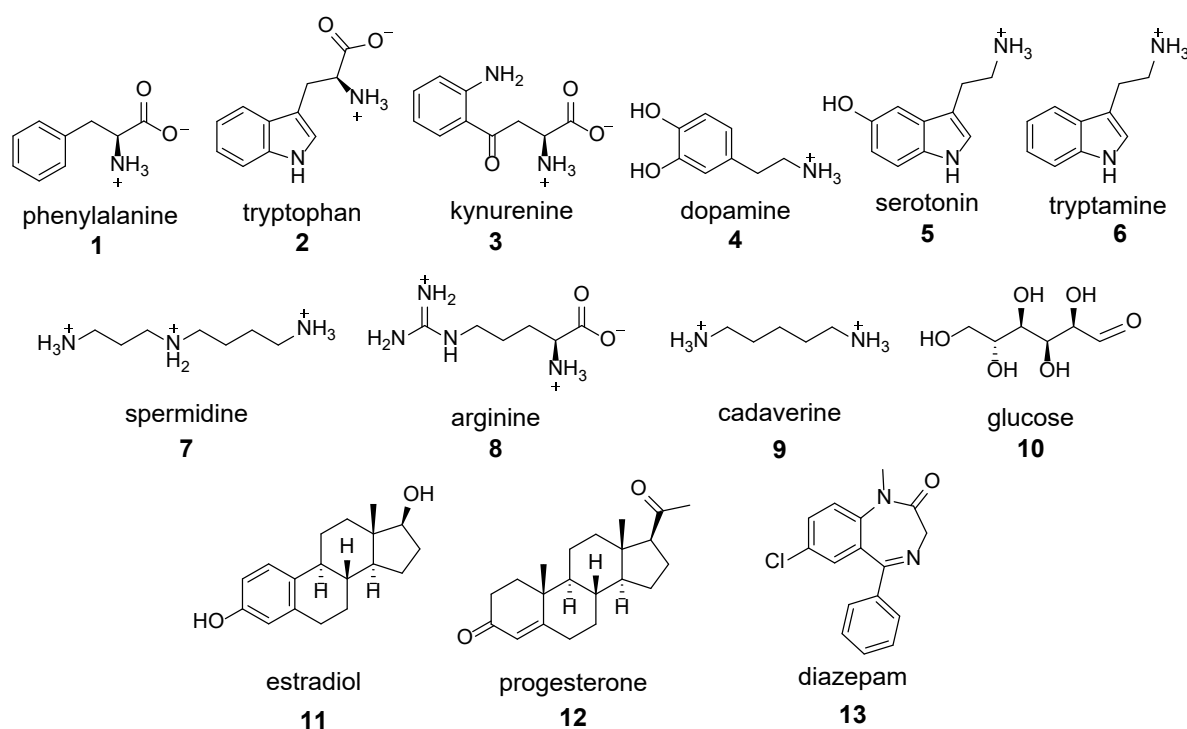


**Figure 1.** Selected examples of body-inherent biomarkers whose altered biofluidic concentrations are associated with specific diseases and commonly administered drugs.

Current detection methods for metabolites in biofluids are typically either based on biosensors that rely on molecular recognition or are instrumental analytical techniques, such as nuclear magnetic resonance (NMR) spectroscopy and mass spectrometry (MS)-based methods, *i.e.*, mass-coupled high-performance liquid chromatography (HPLC-MS) or gas chromatography (GC-MS).

These techniques are well established to date and show high-precision results. However, they also have significant drawbacks. Due to their (technical) requirements, they can usually only be conducted in specialized laboratories with the appropriate equipment and trained personnel.

Additionally, the samples can typically not be tested on-site but must be sent to specialized laboratories, often requiring cumbersome additional pre-treatment, such as deproteinization before testing. Besides high-throughput screening capabilities are limited. Consequently, these techniques are rather laborious and costly, which rules out the desired regular monitoring of a larger number of patients. Therefore, to evolve molecular diagnostics, we must step away from specialized laboratories and move to direct detection and quantification on-site. Artificial sensors based on molecular recognition are the first step in this direction.

### 3.1. (Supra)Molecular recognition

Molecular recognition is one of the fundamental principles in nature on which essential biological processes, such as cell-cell recognition, enzymatic reactions, *i.e.*, biocatalysis, or cellular signal transduction, are based.<sup>27,28</sup> The recognition process occurs between two or more molecules, where one molecule acts as a receptor that can selectively bind a substrate molecule, *i.e.*, an analyte.<sup>29</sup> This recognition event is usually highly specific. It is mainly mediated by intermolecular non-covalent interactions such as electrostatic effects, hydrogen bonding, metal coordination, or hydrophobic forces, to name but a few. Enzymes are typical bioreceptors involved in biological processes such as DNA transcription (*e.g.*, polymerase) or food digestion (*e.g.*, peptidase pepsin), where a particular enzyme can only bind to specific molecules (substrate), catalyzing the conversion of the substrate into a product.

Inspired by nature, (supramolecular) chemists have worked intensively for half a century, mimicking nature's molecular recognition to develop artificial receptors and sensing systems that allow selective analyte detection.<sup>7</sup> Different design approaches for the development of artificial sensors were pursued. On the one hand, natural bioreceptors, such as an antibody or enzyme, can be combined with molecular signaling units (signal transducer), resulting in a biosensor.<sup>30</sup> On the other hand, artificial receptor molecules, such as macrocyclic cucurbit[*n*]urils, can be combined with a signaling unit (*e.g.*, a fluorophore), resulting in a chemosensor. In both cases, selective recognition of a target analyte leads to a measurable signal change (see **Figure 2a**).<sup>7,31</sup>

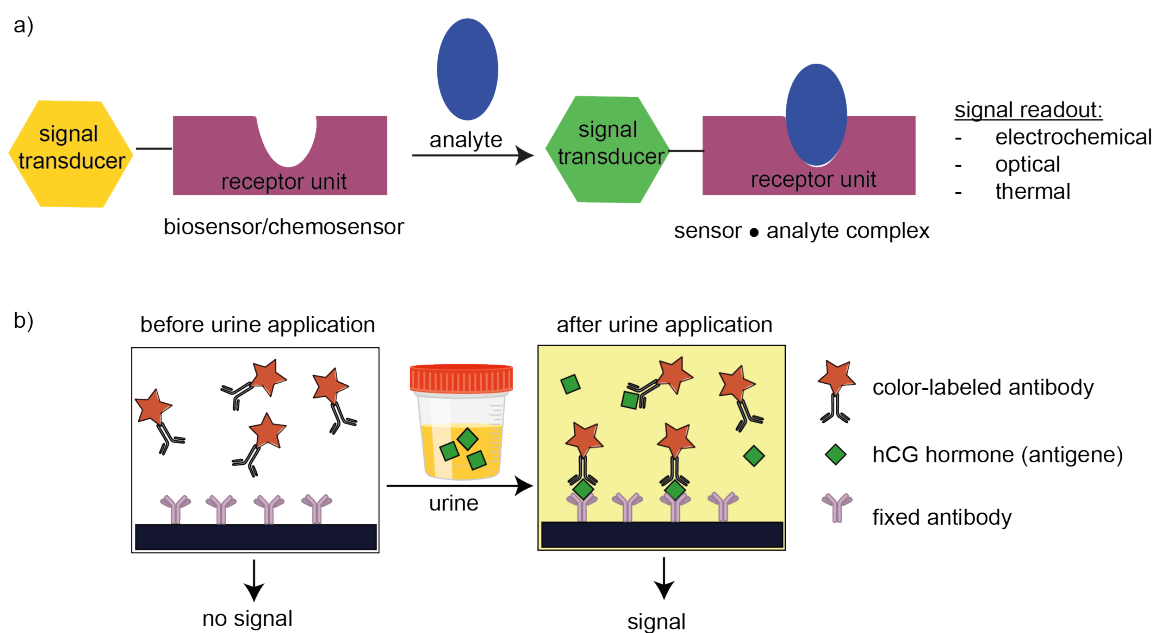


**Figure 2.** Schematic representation of a) the molecular recognition and subsequent signal transduction of a biosensor or chemosensor upon analyte recognition. The sensor•analyte complex formation can be detected electrochemically, optically, or thermally, depending on the sensor properties. b) Schematic representation of the working principle of a pregnancy immunoassay test.<sup>32,33</sup>

Many diagnostic sensing technologies based on molecular recognition have been developed in the past decades. However, most sensors that have found their way into clinical diagnostics or even home tests were based on bioreceptors.<sup>7</sup> The pregnancy test is a well-known example of a successful biosensor implementation into home use.<sup>32,33</sup> This immunoassay diagnostic test relies on the specific recognition of the pregnancy hormone human chorionic gonadotropin (hCG).<sup>33</sup> The test consists of two antibodies recognizing different hormone regions (epitopes). One antibody is immobilized on a nitrocellulose test strip, whereas the second antibody labeled with a colored marker remains freely on the strip (see **Figure 2b**).<sup>33</sup> Once the strip comes in contact with urine, potential hCG in the urine forms a half-sandwich complex with the mobile color-marked antibody. The capillary effect transports the complex to the immobilized antibody, forming a sandwich complex and resulting in an optically detectable readout signal.<sup>33</sup>

Besides immunoassay diagnostics, bioreceptor-based methods such as DNA and RNA technologies (including polymerase chain reaction (PCR) tests)<sup>34-36</sup> or enzymatic reaction-based methods are also frequently applied in clinical diagnostics.<sup>37,38</sup> In general, sensing techniques adapted from biological building blocks and processes offer high selectivity and specificity advantages.<sup>7</sup> However, their application is still primarily dependent on specialized laboratories. In addition, biosensors are cumbersome due to their complex isolation procedures and limited storage options, making these methods time-consuming and costly.<sup>7</sup> A totally different sensing approach relies on electrochemistry, and a number of the developed sensors are already highly

advanced.<sup>39</sup> For example, a zinc oxide (ZnO) sensor was developed that detects electroactive glucose in blood.<sup>40</sup> In this process, glucose is enzymatically oxidized to glucoactone, producing hydrogen peroxide. The working electrode can then detect the free electrons produced during the dissociation of hydrogen peroxide.<sup>40</sup> Unfortunately, electrochemical sensors only apply to a small range of redox-active biorelevant analytes, such as catecholamine-based neurotransmitters.<sup>41</sup>

## 3.2. Artificial chemosensors for biomarker detection

The current hurdles of biosensors and electrochemical sensors lead to the need for an alternative detection method that takes advantage of molecular recognition processes and combines them with the desired faster response times and lower manufacturing and application costs. Artificial chemosensors are a promising alternative to overcome these hurdles.<sup>7</sup> They are particularly attractive due to their faster and easy readout capabilities that can result in a significant time gain during diagnostics, which is especially important in medicine. The following will explain artificial sensors based on covalent and non-covalent interactions in more detail. Since the practical part of this work deals exclusively with optical readout methods based on absorption and fluorescence emission, the scope of this introduction will focus mainly on absorption- and emission-based chemosensors.

### 3.2.1. Molecular probes based on covalent interactions

According to IUPAC, a chemosensor is “*a device that transforms chemical information, ranging from the concentration of a specific sample component to total composition analysis, into an analytically useful signal*”.<sup>42</sup> In other words, one can speak of a chemosensor in the case that the receptor unit recognizes an analyte and a selective interaction occurs between the receptor and the analyte. This recognition event is characterized by a measurable signal change, *e.g.*, thermal, absorbance, or fluorescence emission change, which can be analyzed qualitatively or quantitatively.<sup>43,44</sup>

The interaction type depends on the nature of the artificial receptor and the analyte. For example, an analyte can irreversibly bind to a receptor by forming a covalent bond during an organic chemical reaction of a functional group attached to the analyte and a receptor (see **Figure 3a**).<sup>7,45</sup> Unlike the classical covalent attachment, which is usually kinetically stable, dynamic covalent bonds can be formed between certain functional groups, *e.g.*, diols and boronic acids. Dynamic covalent bonds are covalent bonds that are formed reversibly (see **Figure 3b**).<sup>7,46,47</sup> Typical examples of dynamic covalent interactions are imine formation, disulfide exchange, hydrazone

formation, or cyclic boronate ester bond formation.<sup>46</sup> Furthermore, metal complexes that strongly bind an analyte can form kinetically nearly inert metal-analyte complexes that resemble a covalent bond, as schematically presented in **Figure 3c**.<sup>7,45</sup> Chemosensors that can engage in covalent(-like) interactions with an analyte will be called “molecular probes” in the following.

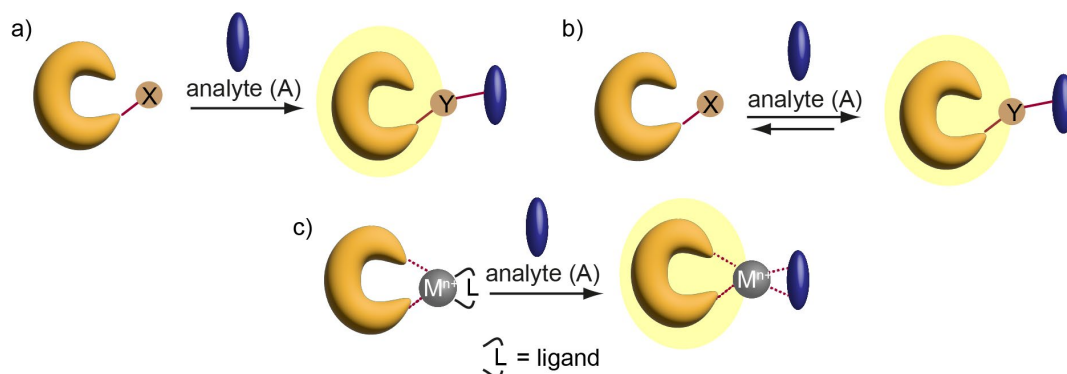


**Figure 3.** Schematic representation of the interaction of a molecular probe with an analyte forming a) a covalent bond, b) a dynamic covalent bond, and c) a kinetically inert metal-analyte complex resulting in a measurable change of the spectroscopic properties of the probe. Adapted with permission from ref.<sup>7</sup> Copyright 2022 American Chemical Society.

Since the type of the covalent interaction depends on the nature of the analyte, it is worth taking a closer look at the functional groups of individual biomarkers. Amino acids, for example, all share the same functional amino and carboxylate groups and differ only in their organic residue at the  $\alpha$ -C atom.<sup>7</sup> Accordingly, amine-reactive molecular probes such as ninhydrin can detect amino acids as they react with the primary amino group in a stepwise condensation-decarboxylation reaction. However, this method is non-selective; all amino acids present in a sample are indistinguishably detected simultaneously.<sup>7,48,49</sup> To increase selectivity, additionally targeting the organic residues of the amino acids is useful. Especially for thiol-containing amino acids and derivatives such as cysteine (Cys, **15**) and homocysteine (HCys, **16**), there are already countless probes that utilize the ability of thiols to undergo nucleophilic substitution ( $S_N$ )-reactions, Michael additions or addition-condensation reactions for the recognition process.<sup>7</sup> A benzothiazole fluorophore with a 3'-methoxyphenyl acrylate moiety (**14**) was used to detect and distinguish the thiol-containing amino acids **15** and **16** in 20 mM phosphate buffer (with 1 mM hexadecyltrimethylammonium bromide (CTAB)) and in diluted deproteinized human plasma at low  $\mu$ M concentrations.<sup>7,50</sup> As shown in **Figure 4a**, the thiol residues of both Cys and HCys undergo a Michael addition with the  $\alpha,\beta$ -unsaturated carbonyl moiety, causing a fluorescence emission turn-on at 377 nm ( $\lambda_{\text{ex}} = 304$  nm). The unique feature of this molecular probe **14** is that it can undergo a rapid addition-elimination reaction with Cys, resulting in the cleavage of a lactam. This leads to the unmasking of the hydroxyl moiety of the 2-(2'-hydroxy-3'-methoxyphenyl) benzothiazole (HMBT), which can undergo an excited-state intramolecular

photon transfer (ESIPT)<sup>51</sup> process upon photoexcitation. A subsequent rapid photoinduced proton transfer leads to the tautomerization of HMBT, exhibiting the keto emission at a longer wavelength ( $\lambda_{em} = 487$  nm).<sup>50</sup> The second step is kinetically favored for Cys, allowing a kinetic differentiation between Cys and HCys.<sup>50</sup> An alternative option for detecting thiol-containing amino acids is to take advantage of thiols' strong, near-covalent binding interactions with soft transition metal ions in aqueous media. For example, the turn-on Pt(II) probe (**17**), in **Figure 4b**, which was recently introduced by our group, can detect cysteine in buffered aqueous media in  $\mu$ M concentrations ( $\sim 50$   $\mu$ M).<sup>52</sup> The binding of the thiol leads to cleavage of the small green-emitting fluorophore 3-hydroxyisonicotine aldehyde (HINA), resulting in an emission increase.<sup>52</sup>

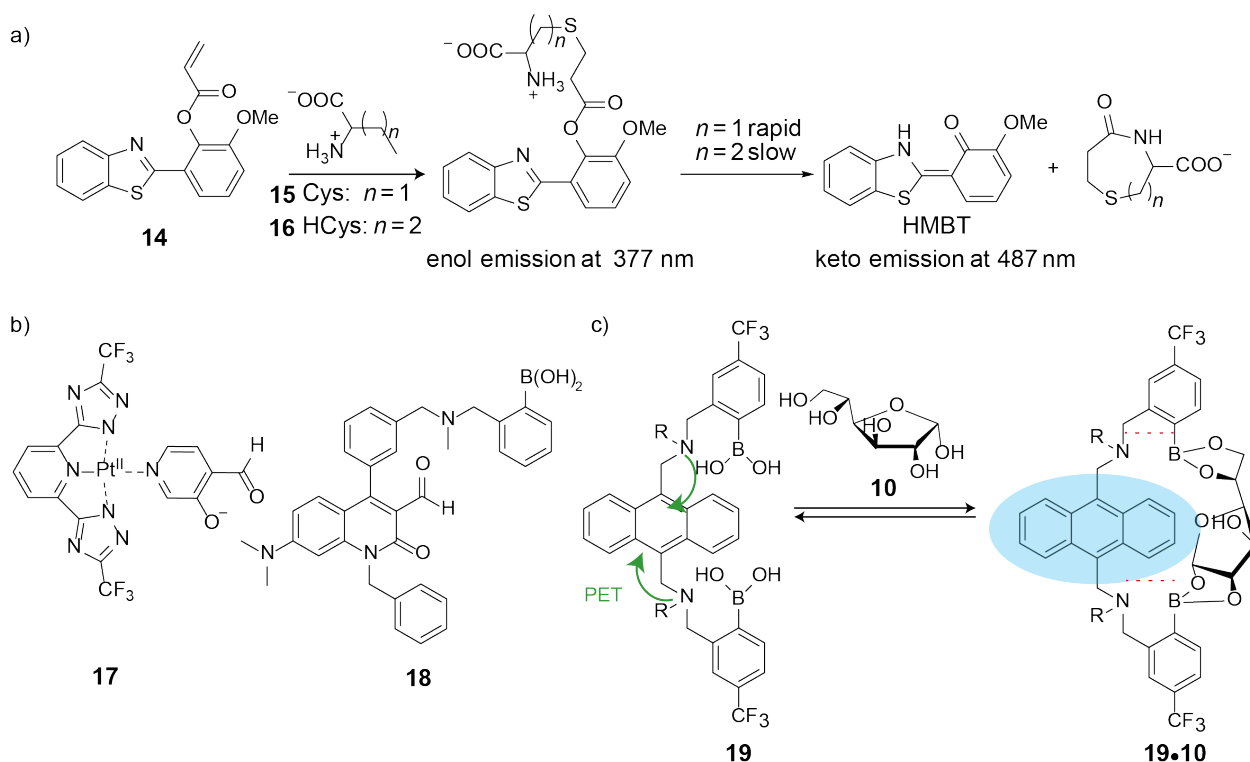


**Figure 4.** a) Chemical reaction of probe **14** with Cys (**15**) and HCys (**16**).<sup>7,53</sup> b) Chemical structures of a thiol-reactive turn-on Pt(II) molecular probe **17** and a molecular probe **18**, which is selective for catecholamines due to boronic acid and aldehyde recognition motifs.<sup>7,53</sup> c) Schematic representation of glucose detection by the boronic acid-based molecular probe **19** with an anthracene signaling unit developed by Senseonics™. The covalent bond formation between the target analyte glucose (**10**) and the boronic acid moieties of the molecular probe leads to the disruption of the intramolecular photoinduced electron transfer (PET), causing an emission turn-on. Adapted with permission from ref.<sup>54</sup> Copyright 2014 Elsevier BV.

Another functional group frequently used as an anchor point for artificial molecular probes is the amine group, which can form imine bonds with aldehyde groups and is mainly exploited for neurotransmitters such as serotonin (**5**). In addition to the amino group as the primary recognition motif, the hydroxy groups (OH) of catecholamines, such as dopamine (**4**), allow a reaction with aryl boronic acids.<sup>7,53</sup> If both detection motifs are combined within a molecular probe, selective detection of catecholamines, for example, can be achieved. GLASS and coworkers developed a

catecholamine-selective molecular probe **18** shown in **Figure 4b**. The structural design of **18** allowed the boronic acid (OH recognition unit) and the aldehyde group (amine recognition unit) to be spatially close, thereby selectively targeting the amino group and diol of catecholamine.<sup>7,55</sup>

Despite many different design strategies, of which some are shown within this thesis and highlighted by various reviews,<sup>7,45,56</sup> only a small selection of sensor systems based on molecular recognition are applied in medical diagnostics. Two inspiring examples are the glucose sensors from Senseonics™ and GlySure Ltd, based on fluorescent boronic acid probes embedded in polymers.<sup>54,57</sup> **Figure 4c** shows the structure and underlying reaction for detecting glucose (**10**) with the diboronic acid-based molecular probe **19** used in Senseonics™' invasive glucose sensor.<sup>54</sup> The fluorescence of the anthracene signaling unit of the *o*-amino-methylphenylboronic acid-base molecular probe **19** is quenched due to a photoinduced electron transfer (PET) from the electron lone pairs of the ternary amines. The reversible binding of glucose leads to weak N-B interactions due to increased Lewis acidity of the boron upon glucose binding, disrupting the PET and allowing an emission turn-on.<sup>54</sup> The molecular probe is embedded into a polymer matrix and, together with a light-emitting diode for excitation and two photodiodes for emission readout, this sensor can be implanted subcutaneously and allows for the dynamic monitoring of glucose levels.<sup>7,54</sup> Enzymatic digestion of carbohydrates (*e.g.*, the polysaccharide starch) produces monosaccharides such as glucose, which are associated with various functional disorders such as diabetes as a common disease, making their continuous monitoring important.<sup>20,22</sup> Molecular probes for carbohydrates are usually derived from boronic acids, as these engage in dynamic covalent interactions with the OH groups of the carbohydrate, forming five- and six-membered cyclic esters.<sup>58-61</sup> However, since carbohydrates all share the same structural motif (OH groups) and only differ in size and stereocenter configurations, it is difficult to ensure the selectivity of a probe for a certain carbohydrate.<sup>62</sup>

Overall, artificial molecular probes are powerful tools for detecting (small) substances, reflected in the myriad of examples of artificial probes.<sup>7,63</sup> However, they have some limitations, especially for biomarker sensing, which restricts their practicality for diagnostic devices. For example, a significant drawback is that they give only a static image, as they form irreversible bonds to the analyte.<sup>7</sup> Therefore, they cannot be used to study dynamic systems (*e.g.*, enzymatic reactions). Furthermore, the performance of boronic acid-based probes, for example, depends on external conditions such as pH and solvent.<sup>64</sup> An alternative approach is using chemosensors based on supramolecular host-guest chemistry, which is attractive due to the reversible non-covalent interactions allowing examination of dynamic processes.

### 3.2.2. Non-covalent interaction-based chemosensors

Supramolecular host-guest chemistry is based on molecular recognition through non-covalent interactions between a synthetic recognition unit (host (H)) and an analyte, further called guest (G). This concept is inspired by biomolecules such as proteins, which can bind (smaller) molecules in their binding pocket.<sup>65</sup> Artificial chemosensors following the principle of host-guest chemistry consist of a large macrocyclic or clamp-like synthetic host molecule with a cavity equipped with convergent binding sites resembling the binding pocket of a protein. A complementary guest molecule can be encapsulated in the host cavity, forming a host•guest inclusion complex.<sup>66,67</sup> The formation of the host•guest complex leads to a measurable change in chemical and or physical properties, *e.g.*, heat change due to the uptake or release of binding energy, a chemical shift in the NMR spectrum, or an optical signal alteration.<sup>45</sup> The complex formation is driven by non-covalent interactions such as hydrogen bonding, electrostatic interactions, and hydrophobic forces in combination with the match of size and shape of host and guest (see **Figure 5**).<sup>66,67</sup>

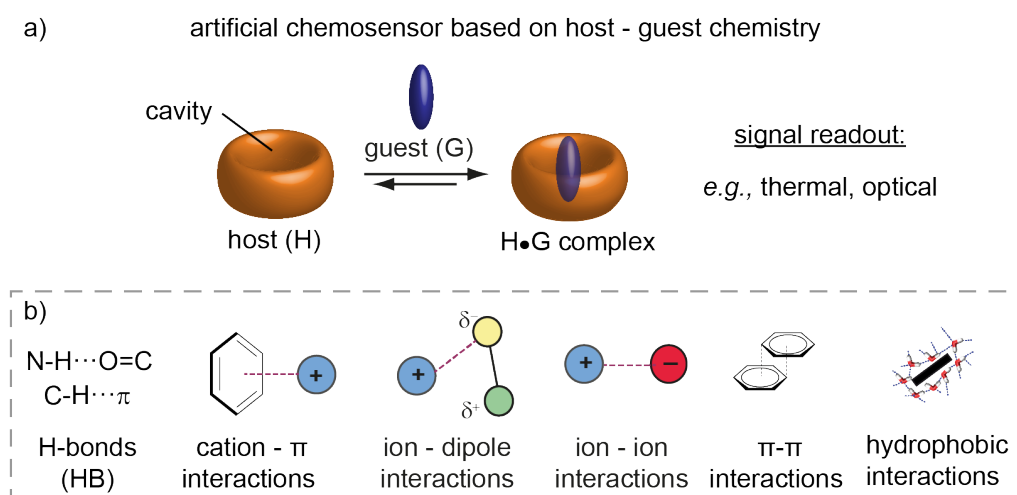


**Figure 5.** Schematic representation of a) the complexation of a guest (G) inside the cavity of a macrocyclic host (H) of an artificial chemosensor and b) possible non-covalent interactions.

The design of the host molecule for an analyte-specific chemosensor depends on the analyte one wishes to detect. Based on the nature of the analyte, specific non-covalent binding motifs are a prerequisite for host-mediated guest complexation. Thus, natural binding motifs and patterns are often adapted into synthetic host molecules to detect small biomarkers by mimicking the analyte's natural bioreceptor. One example is the development of artificial chemosensors for the detection of carbohydrates by mimicking the corresponding protein–analyte interactions.<sup>62,68</sup>

In nature, carbohydrate recognition is carried out by proteins called lectins, which can be found in many organisms, from animals to viruses to plants.<sup>69-71</sup> Lectins interact with carbohydrates in

their binding pockets through non-covalent hydrophobic interactions and hydrogen bonding (HBs).<sup>69-71</sup> HBs are the best-known examples of non-covalent interactions in nature. Not only do they contribute significantly to the stability of proteins and the formation of the DNA double helix, but they also explain the peculiarities of water with regard to its relatively high boiling point, its volumetric anomaly, and its high viscosity.<sup>72</sup> Hydrogen bonds are usually considered electrostatic interactions. However, the simplification of this type of interaction is not fully correct, as they consist of a complex interplay of polarization, electrostatic, and dispersion forces.<sup>73</sup> According to IUPAC, hydrogen bonds can generally be formed between a hydrogen atom bound to an electronegative atom (hydrogen bond donor) and a neutral or positively charged atom (hydrogen bond acceptor).<sup>56,66,67,74</sup> This definition also includes structural fragments such as  $\pi$ -systems. The HB between a positively polarized hydrogen atom and an electron lone pair of an acceptor is directional. Depending on the number of lone pairs and the acceptor molecule's general geometry, different geometries, hydrogen "bond" lengths, and strengths can appear.<sup>67</sup> The hydrogen bond interactions between a carbohydrate and the different amino acid residues of lectin in its binding pocket are exemplarily shown in **Figure 6a**.

Besides the depicted conventional hydrogen bonds, CH- $\pi$  interactions<sup>73</sup> are considered essential for binding carbohydrates in an aqueous environment due to the hydrophobic effect. CH- $\pi$  interactions are the weakest of the hydrogen bonds, and dispersion energy is usually the main energy contribution.<sup>73</sup> The stabilizing effect of such CH- $\pi$  bonds is dependent on the proton-donating ability of the CH group and the electron density of the acceptor  $\pi$ -system.<sup>73,75</sup>

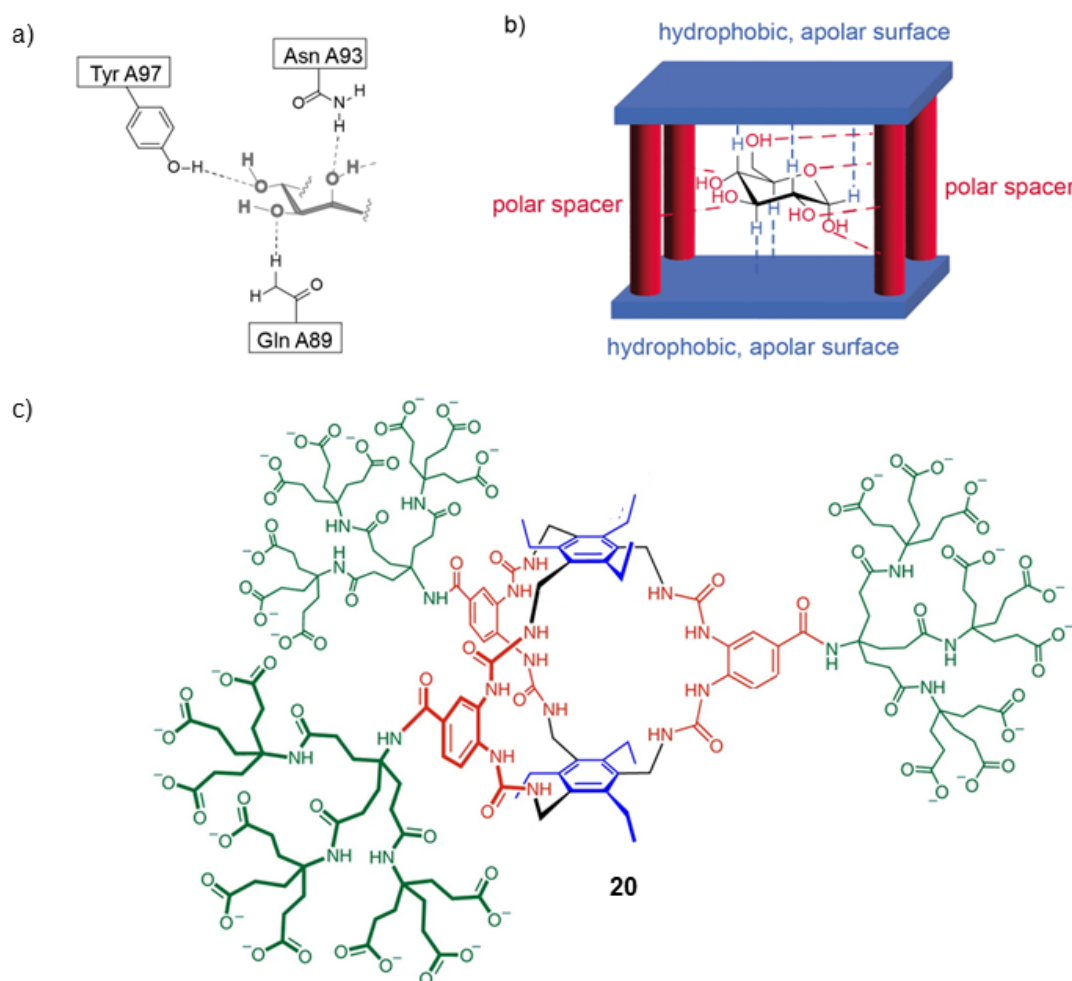


**Figure 6.** a) Exemplary depiction of O-H-O hydrogen bonds in a *Galanthus nivalis* lectin complex with mannose. Reproduced with permission from ref.<sup>76</sup> Copyright 2008, WILEY-VCH Verlag GmbH & Co. KGaA, Weinheim. b) Schematic representation of the temple-like design of an artificial carbohydrate chemosensor. Adapted with permission from ref.<sup>73</sup> Copyright 2011, Royal Society of Chemistry. c) Chemical structure of a monocyclic lectin-derived chemosensor (**20**). Reproduced with permission from ref.<sup>77</sup> Copyright 2019, Nature Publishing Group.

Lectins show binding affinities in the millimolar range for monosaccharides,<sup>78</sup> whereas oligosaccharides are usually bound stronger due to more interaction possibilities.<sup>76</sup> A single non-covalent interaction is comparably weak and will most likely not ensure the stability of a complex. However, the summative effect and positive interplay of various non-covalent interactions (cooperativity) add up to the stability of a complex.<sup>56,66</sup>

The structure of the lectin binding pockets and the non-covalent recognition motifs inspired the design of artificial lectins based on a temple-like structure for carbohydrate detection. The designed host molecules feature a hydrophobic, apolar (aromatic) bottom and top surface separated by polar spacers, creating a cavity that resembles a protein binding pocket. Within this cavity, neutral and charge-reinforced hydrogen bonds (dashed red lines in **Figure 6b**) and CH- $\pi$  interactions (dashed blue lines in **Figure 6b**) stabilize the bound carbohydrate.<sup>62,73</sup> Several research groups utilized the lectin-mimicking approach for carbohydrate detection. They initially

focused on organic solvents since water is generally a highly competitive solvent for carbohydrates due to its high polarity and ability to form HBs.<sup>68</sup> This results in low binding affinities ( $\log K_a = 2-3$ ) in aqueous media.<sup>62</sup> Therefore, the temple-like glucose sensor **20** developed by the DAVIS group is even more impressive as it offers a high binding affinity for glucose in phosphate buffer ( $K_a = 1.8 \times 10^5 \text{ M}^{-1}$ ) and human blood serum ( $K_a = 1.1 \times 10^5 \text{ M}^{-1}$ ).<sup>77</sup> **Figure 6c** shows the chemical structure of sensor **20**. The remarkably high binding affinity can be derived from extensive hydrogen bonding with the twelve urea-NH groups and the CH- $\pi$  interactions of glucose with the aromatic top and bottom fields. This sensor shows a high glucose selectivity compared to other monosaccharides due to the “perfect fit” of glucose into the host cavity with its all-equatorial OH groups.

In addition to the cavity design itself, the medium in which the chemosensor is supposedly applied is another important aspect. In a liquid system, each component is solvated, affecting the strength of the non-covalent bonds and, hence the complex stability/strength. For the application of artificial chemosensors to detect biomarkers in biological fluids, it is, therefore, essential that the host is water-soluble and that molecular recognition is guaranteed. Since the concept of artificial supramolecular host-guest inclusion complexes emerged, many different classes of synthetic hosts have been reported that allow application in aqueous media. The following section will briefly summarize the macrocycle classes of cucurbit[*n*]urils, cyclodextrins,<sup>79,80</sup> and calix[*n*]arenes,<sup>81-83</sup> commonly used for the sensing of small biomolecules. The main focus here is on cucurbit[*n*]urils, which were primarily used in this work.

### 3.2.3. Artificial macrocyclic hosts suitable for chemosensor design

#### 3.2.3.1. Cucurbit[*n*]urils as promising host molecules for chemosensor design

Cucurbit[*n*]urils (CB*n*) are macrocyclic host molecules composed of five to fourteen methylene-bridged glycoluril units.<sup>84</sup> Their initial discovery was reported by BEHREND ET AL.<sup>85</sup> in 1905 when an insoluble polymeric compound was isolated after the condensation of glycoluril and formaldehyde. However, due to technical limitations, the symmetric macrocyclic structure was not uncovered until almost 80 years later by MOCK ET AL.<sup>86</sup> Due to CB*n*'s close resemblance to a pumpkin from the *Cucurbitaceae* family, the identified molecules were named cucurbit[*n*]urils. In the following years, CB*n* were analyzed further, and their supramolecular properties were uncovered through the work of KIM, NAU, BUSCHMANN, and MOCK.<sup>87-90</sup> Various homologs of the CB*n* family have been isolated.<sup>87,91,92</sup> The synthesis of cucurbit[*n*]urils is based on the condensation reaction of formaldehyde and glycoluril in an acidic environment, where the number

of glycoluril units can be controlled by choosing certain reaction conditions (see **Figure 7a**). Under harsh conditions (conc. HCl or H<sub>2</sub>SO<sub>4</sub> with T > 110 °C), mainly CB6 is formed. In contrast, the homologs CB5, CB7, CB8, and CB10 are formed under milder conditions (9 M H<sub>2</sub>SO<sub>4</sub> with T = 75-90 °C). They can be separated by various dissolution and fractional crystallization steps.<sup>91,93</sup> So far, the formation of CB<sub>n</sub> is not fully elucidated, but it is suggested to run *via* a stepwise elongation process similar to a classical polymerization reaction and ends with the macrocyclization.<sup>91</sup>

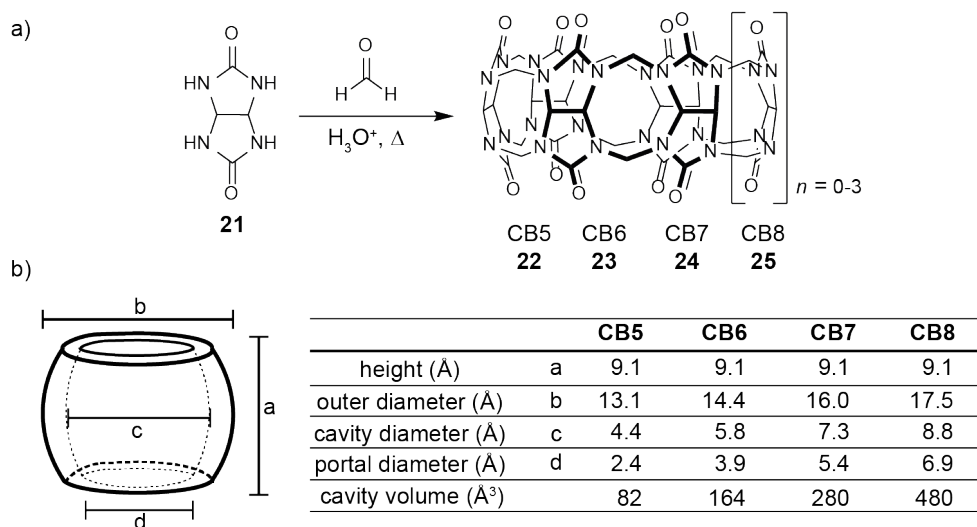


**Figure 7.** a) Synthesis of cucurbit[*n*]urils (*n* = 0-3) under acidic conditions. b) Structural parameters of the macrocyclic cucurbit[*n*]urils (*n* = 0-3).

The barrel-shaped structure of methylene-bridged glycoluril units provides a uniform height of 9.1 Å for all homologs of the CB<sub>n</sub> family. However, if other parameters, such as the diameter or the cavity volume, are considered, clear differences between the individual homologs become apparent. For example, the diameter of the carbonyl-fringed edges (portals) and the volume of the cavity, increase with the number of glycoluril units (see **Figure 7b**). This also determines their guest-binding properties and preferences, which are further discussed below. CB<sub>n</sub> possess a high thermal stability (370 °C for CB7 and 420 °C for CB5, CB6, and CB8) and are non-toxic, which is advantageous for potential applications in biological systems.<sup>94,95</sup> However, their moderate to poor water solubility is a minor drawback. Literature reports water solubilities for pure CB5 and CB7 of 20 - 30 mM<sup>84</sup> and CB6 and CB8 between 0.02 and 0.12 mM,<sup>93,96,97</sup> although adding acids or salts can significantly increase the solubility.<sup>89,93,94</sup>

The inner cavities of CB<sub>n</sub> are highly hydrophobic due to a lack of functional groups, electron lone pairs, or conjugated π-systems, which is accompanied by low polarizability inside the cavity.<sup>89</sup> The electron density of the lone nitrogen pairs of the ureido groups is mesomerically delocalized to the carbonyl-oxygen atoms of the ring.<sup>89,94</sup> This leads to a negative electrostatic potential at the

carbonyl rims, promoting directional ion-dipole interactions of a cationic guest with the dipole of the carbonyl groups of the  $CBn$ .<sup>98</sup> The strength of this interaction strongly depends on the solvation of the examined system as highly polar solvents such as water also interact with the ions through ion-dipole interactions causing a weaker effective charge of the ion.<sup>56,67</sup> Generally,  $CBn$  exhibit remarkably high binding affinities to a variety of neutral and cationic guests, preferentially binding hydrophobic and cationic ones that offer good shape-to-size complementarity (lock-and-key principle) with the cavity over neutral guests. This was, for example, shown for  $CB7$  with various adamantane guests.<sup>99</sup> The neutral 1-adamantanol (**26**) showed a binding affinity of four orders of magnitude lower than its cationic 1-amantadine analog (**27**), whose binding into the cavity is further stabilized by ion-dipole interactions with the carbonyl rims.<sup>99</sup> **Figure 8** shows a schematic representation of a  $CBn$  macrocycle with its hydrophobic cavity. The red-marked regions represent the specific binding sites for cationic species, which is elucidated by comparing the non-charged **26** and the cationic **27**.

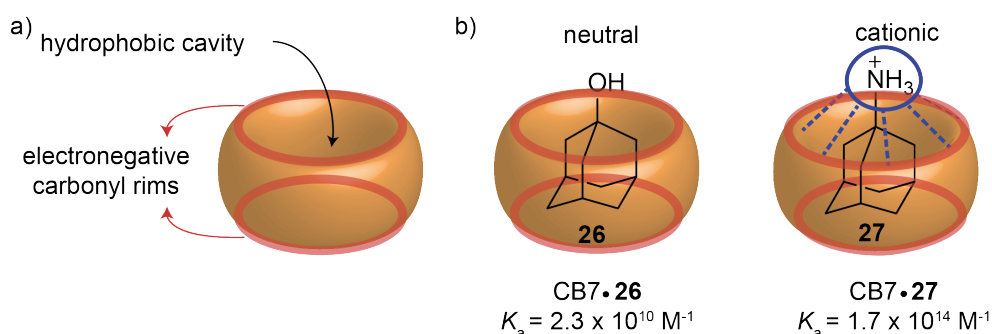


**Figure 8.** Schematic illustration of a) the different binding sites and non-covalent interaction motifs of  $CBn$  and b) the complexation of the neutral guest **26** and the cationic guest **27** by  $CB7$  with the corresponding binding affinities ( $K_a$ ) of each complex.<sup>99</sup> The cationic guest engages in ion-dipole interactions with the carbonyl rim depicted as dashed blue lines.

It has long been a mystery why  $CBn$  generally exhibit extremely high binding affinities for a wide range of guest molecules. Compared to other macrocycles of comparable size, the binding affinities for  $CBn$  are record-holding. Moreover, it is intriguing that the highest binding affinities of known  $CBn$  complexes follow the binding affinity trend  $CB6 < CB7 > CB8$ .<sup>100,101</sup> The classical entropy-driven hydrophobic effect generally explains why hydrophobic guests bind more strongly to hydrophobic cavities or tend to aggregate in aqueous media since a reorganization of the water molecules results in an entropy gain.<sup>66,67</sup> However, this does not explain why  $CBn$  have significantly higher binding affinities than CDs with similar hydrophobic cavity sizes.<sup>100</sup>

In 2012, a molecular dynamics (MD) simulation-based approach combined with isothermal titration calorimetry (ITC) measurements identified the release of "high-energy" water as the main driving force for the complexation of hydrophobic residues to  $CBn$ .<sup>98,102</sup> The encapsulated water

molecules form fewer hydrogen bonds than the maximum amount in bulk, resulting in so-called "high-energy water molecules" or energetically frustrated water molecules, see **Figure 9**. The complexation of hydrophobic guests leads to the release of some or all of the "high-energy water molecules" back into the bulk, thus driving the formation of the host•guest complex.<sup>102</sup> The release of encapsulated water molecules from a hydrophobic cavity often leads to an enthalpic gain. Therefore, contrary to the classical hydrophobic effect, this enthalpic-driven association of hydrophobic molecules is named the "non-classical hydrophobic effect."<sup>102</sup>

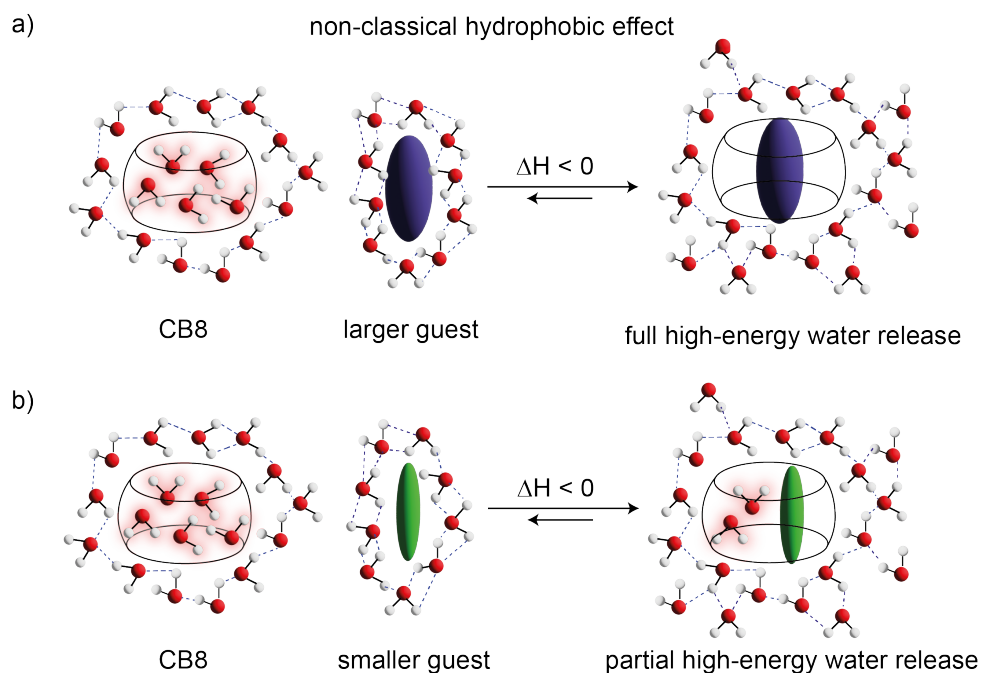


**Figure 9.** Schematic illustration of the a) full and b) partial release of high-energy water from the hydrophobic cavity due to the complexation of a larger (in a) and a smaller (in b) hydrophobic guest.

As a result of the cavity size, the number of "high-energy water molecules" is the smallest for CB5 (two water molecules located in the cavity obtained by simulation). The number increases with the size of the  $CB_n$  cavity (*e.g.*, CB7 ~ eight water molecules, CB8 ~ thirteen water molecules).<sup>89,103</sup> Intuitively, one might think that in the series from CB5 to CB8, the complex formation with CB8 as host should provide the highest enthalpy gain since it has the largest number of cavity water molecules. However, the experimental values showed that the highest enthalpy contribution is obtained with CB7 as host molecule. This can be explained by the fact that, due to the size of the cavities, the water molecules in CB8 can engage in more hydrogen bonds and are, therefore, energetically closer to bulk water again, compared to the ones bound in the CB7 cavity.<sup>94</sup>

Cucurbit[ $n$ ]urils find applications in various fields such as catalysis,<sup>89,104</sup> material science,<sup>105,106</sup> drug delivery,<sup>107,108</sup> or enzymatic assays<sup>109-111</sup> due to their unique (binding) properties such as high

binding affinities, chemical robustness, and toxicological safety. Due to their non-toxicity and excellent binding affinities towards various (biologically relevant) substance classes, they are commonly utilized host molecules for developing artificial chemosensors for sensing applications.<sup>7</sup> Since they are spectroscopically inactive,<sup>112</sup> *i.e.*, they do not show fluorescence emission and only absorb light in the UV region of the electromagnetic spectrum, they are usually combined with a fluorescent dye, which will be further discussed in Section 3.2.4.1.

### 3.2.3.2. Other artificial macrocyclic hosts suitable for chemosensor design

Cyclodextrins (CDs) are another class of macrocyclic hosts commonly used in artificial supramolecular host•guest inclusion complexes for sensing applications. Cyclodextrins are cyclic oligomers composed of 1,4-linked  $\alpha$ -D-glucose subunits. The three native cyclodextrins, namely  $\alpha$ ,  $\beta$ , and  $\gamma$ -CDs, composed of six, seven, and eight  $\alpha$ -D-glucose subunits, are extracted from starch by enzymatic degradation.<sup>113</sup> Their cyclic structure adopts a truncated cone shape, where the formation of the truncated cone causes the hydroxyl (OH) groups to point to the outsides of the cyclodextrins (see **Figure 10**). This arrangement of OH groups enables the CDs to form hydrogen bonds with water molecules, resulting in good water solubility of the CDs compared to cucurbit[*n*]urils ( $\alpha$ -CD: 149 mM,  $\beta$ -CD: 16.2 mM and  $\gamma$ -CD: 179 mM).<sup>114</sup> Because the C6-OH groups point towards the narrow (lower) rim, cyclodextrins have an outer diameter of 14.6 to 17.5 Å and an inner cavity diameter of 4.7 to 5.3 Å, depending on the number of glucose subunits.

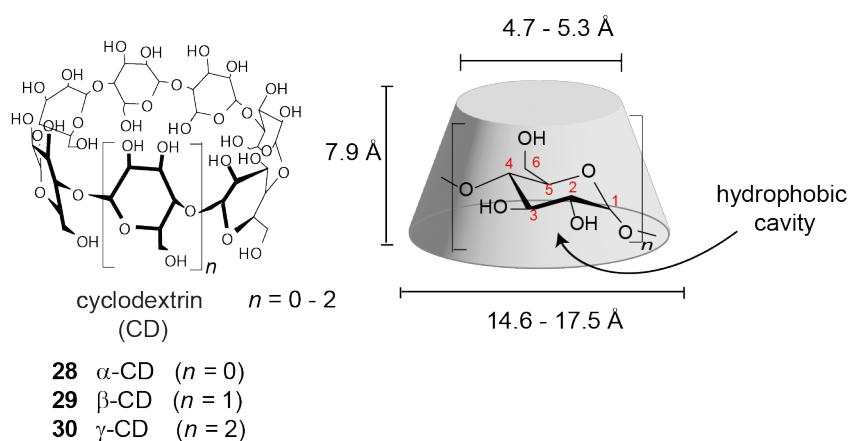


**Figure 10.** Chemical structure and schematic representation of cyclodextrins with  $n = 0 - 2$ .

Cyclodextrins are comparable in size to the CB $n$  analogs and feature a hydrophobic cavity.<sup>115</sup> Cyclodextrins can form host•guest inclusion complexes with charged and neutral guests ranging from small organic molecules, *e.g.*, steroids, small acids, adamantane, and derivatives to synthetic drugs and proteins.<sup>113</sup> The complexes are stabilized by hydrophobic interactions inside the cavity as well as hydrogen bonding with/to the CD portals. Compared to CB $n$ , CDs exhibit much lower

binding affinities ( $K_a = 10 - 10^5 \text{ M}^{-1}$ ) despite their similar cavity size, as their cavity shape allows the formation of HB between the encapsulated water molecules and the CD, leading to a lower enthalpic gain due to the water-release upon guest binding.<sup>100</sup> Thus, they require millimolar guest concentrations to form a stable complex.<sup>116,117</sup>

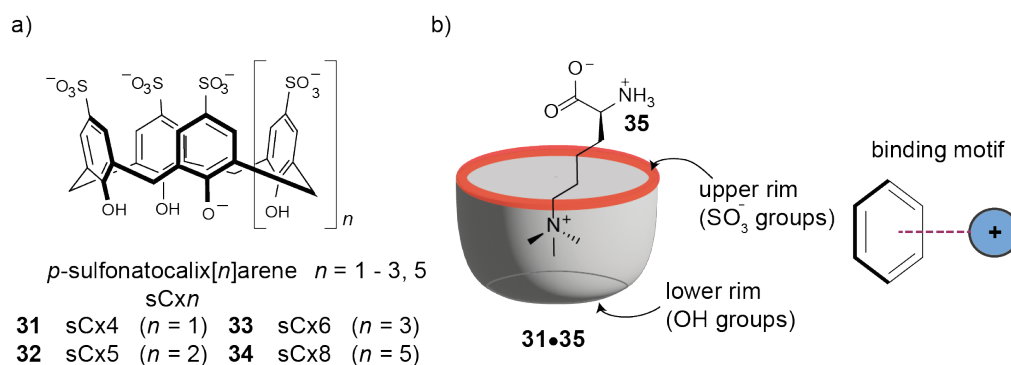


**Figure 11.** a) Chemical structure of *p*-sulfonatocalix[ $n$ ]arenes (sC $xn$ ) with  $n = 1 - 3, 5$ . b) Schematic representation of the cone-like structure of sC $x4$  in a complex with trimethyl lysine (**35**) engaging in cation- $\pi$ , hydrophobic, and ion-ion interactions.

The third class of macrocycles that is used within this work are *p*-sulfonatocalix[ $n$ ]arenes (sC $xn$ ), a subclass of calix[ $n$ ]arenes (C $xn$ ). Calix[ $n$ ]arenes are cyclophanes in which a methylene bridge links the phenol moieties at the meta positions of the aromatic rings.<sup>66</sup> This family of macrocycles is synthesized *via* an acid-catalyzed condensation reaction of phenol and formaldehyde, similar to C $Bn$ .<sup>118</sup> The most commonly used and commercially available sizes are C $x4$  ( $n = 4$ ) to C $x8$  ( $n = 8$ ), with  $n$  describing the number of phenolic subunits within the ring. Calix[4]arene typically adapts a cone conformation, with a wider upper rim (diameter of C $x4 = 3.8 \text{ \AA}$ )<sup>119</sup> and a narrow lower rim.<sup>66,120</sup> The upper and lower rim of the host scaffold can be functionalized with various anionic, cationic, and neutral functional groups. The upper rim can be sulfonated through treatment with sulfuric acid, thus creating the water-soluble analogs *p*-sulfonatocalix[ $n$ ]arenes.<sup>81,121</sup> The *p*-sulfonatocalix[ $n$ ]arenes **31 - 34** (see **Figure 11a**) offer a hydrophobic cavity in which cationic guests, such as metal cations,<sup>122</sup> amino acids,<sup>123</sup> drugs,<sup>83</sup> or peptides, are bound.<sup>124,125</sup> The formation of these complexes is mediated by non-covalent cation- $\pi$  and  $\pi$ - $\pi$  interactions, hydrophobic interactions, and hydrogen bond formation. **Figure 11b** shows an inclusion complex of trimethyl lysine (**35**) with sC $x4$  (**31**) ( $K_a = 3.7 \times 10^5 \text{ M}^{-1}$ ) where the main driving force of the complex formation can be assigned to the cation- $\pi$  interaction of the ternary amine moiety of **35** and the electron-rich aromatic core of the calix[ $n$ ]arene.<sup>126</sup> Although conjugated systems are generally considered apolar, the nature of the attractive interaction between a positively charged moiety and the  $\pi$ -system of a benzene ring is rooted in the electron density distribution within the planar molecule.<sup>127</sup> Due to the higher electronegativity (EN) of

carbon compared to hydrogen, the C-H bonds experience a shift of the electron density towards the ring centre, forming a permanent quadrupole moment. This allows the formation of two opposite axial dipole moments, enabling an attractive electrostatic interaction between the cation and the electron density of the aromatic ring.<sup>56,67,128</sup> Compared to CB*n*, *p*-sulfonatocalix[*n*]arenes generally show weaker binding affinities ( $K_a \sim 10^2 - 10^7 \text{ M}^{-1}$ ) and are generally limited to cationic guests. However, due to their low toxicity, they are commonly used in biological applications such as enzymatic reaction monitoring.<sup>129,130</sup> In such applications, the *p*-sulfonatocalix[*n*]arenes are usually combined with a fluorescent dye to form an optical chemosensor since the parent host is spectroscopically silent. A general discussion on possible optical-based sensing assays for spectroscopically silent hosts is given in Section 3.2.4.1.

### 3.2.4. Determination of binding affinities ( $K_a$ ) of supramolecular host•guest complexes

The knowledge of the binding affinity and the resulting stability of a supramolecular host•guest complex is essential when considering potential applications. For example, for artificial chemosensors, which are intended to detect small biomolecules, it is important that they selectively bind an analyte (guest) molecule with high affinity to obtain the most accurate result. The stability of the host•guest complex is defined by the binding affinity  $K_a$ , also called the binding constant or association constant.<sup>131</sup> In the means of a host•guest complex, this thermodynamic constant is a special type of the equilibrium constant  $K$  and characterizes the binding reaction of a host (H) and a guest (G) using the following equilibrium equation (Eq. 1):<sup>66,132,133</sup>



Eq. 1 describes the formation of a 1:1 complex and can be reformulated as binding affinity  $K_a^{HG}$  as showcased in Eq. 2. with [HG] corresponding to the concentration of the host•guest complex (H•G) at equilibrium and [H] and [G] corresponding to the concentrations of host and guest at equilibrium, respectively.

$$K_a^{HG} = \frac{[\text{HG}]}{[\text{H}][\text{G}]} \quad \text{Eq. 2}$$

$K_a$  is a dimensionless constant since, strictly speaking, not the concentrations but the dimensionless activities of the respective partners are considered.<sup>132</sup> However, these are assumed to be nearly identical for all species involved in the complex formation since the binding affinities

are determined at high dilutions.<sup>132</sup> With this assumption, the activity coefficients are neglected, and only the concentrations of the species are used here, resulting in the dimension  $M^{-1}$ .<sup>132</sup> In biochemistry, the stability of a complex is often denoted in terms of dissociation constants  $K_d^{HG}$ , which equals the reciprocal values of the binding affinities  $K_a$ , see **Eq. 3**.

$$K_a^{HG} = \frac{1}{K_d^{HG}} \quad \text{Eq. 3}$$

It generally applies that the larger the binding constant or, the smaller the dissociation constant, the more stable the complex. Since binding constants are thermodynamic parameters, they can be transformed into free binding energies  $\Delta G^0$  using the Gibbs equation (**Eq. 4**) with R as the universal gas constant and T as temperature.<sup>66</sup>

$$\Delta G^0 = -RT \ln K_a \quad \text{Eq. 4}$$

The dependence of the binding constant on temperature becomes obvious with **Eq. 4**. For the application of an artificial supramolecular chemosensor, especially in the field of biomarker detection, it is vital that the selected chemosensor has a high selectivity and sensitivity for the desired analyte. Please note that systems are generally only directly comparable regarding complex stability when parameters such as solvent and temperature are identical.

Depending on the chemosensing system, the experimental investigation of the complexation parameters of a selected host•guest complex can be conducted using various methods. For example, the release or consumption of energy (mostly in the form of heat) during guest complexation by a host molecule can be determined by isothermal titration calorimetry (ITC).<sup>134,135</sup> It is also possible to investigate the complexation event using nuclear magnetic resonance (NMR), but this method requires mM concentrations.<sup>67,136</sup> Since many biomarkers are present in the  $\mu M$  concentration range in biofluids, NMR is, rather unsuitable for biomarker detection.<sup>7</sup>

Optical-based detection methods, *i.e.*, UV-Vis and emission spectroscopy, are commonly employed for the photophysical determination of  $K_a$ .<sup>132,133</sup> due to their easy use at low costs and straightforward data interpretation. Emission-based detection methods are often preferred since they are highly sensitive even for small sample amounts compared to absorbance. The underlying photophysical processes for absorbance and emission spectroscopy can be explained by a Jablonski diagram (see **Figure 12**).<sup>137</sup> The diagram illustrates potentially occurring transitions between different electronic states (S = singlet, T = triplet) of a molecule after absorption of a photon with suitable energy. The irradiation of a molecule with light can lead to the absorption of

a photon. Thereby an electron can be raised from the ground state ( $S_0, v_0$ ) to an excited state ( $S_x$ ) with a higher vibrational level (grey lines in **Figure 12**), resulting in the molecule in the excited state. The required energy of the absorbed photon depends on the energy gap between  $S_0$  and  $S_x$  and is characteristic of each molecule.<sup>138</sup> The absorption of a photon is a fast process that occurs within  $10^{-15}$  s without changes in the atomic nuclei configuration (Franck-Condon principle).<sup>139</sup> The electron in the excited state can undergo several relaxation processes from the higher vibrational level. Usually, the electron relaxes *via* internal conversion (IC) into the energetically lowest-lying vibrational state of  $S_1$  (Kashas's rule).<sup>140</sup> This process occurs at a times scale of  $12^{-12}$  s.<sup>141</sup> From the vibrational ground state of  $S_1$  ( $S_1, v_0$ ), the electron can return to the  $S_0$  ground state by non-radiative relaxation ( $Rel_{vib}$ ) or by radiative transmission called fluorescence emission (Fl), which occurs at a more red-shifted wavelength than the wavelength of the absorbed photon. The lifetime of fluorescence emission is  $10^{-8}$  s. The radiative return is usually to a higher vibrational level of the ground state, from which a rapid return ( $10^{-15}$  s) to the vibrational ground state  $S_0$  occurs.<sup>141</sup>

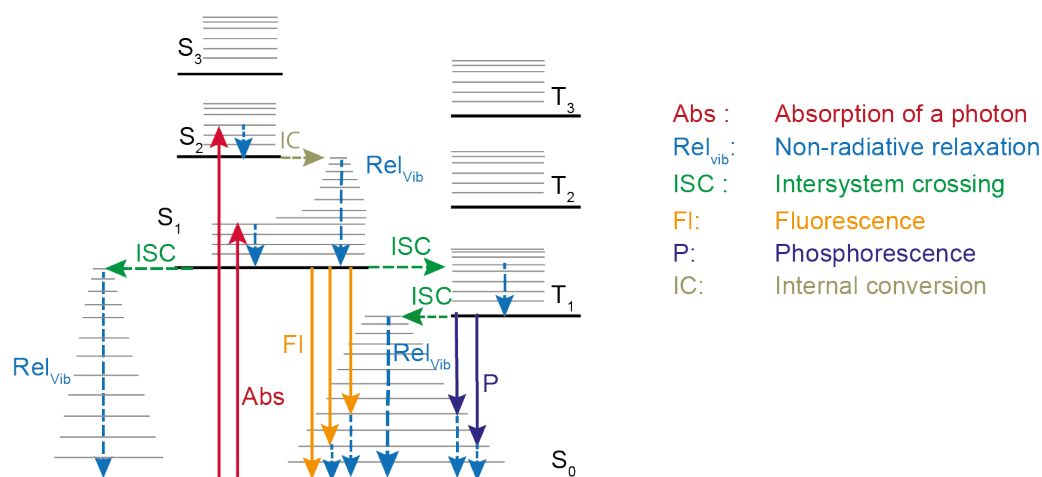


**Figure 12.** Jablonski diagram.

A direct excitation from a singlet into a triplet state is quantum mechanically forbidden according to the selection rules since the multiplicity of an electron is not allowed to change within the excitation.<sup>142</sup> However, due to intersystem crossing (ISC), which results from spin-orbit coupling, the transition of an electron into a state with a different multiplicity is still possible after excitation to the excited state.<sup>141,142</sup> Conversely, the return from the triplet to the singlet ground state is also forbidden, as a result of which light is emitted over a significantly longer time. This radiative relaxation over a longer time is called phosphorescence (P) and shows lifetimes of  $10^{-2}$  to  $10^4$  s.<sup>142,143</sup>

The macrocyclic hosts  $CB_n$ , CDs, and  $sC_xn$  presented in Section 3.2.3 are suitable receptor units for artificial chemosensors to detect biologically relevant molecules because of their binding properties (affinities and selectivity), their symmetric cavities, chemical robustness, and toxicological safety. However, all three host classes are inherently spectroscopically inactive, *i.e.*, non-emissive and only active in the short wavelength UV region of the electromagnetic spectrum.<sup>45,112</sup> In order to still be able to use these hosts for optical sensing, especially emission-based sensing, there are several ways to convert the analyte binding into a readable optical signal. The following section will schematically describe three types of binding assays commonly used for optical-based artificial chemosensors.

#### 3.2.4.1. Types of binding assays for emission-based sensing

The direct binding assay (DBA) is the most straightforward sensing assay, provided it is usable to the system under investigation since it involves only the host as receptor and the guest (see **Figure 13a**).<sup>112</sup> Within this type of binding assay, the associative interaction between a host (H) and a guest (G) molecule results in a directly measurable and easily quantifiable signal change, such as the emergence or disappearance of an absorbance or emission band.<sup>144</sup> In optical sensing, the type of binding assay is generally only applicable to host-guest pairs in which one of the two is spectroscopically active, *i.e.*, the photophysical properties of one compound change due to complex formation.<sup>144</sup> Thus, DBAs are attractive for systems where the guest (*i.e.*, the target analyte) shows a unique spectroscopic response that allows for the discrimination from signals caused by cross-reactive analytes.<sup>7</sup> For unmodified hosts such as cucurbit[ $n$ ]urils, cyclodextrins, or calix[ $n$ ]arenes, DBA is typically used for the examination of the complex formation of fluorescence dyes such as berberine chloride (BC, **38**),<sup>7,145-147</sup> lucigenin (**39**),<sup>130</sup> or 2,7-dimethyl diazapyrene (MDAP, **40**)<sup>147,148</sup> shown in **Figure 14**. Due to the low polarizability of the inner cavity of  $CB_n$ , solvatochromic dyes encounter a change in absorbance, fluorescence, or phosphorescence when encapsulated in  $CB_n$ .<sup>95</sup> Modifying spectroscopically silent macrocycles is possible so the host can act as a signaling entity itself. The fluorescent chemosensor **36** shown in **Figure 13b** is an example of a chemosensor using a  $CB_6$  modified with naphthalene, which can sense aliphatic amino acids in the presence of  $Eu^{3+}$  salts.<sup>149</sup> However, this type of approach is synthetically often challenging.

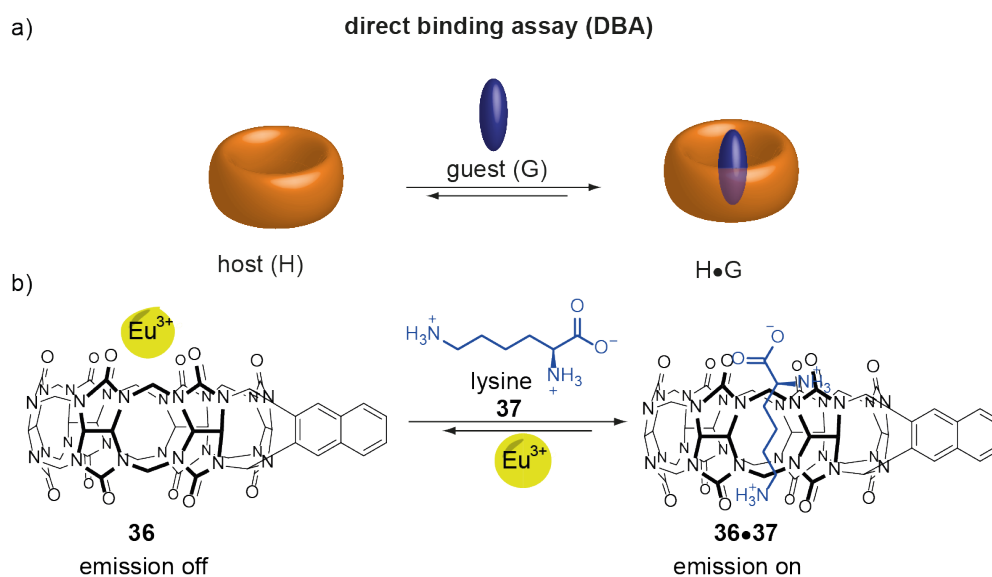


**Figure 13.** Schematic representation of the mechanism of a) a **direct binding assay (DBA)** for spectroscopically active guests, and b) the detection of the amino acid lysine (**37**) with the naphthalene- modified CB6 (**36**). Europium cations ( $\text{Eu}^{3+}$ ) are binding to the carbonyl rim of CB6, quenching the fluorescence of **36**, the displacement of  $\text{Eu}^{3+}$  by lysine leads to an emission turn-on.<sup>149</sup>

If a DBA is not possible with the system under investigation, an **indicator displacement assay (IDA)** is a viable option.<sup>150,151</sup> An IDA is a **competitive binding assay (CBA)** based on the competition between two different guest molecules for a host molecule.<sup>152</sup> In an IDA, a host is self-assembled with a chromophoric indicator dye in a pre-equilibrium, forming a host•dye complex (see **Figure 14**). The subsequent addition of a competing guest leads to the displacement of the dye from the host cavity, which is followed by a measurable change in the spectroscopic properties of the indicator dye.<sup>7,112,144,147,152</sup> In contrast to its simplicity, IDA-based sensing arrays are often unsuitable for distinguishing target analytes from interfering analytes (with unknown concentrations) as the displacement of the indicator is only dependent on the concentration and binding affinity of the guest and results in an analyte-independent spectroscopic response.<sup>7</sup>

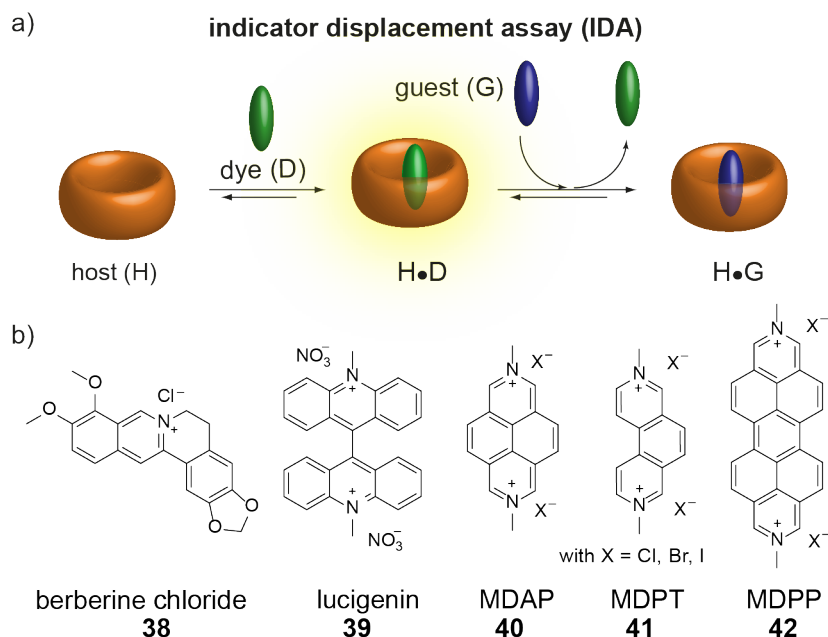


**Figure 14.** a) Schematic representation of a competitive **indicator displacement assay (IDA)** mechanism with an indicator dye as signaling unit. b) Chemical structures of selected dyes commonly used in DBA, IDA, and ABA.

The **associative binding assay (ABA)** is a special assay that only applies to specific host molecules. ABA is based on the simultaneous binding of two guests in a single host cavity (see **Figure 15a**). Therefore, an ABA is only applicable if the host molecule has a sufficiently large cavity that can simultaneously encapsulate two guest molecules of suitable size.<sup>109,112,153,154</sup> When using an ABA for the optical detection of analytes with a spectroscopically silent host, the host is pre-equilibrated with an indicator dye similar to IDAs. However, the guest added in a second step does not displace the dye but binds in close proximity to it in the host cavity, resulting in an electronic coupling between the two molecules.<sup>112</sup> An ABA is commonly used with CB8, where an aromatic electron-poor molecule (*e.g.*, an indicator dye such as **38-42** in **Figure 14b**) and an aromatic electron-rich guest (*e.g.*, the target analyte) form a charge transfer (CT) complex inside the cavity.<sup>155,156</sup> Due to the analyte-specific interaction with the indicator dye, spectroscopic “fingerprints” can be observed, allowing discrimination of different analytes.<sup>7</sup>

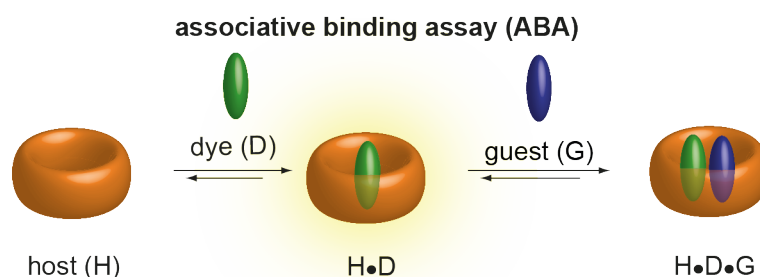


**Figure 15.** Schematic representation of an **associative binding assay (ABA)** mechanism with an indicator dye as a signaling unit.

Titration can be performed with a guest molecule using one of the assay methods presented to determine the binding affinity of the host•guest complex. As a result of the guest addition, the host•guest complex is formed, changing the components' microenvironment and leading to an electron or energetic transfer or aggregation-induced emission changes. The resulting emission enhancement or quenching can be recorded as binding titration isotherms<sup>157</sup> and fitted according to **Eq. 9** (DBA)<sup>139,157</sup> or **Eq. 16** (IDA).<sup>150,158</sup>



$$K_a^{\text{HD}} = \frac{[HD]}{[H][D]} \quad \text{Eq. 6}$$

**DBA**

$$[H]_0 = [HD] + [H] \quad \text{Eq. 7}$$

$$[D]_0 = [HD] + [D] \quad \text{Eq. 8}$$

$$I_c = I^0 + I^{\text{HD}} \cdot [HD] + I^{\text{D}} \cdot [D] \quad \text{Eq. 9}$$

**IDA**

$$K_a^{\text{HD}} = \frac{[HD]}{[H][D]} \quad K_a^{\text{HG}} = \frac{[HG]}{[H][G]} \quad \text{Eq. 12}$$

$$[H]_0 = [HD] + [H] + [HG] \quad \text{Eq. 13}$$

$$[D]_0 = [HD] + [D] \quad \text{Eq. 14}$$

$$[G]_0 = [HG] + [G] \quad \text{Eq. 15}$$

$$I_c = I^0 + I^{\text{HD}} \cdot [HD] + I^{\text{D}} \cdot [D] \quad \text{Eq. 16}$$

Parameters for **Eq. 5** to **Eq. 16** were assigned as follows: [H]: host concentration at equilibrium, [H]<sub>0</sub>: initial host concentration, [D]: dye concentration at equilibrium, [D]<sub>0</sub>: initial dye concentration, [G]: guest concentration at equilibrium, [G]<sub>0</sub>: initial guest concentration, [HD]: host•dye (H•D) concentration at equilibrium, [HG]: host•guest (H•G) concentration at equilibrium,  $K_a^{\text{HD}}$ : binding constant of the host•dye (H•D) complex,  $K_a^{\text{HG}}$ : binding constant of the host•guest (H•G) complex,  $I^0$ : background signal,  $I^{\text{HD}}$ : signal from host•dye (H•D) complex,  $I^{\text{D}}$ : signal from the free dye (D),  $I_c$ : observable signal as a function of concentration.

### 3.2.5. Sensing of biorelevant molecules in aqueous media and biofluids

Artificial chemosensors based on water-soluble macrocycles are a promising option for detecting biorelevant molecules in aqueous media. The combination of macrocyclic hosts with different indicator dyes in an IDA or ABA approach allows the generation of a variety of chemosensors with different optical properties in a simple way without tedious synthetic procedures. There are many examples in literature<sup>7,45,159</sup> for the detection of small (bio-)molecules in aqueous media using artificial chemosensors. Some selected examples are presented in this section, reflecting the current state of the art in this area as well as current limitations.

Over the past years, cucurbit[*n*]uril-based chemosensors have emerged as an interesting class of macrocycles due to their unprecedentedly high binding affinities for neutral and cationic organic small molecules. For example, they have been used in various assays to detect amino acids and peptides in aqueous media and low saline buffers.<sup>160,161</sup> In this context, various IDA-based assays were developed that enabled the detection of enzymatic degradation of amino acids or peptides in a time-resolved manner.<sup>111,162,163</sup> For example, NAU ET AL. introduced a CB7-based tandem assay<sup>110,164</sup> that allows for the selective detection of various aliphatic amino acids. Despite their high binding affinities, CB*n* generally bind a wide range of analytes, making the selective detection of, *e.g.*, a certain amino acid difficult, especially when measuring in a complex mixture of various amino acids.<sup>7</sup> By utilizing a substrate-specific enzyme, *i.e.*, a decarboxylase, it was possible to selectively sense a specific amino acid, *e.g.*, lysine, tryptophan, using a CB7•dapoxyl emission turn-off chemosensor in a 10 mM ammonium acetate buffer, pH 6.0. The substrate-specific enzyme can only decarboxylate its matching substrate (zwitterionic amino acid), transforming it into the decarboxylated product (cationic amine). The decarboxylated product shows a higher binding affinity for CB7 and, thus, replaces the dapoxyl dye (**43**) from the CB7 cavity. Besides the CB7•dapoxyl, they also used a sCx4•DBO in the same experimental setup, getting similar selectivity results. A schematic depiction of the substrate-specific tandem assay is shown in **Figure 16a**, and the chemical structures of the dyes dapoxyl and DBO are shown in **Figure 16b**. A comparable approach was taken for monitoring the enzymatic methylation of a lysine-containing peptide utilizing a sCx4•lucigenin emission turn-on chemosensor in 5 mM glycine buffer, pH 2.0.<sup>162</sup>

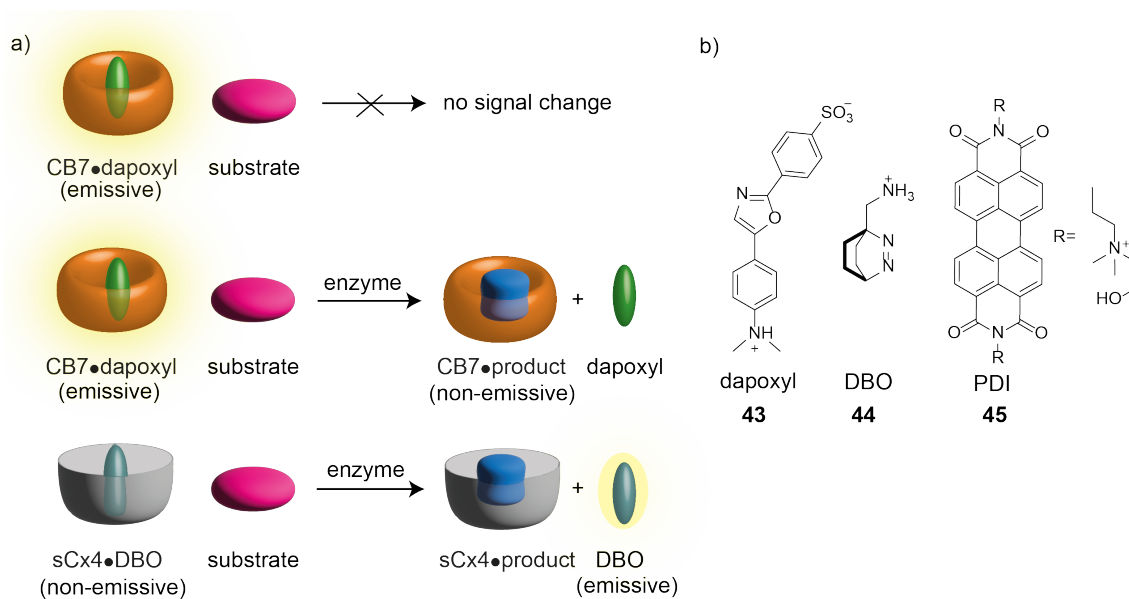


**Figure 16.** a) Schematic representation of the enzyme tandem assay with CB7•dapoxyl and sCx4•DBO. The substrate is a weak competitor that cannot displace the dye, thus, no signal change is observed. The enzymatic conversion of the substrate into the product leads to the displacement of the dye from the host due to the product's higher binding affinity towards the host. An emission turn-off was observable for CB7•dapoxyl and an emission turn-on for sCx4•DBO upon dye displacement. b) Chemical structures of dapoxyl (**43**), DBO (**44**), and PDI (**45**).

The detection of neurotransmitters has been investigated by SCHERMAN and coworkers using an ABA with CB8•PDI as a chemosensor.<sup>165</sup> Dopamine (**4**) was selectively detected in water with a detection limit lower than  $2 \times 10^{-5}$  M by quenching the emission of perylene bisdiimide (PDI **45**, in **Figure 15b**) during the formation of a 1:1:1 hetero-ternary complex. The presence of the known interferents epinephrine, norepinephrine, and ascorbic acid did not alter the spectroscopic readout for dopamine, proving the chemosensor's selectivity in this context.

The presented chemosensors have a crucial drawback, transferable to almost all self-assembled chemosensors for IDAs and ABAs developed so far. These chemosensors have previously only been tested in aqueous media and low-saline buffers, which is a good starting point for sensing applications related to biorelevant substances. However, the transfer of the chemosensors into high-saline buffers and biofluids needs to be possible to realize their application in molecular and clinical diagnostics. A major hurdle for this step, especially for CB $n$ , is the presence of large amounts of salt or other competitive substances.<sup>166</sup> Alkali metal and alkaline earth metal cations such as Na<sup>+</sup> or K<sup>+</sup> act as competitors for CB $n$ , as they bind to their portals and reduce the binding affinity of an analyte by a factor of up to 1000.<sup>166</sup> This is problematic because salts occur in millimolar concentrations in all biofluids. Thus, those chemosensors cannot be applied in biofluids, as the host•dye complex disassembles in the presence of high amounts of salts. Besides, certain anions such as halogenides perturb the photophysical properties of indicator dyes such as lucigenin,<sup>167</sup> by emission quenching, giving false emission readouts. Biofluids such as urine or

blood serum are of high diagnostic relevance for detecting diseases, as their metabolome reveals information about a person's health condition.<sup>168,169</sup> They contain several hundred organic substances and proteins, many of which serve as biomarkers for specific health conditions.<sup>7</sup> However, this large number of substances combined in one medium also presents a challenge for chemosensors. Due to competitive interactions, the presence of many different substances often makes selective and sensitive detection of target analytes difficult.

A common workaround for the low selectivity of a single chemosensor is the use of a sensor array. In this approach, various cross-reactive chemosensors are combined in an array format, where the interactions of the chemosensors are not selective, but they detect the analytes to different extents.<sup>170</sup> Thus, a unique pattern (*i.e.*, fingerprint) is obtained for each analyte that can be simplified and visualized by chemometric analysis, such as principal component analysis (PCA) or linear discriminant analysis (LDA).<sup>171</sup> Those statistical methods reduce the multidimensionality of the data to scores plots, which visualize the differentiation of the different analytes present in the sample. This differential sensing approach was popularized by ANSYLN ET AL. and raised to a common sensing approach that circumnavigates the cumbersome preparation of selective chemosensors for a specific analyte.<sup>170,172-174</sup> ANZENBACHER ET AL. showcased the sensing and discrimination of fourteen commonly administered carboxylate drugs, such as ibuprofen and diclofenac, by a supramolecular array of eight chemosensors based on octamethyl calix[4]pyrrole (**46**) immobilized in a hydrogel matrix. It was even possible to discriminate the different drugs over concentration ranges of 0.5 - 100 ppm, which covers the typical concentrations of those carboxylate drugs found in urine.<sup>175</sup> A similar experiment was performed by the same group for nine common over-the-counter cold and flu drugs, such as acetaminophen or doxylamine, where mixtures of different drugs were discriminated by a sensor array of two fluorescent CB $n$ -type chemosensors.<sup>176</sup> A schematic description of a typical chemosensor array design is shown in

**Figure 17.**

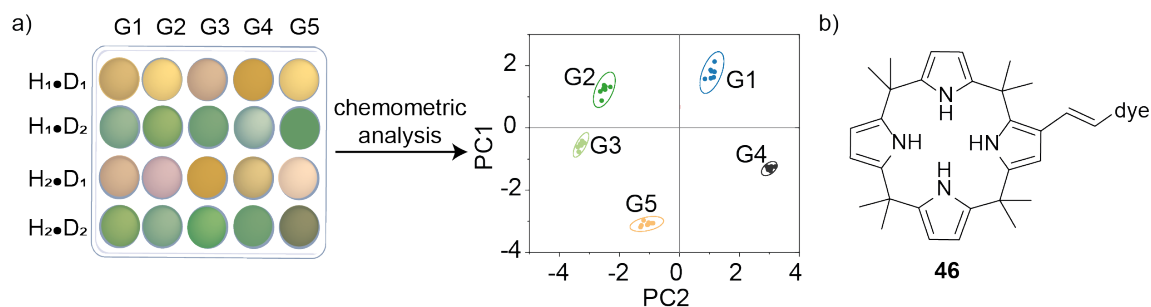


**Figure 17.** a) Schematic representation of an array of different hosts (H<sub>x</sub>) and dyes (D<sub>y</sub>) that can cross-detect a variety of analytes (G<sub>z</sub>). The obtained multidimensional data can be reduced to a 2D-scores plot by chemometric analysis such as PCA. b) Chemical structure of the octamethylcalix[4]pyrrole core (**46**) of the chemosensors used for the discrimination of fourteen different drugs, such as ibuprofen.

## 4. Aim

The field of molecular diagnostics requires detection methods that are capable of rapidly and accurately discovering natural metabolites and disease indicators, as well as monitoring the therapeutic effects of administered pharmaceuticals. A criterion for these techniques is the ability to recognize a specific analyte or biomarker from a complex matrix under physiological conditions, thus enabling accurate and timely diagnoses and treatments. In this context, artificial chemosensors based on supramolecular host•guest interactions are a promising alternative to antibody-based natural receptors for reaching this aim as the latter often lack stability and are cost- and time-intensive and show cross-reactivity.<sup>38,177</sup> Furthermore, artificial chemosensors can easily outperform instrumental-based analysis methods such as HPLC-MS or NMR in terms of lower costs, shorter assay times, and no need for trained personnel.<sup>7</sup> Consequently, the development of fast-responding chemosensor systems using host molecules has been firmly pushed within the last decade. However, despite many promising results, it remains challenging to develop robust chemosensors that allow for both the sensitive and selective recognition of target analytes within a complex media, *e.g.*, urine or blood serum, containing high amounts of salts or other biologically relevant interferents.

Therefore, the overarching aim of this work was the design and development of new, robust supramolecular chemosensing systems that allow for the selective detection of health-related and biologically relevant small molecules in salt-containing media and biofluids.

At the beginning of my PhD studies, deeper insight and a fundamental understanding of host•guest interactions were gained by developing a new type of binding assay named **guest displacement assay (GDA)**. It is a label-free method through which accurate binding affinity constants ( $K_a$ ) can be accessed for spectroscopically silent guests, both soluble and insoluble. Binding affinities are generally utilized to generate and assess binding models and predict structure and property-related correlations. Thus, they are crucial for designing alternative and superior chemosensors with improved binding affinities and selectivities. However, the accurate determination of binding affinities of very weakly soluble or even insoluble guests is difficult to date. Hence, the performance of the herein newly developed assay was evaluated for macrocyclic cucurbit[*n*]urils (CB*n*),  $\beta$ -cyclodextrin ( $\beta$ -CD), and the protein HSA (human serum albumin) with different weakly binding or insoluble guest molecules.

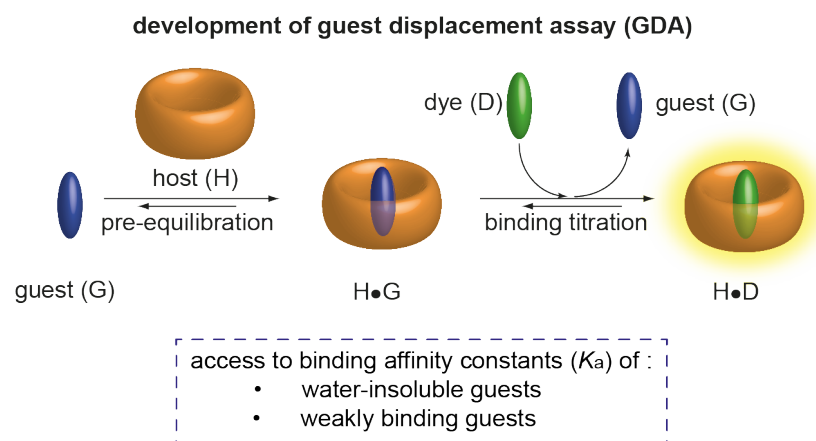


**Figure 18.** Schematic illustration of the **g**uest **d**isplacement **a**ssay (GDA) working principle.

The second part of this thesis was conducted during a research visit at the University of Victoria (UVic) in Canada, at the HOF group, as part of a project collaboration on a “*New sensing approach for illicit drugs by supramolecular chemosensors.*” The project aimed to develop a new sensor system using a combinatorial approach to distinguish commonly found illicit drugs. This conceptual study was intended to provide further insights into host•guest interactions. The HOF group is one of the leading experts in calixarene-based supramolecular chemistry and sensing. Therefore, I intended to combine their recently developed calixarene-based DimerDye (DD) chemosensors with the macrocyclic cucurbit[*n*]urils (CB*n*) to develop a new type of sensing system (DD•CB*n*-complex). Applying this new chemosensor array approach should allow the detection and differentiation of pharmaceutical-relevant agents (*i.e.*, (illicit) drugs) such as anesthetics or opioids.<sup>83</sup> Combining the DimerDyes with the cucurbit[*n*]urils was expected to extend the range of possible analytes from purely cationic to even neutral and larger analytes.

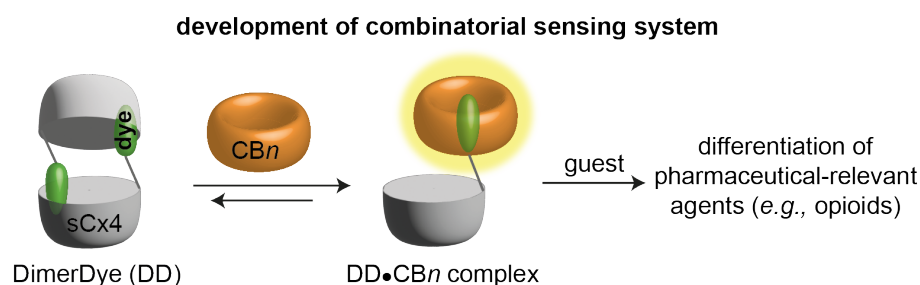


**Figure 19.** Schematic illustration of the design strategy for a combinatorial sensing system based on cucurbit[*n*]uril (*n* = 7 or 8) and a *p*-sulfonatocalix[4]arene (sCx4)-based DimerDye (DD) sensor for the differentiation of cationic and neutral pharmaceutical-relevant agents.

In the third part of my work, the acquired detailed understanding of the supramolecular host•guest interactions was used to take the next step from assay development toward the design of a salt-stable chemosensing system that is even functional in biofluids. The latter is a major challenge to address during real-world assay development. Current self-assembled chemosensors consisting of

a macrocyclic host molecule and an indicator dye as a signaling unit tend to dissociate in complex media (buffered media or biofluids) due to adverse interactions with salt ions, proteins, and other biofluid components. By combining the concept of mechanically interlocked molecules (MIMs) with the excellent binding properties of cucurbit[8]uril, I aimed to establish a new chemosensor that can overcome the limitations of current supramolecular chemosensors for sensing applications in saline media and biofluids. The proposed design was based on the interlock of an aromatic dye into the CB8 cavity through a mechanical bond by installing larger stopper groups that lead to the formation of a functional rotaxane that still possesses the capacity to bind an analyte. The stability and functionality of the rotaxane chemosensor was verified by sensing the biomarker tryptophan in salt-containing buffers and biofluids. Biofluids, such as blood serum and urine, were aimed for since both media contain a rich amount of potentially relevant target analytes and are routinely used in clinical diagnostics.

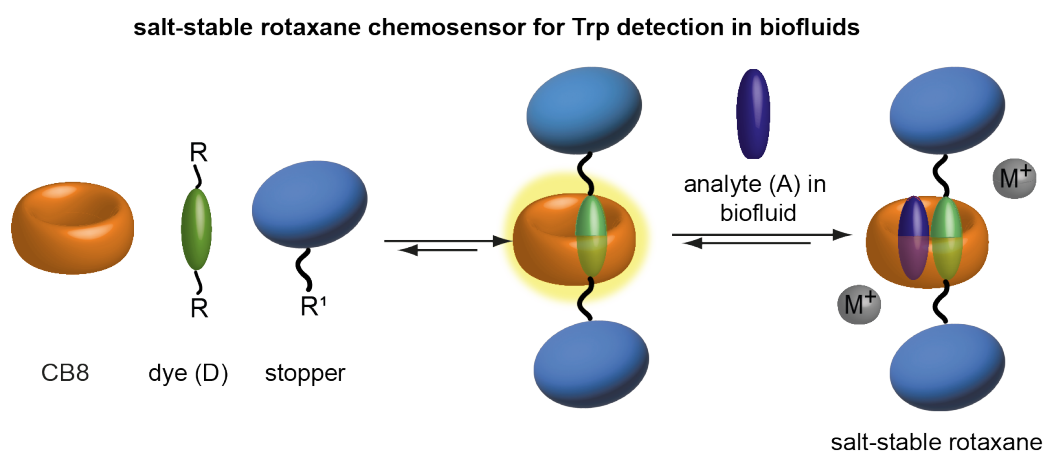


**Figure 20.** Schematic illustration of the design principle of a CB8-rotaxane chemosensor.

## 5. Results and discussion

This work's overarching aim was the development of novel and functional chemosensing systems in biofluids that selectively capture health-related and biologically relevant small molecules. These chemosensors need to retain their functionality even when exposed to high salt concentrations, such as saline buffers or biofluids. Furthermore, high affinities for target analytes are needed as their concentration range often lies in the  $\mu\text{M}$  to nM regime. Besides, high selectivity for target analytes is necessary to avoid false readouts due to cross-reactivity. A fast response unit and easy readout behavior are required for future applications in practical sensing assays.

The thesis is split into three result parts. The first part covers the fundamental understanding of supramolecular host•guest interactions in the context of developing a new type of binding assay that allows for determining the binding affinity of insoluble and weakly binding guest molecules. The second part covers a conceptual study of a new combinatorial chemosensor system for the detection and discrimination of various (illicit) drugs within their drug class as well as commonly found adulterants. The third part presents the design and development of a salt-stable rotaxane-based chemosensing system that enables the detection of tryptophan in biofluids.

### 5.1. Fundamental studies and assay development for insoluble guests

*The results of the following chapter have been published in a Chemical Communication article<sup>144</sup> titled “Teaching old indicators even more tricks: binding affinity measurements with the guest-displacement assay (GDA)” in 2020. J.K. performed the experimental setup and measurements, and assisted in data analysis under the supervision of S.S. and F.B.. Section 5.1 has been partially adapted and modified from the ref.<sup>144</sup> with permission from the Royal Society of Chemistry.*

Molecular recognition plays a crucial role in many biological processes and supramolecular systems, *e.g.*, host•guest complexes, where non-covalent interactions between the individual components control the self-assembly of two or more interacting molecules.<sup>67</sup> The use of supramolecular systems in biomedical applications such as hydrogels, chemosensors, or drug delivery systems is of great importance. The development of such systems requires a fundamental understanding of the recognition processes between a host and a guest.

Supramolecular host•guest complexes are usually characterized by their thermodynamic properties, with the binding affinity  $K_a$  being the most important thermodynamic parameter describing the stability of a formed complex. They are used for developing binding models and predicting possible interaction motifs of a new host design by correlating the structure of existing host molecules with their  $K_a$  values.<sup>131,178-188</sup>

### 5.1.1. Investigation of existing types of binding assays for insoluble guests

The solubility of a guest often determines whether an interaction or reaction between two or more molecules can be studied. Macrocycles can increase the solubility of hydrophobic molecules by breaking up the aggregation due to the formation of an inclusion complex.<sup>189,190</sup> As a result, molecules that were previously inaccessible to sensing systems suddenly become accessible. Particularly in spectroscopic displacement experiments, knowledge of the binding affinity to the host molecule is essential.

The two main optical spectroscopy-based methods that allow for binding affinity determination of host•guest complexes are **direct binding assays** (DBA) and competitive binding assays such as **indicator displacement assays** (IDA).<sup>144</sup> In a DBA, the analyte binding can, for instance, directly result in an easily quantifiable change of a spectroscopic property (*e.g.*, the emergence/disappearance of absorbance and/or emission signals).<sup>45,133</sup> Another option is to record the reaction heat in an isothermal titration calorimetry (ITC) experiment to construct an analyzable binding isotherm.<sup>131,136,191</sup> In any case, either a host (H) is titrated with a guest (G) solution or vice versa, requiring that host and guest are both soluble in the solvent used.<sup>144</sup> For host•guest (H•G) systems in which neither component is chromophoric/emissive nor significant spectroscopic response upon guest binding is obtained, IDA is the practical option.<sup>45,112</sup> In IDA, a complex is formed between a host and an indicator dye (H•D complex) before titration with the guest molecule. The indicator dye (D) is displaced by the stronger binding guest or due to the higher concentration of the analyte/guest.<sup>150</sup>

Both the DBA and IDA methods are widely employed for determining binding affinities of various host•guest systems, but they are restricted to soluble guests.<sup>144</sup> A standard solution to such solubility limitations is using solvent mixtures with polar and apolar solvents in appropriate ratios to solubilize both the host and the guest (*e.g.*, biphasic extraction).<sup>136,191,192</sup> Additives such as salts can also support dissolving hosts or guests.<sup>166</sup> Both practically motivated approaches can cause fundamental problems even at low cofactor percentages (solvent or additive).<sup>193</sup> On the one hand, miscible solvents, *e.g.*, water and methanol, might not mix at the molecular level,<sup>194</sup> resulting in preferential solvation of the host or guest by a solvent component.<sup>195,196</sup> On the other hand, competitive binding of solvents or salts to the host may lead to apparent binding affinities of the host•guest complex of interest.<sup>166,197</sup> Most insoluble guests typically exhibit the strongest binding affinities for supramolecular hosts,<sup>181,182,187,198,199</sup> due to the solvophobic effect. However, current methods cannot be used to determine the binding affinities of such compounds accurately.<sup>144</sup> In other words, there is a practical need for methods that enable binding affinity determination of

insoluble compounds. Fortunately, macrocyclic hosts, *i.e.*, cyclodextrins and cucurbit[*n*]urils, are widely recognized as solubility-enhancing excipients in pharmacology and industry.<sup>189,190,200-203</sup> Therefore, the idea was to develop a new assay method that overcomes the fundamental solubility limitations.

### 5.1.2. Guest displacement assay - a new method to solve current assay limitations

In the present work, an alternative approach for determining binding affinities of host•guest complexes with insoluble or weakly binding guests is introduced by following a competitive assay design. The developed **guest displacement assay (GDA)** exploits the solubility-increasing effect of macrocyclic hosts, especially on hydrophobic guest molecules.<sup>189,190,204</sup> By encapsulating the guest in the solvent-protected hydrophobic cavity of the host, it is possible to form a stable complex between a spectroscopically silent and potentially insoluble guest (G) with a host molecule (H). The pre-equilibrated host•guest complex (H•G) is subsequently mixed with aliquots of an indicator dye (D) solution, leading to the competitive displacement of the guest and the formation of the host•dye complex (H•D).<sup>144</sup> A prerequisite for this setup is a similar or greater binding affinity (see Section 5.1.2.2) of the indicator dye molecule for the host than the guest molecule. **Figure 21** contrasts the state-of-the-art indicator displacement assay (IDA)<sup>42</sup> and the newly developed guest displacement assay (GDA).

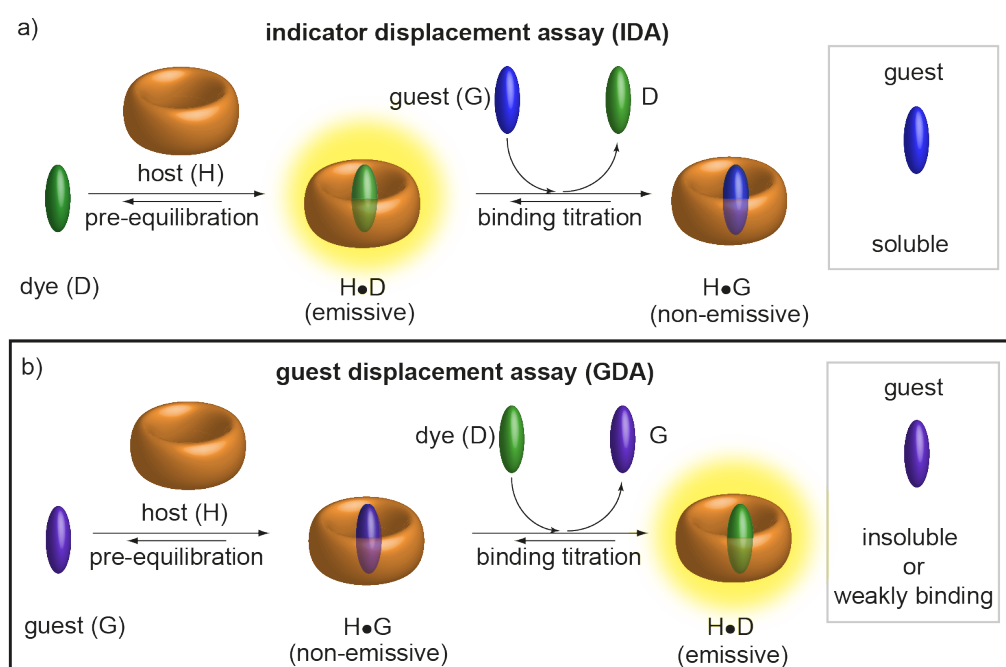


**Figure 21.** Conceptual depiction of competitive binding assays involving a macrocyclic host (H, orange), a spectroscopically silent guest (G, blue), and an indicator dye (D, green). a) **Indicator displacement assay (IDA)**, primarily applicable for soluble guests, and b) **guest displacement assay (GDA)** for insoluble or weakly binding guests. Figure modified and reproduced with permission from ref.<sup>144</sup> Copyright 2020 Royal Society of Chemistry.

GDA can be mathematically expressed by **Eq. 17-24**. Here, the overall equilibrium binding constant  $K_a$  (**Eq. 18**) of the displacement of the guest (G) from the host (H) by the dye (D) can be split into two binding constants (H•D and H•G complex formation), which are denoted as  $K_a^{\text{HD}}$  and  $K_a^{\text{HG}}$ .<sup>144</sup> It is assumed that H and D are both spectroscopically silent. The observable signal change ( $I_c$ ) solely results from the formation of the H•D complex formation upon the subsequent addition of D to H•G. Fitting the experimentally measured signal-concentration curve by following **Eq. 17-24** leads to the binding constant  $K_a^{\text{HG}}$  of the H•G complex. Within the setup, it is necessary to determine the binding constant ( $K_a^{\text{HD}}$ ) of the H•D complex and the signal factors of the H•D complex ( $I^{\text{HD}}$ ) and the unbound dye ( $I^{\text{D}}$ ) by a direct binding assay in advance. These values are then used to solve the GDA equations.



$$K_a = \frac{[\text{HD}][\text{G}]}{[\text{HG}][\text{D}]} \quad \text{Eq. 18}$$



$$K_a^{\text{HG}} = \frac{[\text{HG}]}{[\text{H}][\text{G}]} \quad K_a^{\text{HD}} = \frac{[\text{HD}]}{[\text{H}][\text{D}]} \quad \text{Eq. 20}$$

$$[\text{H}]_0 = [\text{HD}] + [\text{H}] + [\text{HG}] \quad \text{Eq. 21}$$

$$[\text{D}]_0 = [\text{HD}] + [\text{D}] \quad \text{Eq. 22}$$

$$[\text{G}]_0 = [\text{HG}] + [\text{G}] \quad \text{Eq. 23}$$

$$I_c = I^0 + I^{\text{HD}} \cdot [\text{HD}] + I^{\text{D}} \cdot [\text{D}] \quad \text{Eq. 24}$$

[H]: host concentration at equilibrium,  $[\text{H}]_0$ : initial host concentration, [D]: dye concentration at equilibrium,  $[\text{D}]_0$ : initial dye concentration, [G]: guest concentration at equilibrium,  $[\text{G}]_0$ : initial guest concentration, [H•D]: host•dye concentration at equilibrium, [H•G]: host•guest concentration at equilibrium,  $K_a$ : overall binding constant of the competitive GDA,  $K_a^{\text{HD}}$ : binding constant of host•dye (H•D) complex,  $K_a^{\text{HG}}$ : binding constant of host•guest (H•G) complex,  $I^0$ : background signal,  $I^{\text{HD}}$ : signal of host•dye (H•D) complex,  $I^{\text{D}}$ : signal of free dye (D),  $I_c$ : observable signal as a function of concentration.

At first glance, GDA is simply a reversed IDA, but the swapped order of the compound addition is crucial from a fundamental and practical point of view, as shown in Section 5.1.2.1.<sup>144</sup> It may seem counterintuitive to titrate the dye into the H•G complex solution rather than keep it constant as in an IDA, given that the optical density within the solution will increase with the rising dye concentration. With increased optical density, the occurrence of inner-filter effects becomes more probable.<sup>144,205,206</sup> However, the negative interference of the inner filter effect on the emission intensity and, thus, on the fitted binding constant can be avoided by carefully designing the GDA experiments. For example, the absorbance of the dye at the selected wavelength should be less

than 0.1, or a wavelength should be chosen at which the absorption and emission spectra of the dye overlap little or not at all.<sup>144</sup>

#### 5.1.2.1. Determination of binding affinities for selected host-guest complexes

The new type of binding assay was used to determine the binding affinity constants ( $K_a$ ) of selected spectroscopically silent, insoluble and/or weakly binding guests with different host molecules. Cucurbit[ $n$ ]urils (CB $n$ : with  $n = 7$  (CB7, **24**) and  $n = 8$  (CB8, **25**))<sup>87,90,207</sup> and  $\beta$ -cyclodextrin ( $\beta$ -CD, **29**) were chosen as representative macrocyclic hosts (see **Figure 22a**). Both CB $n$  and  $\beta$ -CD are commercially available, water-soluble, non-toxic,<sup>87,90,207-212</sup> and are used in a wide range of applications in both pharmacology and industry.<sup>79,189,190,200-203</sup> They have shown to be suitable solubility enhancers for various poorly water-soluble substances, making them ideal test substances for the GDA setup with insoluble guests.<sup>189,190,204</sup> In addition to macrocyclic host molecules, human serum albumin (HSA, **47** in **Figure 22a**) was selected as a model protein. It is the most abundant protein in the human blood plasma<sup>213</sup> and is commercially available in high purity (fatty acid-free). In addition, it is known to interact with various hydrophobic drugs and dyes.<sup>214,215</sup> A total of twelve organic compounds (see **Figure 22b**), both hydrophilic, *e.g.*, alcohols and cadaverine, and hydrophobic compounds, such as steroids and phenylbutazone, were selected as representative guests for CB $n$ ,  $\beta$ -CD, and HSA. Berberine chloride (BC, **38**), 2,7-dimethyl diazapyrene (MDAP, **40**), and 2-(*p*-toluidino)-naphthalene-6-sulfonate (2,6-TNS, **56**) were selected as dyes for the macrocyclic hosts and warfarin (**57**) as dye for HSA (see **Figure 22c**). The chemical structures of all molecules used in this study are shown in **Figure 22** along with their solubility in water (in italics).

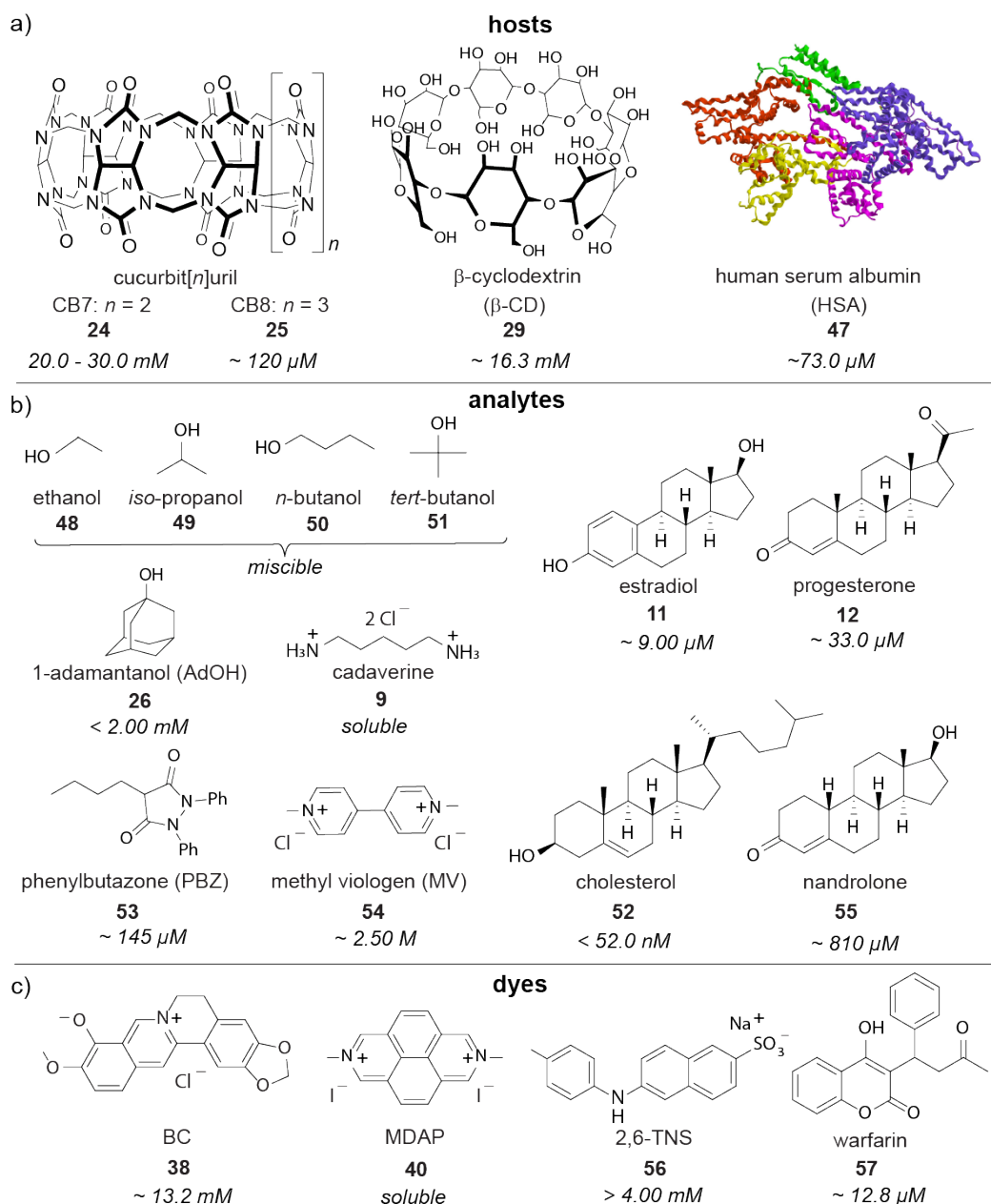


**Figure 22.** Chemical structures and solubilities in water (in italics) of a) host molecules, b) water-soluble and water-insoluble guest molecules, and c) fluorescent indicator dyes used within the GDA study. The solubilities of H, G, and D in water and the photophysical properties of D and H•D are shown in **Table 11** and **Table 12** in the experimental Section 7.2.

First, the binding affinities of the used host•dye pairs were determined in direct binding assays (DBA) by titrating aliquots of the aqueous host solution into a solution of the examined dye at a fixed concentration.<sup>144</sup> The obtained binding isotherms with their subsequent fitting are shown in **Figure 23**. The fitted binding affinities of each dye towards the host are given as log  $K_a$  values in **Table 1**. Those values were then used as input parameters for fitting the respective GDA isotherms for different host•guest systems, with the exception of MDAP.<sup>144</sup> The indicator dye MDAP has a binding affinity towards CB $n$  that is too strong ( $K_a > 10^9 \text{ M}^{-1}$ ) to determine through a DBA. Therefore, an IDA with BC as an indicator dye was used instead.

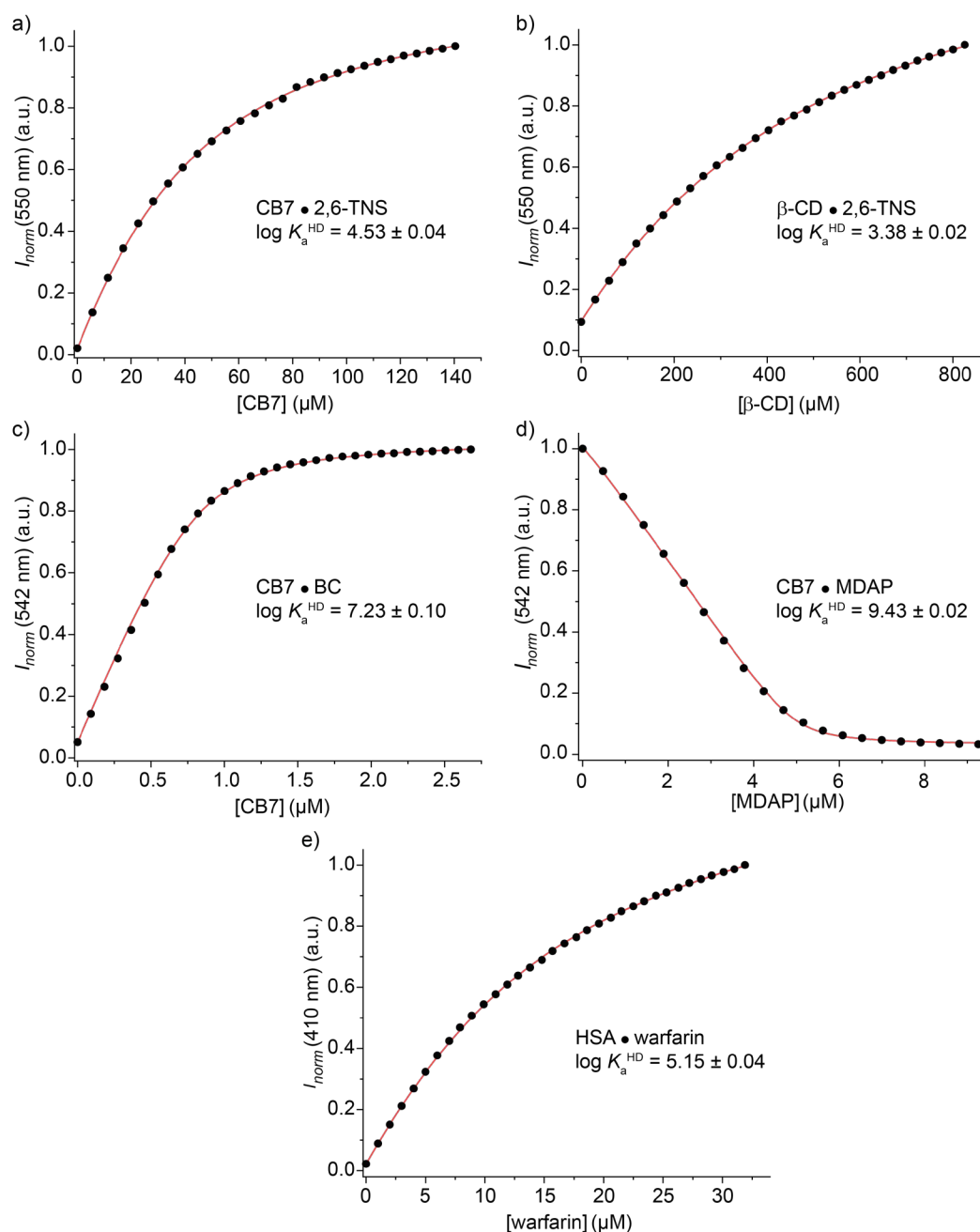


**Figure 23.** Representative binding isotherms for the titration of a) 2,6-TNS (27.0  $\mu$ M) with CB7 (0 - 140  $\mu$ M), ( $\lambda_{ex} = 405$  nm,  $\lambda_{em} = 550$  nm), b) 2,6-TNS (151  $\mu$ M) with  $\beta$ -CD (0 - 840  $\mu$ M), ( $\lambda_{ex} = 405$  nm,  $\lambda_{em} = 550$  nm), c) BC (800 nM) with CB7 (0 - 2.70  $\mu$ M), ( $\lambda_{ex} = 421$  nm,  $\lambda_{em} = 542$  nm), d) CB7•BC (BC: 6.00  $\mu$ M, CB7: 5.00  $\mu$ M) with MDAP (0 - 9.30  $\mu$ M), ( $\lambda_{ex} = 421$  nm,  $\lambda_{em} = 542$  nm), and e) HSA (10.0  $\mu$ M) with warfarin (0 - 32.0  $\mu$ M), ( $\lambda_{ex} = 335$  nm,  $\lambda_{em} = 410$  nm). Measurements were conducted in water (1X PBS for HSA) at 25  $^{\circ}$ C. Acquired data is represented as black dots and the fits are shown as red lines. The  $\log K_a$  for the H•D complex formation is given as an inset in each graph.<sup>144</sup>

**Table 1.** Summary of the experimentally determined binding affinities given as  $\log K_a^{\text{HG}}$  for host-dye complexes determined by DBA/IDA.<sup>144</sup> Unless otherwise stated, all measurements were conducted in water at 25 °C.

host	guest	method	$c^{\text{guest}}$ ( $\mu\text{M}$ )	$c^{\text{host}}$ ( $\mu\text{M}$ )	$\log K_a^{\text{HG}}$	ref.
CB7	BC (38)	DBA	0.80	0 - 2.70	$7.23 \pm 0.10$	this work
	MDAP (40)	IDA <sup>[d]</sup>	0 - 9.30	5.00	$9.43 \pm 0.02$	this work
	2,6-TNS (56)	DBA	27.0	0 - 140	$4.53 \pm 0.04$	this work
CB8	BC (38)	DBA	2.00	0 - 9.00	$13.01 \pm 0.14$ <sup>[e]</sup>	<sup>216</sup>
$\beta$ -CD	2,6-TNS (56) <sup>[a]</sup>	DBA	151	0 - 840	$3.38 \pm 0.02$	this work
HSA	warfarin (57) <sup>[b,c]</sup>	DBA	10.0	0 - 32.0	$5.15 \pm 0.04$	this work

Literature reference: <sup>[a]</sup>  $\log K_a = 3.04$ .<sup>217</sup> <sup>[b]</sup>  $\log K_a = 5.44$  (binding affinity was determined *via* Scatchard plot).<sup>215</sup>  
<sup>[c]</sup> Measured in 1X PBS at 25 °C. <sup>[d]</sup> Determined by an IDA with BC (6.0  $\mu\text{M}$ ). <sup>[e]</sup> Binding affinity for the CB8•BC<sub>2</sub> ternary complex.

Before using GDA with insoluble guests, it was necessary to investigate the general reliability of the results obtained by this method. Therefore, an IDA and a GDA (see **Figure 24**) were performed for selected H•G pairs with soluble guests, and the obtained binding affinities were compared. CB7 was chosen as the host, *n*-butanol (*n*-BuOH, **50**) as the spectroscopically silent guest, and 2,6-TNS as the fluorescent dye. In the IDA experiment, CB7 and 2,6-TNS (**56**) were equilibrated in water at a molar ratio of  $\sim 1:3$  to ensure that a total degree of complexation  $\geq 50\%$  was achieved.<sup>144</sup> Subsequent titration of an aqueous *n*-BuOH solution to the H•D complex solution gave the binding isotherm shown in **Figure 24c**. For the GDA approach, CB7 and *n*-BuOH were equilibrated in water at a ratio of 1:6, and the subsequent addition of an aqueous 2,6-TNS solution led to the binding isotherm shown in **Figure 24d**. Fitting the obtained binding isotherms yielded  $\log K_a = 4.89 \pm 0.04$  for the GDA experiments, which is in good agreement with  $\log K_a = 4.69 \pm 0.02$  obtained in the IDA (see also **Table 2**).<sup>144</sup>

Similarly, for methyl viologen (MV, **54**), GDA and IDA yielded matching affinities for the CB7•MV complex formation, with  $\log K_a = 8.78 \pm 0.01$  (GDA) and  $\log K_a = 8.84 \pm 0.04$  (IDA), as well as for the CB7•cadaverine complex formation, with  $\log K_a = 8.64 \pm 0.03$  (GDA) and  $\log K_a = 8.37 \pm 0.05$  (IDA) (see **Figure 24e-g** and **Table 2**).<sup>144</sup>

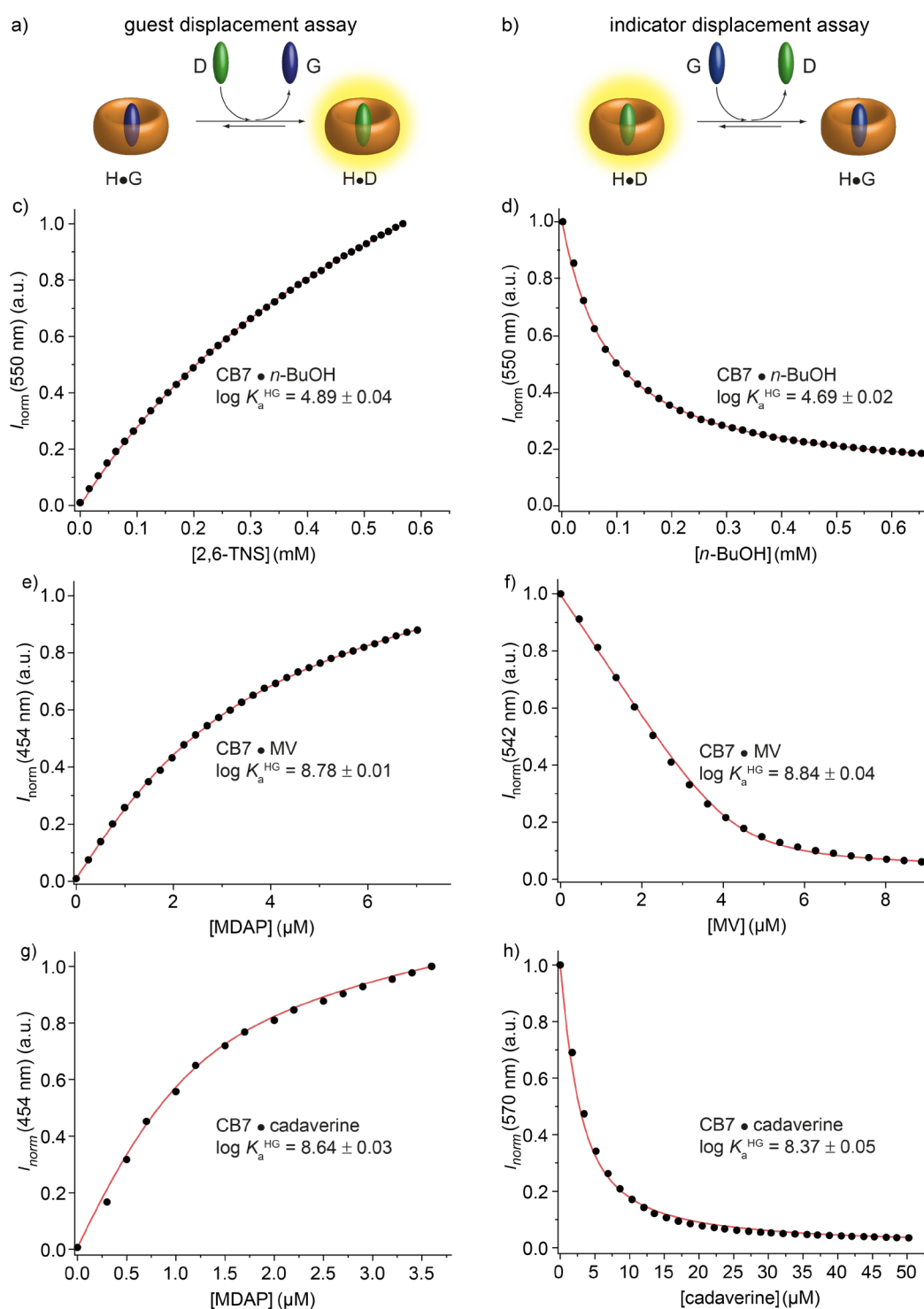


**Figure 24.** Conceptual depiction of a) GDA and b) IDA and representative binding isotherms of competitive binding assays for the binding affinity determination of CB7•*n*-BuOH in c) and d) and of CB7•MV in e) and f), and CB7•cadaverine in g) and h). c) GDA: CB7•*n*-BuOH (*n*-BuOH: 292  $\mu$ M, CB7: 50.0  $\mu$ M) with 2,6-TNS (0 - 568  $\mu$ M), ( $\lambda_{\text{ex}} = 405$  nm,  $\lambda_{\text{em}} = 550$  nm), d) IDA: CB7•2,6-TNS (2,6-TNS: 79.0  $\mu$ M, CB7: 21.0  $\mu$ M) with *n*-BuOH (0 - 654  $\mu$ M), ( $\lambda_{\text{ex}} = 405$  nm,  $\lambda_{\text{em}} = 550$  nm), e) GDA: CB7•MV (MV: 4.00  $\mu$ M, CB7: 3.00  $\mu$ M) with MDAP (0 - 7.00  $\mu$ M), ( $\lambda_{\text{ex}} = 343$  nm,  $\lambda_{\text{em}} = 454$  nm), f) IDA: CB7•BC (BC: 6.00  $\mu$ M, CB7: 4.30  $\mu$ M) with MV (0 - 9.00  $\mu$ M), ( $\lambda_{\text{ex}} = 421$  nm,  $\lambda_{\text{em}} = 542$  nm), g) GDA: CB7•cadaverine (cadaverine: 2.00  $\mu$ M, CB7: 1.30  $\mu$ M) with MDAP (0 - 3.60  $\mu$ M), ( $\lambda_{\text{ex}} = 343$  nm,  $\lambda_{\text{em}} = 454$  nm), and h) IDA: CB7•BC (BC: 23.0  $\mu$ M, CB7: 1.30  $\mu$ M) with cadaverine (0 - 51.0  $\mu$ M) ( $\lambda_{\text{ex}} = 421$  nm,  $\lambda_{\text{em}} = 542$  nm). All measurements were conducted in water at 25 °C. Acquired data is represented by black dots, and fits are shown as red lines. The  $\log K_a$  for the H•G complex formation is given as an inset in each graph.<sup>144</sup>

After successfully verifying the GDA as a practical method for  $K_a$  determination, the next step was the examination of insoluble guests. Unlike IDA or DBA, GDA allows for the analysis of insoluble guests, provided they form a soluble host•guest complex without the need to add organic solvents or salt. Therefore, the nearly water-insoluble steroid estradiol (**11**) (solubility  $S_{\text{water}} \approx 9 \mu\text{M}$ , see **Table 13** in Section 7) was selected as an example guest. In combination with the macrocycle CB7, it forms a water-soluble CB7•estradiol complex. The concentration of both components in the stock solution was determined by  $^1\text{H}$  NMR analysis using dimethyl sulfone as an internal standard (see Section 7.2 for experimental details).<sup>144</sup> Subsequently, the CB7•estradiol solution was titrated in aliquots with the water-soluble indicator dye berberine chloride (BC) (see **Figure 25a**), and  $\log K_a = 6.25 \pm 0.11$  was obtained for the CB7•estradiol complex from these binding isotherms.<sup>144</sup> This binding strength is similar to that of the structurally related water-soluble estrane nandrolone (**55**) with CB7 ( $\log K_a = 7.00$ ), previously determined by IDA and ITC experiments,<sup>200</sup> supporting the applicability of GDA. Analogously to the procedure described above, the affinity of the bulkier, nearly insoluble progesterone (**12**) ( $S_{\text{water}} \approx 33 \mu\text{M}$ , see **Table 13** in Section 7) for CB7 ( $\log K_a = 4.77 \pm 0.08$ ) was determined by GDA (see **Figure 25b**).

As mentioned earlier, determining a water-insoluble guest with an IDA would generally require the dissolving of the guest in a suitable organic solvent. As a result, the subsequent IDA titration would lead to a constant change in the solvent-to-cosolvent ratio during the titration, resulting in an inaccurate binding affinity.

Alternatively, GDA titrations can be performed at a low and *constant* vol% of co-solvent if the selected guest is so sparingly soluble that even the addition of the host does not result in the formation of a soluble H•G complex at a sufficient concentration.<sup>144</sup> This approach was utilized for the GDA of the complex formation of CB7 with cholesterol (**52**) by adding 0.5 vol% of ethanol, thereby forming a water-soluble CB7•cholesterol complex. The fitted binding isotherm gave a  $\log K_a = 5.91 \pm 0.04$  (in  $\text{H}_2\text{O}/\text{ethanol}$ , 99.5/0.5, %v/v) for the CB7•cholesterol complex formation shown in **Figure 25c** and **Table 2**.<sup>144</sup> This setup option enables GDA to outperform other binding affinity techniques, such as ITC-based  $K_a$  determinations, where the addition of co-solvents complicates the evaluation of the gained data to such an extent that it is almost always avoided.<sup>218</sup>

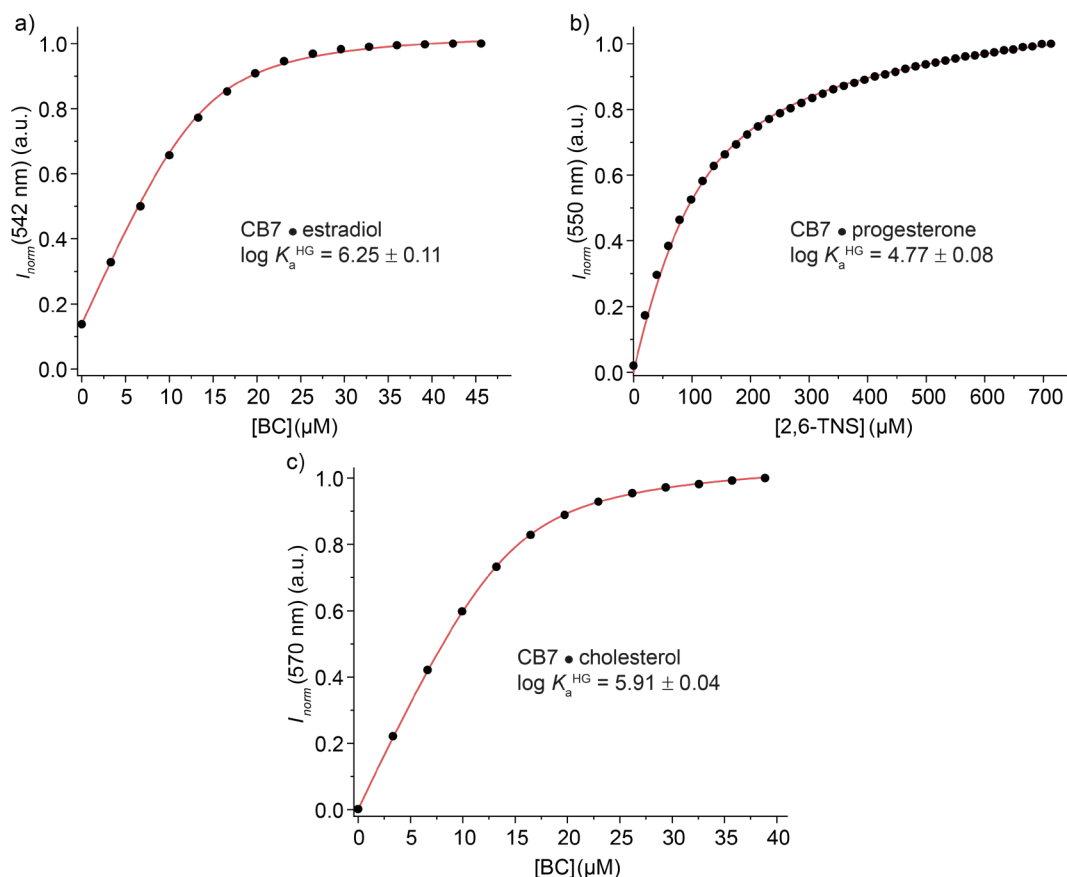


**Figure 25.** Representative GDA binding isotherm for the titration of a) CB7•estradiol (estradiol: 13.0  $\mu\text{M}$ , CB7: 16.5  $\mu\text{M}$ ) with BC (0 - 45.6  $\mu\text{M}$ ), ( $\lambda_{ex} = 421 \text{ nm}$ ,  $\lambda_{em} = 542 \text{ nm}$ ), b) CB7•progesterone (progesterone: 36.0  $\mu\text{M}$ , CB7: 93.0  $\mu\text{M}$ ) with 2,6-TNS (0 - 713  $\mu\text{M}$ ), ( $\lambda_{ex} = 405 \text{ nm}$ ,  $\lambda_{em} = 550 \text{ nm}$ ), c) CB7•cholesterol (cholesterol: 25.0  $\mu\text{M}$ , CB7: 15.0  $\mu\text{M}$ ) with BC (0 - 39.0  $\mu\text{M}$ ) in  $\text{H}_2\text{O}/\text{ethanol}$  (95.5/0.5, %v/v), ( $\lambda_{ex} = 463 \text{ nm}$ ,  $\lambda_{em} = 570 \text{ nm}$ ). a) and b) were conducted in water at 25  $^\circ\text{C}$ . Acquired data is represented as black dots, and fits are shown as red lines. The  $\log K_a$  for the H•G complex formation is given as an inset in each graph.<sup>144</sup>

With the GDA method, the insoluble guest is displaced from the host cavity by gradually adding the indicator dye, raising the question of whether the GDA method has drawbacks due to the potential precipitation of the released insoluble guest. However, after careful examination, no interferences with data quality or reproducibility due to precipitation were observed during any of the titrations performed.<sup>144</sup> For example, homogeneous aqueous solutions of CB7•estradiol titrated with a BC (**38**) solution remained clear. They did not scatter light even after the endpoint of the titration was reached since only micromolar amounts of the unbound guest were released.<sup>144</sup> In addition, precipitation or crystallization of organic compounds from saturated solutions can be slow due to the associated small free energy of the crystallization process.<sup>219,220</sup>

Furthermore, the GDA of CB7 was extended to other representative host molecules such as CB8 (**25**), HSA (**47**), and  $\beta$ -CD (**29**). For example, the binding affinity of the CB8•nandrolone complex was determined using BC as a dye ( $\log K_a = 8.19 \pm 0.09$ , see **Figure 26**). Additionally, GDA gave an accurate binding affinity of  $\log K_a = 5.83 \pm 0.04$  for the modestly soluble anti-inflammatory

drug phenylbutazone (PBZ (**53**), **Figure 26**) for HSA using warfarin (**57**) as a dye, which is in good agreement with the literature value.<sup>221</sup>

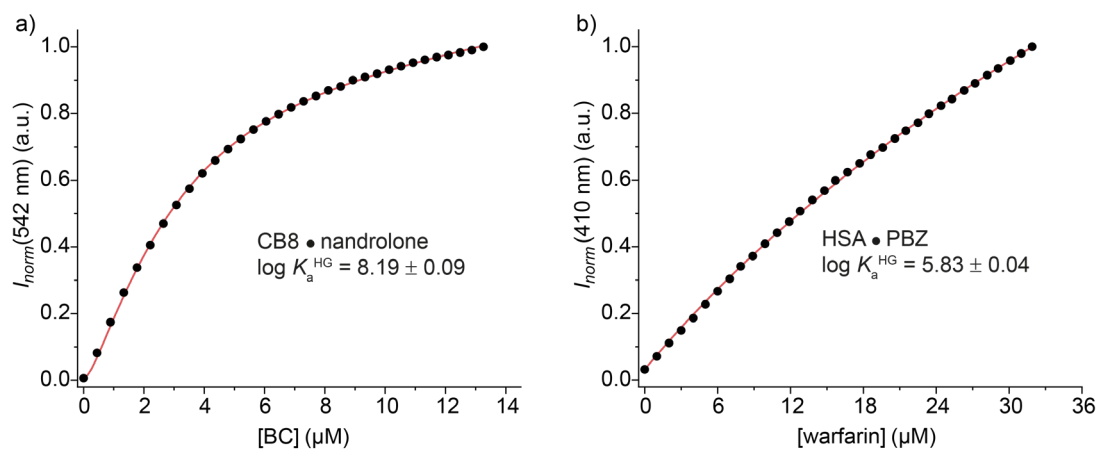


**Figure 26.** Representative GDA binding isotherms for the titration of a) CB8•nandrolone (nandrolone: 700 nM, CB8 600 nM) with BC (0 - 13.0  $\mu\text{M}$ ), ( $\lambda_{\text{ex}} = 421 \text{ nm}$ ,  $\lambda_{\text{em}} = 542 \text{ nm}$ ) in water at 25  $^{\circ}\text{C}$ , and b) HSA•PBZ (PBZ: 21.0  $\mu\text{M}$ , HSA: 10.0  $\mu\text{M}$ ) with warfarin (0 - 32.0  $\mu\text{M}$ ), ( $\lambda_{\text{ex}} = 335 \text{ nm}$ ,  $\lambda_{\text{em}} = 410 \text{ nm}$ ) in 1X PBS at 25  $^{\circ}\text{C}$ . Acquired data is represented as black dots, and fits are shown as red lines. The  $\log K_a$  for the H•G complex formation is given as an inset in each graph.<sup>144</sup>

The second significant advantage of GDA is its superior performance with weakly binding guests (*i.e.*,  $\log K_a \leq 3$ ), which both simulations of binding isotherms and experiments have revealed. For example, it was possible to determine the binding affinity of *n*-BuOH (**47**) to  $\beta$ -CD ( $\log K_a = 2.00 \pm 0.04$ ) by GDA (see **Figure 27a**).<sup>144</sup> In contrast, IDA titrations required adding significantly larger amounts of the weak binding guest and resulted in a poor mathematical fit of the binding isotherm, as shown in **Figure 27b**. Besides, high concentrations of guests can cause aggregation, which can lead to solubility limitations for the experiment.

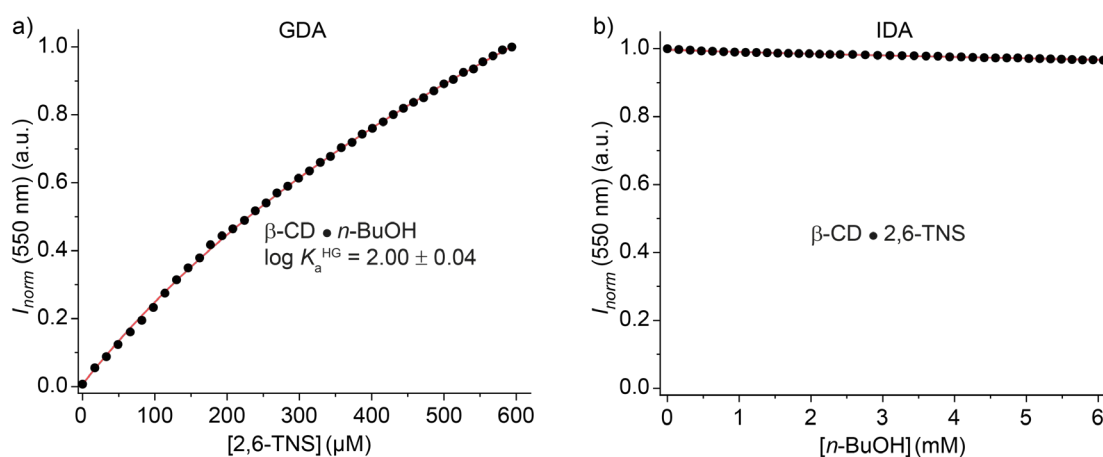


**Figure 27.** Representative binding isotherm of competitive binding assays for the binding affinity determination of  $\beta$ -CD•*n*-BuOH. a) GDA:  $\beta$ -CD•*n*-BuOH (*n*-BuOH: 884  $\mu\text{M}$ ,  $\beta$ -CD: 100  $\mu\text{M}$ ) with 2,6-TNS (0 - 594  $\mu\text{M}$ ), ( $\lambda_{\text{ex}} = 405 \text{ nm}$ ,  $\lambda_{\text{em}} = 550 \text{ nm}$ ) and b) IDA:  $\beta$ -CD•2,6-TNS (2,6-TNS: 703  $\mu\text{M}$ ,  $\beta$ -CD: 60.0  $\mu\text{M}$ ) with *n*-BuOH (0 - 6.00 mM) by IDA, ( $\lambda_{\text{ex}} = 405 \text{ nm}$ ,  $\lambda_{\text{em}} = 550 \text{ nm}$ ). All measurements were conducted in water at 25  $^{\circ}\text{C}$ . Acquired data is represented as black dots, and fits are shown as red lines. The  $\log K_a$  for the H•G complex formation is given as an inset in each graph. The accurate determination of  $\log K_a$  for  $\beta$ -CD•*n*-BuOH can only be achieved with GDA. IDA yielded a linear binding curve with a small total signal change since the weakly binding guest cannot displace the stronger binding dye.<sup>144</sup>

The applicability of GDA for weakly binding guests was further demonstrated by the determination of the binding strengths of other weakly binding guests (*i.e.*, ethanol (**48**), iso-propanol (**49**), and *tert*-butanol (**51**)) for  $\beta$ -CD and CB7 by GDA. The fitted binding isotherms and the log  $K_a$  values of the systems investigated are shown in **Figure 28** and **Table 2**.<sup>144</sup>

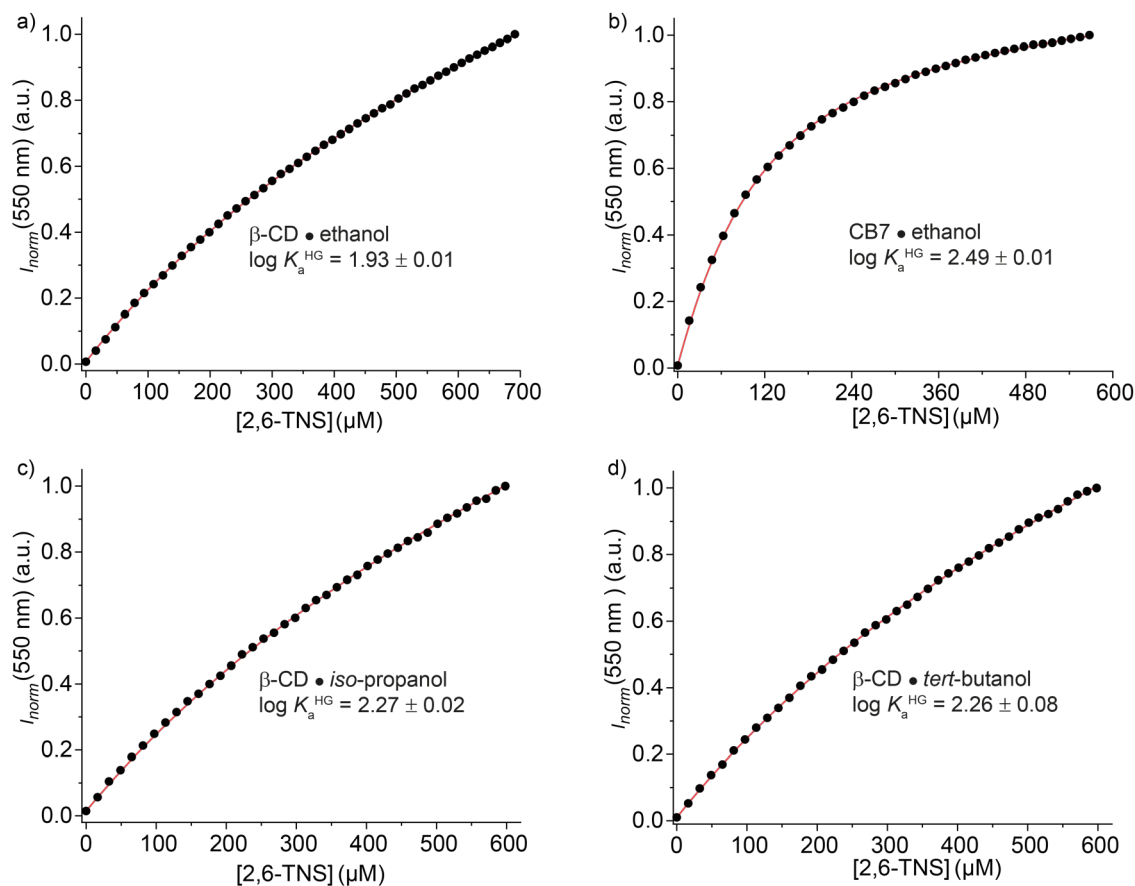


**Figure 28.** Representative GDA binding isotherms for the titration of a)  $\beta$ -CD•ethanol (ethanol: 7.05 mM,  $\beta$ -CD: 100  $\mu\text{M}$ ) with 2,6-TNS (0 - 691  $\mu\text{M}$ ), ( $\lambda_{ex} = 405 \text{ nm}$ ,  $\lambda_{em} = 550 \text{ nm}$ ), b) CB7•ethanol (ethanol: 5.30 mM, CB7: 56.0  $\mu\text{M}$ ) with 2,6-TNS (0 - 568  $\mu\text{M}$ ), ( $\lambda_{ex} = 405 \text{ nm}$ ,  $\lambda_{em} = 550 \text{ nm}$ ), c)  $\beta$ -CD•*iso*-propanol (*iso*-propanol: 1.05 mM,  $\beta$ -CD: 103  $\mu\text{M}$ ) with 2,6-TNS (0 - 598  $\mu\text{M}$ ), ( $\lambda_{ex} = 405 \text{ nm}$ ,  $\lambda_{em} = 550 \text{ nm}$ ), and d)  $\beta$ -CD•*tert*-butanol (*tert*-butanol: 932  $\mu\text{M}$ ,  $\beta$ -CD: 100  $\mu\text{M}$ ) with 2,6-TNS (0 - 598  $\mu\text{M}$ ), ( $\lambda_{ex} = 405 \text{ nm}$ ,  $\lambda_{em} = 550 \text{ nm}$ ). All measurements were conducted in water at 25  $^{\circ}\text{C}$ . Acquired data is represented as black dots, and fits are shown as red lines. The log  $K_a$  for the H•G complex formation is given as an inset in each graph.<sup>144</sup>

**Table 2.** Summary of the determined binding affinities given as  $\log K_a$  in deionized water. Errors (StDev) were obtained from triplicate measurements. Unless otherwise stated, all measurements were conducted in water at 25 °C.

host	guest	method	$c^{\text{guest}}$ ( $\mu\text{M}$ )	$c^{\text{host}}$ ( $\mu\text{M}$ )	dye	$c^{\text{dye}}$ ( $\mu\text{M}$ )	$\log K_a^{\text{HG}}$
CB7	ethanol (48)	GDA	5270	56.0	2,6-TNS	0 - 568	$2.49 \pm 0.01$
	<i>n</i> -butanol (50)	GDA	292	50.0	2,6-TNS	0 - 568	$4.89 \pm 0.04$
		IDA	0 - 654	21.0	2,6-TNS	79.0	$4.69 \pm 0.02$
	cadaverine (9)	GDA	4.30	2.00	BC	0 - 26.0	$\sim 8.00^{\text{[a]}}$
		IDA	0 - 51.0	1.30	BC	23.0	$8.37 \pm 0.05$
		GDA	2.00	1.30	MDAP	0 - 3.60	$8.64 \pm 0.03$
	MV (54)	GDA	4.00	3.00	MDAP	0 - 7.00	$8.78 \pm 0.01$
		IDA	0 - 9.00	4.30	BC	6.00	$8.84 \pm 0.04$
	cholesterol (52) <sup>[b]</sup>	GDA	25.0	15.0	BC	0 - 39.0	$5.91 \pm 0.04$
	estradiol (11)	GDA	13.0	16.0	BC	0 - 45.6	$6.25 \pm 0.11$
	progesterone (12)	GDA	36.0	93.0	2,6-TNS	0 - 713	$4.77 \pm 0.08$
	CB8	nandrolone (55)	GDA	0.700	0.600	BC	0 - 13.0
$\beta$ -CD	ethanol (48)	GDA	7050	100	2,6-TNS	0 - 691	$1.93 \pm 0.01$
	<i>iso</i> -propanol (49)	GDA	1050	103	2,6-TNS	0 - 598	$2.27 \pm 0.02$
	<i>n</i> -butanol (50)	GDA	884	100	2,6-TNS	0 - 594	$2.00 \pm 0.04$
		IDA	0 - 6000	60.0	2,6-TNS	703	$\sim 2.20^{\text{[a]}}$
	<i>tert</i> -butanol (51)	GDA	932	100	2,6-TNS	0 - 598	$2.26 \pm 0.08$
	AdOH (26)	GDA	100	33.0	2,6-TNS	0 - 598	$\sim 4.80^{\text{[a]}}$
		IDA	0 - 366	100	2,6-TNS	100	$5.01 \pm 0.08$
HSA <sup>[c]</sup>	PBZ (53) <sup>[d]</sup>	GDA	21.0	10.0	warfarin	0 - 32.0	$5.83 \pm 0.04^{\text{[e]}}$

<sup>[a]</sup> Due to a mismatch of the binding affinities of the dye (see Eq. 27 and 28), this value is not as accurate as the one determined by the alternative competitive binding assay or a modification of the reporter pair setup. Values of  $\log K_a^{\text{HG}}$  and  $\log K_a^{\text{HD}}$  are outside the recommended range for GDA or IDA; see Section 5.1.2.2. <sup>[b]</sup> Measured in 0.5% ethanol in H<sub>2</sub>O. <sup>[c]</sup> Fatty acid-free HSA. <sup>[d]</sup> Measured in 1X PBS. <sup>[e]</sup> Literature reference:  $\log K_a$  was determined *via* Scatchard plot yielding  $\log K_a = 5.70$ .<sup>221</sup>

### 5.1.2.2. Performance window

Despite their complementarity for binding affinity determination, GDA and IDA cannot be considered as direct mirror images of each other due to the different requirements for selecting suitable indicator dyes for each method.<sup>144</sup> Accurate binding affinities from competitive binding titrations can only be obtained if it is possible to fit the measured data reasonably. This means that the titration curve should be neither too linear nor too curved. Otherwise, a variety of binding affinities could visually fit the same curve, yielding no accurate and reasonable binding affinity. Therefore, a procedure was developed to predict and classify the curvature behavior of a titration curve using mathematical simulations of binding isotherms, which will be explained in the following by using an example GDA system with a  $\log K_a^{\text{HG}} = 4$  for the H•G complex.

Based on this H•G system, a dye with a sufficiently high binding constant for the host, which could displace the guest from the H•G complex, was sought. In order to simulate scenarios with different binding constants of the dye, it was assumed that the observed signal intensity ( $I_c$ ) would only result from the formation of the H•D complex. The H•G complex, G, H, and D alone were considered spectroscopically inactive. Using these input parameters (*i.e.*,  $I^0 = 0$ ,  $I^D = 0$ ,  $I^{\text{HD}} = 1$ ) reduced **Eq. 25** to **Eq. 26**, which was utilized for the simulation of different H•D binding isotherms with  $\log K_a^{\text{HD}} = 0 - 10$  (**Table 15** in Section 8.1). The simulated binding isotherms of the GDA test system (with  $[H]_0 = [G]_0 = 200 \mu\text{M}$  and  $[D]_0 = 0 - 1 \text{ mM}$ ) are shown in **Figure 29a**.

$$I_c = I^0 + I^{\text{HD}} \cdot [\text{HD}] + I^D \cdot [\text{D}] \quad \text{Eq. 25}$$

$$I_c = I^{\text{HD}} \cdot [\text{HD}] \quad \text{Eq. 26}$$

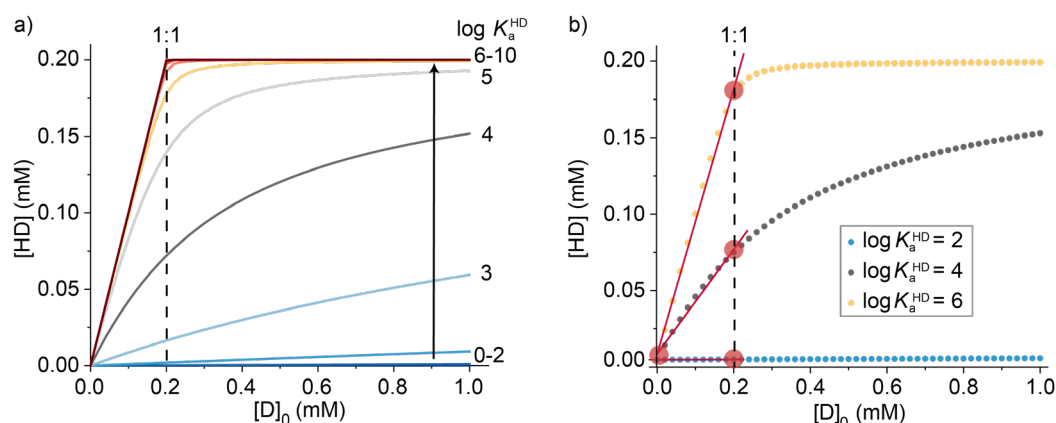


**Figure 29.** a) Simulation of the GDA binding isotherms for dyes with different  $\log K_a$  values competing with a guest ( $\log K_a^{\text{HG}} = 4$ ) for a host. b) Selected simulated GDA binding isotherms for dyes with  $\log K_a = 2, 4$ , and  $6$  (single points) competing with a guest ( $\log K_a^{\text{HG}} = 4$ ) for a host. The linear fit (red line) was calculated from the beginning of each curve to the corresponding equilibration point indicated by the dashed black line at  $0.2 \text{ mM}$  where 1:1 host:guest binding applies. The red circles indicate the starting point and the endpoint of the linear fit (equilibration point  $[H]_0 = [D]_0$ ) for the linear fitting. **Figure 29b** was adapted with permission from ref.<sup>144</sup> Copyright 2020 Royal Society of Chemistry.

In the next step, the slope of the initial linear part of each simulated curve was obtained by linear fitting. Therefore, a border was defined in the signal-intensity titration plot (dashed line in **Figure 29a**) by linking the starting point with the equilibrium point where  $[D]_0 = [H]_0 = 0.2$  mM (1:1 host:guest binding). Subsequently, the slope of each curve was obtained by a linear fit of the signal ( $[HD]$ ) from 0 to 0.2 mM ( $\cong [H]_0$ ). **Figure 29b** shows the simulated binding isotherms and the fitted linear region of three different  $\log K_a^{\text{HD}}$  as examples. Generally, the slope is relatively flat if the competitor binds weaker than the guest, which is the case for the blue curve ( $\log K_a^{\text{HD}} = 2$ ). Does the competitor binds more strongly than the guest, a steep curve is obtained, which is exemplified by the yellow curve ( $\log K_a^{\text{HD}} = 6$ ). In the next step, all determined slopes of the simulated binding curves for  $\log K_a^{\text{HD}} = 0 - 10$  were plotted against their respective assumed  $\log K_a^{\text{HD}}$ , yielding a sigmoidal curve with a very flat beginning and end (see **Figure 30**).<sup>144</sup> The analysis of those slopes showed that an accurate binding affinity can only be obtained when the slope lies in the range of 0.1 - 0.9, indicated by the horizontal red lines in **Figure 30**. Only in the range 0.1 - 0.9, a discriminability greater than 5% of the two linear lines is given.<sup>144</sup> This means that, for the GDA test system shown, a guest with a affinity of  $\log K_a^{\text{HG}} = 4$  for the host can only be determined by competing indicator dyes in the range from  $\log K_a^{\text{HD}} = 3 - 6$ , whereas  $\log K_a^{\text{HD}} < 3$  yields a simulated titration curve that is too flat. The use of such a curve as a model curve for fitting of  $\log K_a^{\text{HG}}$ , leads to a variety of  $\log K_a^{\text{HG}}$  values that can visually fit the model data equally well. This means such a scenario is unsuitable in practice. Likewise,  $\log K_a^{\text{HD}} > 6$  gives a too-steep simulated binding curve that is unsuitable for the fitting of reliable  $\log K_a^{\text{HG}}$  values.<sup>144</sup>

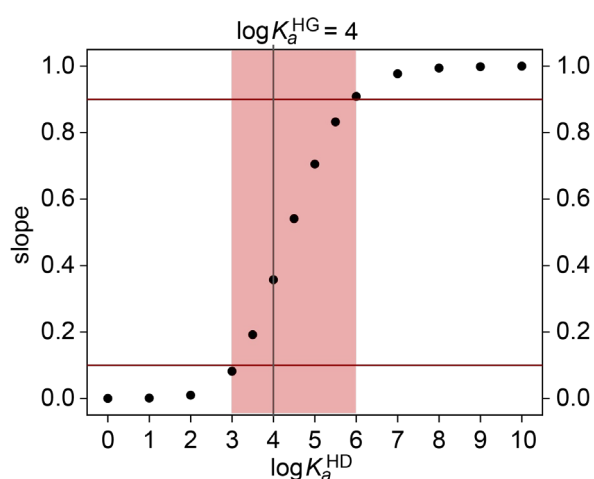


**Figure 30.** GDA performance chart to accurately determine the binding constant of the host•guest pair with a  $\log K_a^{\text{HG}} = 4$  (indicated by the black vertical line). The red window indicates the range of  $\log K_a$  values of an indicator dye suitable for a GDA with a  $\log K_a^{\text{HG}} = 4$  for the guest. This range is defined by the upper (0.9) and lower (0.1) slope boundaries (horizontal dark red lines). Adapted with permission from ref.<sup>144</sup> Copyright 2020 Royal Society of Chemistry.

Analogously to the example described above, simulations were also performed for other H•G example complexes with different  $\log K_a^{\text{HG}}$  values, which showed that only binding curves with a slope greater than 0.1 and less than 0.9 yield a reasonable binding constant for  $\log K_a^{\text{HG}}$ . Therefore, based on these results, it was possible to define the following general performance window for GDA:<sup>144</sup>

$$\log K_a^{\text{HG}} + 2 \geq \log K_a^{\text{HD}} \geq \log K_a^{\text{HG}} - 1 \quad \text{Eq. 27}$$

This equation states that the indicator dye must not bind more than a factor of 10 weaker to the host than the guest. Otherwise, the dye cannot efficiently displace the guest from the H•G complex, resulting in a flat binding isotherm that cannot be reliably fitted. In contrast, the indicator dye can bind up to a factor of 100 more strongly than the guest and still generate a binding isotherm that can be fitted reasonably well.

On a side note, as for GDA, performance analysis can be similarly created for IDA. Here the  $\log K_a^{\text{HD}}$  of the H•D complex is pre-set and binding isotherms for various  $\log K_a^{\text{HG}}$  are simulated. The derived performance window for IDA can therefore be formulated according to **Eq. 28**, which states that the guest should have a  $\log K_a^{\text{HD}}$  of no more than two orders of magnitude less or one order of magnitude greater than the  $\log K_a^{\text{HG}}$ .<sup>144</sup> **Figure 31** summarizes these results in a graphical overview.

$$\log K_a^{\text{HG}} + 1 \geq \log K_a^{\text{HD}} \geq \log K_a^{\text{HG}} - 2 \quad \text{Eq. 28}$$

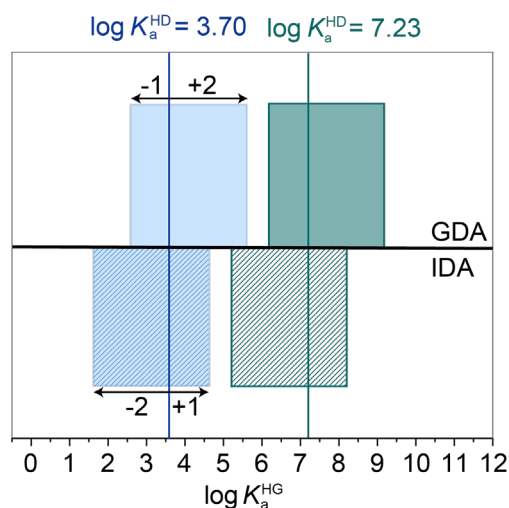


**Figure 31.** Performance analysis charts for the competitive binding assays GDA (top) and IDA (bottom). The colored squares indicate the suitable affinity range of a H•G that can be determined by an indicator dye with an estimated affinity of  $\log K_a = 3.70$  (blue, *e.g.*, 2,6-TNS and  $\beta$ -CD) or  $\log K_a = 7.23$  (green, *e.g.*, BC and CB7) by GDA (solid bar, top) or IDA (stripped bars, bottom).<sup>144</sup>

### 5.1.2.3. Limitations of GDA

Having confirmed that GDA is more suitable for studying the binding strength of insoluble or weakly binding guests compared to other methods, the limitations of GDA also need to be discussed. Unlike IDA, GDA requires that the dye used for a particular host•guest pair has a similar or stronger binding affinity for the host compared to the guest under investigation (see Eq. 27). If this is not the case, displacement of the guest may not be possible, resulting in only approximate  $K_a$  values. Accordingly, the IDA method should be preferred for soluble high-affinity guests, as suitable indicator dyes with sufficiently high binding affinity may not always be available, depending on the host used. For example, obtaining a reliable binding constant for  $\beta$ -CD•AdOH by GDA was impossible since the affinity of the commercially available indicator dye 2,6-TNS<sup>120</sup> ( $\log K_a = 3.38 \pm 0.02$  for  $\beta$ -CD) lies outside of the performance range for the GDA method (see Figure 32).<sup>144</sup> However, IDA titration gave a reliable binding affinity ( $\log K_a = 5.01 \pm 0.08$ ) for this host•guest pair. Additional development of new high-affinity indicator dyes will expand the scope of the GDA method for CDs.<sup>222</sup>

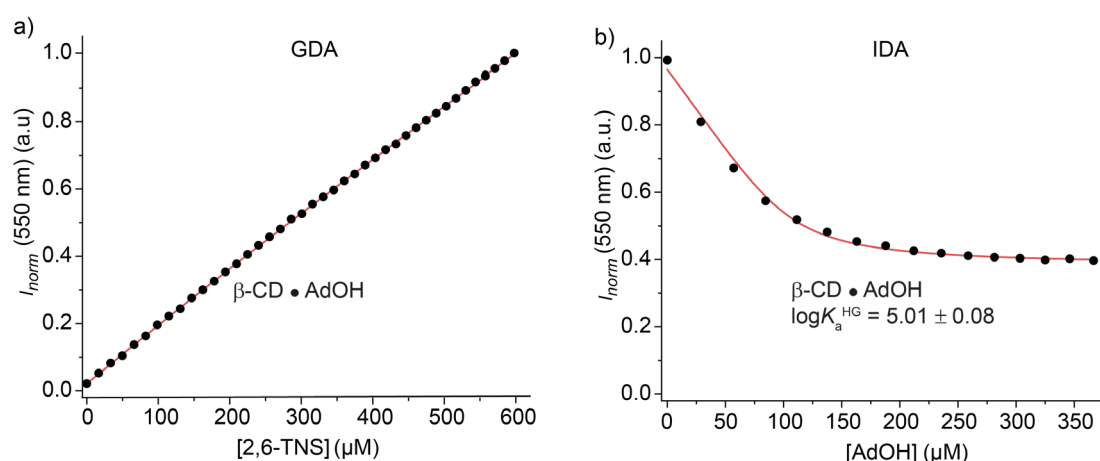


**Figure 32.** Representative binding isotherm of competitive binding assays for the binding affinity determination of  $\beta$ -CD•AdOH a) GDA:  $\beta$ -CD•AdOH (AdOH: 100  $\mu$ M,  $\beta$ -CD: 33.0  $\mu$ M) with 2,6-TNS (0 - 598  $\mu$ M), ( $\lambda_{ex} = 405$  nm,  $\lambda_{em} = 550$  nm), b) IDA:  $\beta$ -CD•2,6-TNS (2,6-TNS: 100  $\mu$ M,  $\beta$ -CD 33.0  $\mu$ M) with AdOH (0 - 366  $\mu$ M). All measurements were conducted in water at 25 °C. Acquired data is represented as black dots, and fits are shown as red lines. The  $\log K_a$  for the H•G complex formation is given as an inset in each graph. The accurate determination of  $\log K_a$  for  $\beta$ -CD•AdOH can only be achieved with IDA since the GDA performance window of 2,6-TNS with  $\beta$ -CD does not match the strong binding affinity of AdOH.<sup>144</sup>

Using the developed performance windows for GDA and IDA, it can now also be clearly explained why no accurate binding constant was obtained by GDA for the CB7•cadaverine complex formation with BC as indicator dye. The strong binding of CB7•cadaverine ( $\log K_a = 8.37 \pm 0.05$ ) lies outside of the performance range of BC ( $\log K_a = 7.23 \pm 0.10$ ) for a GDA with CB7 (see Figure 31). Instead, a much stronger indicator dye, such as MDAP<sup>223</sup> ( $\log K_a = 9.43 \pm 0.02$ ), leads to a more accurate binding affinity value ( $\log K_a = 8.64 \pm 0.03$ ),

which is comparable to the one determined by an IDA (see **Figure 24e-f**). Similarly, the performance chart of IDA (see **Figure 31**) explains why the binding of *n*-BuOH to  $\beta$ -CD ( $\log K_a = 2.00 \pm 0.04$ ) cannot be accurately determined by an IDA using 2,6-TNS ( $\log K_a = 3.38 \pm 0.02$  for  $\beta$ -CD). The corresponding GDA performance chart for this indicator for  $\beta$ -CD (see **Figure 31**) predicts reasonable data for the titration experiment, which was experimentally validated (see **Figure 27**). Overall, GDA showed to be superior to IDA for insoluble and weakly binding guests and allows for the binding constant determination of previously inaccessible guests.

## 5.2. Conceptual study of a new sensing system for (illicit) drug detection

*This work was performed during a research stay in the HOF group at the University of Victoria, Canada, as part of a collaboration project. The results discussed in this chapter are the basis of a publication, which is currently in preparation. The here provided data and their analysis is thus similar to the ones in the planned publication.*

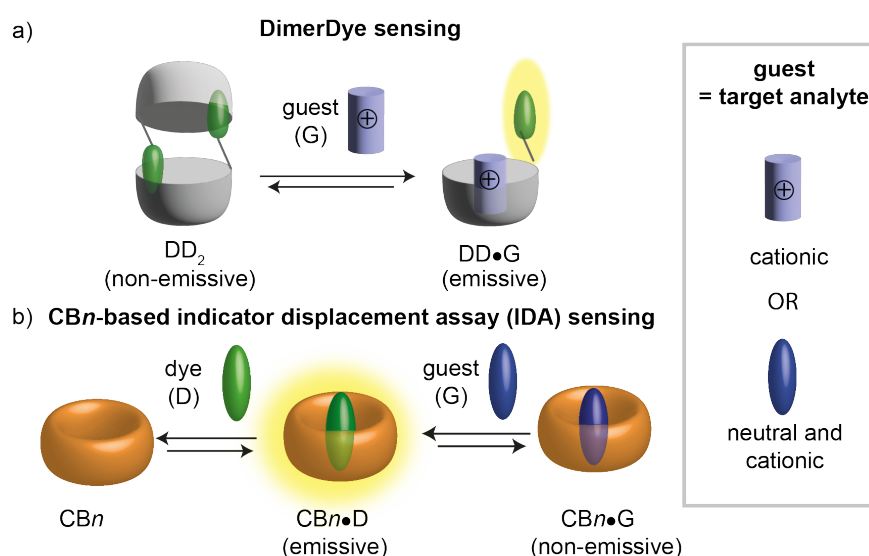
In the second part of the work, a new array-based assay was developed to detect cationic and neutral analytes in aqueous media. As such, a combinatorial approach was taken to assemble systems containing two different binding elements while incorporating different chemosensor types to achieve differential cross-reactive detection for a range of analyte interactions. These conceptual studies provided insights into the host•guest interactions of this novel system.

Conventional sensing systems require chemosensors that offer a high selectivity to differentiate structurally similar analytes. This can be synthetically very challenging if a new sensor is needed for each analyte. A typical workaround is using an array of indicator displacement assays (IDA), where a host molecule is combined with different dyes, forming various chemosensor units (CU).<sup>224</sup> Each CU's response (*e.g.*, optical signal change) is then monitored for various analytes. The obtained response of each chemosensor•analyte pair alone is barely informative as the chemosensors are usually not selective for one analyte. However, combining all output data creates a unique fingerprint for each analyte, which can be analyzed using multivariate methods such as principle component analysis (PCA).<sup>171</sup> This reduces the dimensionality of the data to represent the chemosensor array's differential responses. Some of the earliest examples of the application of this assay design can be related to ANSLYN ET AL.<sup>170,173,225</sup> Within this work, a new sensing system approach is introduced that broadens the scope of targeted analytes by combining two binding elements with different analyte affinities in one solution.

### 5.2.1. Design concept

The objective of this collaboration project with the HOF group was to create a new array-based sensor system that can detect and discriminate neutral and cationic drugs within different drug classes. The HOF group recently reported novel DimerDye chemosensors (further called DD with DD<sub>2</sub> in their assembled dimeric and DD in their monomeric form) that operate successfully on cationic drugs like cocaine, amphetamines, and opioids.<sup>83,226</sup> These self-assembled DimerDyes are built upon the macrocycle *p*-sulfonatocalix[4]arene (sCx4), functionalized with various merocyanine-based dyes by parallel synthesis. The self-assembly of two sCx4s into a dimer forms a non-emissive complex.<sup>83,226</sup> The addition of an analyte, *i.e.*, guest, causes an observable

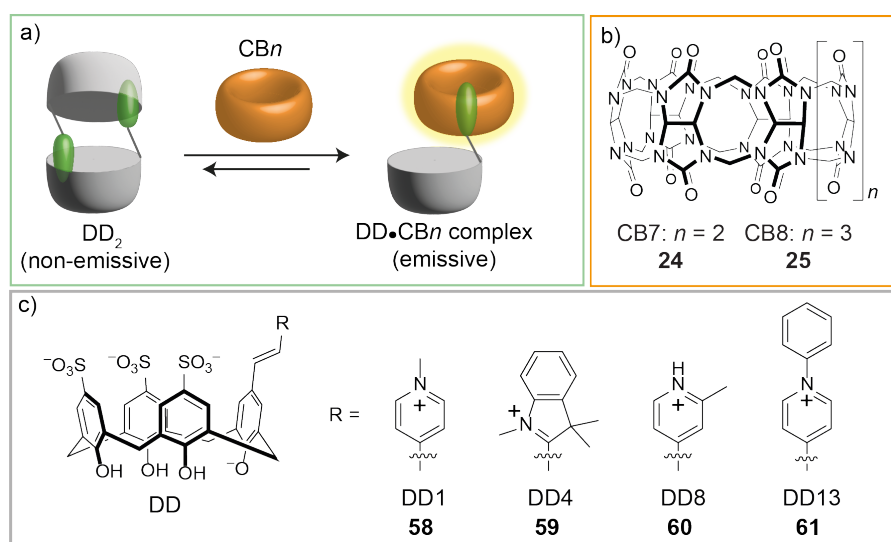
fluorescence emission enhancement as the analyte binds in the host cavity, thereby disassembling the dimer (see **Figure 33a**). DimerDye sensing responses were so far limited to small cationic drugs.<sup>83</sup> In order to expand their sensing capabilities, DimerDyes were combined with the macrocyclic hosts cucurbit[*n*]uril (CB*n*) to form new sensing systems. Cucurbit[*n*]urils can bind both neutral and cationic guests in their cavities.<sup>99</sup> Typically, CB*n*-based sensing in an IDA setup utilizes a preformed cucurbit[*n*]uril•dye complex (CB*n*•D) to detect an analyte, as shown in **Figure 33b**. Therefore, by combining DDs with CB*n*, the detection of cationic drugs (*e.g.*, 3,4-methylenedioxy-*N*-methylamphetamine (MDMA) or opioids) is extended to larger and neutral drugs (*e.g.*, tetrahydrocannabinol (THC) derivatives or benzodiazepines).



**Figure 33.** Schematic illustration of a) DimerDye disassembly assay (DDA) of the *p*-sulfonatocalix[4]arene-based DimerDye (DD<sub>2</sub> as its dimeric form is preferred without a guest present) and b) indicator displacement assay (IDA) of a cucurbit[*n*]uril-based chemosensor (CB*n*•D). The addition of an analyte (*i.e.*, guest) leads to the disassembly of a) the dimeric DD<sub>2</sub>, causing a fluorescence emission turn-on, and b) the CB*n*•D complex, causing a fluorescence emission turn-off.

There are few examples of the interaction of macrocyclic *p*-sulfonatocalix[4]arenes and cucurbit[*n*]urils forming self-assembled architectures.<sup>227</sup> These architectures have been reported with different stoichiometries between the CB*n* and the calixarenes (1:2, 1:3),<sup>228,229</sup> highlighting the potential diversity these two hosts can induce when combined. The host-guest interactions formed in these complexes can also give way to a potential sensing system by combining the DDs with CB*n*.<sup>230</sup> Apart from their macrocyclic structure and hydrophobic cavity, the two hosts differ in their properties. CB*n*s have a rigid barrel-shaped structure, where both size and shape complementarity plays a crucial role in binding affinity for a complexed guest.<sup>94,203</sup> Conversely, calixarenes have a more flexible cup-shaped structure, reducing the role of size and shape complementarity of analyte binding.

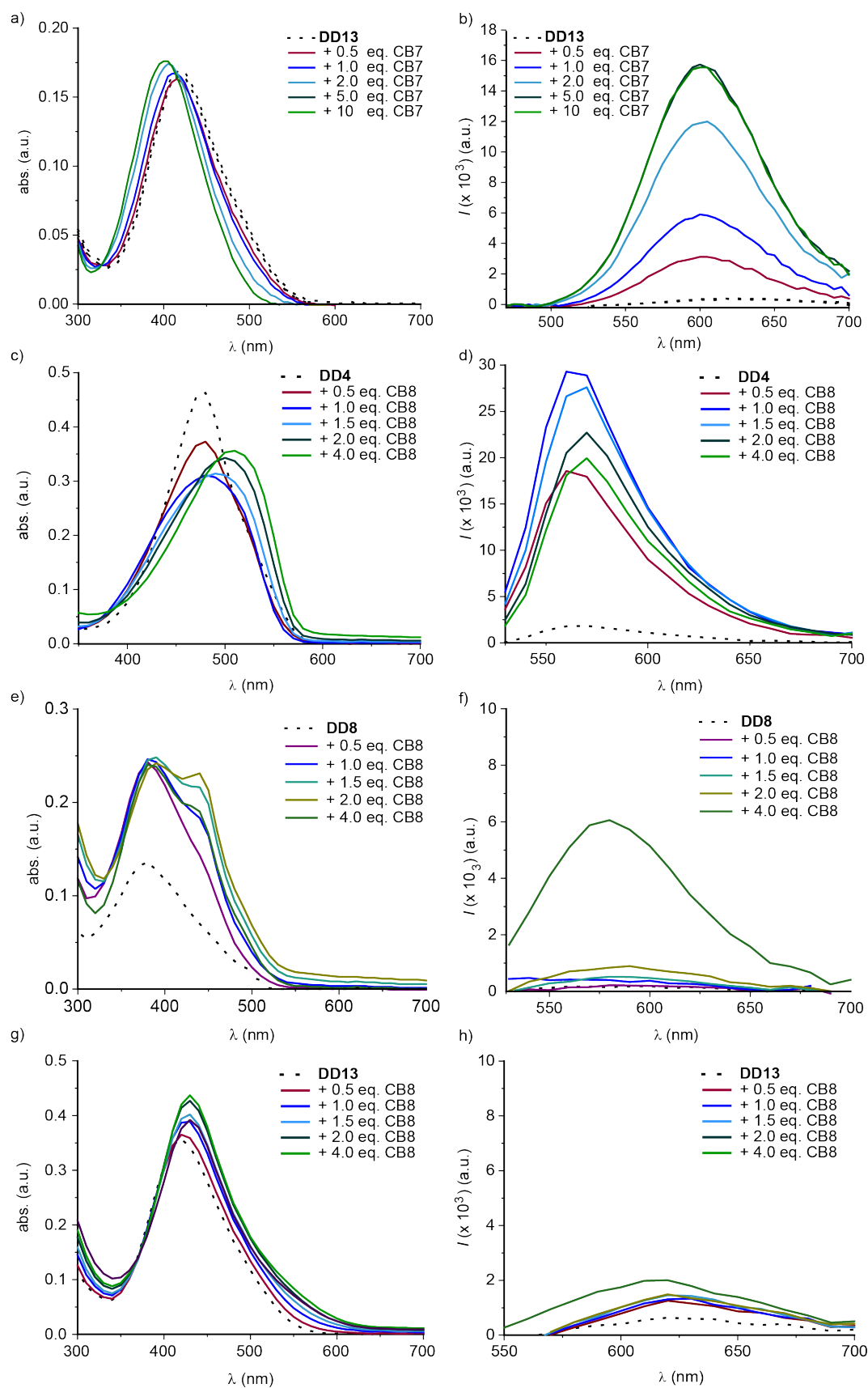
Mixing the sCx4-based DD sensors with the larger macrocyclic cucurbit[*n*]urils CB7 and CB8 forms new self-assembled complexes. The attached dye arm of a DimerDye was proposed to bind into the CB $n$  cavity forming a hetero complex and altering the DDs photophysical response. The disruption of this hetero self-assembled complex by an added analyte would allow for sensing a larger range of analyte structures (cationic, bulky, and neutral). From a collection of 13 DimerDye chemosensors,<sup>83</sup> four structurally diverse DDs (DD1, DD4, DD8, and DD13), with suitable structures to bind cucurbit[*n*]uril, were selected. The most suitable structures were based on the literature-known binding strength of CB $n$  towards pyridine, pyridinium, and indole compounds.<sup>7,153,164,231-233</sup> The selected DDs contain a cationic heteroaromatic pendant arm (see **Figure 34a**). It was expected that CB $n$  would form an inclusion complex with the attached dye arm, disrupting the dimer (DD<sub>2</sub>) complex. In general, DDs show quenched fluorescence in the dimer complex due to the antiparallel stacked arrangement of the fluorophores quenching the excited state. Adding an analyte that binds to the calixarene cavity disrupts the dimerization, and the emission of the dye turns on.<sup>226</sup> Therefore, the binding event of a CB $n$  macrocycle with the dye was expected to change the photophysical properties of the DDs (*e.g.*, emission turn-on, shifts in emission, and absorbance) due to a change in the microenvironment of the dye. **Figure 34** shows the proposed complex formation of the DD and the cucurbit[*n*]uril, the chemical structures of the cucurbit[*n*]urils, and the used monomeric DDs.



**Figure 34.** a) Schematic representation of the proposed complex formation of the DimerDye (DD<sub>2</sub>) with the cucurbit[*n*]uril macrocycle; b) chemical structure of CB7 ( $n = 2$ ) and CB8 ( $n = 3$ ); c) chemical structure of the monomeric DimerDyes (DDs), which were selected for the new DD•CB $n$  complex.

### 5.2.2. Evaluation of complex formation and analyte binding

First, the general behavior of the selected DDs was investigated with CB7 and CB8. For this purpose, a 96-well plate was equipped with 10 – 20  $\mu\text{M}$  of each DD in sodium phosphate buffer (8.4 mM, pH 7.4) in separate wells. For each DD, a titration was performed with CB7 and CB8 in a concentration range of 0 to 80/100  $\mu\text{M}$ , and absorbance and emission spectra were recorded during the stepwise addition of  $\text{CB}_n$  (see  $\lambda_{\text{ex}}$  in **Table 14**). After subtraction of the solvent signal, the spectra were analyzed for changes in the DD absorbance and emission in the presence of the cucurbit[ $n$ ]urils. DD1 (**58**), DD4 (**59**), and DD8 (**60**) showed only minor absorbance changes and no significant emission increase upon the addition of CB7, indicating little to no heterocomplexation interactions (see **Figure 85** and **Figure 86** in Section 8.2). For DD13 (**61**), a hypsochromic shift in absorbance and an intense emission turn-on were observed upon the addition of CB7 complex (see **Figure 35a** and **b**). This indicated that CB7 disrupted the DD<sub>2</sub> complex by binding the dye of the calixarene and forming a new fluorescent dual macrocyclic. DD4, DD8, and DD13 showed a bathochromic absorbance shift and/or the development of a shoulder, with a strong turn-on emission upon the addition of CB8 for DD4, and DD8. This strong emission intensity increase indicated that CB8 formed a complex with the DD monomer, disrupting the DD<sub>2</sub> complex. The results are shown in **Figure 35c-h** and **Table 3**. Based on the obtained results, the following four DD•CB $n$  combinations were selected for further experiments: DD13•CB7, DD4•CB8, DD8•CB8, and DD13•CB8. A concentration ratio of 1 DD $n$ : 2 CB $n$  gave the best emission and absorbance responses without having a large excess of free CB $n$  in the solution.

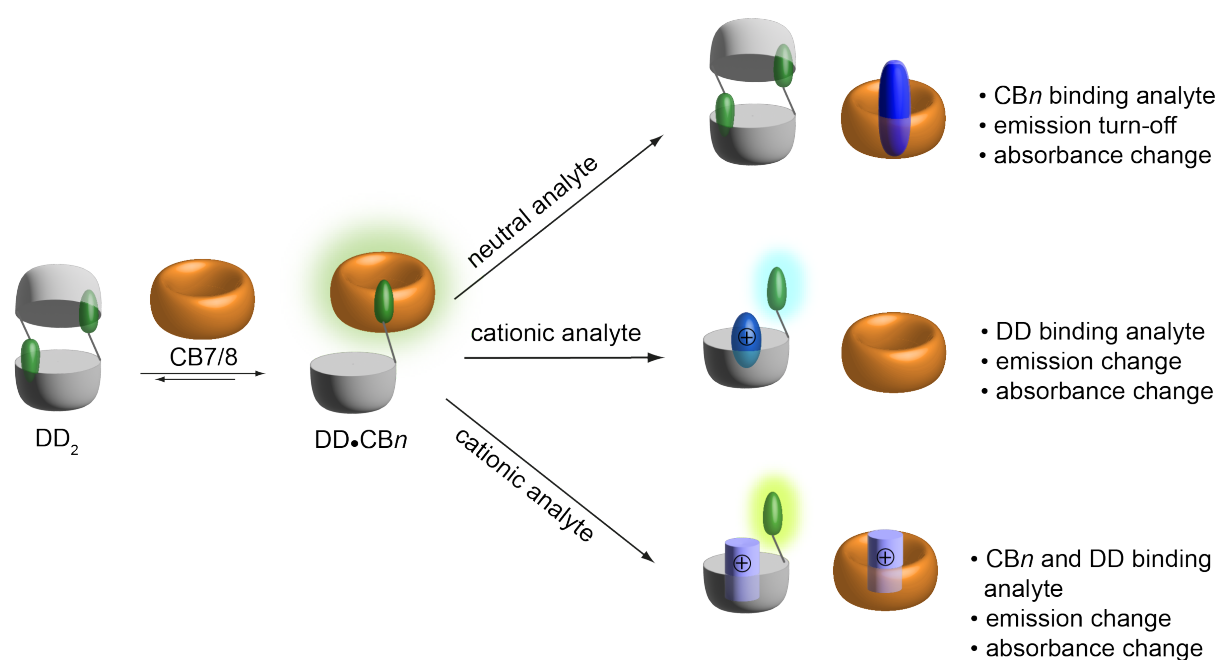


**Figure 35.** Absorbance and emission spectra of selected DDns with CB7 and CB8. a) Absorbance and b) emission spectra of DD13 (10  $\mu\text{M}$ ) upon the addition of CB7 (5 – 100  $\mu\text{M}$ ). c) Absorbance and d) emission spectra of DD4 (20  $\mu\text{M}$ ) upon the addition of CB8 (0 – 80  $\mu\text{M}$ ). e) Absorbance and f) emission spectra of DD8 (20  $\mu\text{M}$ ) upon the addition of CB8 (0 – 80  $\mu\text{M}$ ). g) Absorbance and h) emission spectra of DD13 (20  $\mu\text{M}$ ) upon the addition of CB8 (0 – 80  $\mu\text{M}$ ). All measurements were conducted in triplicates in sodium phosphate buffer (8.4 mM, pH 7.4) at 25  $^{\circ}\text{C}$ .

**Table 3.** Overview of spectroscopic responses of four different DD $n$  upon the addition of CB7 and CB8.

DimerDye (DD $n$ )	CB $n$	absorbance	emission	selected for drug-sensing experiments
<b>DD1</b> (58)	CB7	minor change	no significant change	no
	CB8	minor change	no significant change	no
<b>DD4</b> (59)	CB7	minor change	no significant change	no
	CB8	intensity decrease, bathochromic shift	strong intensity increase	yes
<b>DD8</b> (60)	CB7	minor intensity decrease, appearance of a small shoulder	minor intensity increase	no
	CB8	intensity increase, bathochromic shift, and appearance of a shoulder	intensity increase	yes
<b>DD13</b> (61)	CB7	intensity increase and hypsochromic shift	strong intensity increase	yes
	CB8	intensity decrease, bathochromic shift, and appearance of a shoulder	minor intensity increase	yes

In the next step, the interaction of analytes with the DD•CB $n$  complexes was investigated. The analyte detection strategy of these newly formed complexes is based on several possible interactions of the analyte with the DD•CB $n$  complex, leading to different signal responses that can be detected by absorbance and fluorescence. **Figure 36** shows three possible ways how analyte binding can disrupt the DD•CB $n$  complex and cause the signal responses.

**Figure 36.** Schematic representation of possible analyte binding modes of the proposed DD•CB $n$  complex. Note: Other binding modes are possible, but the mechanistic resolution was out of scope for this proof-of-principle approach.

The most straightforward option would be for an analyte to bind only the CB $n$ . Non-charged analytes can be considered in this case since calixarenes do not bind neutral structures.<sup>83</sup> Accordingly, the analyte would interfere with the DD•CB $n$  complex by binding only CB $n$ . The monomeric DD may recombine to form the non-emissive dimer, leading to an emission turn-off and possible absorbance changes as a signal readout (see **Figure 36a**).

In contrast, a cationic guest could bind exclusively to calixarenes. Analyte binding into the cavity of calixarenes leads to displacement of CB $n$  from the DD•CB $n$  complex. This would result in little to no emission changes but most likely small changes in the absorbance due to the environment and conformational changes of the chromophore (see **Figure 36b**).

The signal response becomes complex when an analyte is not selective for either macrocycle. This leads to multiple equilibria in solution, as disruption of the DD•CB $n$  complex can occur through analyte binding to the CB $n$  and the DD monomer. Varying analyte affinities for the two host cavities result in a unique equilibrium position (*i.e.*, the extent of CB $n$  displaced from the DD and the subsequent extent of preferred binding of the analyte to one host), which is reflected in both absorbance and emission changes (see **Figure 36c**).

Detection of non-charged analytes with the DD•CB $n$  system was examined using 1-adamantanol (AdOH, **26**), which is selective for CB $n$ . A solution of 10  $\mu$ M DD13 (**61**) mixed with 20  $\mu$ M CB7 in sodium phosphate buffer (10 mM, pH 7.4) was prepared. The absorbance and emission spectra were recorded before and after adding 20  $\mu$ M AdOH. The obtained intensities for the analyte binding are shown in **Figure 37**. The addition of AdOH caused a bathochromic shift of 15 nm in the absorbance and an emission intensity quenching, leading to identical spectra for the dimeric DD13 alone. These results indicated that AdOH forms a selective inclusion complex with CB7, allowing the monomeric DD13 to reassemble into its non-emissive dimeric form.

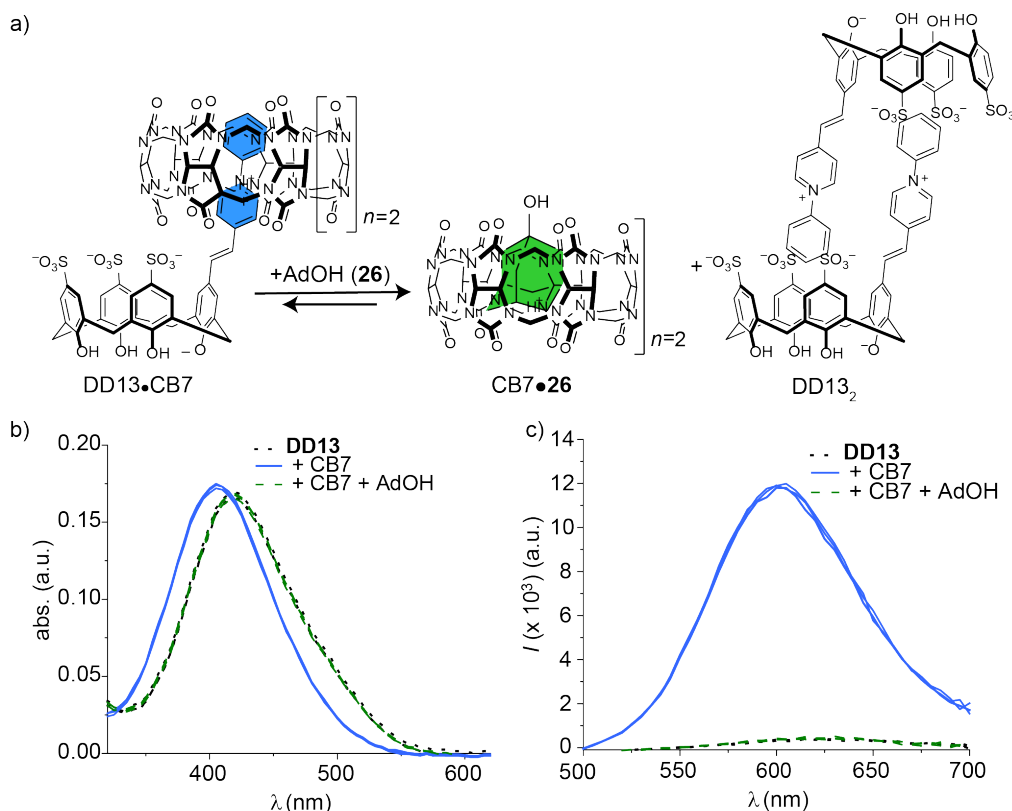


**Figure 37.** a) Inclusion complex formation of CB7•26 upon the addition of 20  $\mu\text{M}$  AdOH (26) to DD13•CB7 (DD13: 10  $\mu\text{M}$ , CB7: 20  $\mu\text{M}$ ). b) Absorbance spectra and c) emission spectra of DD13 alone (dotted black line), upon addition of CB7 (blue line) and subsequent addition of AdOH (dotted green line). All measurements were conducted in triplicates in sodium phosphate buffer (10 mM, pH 7.4) at 25  $^{\circ}\text{C}$ .

In addition,  $^1\text{H}$  NMR studies of analyte binding were performed by ALLISON SELINGER from the HOF group in a similar experiment with DD13•CB7 and another CB7 selective analyte amantadine ( $\text{AdNH}_3^+$ , 27) (see **Figure 38**). When combined in solution, the  $^1\text{H}$  NMR showed resonance broadening and signal splitting of both DD13 and CB7, indicating the formation of the DD13•CB7 complex (**Figure 38a** and **b** vs. **d**). The subsequent addition of amantadine resulted in upfield resonances from CB7-bound amantadine protons in slow exchange (**Figure 38c** vs. **e**). Upon adding amantadine, the DD13 resonances sharpened, returning to the multiplicity of isolated DD13<sub>2</sub> shown in **Figure 38a** and **e**. It must be noted that over a time of  $\sim 40$  min, the formation of precipitate was observed within the NMR tubes for DD13•CB7 with and without analyte. The precipitation upon complex formation of a calixarene with a CB $n$  is a known phenomenon.<sup>229</sup> However, the precipitation does not affect the optical-based analyte sensing experiments as these are performed at a low  $\mu\text{M}$  concentration range, where precipitation was only observed after several hours. In this work, sensing experiments were carried out directly after the preparation of DD•CB $n$  mixtures, which did not exceed the precipitation time.

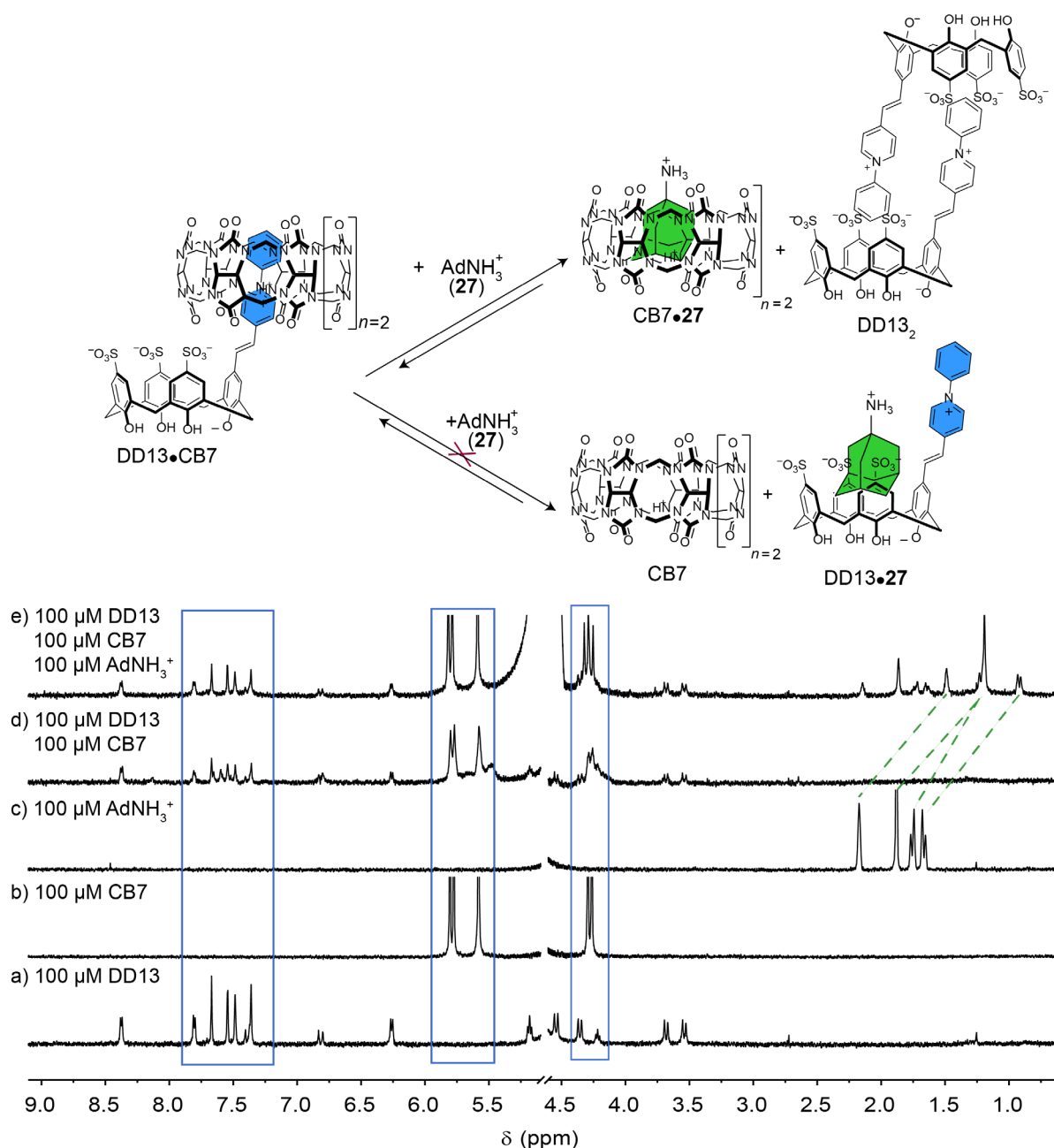


**Figure 38.** Complexation mechanism of DD13•CB7 upon amantadine (AdNH<sub>3</sub><sup>+</sup>, 27) addition and <sup>1</sup>H NMR spectra of a) 100 μM DD13, b) 100 μM CB7, c) 100 μM AdNH<sub>3</sub><sup>+</sup>, d) 100 μM DD13 and 100 μM CB7 and e) 100 μM DD13, 100 μM CB7 and 100 μM AdNH<sub>3</sub><sup>+</sup>. The blue boxes mark the resonance changes of DD13 and CB7; the green traces indicate the upfield shift of the resonance of the AdNH<sub>3</sub><sup>+</sup> upon complexation by CB7. All measurements were performed in deuterated sodium phosphate buffer (NaH<sub>2</sub>PO<sub>4</sub>/Na<sub>2</sub>HPO<sub>4</sub> 10 mM, pD 7.4).

### 5.2.3. Drug sensing experiments

The abuse of illicit drugs is a major worldwide issue causing health-related problems and social conflicts. The widespread misuse of opioids is a major topic in North America, and Canada has become one of the leading countries worldwide in the opioid overdose epidemic.<sup>234,235</sup> The misuse of opioids is often associated with drug adulterants and cutting agents. Drug adulterants are substances added to drugs that illicit a pharmacological effect; they can have similar taste,

sensation, and/or enhance the drug effects, making them more attractive to potential buyers.<sup>236,237</sup> Diluents (also known as fillers or cutting agents) are inert substances that are added to drugs to increase their weight, diluting the drug for increased profit.<sup>238</sup> Adulterants, in particular, pose extreme risks, as they can have negative health consequences and increase the risk of overdose. Therefore, it is essential to detect and classify the components of a drug sample selectively and sensitively.

Fluorescence-based chemosensors are attractive tools for detecting small molecules such as drugs. Emission-based sensing shows high sensitivity allowing the detection of molecules even at low micro- to millimolar concentrations.<sup>7</sup> Therefore, the idea was to apply the DD•CB $n$  sensing concept in an array-based platform to discriminate small molecule illicit drugs, adulterants, and diluents ranging in cationic and neutral structures.

The above selected DD•CB $n$  combinations were tested in a microwell plate format for their sensing and discrimination capabilities of various drugs in a proof-of-concept approach. The chemical structures of drugs investigated within this project are shown in **Figure 39**. They are divided into three groups (A: opioids and benzodiazepines, B: THC derivatives, and C: stimulants and adulterants), within which the different drugs should be discriminated against each other. Since several of the selected drug analytes are structurally very similar (*e.g.*, heroin (**62**) and morphine (**63**)), they may cause the same emission or absorbance response for one DD•CB $n$  complex, not allowing discrimination between the analyte molecules. However, this cross-detection can be overcome by designing a sensor array that cross-reacts with different analytes to different degrees. This means compiling each analyte's absorbance and emission output towards all DD•CB $n$  complexes creates a unique fingerprint of responses.<sup>170</sup> Principal component analysis (PCA)<sup>171</sup> is then applied to reduce the dimensionality of the data, allowing for discrimination and identification of the analytes to be determined.

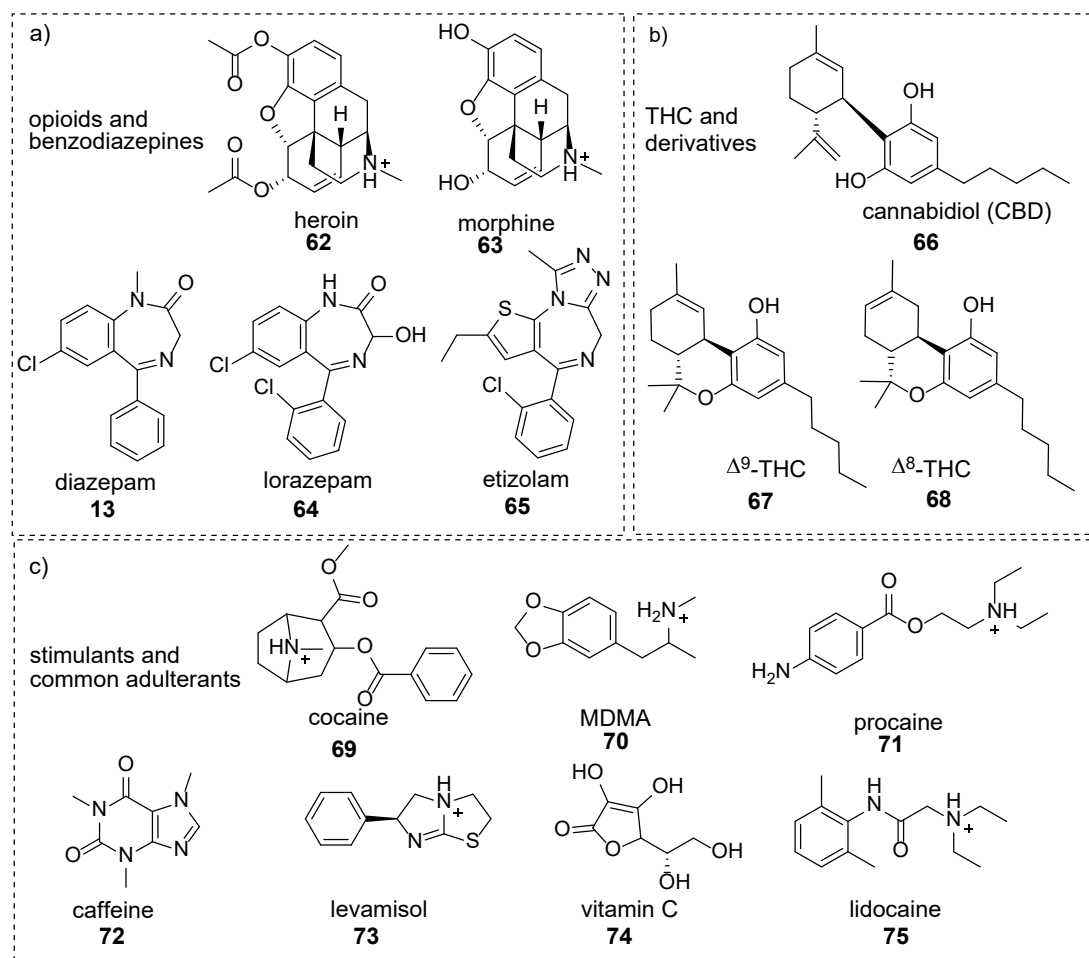


**Figure 39.** Chemical structure of drugs used within this project. a) Opioids and benzodiazepines, b)  $\Delta^9$ -THC and its derivatives, c) stimulants such as cocaine and MDMA, as well as standard adulterants added to the stimulants.

For the detection and discrimination between closely related drugs, a sensor array composed of the above selected four DD•CB $n$  combinations (DD4•CB8, DD8•CB8, DD13•CB8, and DD13•CB7), as well as a CB8•berberine chloride (CB8•BC) chemosensor, was used. The CB8•BC chemosensor was selected as an additional chemosensor because the dye has different spectroscopic properties (*i.e.*, different absorbance and emission wavelength) than the DD•CB $n$  combinations. This allowed for a broader detection range and therefore increased the discrimination possibilities. Therefore, a solution of each DD•CB $n$  combination with 10.5  $\mu$ M DD and 21  $\mu$ M CB $n$  in sodium phosphate buffer (8.4 mM, pH 7.4) was prepared and subsequently mixed with 105  $\mu$ M of the different drugs. Due to solubility issues the drug solutions were prepared in MeOH, yielding a final MeOH amount of 2% for each detection experiment. For each DD•CB $n$  combination (**M**) each drug of its drug class (**N**) was mixed separately, giving **M** x **N** mixture samples per experiment. The mixture samples were added to a 384-microwell plate with every DD•CB $n$  combination in a separate well (12 replicas per DD•CB $n$  combination and drug of which the two highest and lowest values were systematically excluded for further analysis). The absorbance and emission of each DD•CB $n$ •drug combination were measured and

blank corrected. Wavelengths that provided visual discrimination were then selected for multivariate analyses. PCA analysis (correlation) and confidence ellipses (95%) of the obtained data were calculated using the principal component analysis tool from OriginPro (see **Figure 40** for the workflow).<sup>239</sup>

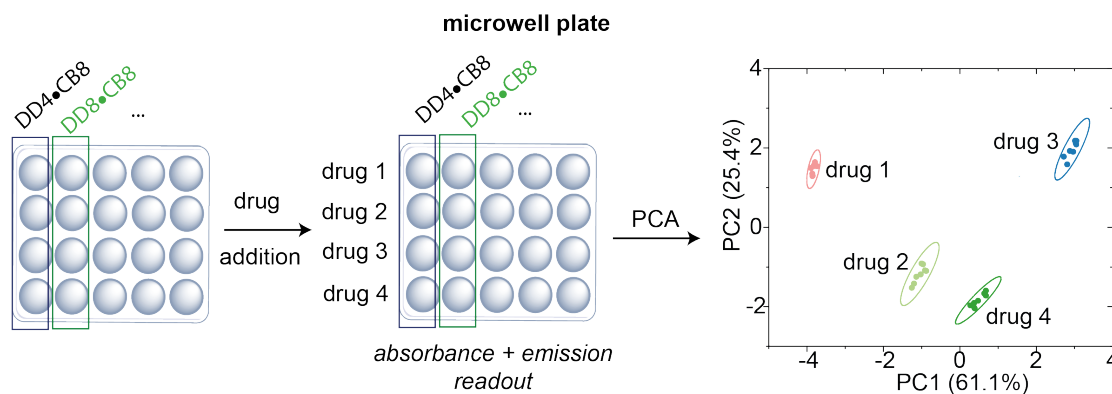


**Figure 40.** Schematic representation of the drug detection and discrimination workflow with the sensor array.

First, the detection and discrimination of opioids and benzodiazepines were examined. The selected analytes are structurally similar cationic drugs and thus pose a challenge for discrimination. The opioids heroin (**62**) and morphine (**63**) only differ by two methoxy groups, and the benzodiazepines (often added to opioids sold on the ‘street’), diazepam (**13**), lorazepam (**64**), and etizolam (**65**) are structurally similar. Here, an array of four chemosensor combinations was sufficient to discriminate all five drugs from each other (see **Figure 41**), measuring absorbance and fluorescence emission at selected wavelengths. The following chemosensors were used in a correlation analysis for the PCA plot: DD4•CB8, DD13•CB8, DD13•CB7 and CB8•BC, and the selected wavelength used are shown in **Table 4**.

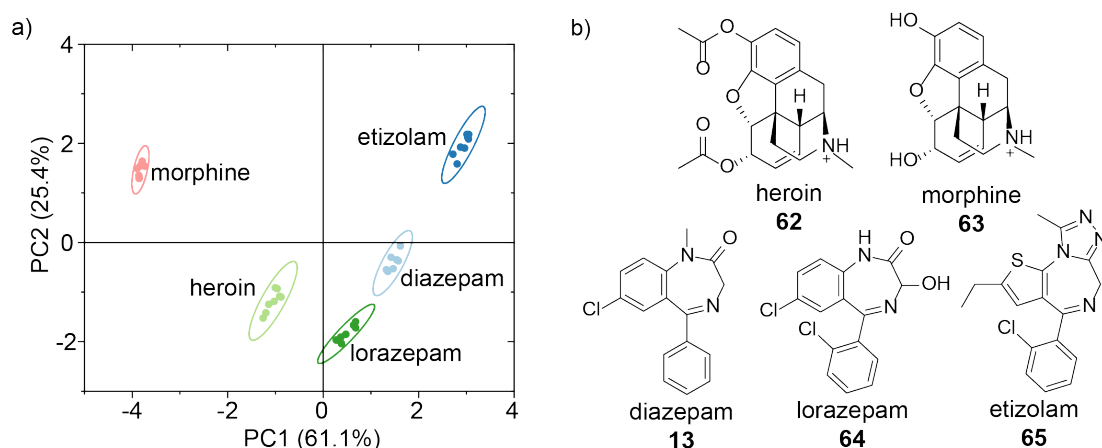


**Figure 41.** a) PCA (correlation) plot of opioids and benzodiazepines obtained from a DD•CB<sub>n</sub> sensor array: DD4•CB8, DD13•CB8, DD13•CB7, and CB8•BC. Each sample set is enclosed by 95% confidence ellipses. All drugs were well discriminated against with complete separation of clustered samples. For DD•CB<sub>n</sub> mixtures: DD (10.5 μM), CB<sub>n</sub> (21 μM), drug (105 μM); for CB8•BC: CB8 (4.5 μM), BC (3.0 μM), drug (30 μM) in 2% MeOH in sodium phosphate buffer (8.4 mM NaH<sub>2</sub>PO<sub>4</sub>/Na<sub>2</sub>HPO<sub>4</sub>, pH 7.4). b) Chemical structures of examined drugs.

Since the discrimination of those structurally closely related drugs was possible, I also investigated the discrimination of the constitutional isomers  $\Delta^9$ -THC (**67**) as well as  $\Delta^8$ -THC (**68**). Those tetrahydrocannabinol (THC) isomers only differ in the position of one double bond and are, therefore, not distinguishable from each other by most chemosensors and arrays.<sup>240</sup> The unique feature of this assay is that all examined analytes of this class are uncharged and cannot be bound by the DDs. Therefore, the emission and absorbance changes will result only from the degree of complexation for the formation of  $CBn$ •drug complexes, whereby the DDs reassemble to their dimeric  $DD_2$  form. A sensor array of both  $DD13$ • $CBn$  sensors successfully detected and discriminated between the two isomers of THC and CBD (cannabidiol, **66**) using emission and absorbance data of  $DD13$ • $CB7$  and  $DD13$ • $CB8$  at the selected wavelength shown in **Table 4**. The corresponding PCA plot (correlation) is shown in **Figure 42**. The unique equilibrium positions induced by neutral analytes binding  $CBn$  result in distinguishable optical responses. This result indicates that even nearly identical neutral molecules can be distinguished with the new sensor array of  $DD$ • $CBn$  complexes.

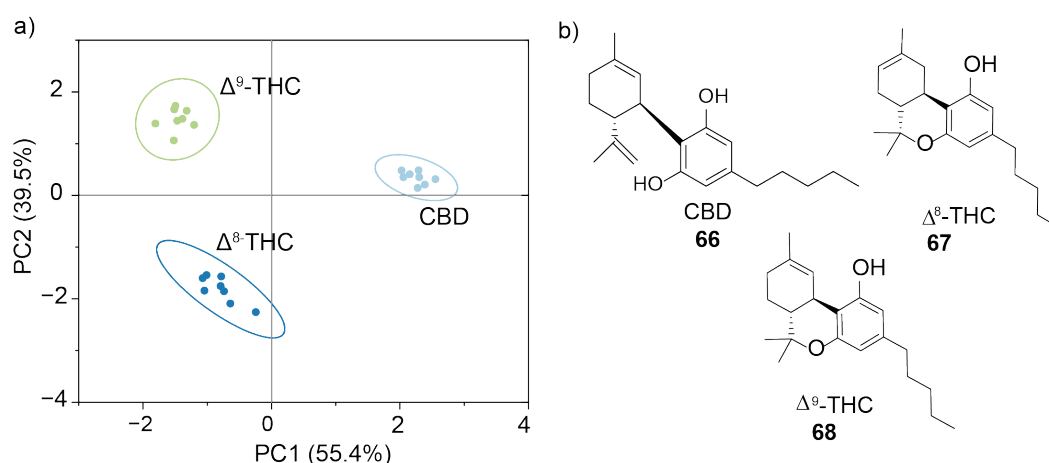


**Figure 42.** a) PCA (correlation) plot of THC derivatives and CBD obtained from the  $DD13$ • $CB8$ , and  $DD13$ • $CB7$  sensor array readout. Each sample set is enclosed by 95% confidence ellipses. All drugs were well discriminated against with complete separation of clustered samples. For  $DD$ • $CBn$  mixtures:  $DD$  (10.5  $\mu$ M),  $CBn$  (21  $\mu$ M), drug (105  $\mu$ M) in 2% MeOH in sodium phosphate buffer (8.4 mM  $NaH_2PO_4/Na_2HPO_4$ , pH 7.4). b) Chemical structures of examined drugs.

Finally, the discrimination of the stimulant drugs cocaine (**69**) and MDMA (**70**) and common adulterants (procaine (**71**), caffeine (**72**), levamisole (**73**), Vitamin C (**74**), lidocaine (**75**) was tested.<sup>236,237</sup> It was possible to discriminate six out of eight compounds using the sensors  $CB8$ • $BC$ ,  $DD4$ • $CB8$ ,  $DD13$ • $CB7$ ,  $DD13$ • $CB8$  for absorbance and emission of the PCA score plots (see **Figure 43**). The selected wavelengths used are shown in **Table 4**.

Notably, the adulterants posing toxicity risks,<sup>241-244</sup> such as the local anesthetics procaine and lidocaine (CNS problems, nausea, vomiting, dizziness, tremors, and convulsions) as well as levamisole (fever, agranulocytosis), were all discriminated. Vitamin C and caffeine were not

discriminated against since only CB7 interacts weakly with those compounds since sCx4 does not bind neutral and anionic guests.<sup>245</sup> However, this does not present a severe limitation of the array, as Vitamin C and caffeine do not pose serious health repercussions. Caffeine facilitates drug administration and complements the high, whereas Vitamin C is used as a weak acid to solubilize the drugs.<sup>246,247</sup>

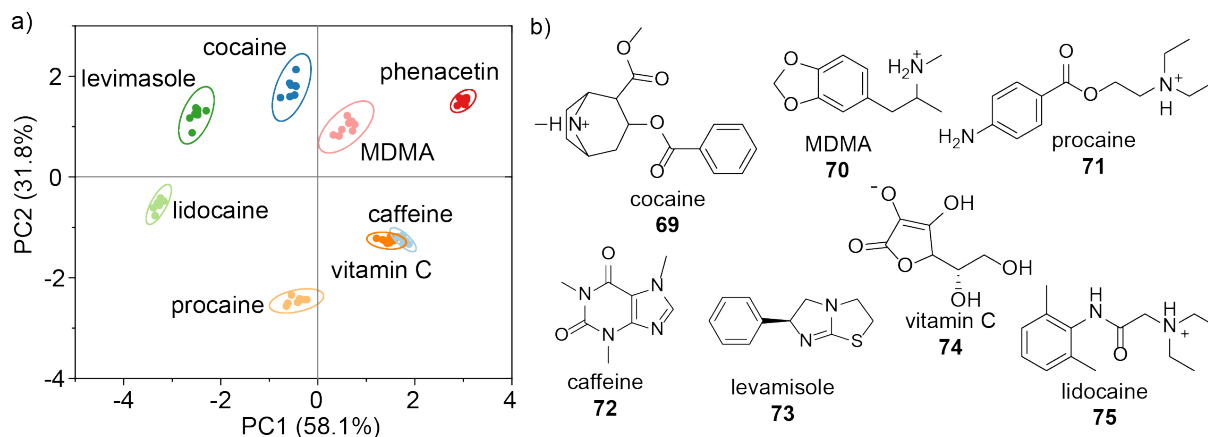


**Figure 43.** a) PCA (correlation) plot of stimulants and their common buffs/adulterants obtained from DD•CB $n$  sensor array: DD4•CB8, DD13•CB8, DD13•CB7, and CB8•BC. Each sample set is enclosed by 95% confidence ellipses. Six out of eight drugs were well discriminated with complete separation of clustered samples. For DD•CB $n$ : DD (10.5  $\mu$ M), CB $n$  (21  $\mu$ M), drug (105  $\mu$ M); for CB8•BC: CB8 (4.5  $\mu$ M), BC (3.0  $\mu$ M), drug (30  $\mu$ M) in 2% MeOH in sodium phosphate buffer (8.4 mM NaH<sub>2</sub>PO<sub>4</sub>/Na<sub>2</sub>HPO<sub>4</sub>, pH 7.4). b) Chemical structures of examined drugs.

After the investigation and successful discrimination of the different analytes within their classes, the final step was to investigate the performance of the new sensor systems in discriminating all drug analytes used in this work in the context of PCA. Of the fifteen different drugs and adulterants, thirteen could be completely discriminated by the array data through the use of PCA. Again, only Vitamin C and caffeine could not be distinguished from each other, which is consistent with the PCA in **Figure 43**. The obtained PCA (correlation) from absorbance and emission data of the sensors CB8•BC, DD4•CB8, DD8•CB8, DD13•CB7, DD13•CB8 at selected wavelengths (see **Table 4**) are shown in **Figure 44**. Overall, the newly developed DD•CB $n$  sensing system provided reliable results for detecting and differentiating various drugs (neutral, cationic, large, small), demonstrating the general utility and future promise of this concept. The results discussed in this chapter are the basis of a publication, which is currently under preparation. The here provided data and their analysis is thus similar to the ones in the planned publication.

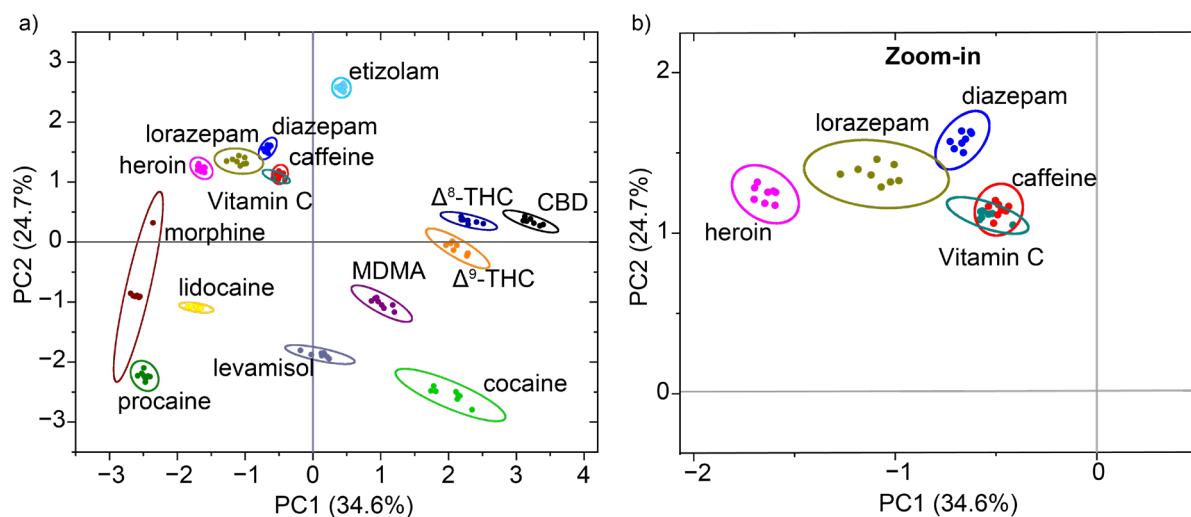


**Figure 44.** a) PCA (correlation) plot obtained from DD•CB $n$  sensor array of all examined drugs examined within this study: DD4•CB8, DD8•CB8, DD13•CB8, DD13•CB7, and CB8•BC. Each sample set is enclosed by 95% confidence ellipses. 13 out of 15 drugs were well discriminated with complete separation of clustered samples. For DD•CB $n$ : DD (10.5  $\mu$ M), CB $n$  (21  $\mu$ M), drug (105  $\mu$ M); for CB8•BC: CB8 (4.5  $\mu$ M), BC (3.0  $\mu$ M), drug (30  $\mu$ M) in 2% MeOH all in sodium phosphate buffer (8.4 mM NaH<sub>2</sub>PO<sub>4</sub>/Na<sub>2</sub>HPO<sub>4</sub>, pH 7.4). b) Zoom-in.

**Table 4.** Overview of the selected wavelengths of each DD•CB $n$  chemosensor complex used for the PCA score plots of the different drug classes. Excitation wavelengths are listed in Section 7.2 in **Table 14**.

sensor ensemble	opioids and benzodiazepines	THC derivatives	stimulants and adulterants	all examined drugs
DD4•CB8	$\lambda_{\text{ems}} = 570$ nm	not used	$\lambda_{\text{abs}} = 480$ nm, $\lambda_{\text{ems}} = 570$ nm, $\lambda_{\text{ems}} = 600$ nm	$\lambda_{\text{abs}} = 480$ nm, $\lambda_{\text{abs}} = 520$ nm, $\lambda_{\text{ems}} = 570$ nm
DD8•CB8	not used	not used	not used	$\lambda_{\text{ems}} = 570$ nm
DD13•CB8	$\lambda_{\text{abs}} = 430$ nm, $\lambda_{\text{ems}} = 600$ nm	$\lambda_{\text{abs}} = 400$ nm, $\lambda_{\text{ems}} = 600$ nm	$\lambda_{\text{abs}} = 400$ nm	$\lambda_{\text{abs}} = 400$ nm, $\lambda_{\text{ems}} = 600$ nm
DD13•CB7	$\lambda_{\text{abs}} = 400$ nm, $\lambda_{\text{abs}} = 430$ nm, $\lambda_{\text{ems}} = 600$ nm	$\lambda_{\text{abs}} = 400$ nm, $\lambda_{\text{abs}} = 430$ nm, $\lambda_{\text{ems}} = 600$ nm	$\lambda_{\text{abs}} = 400$ nm	$\lambda_{\text{abs}} = 400$ nm
CB8•BC	$\lambda_{\text{abs}} = 340$ nm, $\lambda_{\text{abs}} = 460$ nm, $\lambda_{\text{ems}} = 530$ nm	not used	$\lambda_{\text{abs}} = 340$ nm, $\lambda_{\text{ems}} = 530$ nm	$\lambda_{\text{abs}} = 480$ nm, $\lambda_{\text{ems}} = 530$ nm

### 5.3.Salt-stable rotaxane chemosensor

*The results of the following chapter have been published in a Nature Communication article<sup>248</sup> titled “A supramolecular cucurbit[8]uril-based rotaxane chemosensor for the optical tryptophan detection in human serum and urine” in 2023. J.K. performed the experimental setup, measurement, data analysis and manuscript writing under the supervision of F.B.. C.Z. prepared the rotaxane microarrays and performed the measurements. Section 5.3 has been partially adapted and modified from ref.<sup>248</sup> with permission from Springer Nature.*

In addition to gaining a fundamental understanding of molecular recognition-based host•guest chemistry, this work's primary goal was to design and develop a new chemosensing system for detecting tryptophan (Trp, **2**) in buffered media and biofluids. L-Tryptophan (Trp), an essential aromatic amino acid, is a building block in the biosynthesis of proteins and a precursor for various bioactive metabolites produced within the kynurenine pathway.<sup>249,250</sup> Many metabolites and neurotransmitters routed through the Trp metabolism, such as serotonin or melatonin, play a crucial role in regulating sleep-wake rhythm, inflammation, energy homeostasis, and behavior.<sup>11,251,252</sup> Altered concentrations of Trp in blood and urine have been shown to correlate with certain diseases, such as cardiovascular and neurogenerative diseases,<sup>13,249</sup> making its detection and quantification valuable for early disease diagnosis. Selected examples of Trp concentration ranges in biofluids<sup>13,168,253-257</sup> for healthy and diseased human beings reported in the literature are shown in **Table 5**. Please note that there are variations in observed concentration ranges between reported studies. This is likely due to sample preparations, quantification methods and/or other factors such as nutrition, diet, age, weight, sex, and geographical location.<sup>258-262</sup>

**Table 5.** Selected examples of L-tryptophan (Trp) concentration ranges for healthy and diseased adults in blood serum, blood plasma, and urine.

	[Trp] ( $\mu\text{M}$ )	medium	ref.
no disease	41 - 77	blood serum	13,257
	21 - 93	urine	168
Alzheimer's disease	24 - 42	blood serum	263
	15 - 22	urine	263
chronic kidney disease	17 - 26	blood serum	257
cardiovascular disease	27 - 76	blood serum	264
anaemia of inflammation	22 - 43	blood serum	265
coronary heart disease	44 - 63	blood plasma	266
sepsis	25 - 40	blood plasma	267

Overall, detecting small biorelevant molecules (further called biomarkers), *e.g.*, amino acids and their derivatives, is becoming increasingly important in modern molecular diagnostics,<sup>268-271</sup> especially regarding future point-of-care devices and personalized medicine. To date, general detection and quantitative analysis have been primarily limited to clinical laboratories with HPLC-MS or NMR facilities.<sup>272-275</sup> Unfortunately, these are not only cost-intensive, requiring both the equipment and trained personnel, but also often demand extensive handling, such as deproteinization of biofluids,<sup>257</sup> making their application in point-of-care units or ambulances impractical.

Consequently, it is evident that alternative methods for biomarker detection and quantification are needed that are not only easy to use but also fast-responding and inexpensive. It has been shown that chemosensors operating through molecular-recognition principles meet these requirements. Thus, they are an interesting alternative to classical methods.<sup>7,45,129,149,216,226,276,277</sup> However, until now, only a few examples of optical chemosensors have been applied in actual devices used in clinics and personal homes.<sup>7,54,278,279</sup> Most metabolites cannot be detected in biofluids using the optical chemosensors developed so far due to deficiencies concerning affinity, selectivity, signal transduction, and stability.<sup>7,45,112,268,280</sup> Biofluids have a complex matrix environment due to the presence of various bioactive molecules (*e.g.*, proteins) and high concentrations of salts.<sup>169</sup> Both component types can act as competitors for the chemosensor and pose a high risk of interference.<sup>7,281</sup> The absorptivity and autofluorescence emission of biofluids cause further challenges for optical-based sensing methods.<sup>7</sup> Therefore, a new chemosensor design is needed, which overcomes the limitations of current systems in terms of salt stability and interfering competitors.

### 5.3.1. Design concept for a salt-stable chemosensor

In the search for an operational chemosensor for the selective detection of tryptophan (Trp) in biofluids, it is crucial to ensure that the chemosensor is not susceptible to competitive binding of salt cations present in the biofluid. Furthermore, a molecular recognition unit for the detection of Trp must be implemented to ensure strong binding of Trp to the chemosensor. Most known supramolecular chemosensors based on host•guest chemistry are self-assembled systems held together by non-covalent interactions and tend to disassemble in highly complex media (see **Figure 45a**).<sup>112,166</sup> To circumvent this problem, the idea was to use a molecularly interlocked design, *i.e.*, a supramolecular rotaxane, that combines the sensing ability with a salt stability. Rotaxanes<sup>282,283</sup> are molecular interlocked molecules (MIMs) where a dumbbell-shaped molecule (axle) is threaded through a macrocycle (see **Figure 45b**). These molecular constructs have been

applied as molecular machines,<sup>284-286</sup> supramolecular catalysts,<sup>287</sup> and as inorganic anion binders.<sup>288</sup> Following this design principle, the idea was to use the rotaxane structure and install a molecular recognition unit (*i.e.*, an aromatic dye) in the linear axle molecule, which can form a host•guest complex with the macrocycle by threading it. The formed structure is then highly stable as it prevents the disintegration of the host•dye unit and restricts the unfavoured homo-stacking interaction of the dye.<sup>289</sup> In most rotaxanes, the axle molecule almost completely fills the host cavity. However, the essential point is that a macrocyclic host with a big enough cavity is selected, allowing Trp binding alongside the fluorescent dye axle still inside the hydrophobic host cavity. Following this design strategy, molecular interactions between the host (H) and dye axle (D) are enabled, thereby promoting high affinity, selectivity, and signal transduction.

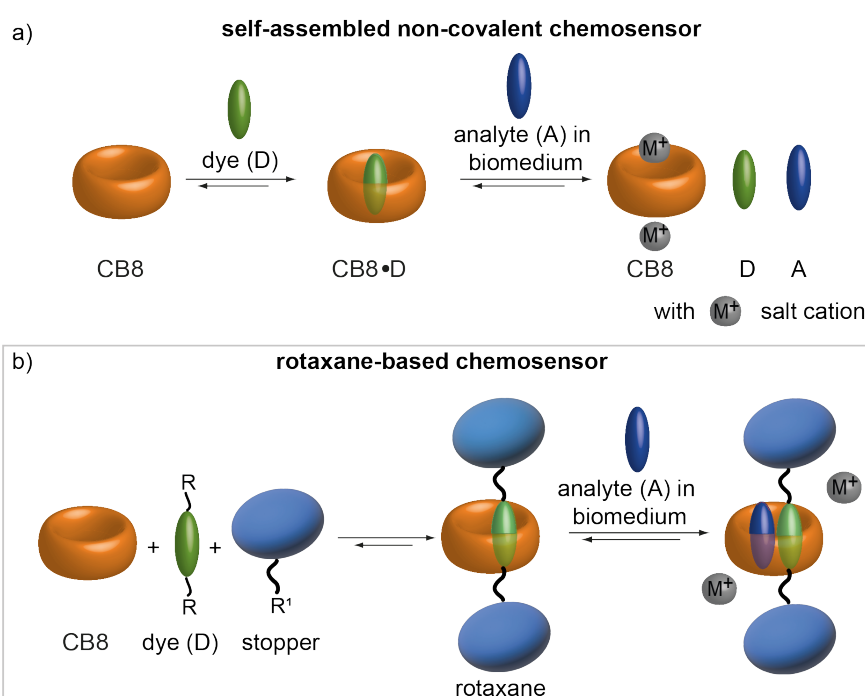


**Figure 45.** Schematic representation of the design and working principle of a) a self-assembled non-covalent chemosensor and b) a rotaxane-based chemosensor in salt-containing biomedium. The self-assembled non-covalent chemosensor is responsive towards salts present in biomedium, leading to the dissociation of the chemosensor. The rotaxane-based chemosensor is salt-stable and, therefore, suitable for analyte sensing in salt-containing biomedium.

Tryptophan does not have a chemically reactive side chain other than the for amino acids characteristic amino- and carboxylate groups, which leaves only the indole moiety as a molecular recognition unit.<sup>248</sup> Consequently, selective molecular recognition of Trp by an artificial receptor requires the integration of non-covalent binding motifs that foster cation- $\pi$ - or  $\pi$ - $\pi$ -stacking interactions with the aromatic indole moiety of Trp. Additionally, the aromatic moiety in Trp allows for hydrophobic interactions within a host cavity.<sup>127,290</sup> Following the established concept of self-assembled host•guest complexes based on cucurbit[*n*]urils (CB*n*), it was apparent to use a cucurbit[*n*]uril as a macrocyclic component and a dicationic aromatic dye as the reporter unit.

CB $n$  show high binding affinities towards hydrophobic analytes as a result of the release of high-energy water molecules from their cavity upon analyte binding (non-classical hydrophobic effect).<sup>102,207</sup> Cucurbit[8]uril (CB8, **25**) was selected as the host molecule due to its unique binding properties, *i.e.*, ternary complex formation with two aromatic compounds.<sup>156,291-294</sup> Besides, self-assembled non-covalent CB8•dye complexes have proven to offer binding affinities towards Trp in the  $\mu\text{M}$  range,<sup>163,295</sup> which is in accordance with the concentration ranges found for Trp in human biofluids (see **Table 5**). Dicationic diazapyrenium (DAP) dyes were chosen as fluorescent reporter dyes as they show high binding affinities for the cation-affine CB8 and are commonly used in competitive or associative binding assays (IDA and ABA) to detect small aromatic analytes.<sup>112,156,294,296</sup> Due to their aromatic nature, they have a rigid, planar structure, which still leaves enough space in the host cavity for the analyte to bind alongside the dye in the CB $n$ . Inside the host cavity, they can engage in non-covalent interactions with an aromatic analyte, which leads to an electron transfer process that can be monitored by absorbance and fluorescence spectroscopy.<sup>156</sup>

Additionally, the DAP core allows variable functionalization at the nitrogen atoms of positions 2 and 7, enabling the attachment of voluminous stopper groups. The stopper group must have a diameter larger than 7 Å to prevent the CB8 macrocycle from slipping off the linear axle. **Figure 46** shows the selected structures of each rotaxane component; their synthesis is discussed in the next section.

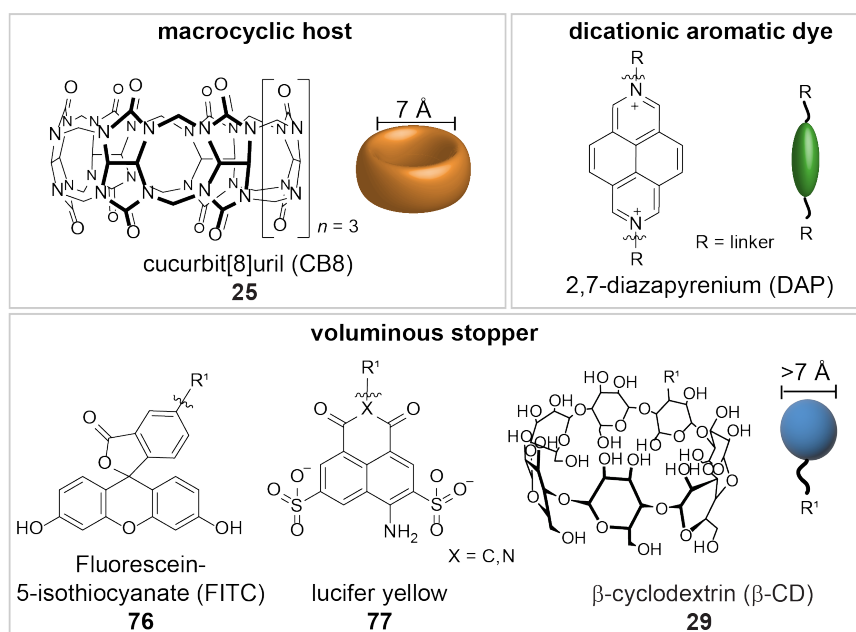


**Figure 46.** Overview of the selected chemical structures for the preparation of the rotaxane chemosensor and their schematic representation.

### 5.3.2. Preparation of a rotaxane-based chemosensor

#### 5.3.2.1. Synthesis of DAP dyes

The non-charged precursor dye 2,7-diazapyrene (**81**) was prepared according to literature procedures in a total of three steps (see **Figure 47**). The first two steps were carried out according to a procedure from STANG and coworkers<sup>297</sup>, and the last step was based on a procedure from HÜNIG and coworkers.<sup>298</sup> First, the dianhydride 1,3,6,8-tetrahydro-2,7-dimethyl-2,7-diazapyrene (**78**) was converted into its diimide **79** by reacting it with methylamine. In the next step, the reduction of **79** was carried out in the presence of lithium aluminium hydride (LiAlH<sub>4</sub>) activated by aluminium chloride (AlCl<sub>3</sub>), yielding the diamine **80** after Soxhlet extraction with chloroform. The subsequent conversion of the diamine into the dye 2,7-diazapyrene **81** was achieved by a solvent-free oxidation using selenium.<sup>298</sup> The crude product was purified by redissolving in 1 M HCl followed by precipitation with NaOH at pH 12. After repeating this procedure twice, the product was obtained with an overall yield of 30 % over a total of three steps.

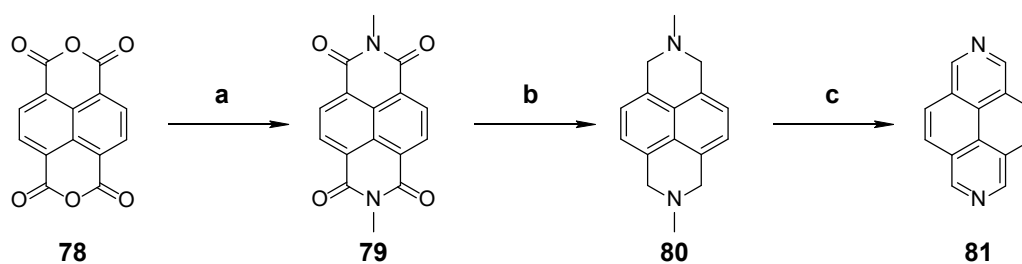


**Figure 47.** Synthetic route of 2,7-diazapyrene (**81**): a) Methylamine (40 %, aq.), 100 °C, 3 h, 56 %.<sup>297</sup> b) AlCl<sub>3</sub>, LiAlH<sub>4</sub>, THF (dry), 66 °C, 4 h, 76 %.<sup>298</sup> c) Selenium, 265 °C, 4 h, 300 °C, 1 h, 70 %.<sup>298</sup>

The neutral 2,7-diazapyrene dye (**81**) was modified with various alkyl and benzyl groups by nucleophilic additions of different halogenated linker molecules, shown in **Figure 48**. The alkyl and benzyl linkers were selected based on their length and functional groups to allow for reactions with the selected stopper groups. Besides, they ensure a sufficiently large distance between the CB8 host and the stopper groups enabling sterically unhindered binding of the Trp analyte. The benzyl-formyl linker forming **82** was introduced by mixing DAP with an excess of the commercially available 4-(bromomethyl) benzaldehyde in dry DMF and heating to 70 °C for two days. The desired product **82** precipitated from the reaction solution and was obtained as a yellow solid with a yield of 55 % after washing with DMF. No further purification was necessary. The symmetric modification of DAP with a butyl thiol and butyl azide linker first required the introduction of the bromobutyl linker **83**. Therefore, DAP underwent an *N*-alkylation with an excess of 1,4-dibromobutane in dry DMF at room temperature, yielding 46 % of **83** as a yellow solid. For **85**, the terminal bromide group of **83** was substituted with a thioacetate group using potassium thioacetate in water yielding **84**. The subsequent deprotection of the thiol group was

achieved with acetyl chloride in dry methanol,<sup>299</sup> yielding the dye **85** in 65 % yield. The synthesis of 2,7-*bis*(azido butyl)-2,7-diazapyrene **86** was also carried out *via* **83** as an intermediate, which was reacted with sodium azide in water, allowing the replacement of the bromide groups by the two azide groups. After lyophilization, product **86** was isolated with a yield of 87 %.

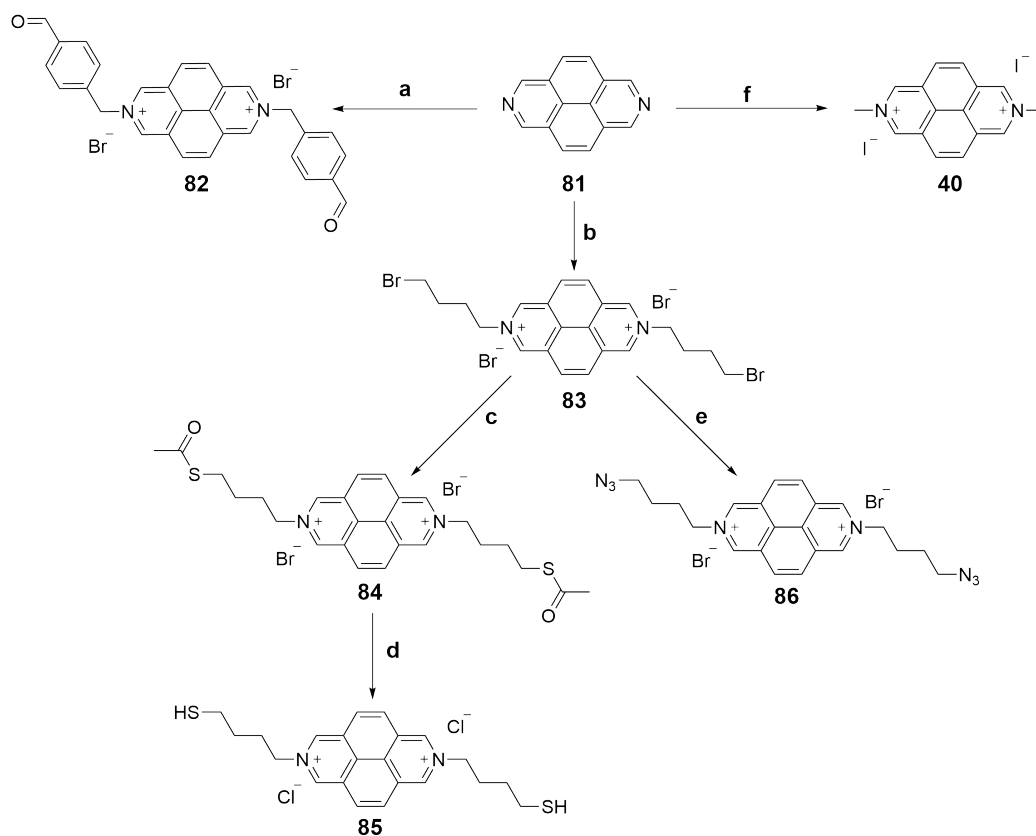


**Figure 48.** Overview of the prepared 2,7-DAP functionalization following nucleophilic additions of benzyl- and alkyl halogenides. a) 4-(Bromomethyl) benzaldehyde, DMF, 70 °C, 2 d, 55 %. b) 1,4-Dibromobutane, DMF, 85 °C, 48 h, 46 %. c) Potassium thioacetate, water, r.t., 3 d,  $\geq 99$  %. d) Acetyl chloride, MeOH (dry), r.t., 1 d, 65 %. e) Sodium azide, water, 3 h, 80 °C, 87 %. f) Methyl iodide, DMF (dry), r.t., 2 d, 34 %.

The cationic DAP modifications **82**, **85**, and **86**, shown in **Figure 48**, were all synthesized as reporter dye units for a possible rotaxane chemosensor. In addition, the cationic dye MDAP (**40**) was prepared for control experiments with a non-rotaxanated dye. The nucleophilic addition was performed in the same style as for **82** and **83** by the reaction with an excess of methyl iodide in dry DMF, yielding the clean yellow product after dissolution in 1 M HCl and subsequent precipitation at 4 °C from acetone.

### 5.3.2.2. Synthesis of the chemosensing rotaxane

In contrast to the dye synthesis and modification, preparing the water-soluble rotaxane chemosensor proved to be much more challenging. As briefly pictured in **Figure 46**, three different stopper groups were considered for preparing a rotaxane with a CB8 macrocycle and a DAP dye as a reporter unit. First, voluminous dyes, *i.e.*, lucifer yellow (**77**) and fluorescein (**76**), were tested as possible stopper groups. The use of a bulky and emissive molecule as stopper groups does not only prevent the disintegration of the chemosensor but also offers the opportunity to serve as a reference signal for the emission readout as the stopper is unaffected by the binding event in the CB8 cavity. The reaction of benzaldehyde-functionalized DAP dye (**82**) with the commercially available carbohydrazide lucifer yellow (**77**) in the presence of CB8 yielded no rotaxane. For fluorescein, a rotaxane was formed from a copper-free click reaction of DAP-azide (**86**) with a strained alkyne (DBCO-fluorescein, **87**) and the thiol-ene reaction of DAP-thiol (**85**) with the maleimide (**88**). However, both products (**89** and **90**) were almost insoluble in water and, therefore, unusable for the sensing application in aqueous media.

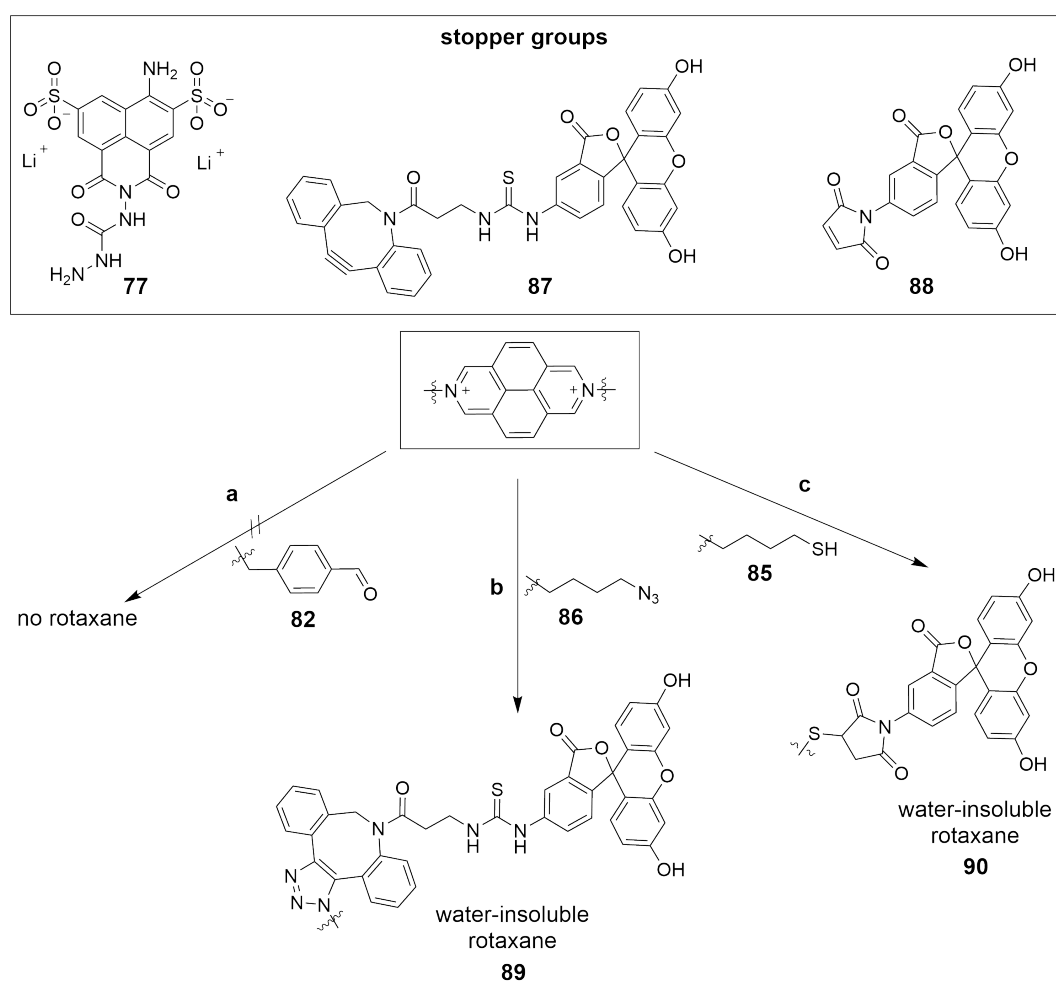


**Figure 49.** Synthesis attempts of a water-soluble CB8-DAP-based rotaxane with three different stopper groups. a) **82**, **77**, aqueous solution, r.t.. b) **86**, **87**, CB8, water, r.t., 4 d. c) **85**, **88**, CB8, water/DMSO, r.t., 3 d.

Since neither the reaction with the CH-active lucifer yellow (**77**) nor with the fluorescein derivatives (**87** and **88**) yielded functional water-soluble rotaxanes, the idea was to introduce a stopper group that might even increase the solubility of the rotaxane in water compared to the CB8 alone. A commercially available amino-functionalized  $\beta$ -cyclodextrin ( $\beta$ -CD, **93**) was selected as a suitable stopper group. The large  $\beta$ -CD ( $> 7 \text{ \AA}$ ) offers not only a high water solubility ( $16.3 \text{ mM}$ )<sup>300</sup>, but the many OH-groups and the hydrophobic cavity of the  $\beta$ -CD give rise to further post-synthetic covalent and non-covalent modification opportunities. Additionally, it was also theorized that the encapsulation of the recognition unit (CB8•DAP) into the hydrophobic binding pocket of serum albumin<sup>301,302</sup> would be hindered by the installation of  $\beta$ -CD stopper groups.<sup>303</sup> This would support the application of the resulting rotaxane chemosensor for sensing in untreated blood serum. In order to covalently link the DAP-dye moiety with the amino-functionalized CD, a maleimide-functionalized polyethylene glycol (PEG, **91**) linker with *N*-hydroxy succinimide functionality (NHS) was used. It was planned to attach the linker *via* a MICHAEL thiol-ene reaction to the thiol-functionalized DAP (**85**) shown in **Figure 50**. Although the thiol-ene reaction between **85** and the maleimide moiety of the linker **91** was successful, the product **92** could not be obtained. During synthesis and the aqueous purification, the NHS ester hydrolyzed, leading to the loss of the NHS ester moiety, making the molecule unusable for the desired conjugation to the primary amine of the stopper group. This was confirmed by <sup>1</sup>H NMR.

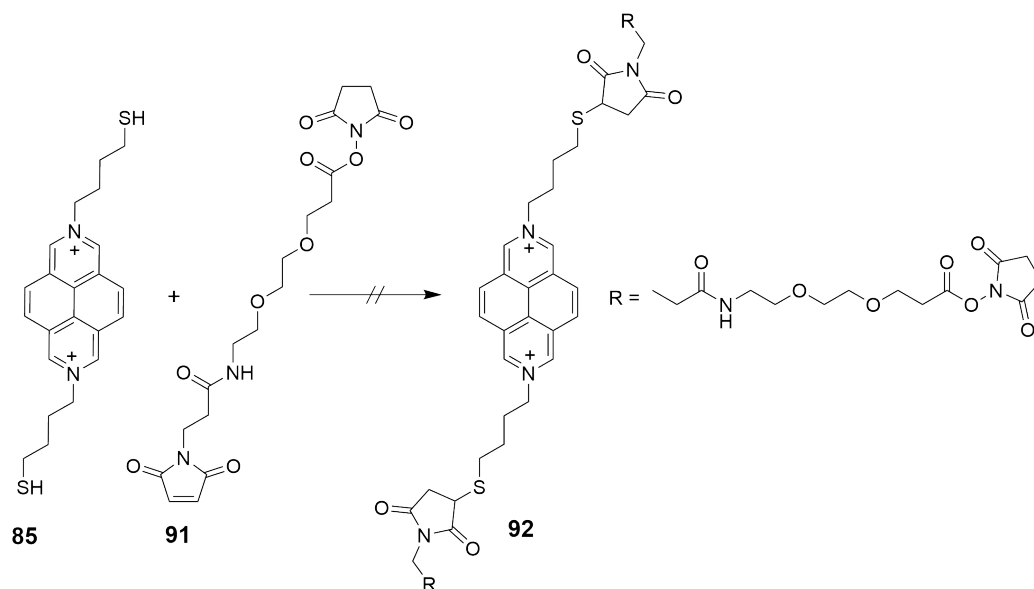


**Figure 50.** Synthesis attempt of **92** in H<sub>2</sub>O/MeOH, Et<sub>3</sub>N, pH 7.0.

Therefore, the linker **91** was first coupled to 3A-amino-3A-deoxy-(2AS,3AS)- $\beta$ -cyclodextrin (**93**) to obtain a thiol-reactive stopper group and avoid the undesired hydrolysis of the NHS ester functionality. Initial attempts were made in aqueous media (sodium phosphate buffer, pH 7 to 9 tested), but the simultaneous hydrolysis of the maleimide moiety accompanied the product

formation. The obtained additional signals around 6 ppm in the proton NMR spectrum indicated the hydrolysis. Maleimides are generally sensitive towards hydrolysis,<sup>304</sup> during which a water-catalyzed ring opening of the maleimide takes place (see **Figure 51**).

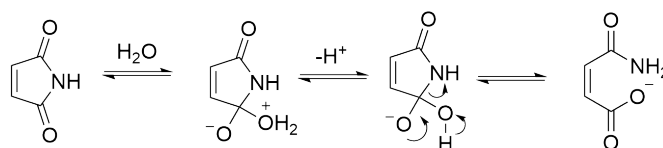


**Figure 51.** Mechanism of water-catalyzed ring opening of maleimides.<sup>304</sup>

Switching from an aqueous sodium phosphate buffer to a dry organic solvent such as DMF reduced the possibility of hydrolysis of the maleimide moiety of **94** during the reaction (see **Figure 52**). Due to its sensitivity to hydrolysis, purification of the crude product obtained by preparative HPLC (0-100 % acetonitrile, 1 % trifluoroacetic acid aq.) had to be performed within 30 min to avoid water-catalyzed ring opening of the maleimide. Overall, the optimized synthesis with DMF as the solvent, the quick purification, and storage under argon at 4 °C improved the yield by almost 20 %. The product was obtained as a colorless powder with a final yield of 85 %.

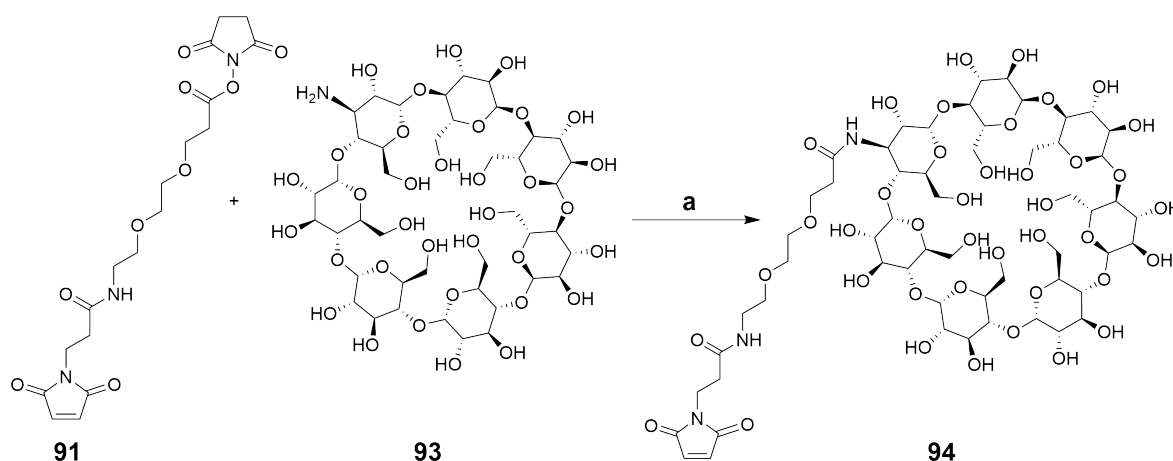


**Figure 52.** Synthesis of the maleimide-PEG- $\beta$ -CD stopper **94**. a) DMF, Et<sub>3</sub>N, r.t., 12 h, 85 %.

The last step marked the rotaxane synthesis, shown in **Figure 53**, where first, the pseudo-rotaxane CB8•**85** was prepared by equilibrating both compounds in a sodium phosphate-buffered solution for 30 min. Subsequently, the stopper (**94**) was added, and the maleimide group was covalently linked to two stopper groups *via* a MICHAEL thiol-ene reaction. The rotaxane was obtained with a yield of 36 % after purification by preparative HPLC (17 % acetonitrile, 1 % trifluoroacetic acid aq.).

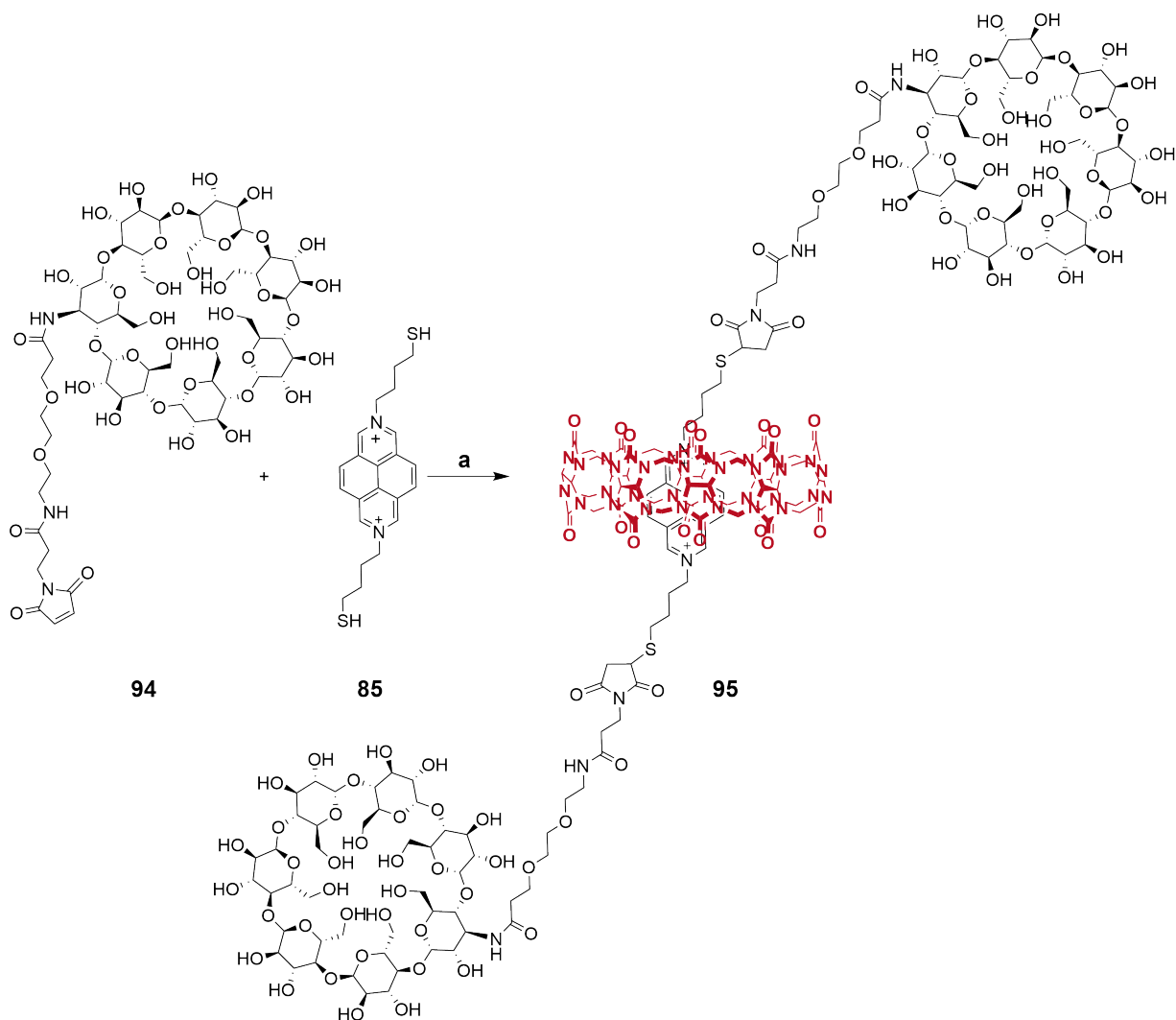


**Figure 53.** Synthesis of CB8-DAP-( $\beta$ -CD)<sub>2</sub>-rotaxane **95**. a) CB8, sodium phosphate buffer, pH 7.7, r.t., 18 h, 36 %.

The success of this final step depended on several factors: for example, the synthesized DAP thiol (**85**) is sensitive to oxidation, causing the undesired oligomerization of the dye monomers. Therefore, the concentration of **85** was determined *via* absorbance spectroscopy using both the extinction coefficient of MDAP (see **Table 11**) and the ELLMAN reagent.<sup>305</sup> This reagent reacts quantitatively with the thiol moiety to give the yellow dye TNB<sup>2-</sup>, the absorbance of which is measured at a wavelength of 412 nm. The concentration of the thiols in the sample can be determined using the extinction coefficient of the dye and is expected to be double the concentration of the DAP since molecule **85** is symmetrically substituted with a thio-butyl linker on each nitrogen atom. The comparison of the determined concentrations for the DAP dye and the thiol of a sample older than three days showed much lower concentrations of the thiol than expected. Consequently, the DAP-thiol had to be freshly prepared prior to rotaxane synthesis to avoid oligomerization and the resulting problems in rotaxane formation, such as the increased formation of rotaxane-like species with only one stopper group and pseudo rotaxanes without covalently attached stopper groups.

Besides that, the formation of the rotaxane is based on the self-assembly of the DAP thiol (dye axle) with the macrocycle CB8, resulting in a pseudo rotaxane CB8•85 (see **Figure 54**). Since the water solubility of CB8 is relatively low ( $\mu\text{M}$  range) compared to the smaller analog CB7,<sup>84,93</sup> sufficient amounts of solvent must be used to dissolve CB8 completely and ensure successful pseudo rotaxane formation. Due to the insolubility of CB8, when a higher concentration was used, not all DAP molecules were complexed by CB8.

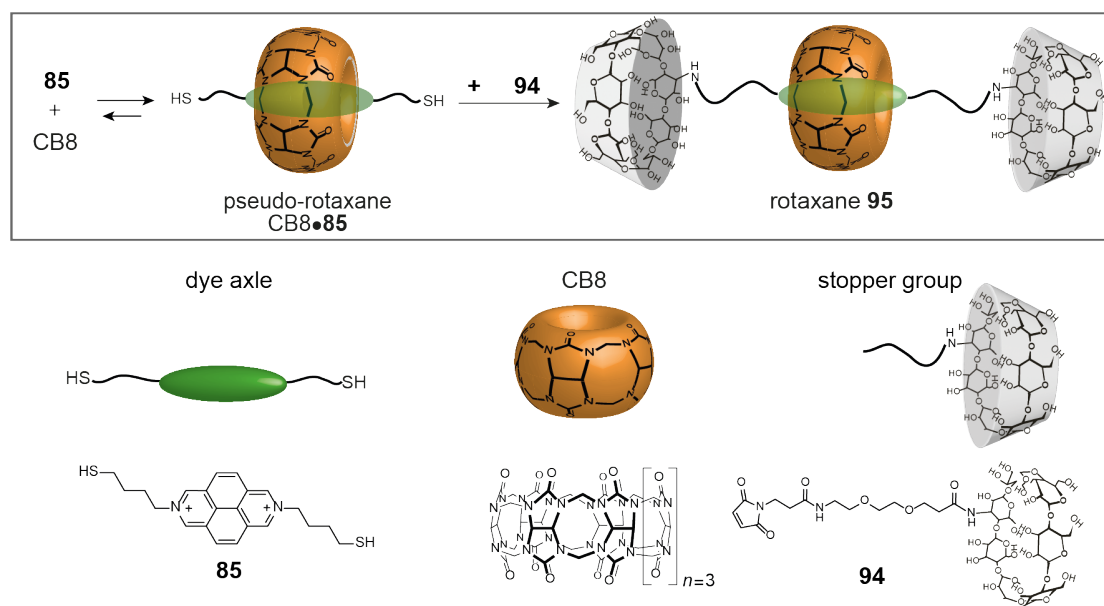


**Figure 54.** Schematic representation of the self-assembly of CB8 and the dye axle forming a pseudo rotaxane and the subsequent formation of the rotaxane (**95**) by covalent attachment of two stopper groups.

The problems described above made a purification process necessary to separate the product from the impurities introduced during the reaction, such as the formation of unsymmetrical pseudo rotaxane. Therefore, the crude product was applied on a preparative HPLC, and several gradients of acetonitrile and water were tested for purification of the rotaxane. Unfortunately, the purification turned out to be highly complex due to similarities in chemical structure and size of the rotaxane and its impurities, *i.e.*, the rotaxane axle without CB8 or an incompletely formed rotaxane leads to similar behavior with respect to their HPLC elution times. However, it was possible to identify a complex purification protocol with the HPLC that allowed the separation of the rotaxane from the main impurities with a yield of 36 %.

### 5.3.2.3. Characterization of rotaxane

The obtained rotaxane **95** was characterized by  $^1\text{H}$  NMR and diffusion-ordered spectroscopy (DOSY), electrospray ionization mass spectrometry (ESI-MS), dynamic light scattering (DLS), and photophysical investigation. Due to the size of the molecule and its complex structure, only molecular regions within the molecule were assigned to the individual signals in the  $^1\text{H}$  NMR

spectrum, shown in **Figure 55a**. DOSY NMR and ESI-MS both indicate that the rotaxane is an intact mechanically interlocked molecule (**Figure 55b** and **c** and Section 8.3).<sup>248</sup>

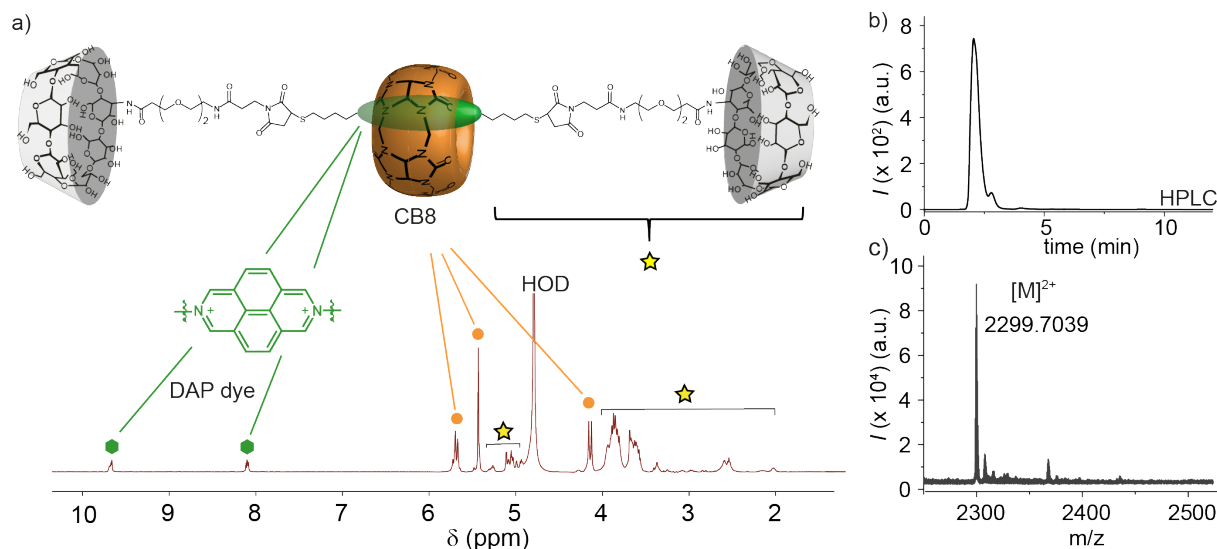


**Figure 55.** Characterization of CB8-DAP-( $\beta$ -CD)<sub>2</sub>-rotaxane **95**: a) <sup>1</sup>H NMR spectrum of rotaxane in D<sub>2</sub>O with signals assigned to the molecular regions. Green hexagons: signals of aromatic DAP dye, orange dots: signals of CB8, and yellow stars: signals of the aliphatic linker and  $\beta$ -CD. b) Analytical HPLC trace of rotaxane **95** (30 % MeCN in H<sub>2</sub>O, 0.1 % trifluoroacetic acid). c) ESI-MS spectra of rotaxane (50 % MeCN in H<sub>2</sub>O, 1 % formic acid). Adapted with permission from ref.<sup>248</sup> Copyright 2023 Springer Nature.

The synthesized rotaxane **95** was further characterized using optical spectroscopy. The absorbance spectrum of **95** shows pyrene-typical absorption bands with  $\pi$ - $\pi^*$  transition character (see the black spectrum in **Figure 56a**). The signals in the region of 310 - 350 nm ( $\lambda_{\text{max}} = 324$  and 337 nm) can be assigned to the allowed S<sub>0</sub> - S<sub>2</sub> transition and the signals in the range of 380 - 430 nm ( $\lambda_{\text{max}} = 398$  and 419 nm) belong to the S<sub>0</sub> - S<sub>1</sub> transition.<sup>306,307</sup> The emission of the synthesized rotaxane ( $\lambda_{\text{ex}} = 393$  nm) is shown as a dark red spectrum in **Figure 56a** with a global maximum at 428 nm, a local maximum at 451 nm, and a shoulder in the range of 470 - 510 nm typical for dicationic 2,7-diazapyrenes.<sup>308</sup> Since fluctuations in the emission intensity of the rotaxane were observed when the rotaxane solution was transferred from a cooled stock solution into a cuvette filled with water at room temperature (r.t.), a deeper investigation on the temperature-dependence of the emission was conducted. The rotaxane **95** was tested on its temperature stability and performance by heating a solution of **95** in a cuvette from 20 °C up to 55 °C and measuring its emission during the heating process. The emission intensity showed a steady decrease with increasing temperature, leading to an emission intensity quenching of 65 %, reaching 55 °C (see **Figure 56b**). This finding indicated a temperature-induced aggregation of the rotaxane, which caused the fluorescence quenching of the sample. The same heating cycle was performed during a DLS (dynamic light scattering) measurement to gain deeper insight into this phenomenon. The increasing average size of the particle with rising temperature indicated the

self-aggregation of the system at higher temperatures (see inset in **Figure 56b**), a known phenomenon for CDs in water.<sup>300</sup> Although both measurements show that the rotaxane is aggregating with higher temperatures, these findings do not affect the sensing with the rotaxane, which is further explained in Section 5.3.3.1.

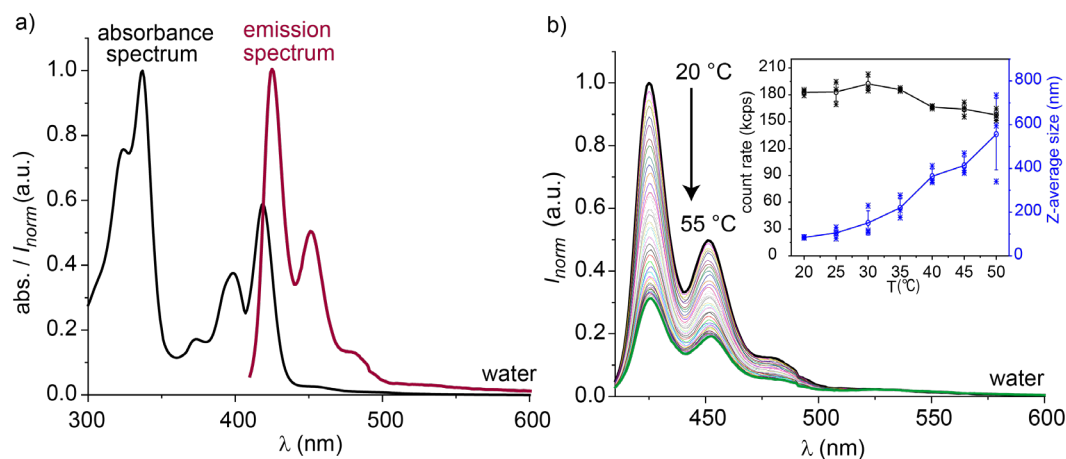


**Figure 56.** a) Absorbance (black) and normalized emission (red,  $\lambda_{\text{ex}} = 393$  nm) spectra of 29  $\mu\text{M}$  rotaxane **95** in water at 25 °C. b) Temperature-dependent normalized emission spectra with decreasing emission from 20 °C to 55 °C. Inset: DLS measurement with temperature-dependent count rates (black) and the Z-average size (blue) of rotaxane from 20 °C to 50 °C. The increase of the Z-average size with rising temperature indicates the formation of large aggregates.<sup>300</sup> Adapted with permission from ref.<sup>248</sup> Copyright 2023 Springer Nature.

### 5.3.3. Emission-based binding studies of the rotaxane-based chemosensor for indole-type analytes

The host-guest binding properties of rotaxane **95** with Trp (**2**) and its analogs, *i.e.*, indole (**96**) and tryptamine (**6**), were investigated by emission-based titration experiments. The analyte binding was expected to result in a detectable spectroscopic change of the chemosensor signal caused by excited state electron transfer processes between the analyte and the dye. Therefore, Trp was titrated to a 29  $\mu\text{M}$  rotaxane solution in water, and the absorbance and emission intensity were detected, see **Figure 57**.<sup>248</sup> The observed strong emission intensity decrease indicated the binding of Trp next to the DAP dye within the CB8 cavity. The complexation of an electron-deficient aromatic dye molecule and an electron-rich aromatic analyte such as Trp inside the host cavity enables parallel, opposite  $\pi$ - $\pi$ -stacking of both molecules, resulting in charge transfer (CT) interactions, which are visible as an arising shoulder in the absorbance spectrum in the range of 420 - 480 nm.<sup>112,155</sup>

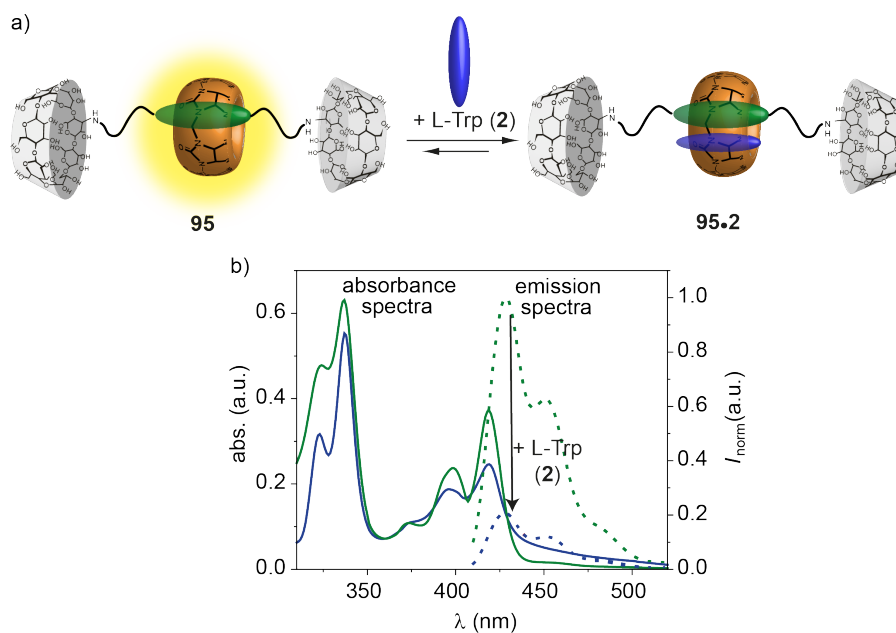


**Figure 57.** a) Schematic representation of host-guest binding interaction of the synthesized rotaxane chemosensor. The binding of an analyte (*i.e.*, Trp) leads to an emission quenching of the rotaxane **95**. b) Absorbance (solid lines) and emission (dashed lines) spectra of 29  $\mu\text{M}$  rotaxane **95** in the absence (green) and the presence (blue) of 450  $\mu\text{M}$  Trp (**2**) in water at 25  $^{\circ}\text{C}$  with  $\lambda_{\text{ex}} = 393$  nm. Adapted with permission from ref.<sup>248</sup> Copyright 2023 Springer Nature.

The stability and analyte-sensing capability of rotaxane **95** as a chemosensor in salt-containing media was further examined by an emission-based assay with indole and 1-adamantanol (AdOH, **26**) as analytes in 1X phosphate-buffered saline (PBS).<sup>248</sup> A mechanistic scheme is shown in **Figure 58**, in which the performance of the rotaxane chemosensor (**a** and **b**) is compared to a self-assembled non-covalent CB8•MDAP chemosensor (**c** and **d**). In both cases, the addition of indole (analyte) to the chemosensor resulted in an emission quenching of the fluorescence intensity caused by the parallel binding of the analyte next to the DAP dye inside the CB8 cavity. The emission response of rotaxane **95** to indole in 1X PBS was similarly strong to the obtained response in water. In contrast, the self-assembled bimolecular chemosensor CB8•MDAP already showed reduced sensitivity in 1X PBS towards indole, indicating that due to competing salt cations, its functionality in 1X PBS is severely reduced. Competitive binding experiments further examined the superior stability of rotaxane **95** over CB8•MDAP in solution. AdOH was selected as a suitable competitive binder for the CB8•indole interaction. Literature data<sup>158</sup> showed that it acts as a stronger binding analyte for CB8•dye complexes compared to indole and should, therefore, displace the DAP dye from the CB8 cavity since its bulkier size restricts the parallel binding next to the dye. The observed emission increase for the bimolecular chemosensor CB8•MDAP confirmed that AdOH displaced the former bound analyte indole as well as the MDAP dye itself.<sup>248</sup> In contrast, the rotaxane **95** showed only little fluorescence change upon the addition of AdOH, as it cannot displace the dye from the rotaxane host cavity regardless of its stronger binding affinity to CB8 due to its interlocked system with the installed stoppers as anchor

groups. The obtained results indicated the superior stability of the synthesized rotaxane chemosensor over competitive binders compared to self-assembled bimolecular chemosensors.<sup>248</sup>

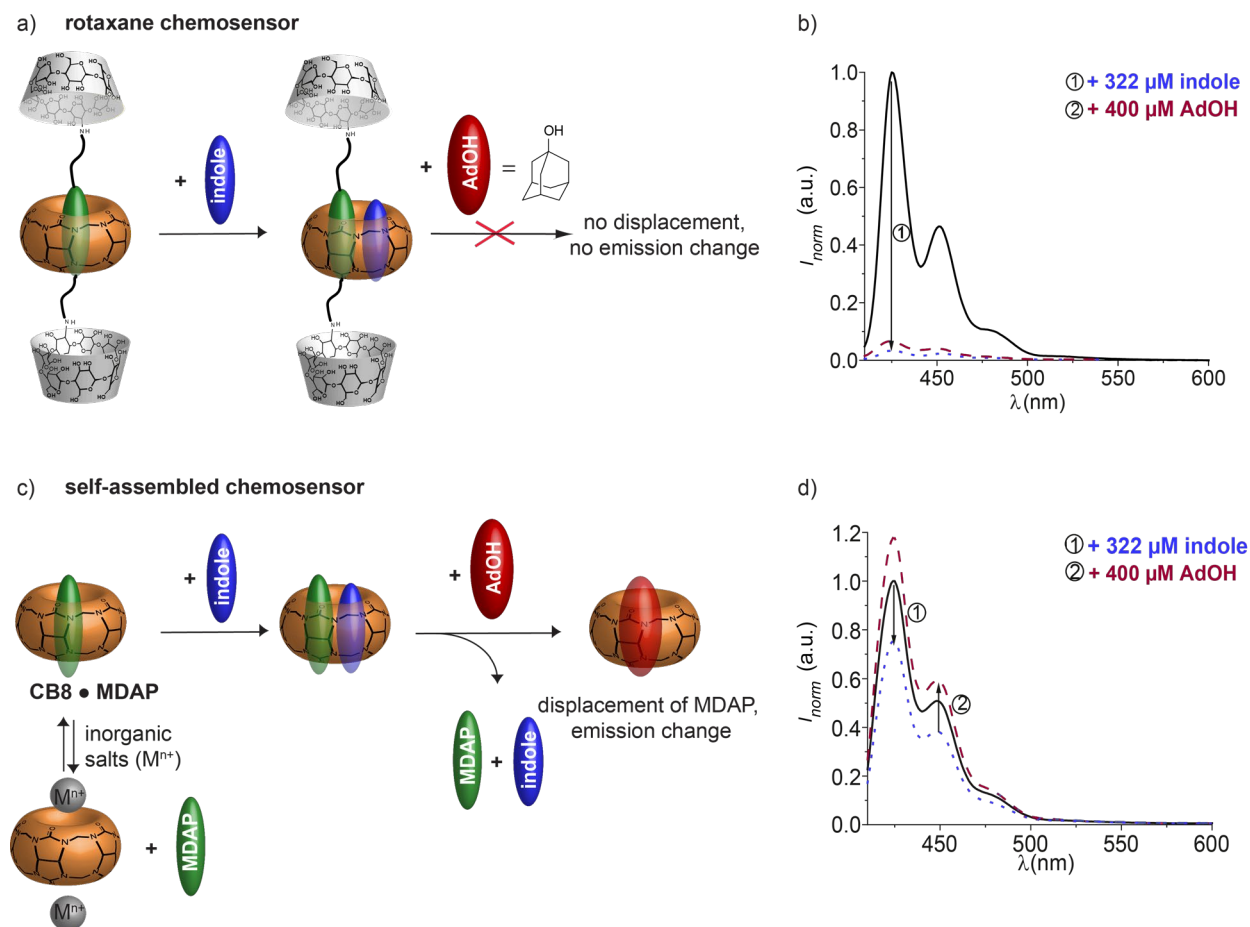


**Figure 58.** a) Schematic representation of the analyte binding of the synthesized rotaxane for the electron-rich aromatic analyte indole and for the bulky (too big for a 1:1 binding next to the dye) analyte 1-adamantanol (AdOH). b) Emission quenching is observed after the addition of indole due to the dye-analyte interaction, whereas 1-adamantanol does not cause any significant signal change. c) Schematic representation of analyte binding to a self-assembled CB8•MDAP chemosensor. Bulky and strongly binding analytes such as 1-adamantanol displace the bound dye and thereby disassemble the chemosensor. d) Emission response of the CB8•MDAP chemosensor to the presence of indole and AdOH. The observed signal change after AdOH addition compared to the starting signal indicates the disassembly. All emission spectra were recorded in 1X PBS (black) at 25 °C ( $\lambda_{ex} = 393$  nm). Adapted with permission from ref.<sup>248</sup> Copyright 2023 Springer Nature.

### 5.3.3.1. Emission-based binding affinities and selectivity of rotaxane chemosensor for biorelevant analytes

Emission-based titration experiments gave more profound insights into the analyte binding of the rotaxane chemosensor with Trp (**2**) and its analogs, *i.e.*, indole (**96**) and tryptamine (**6**) in water. Although indole does not occur naturally in blood serum or human urine, its heteroaromatic core is present in the biorelevant Trp and tryptamine, making its binding affinity determination relevant to the core study (see **Table 7** for concentrations in human urine/serum). In a typical emission-based titration experiment, between 40 and 600 equivalents of an analyte stock solution were titrated into a chemosensor solution, depending on the binding strength of the analyte. The titration

experiment of each analyte was performed in at least triplicates, and the binding isotherms were found to be highly reproducible within the repetitions. The binding isotherms were obtained by plotting the emission intensity of each titration step at a selected wavelength against the analyte concentration. The binding isotherm was fitted by a least-square fit based on a 1:1 binding model using **Eq. 33**. It was assumed that only the rotaxane and the formed host•guest complex of the rotaxane and the guest (analyte) are emissive, giving **Eq. 33** from **Eq. 29-32**.



$$K_a^{\text{rotaxane}\cdot\text{G}} = \frac{[\text{rotaxane} \cdot \text{G}]}{[\text{rotaxane}][\text{G}]} \quad \text{Eq. 30}$$

$$[\text{rotaxane}]_0 = [\text{rotaxane} \cdot \text{G}] + [\text{rotaxane}] \quad \text{Eq. 31}$$

$$[\text{G}]_0 = [\text{rotaxane} \cdot \text{G}] + [\text{G}] \quad \text{Eq. 32}$$

$$I_c = I^0 + I^{\text{rotaxane}\cdot\text{G}} \cdot [\text{rotaxane} \cdot \text{G}] + I^{\text{rotaxane}} \cdot [\text{rotaxane}] \quad \text{Eq. 33}$$

Parameters for **Eq. 29** to **Eq. 33**: [rotaxane]: rotaxane concentration at equilibrium, [rotaxane]<sub>0</sub>: initial rotaxane concentration, [G]: guest/analyte concentration at equilibrium, [G]<sub>0</sub>: initial guest/analyte concentration, [rotaxane•G]: rotaxane•guest concentration at equilibrium,  $K_a^{\text{rotaxane}\cdot\text{G}}$ : binding constant of rotaxane•guest complex,  $I^0$ : background signal,  $I^{\text{rotaxane}\cdot\text{G}}$ : signal of rotaxane•guest (rotaxane•G) complex,  $I^{\text{rotaxane}}$ : signal of free rotaxane,  $I_c$ : observable signal as a function of concentration.

The binding affinity of the three indole-type analytes was determined in water, 1X PBS, and diluted human urine. 1X PBS containing 137 mM NaCl, 2.7 mM KCl, 10 mM Na<sub>2</sub>HPO<sub>4</sub>, and 1.8 mM KH<sub>2</sub>PO<sub>4</sub> was selected as a model buffer for the salt concentrations in biofluids such as urine or blood serum.<sup>168,169,309</sup> Indole, Trp, and tryptamine all caused strong emission quenching of the rotaxane **95** of at least 50 %, with nearly complete fluorescence quenching (~ 90 %) observed for indole in water and 1X PBS (see **Figure 59**). Fortunately, the binding affinities towards the rotaxane **95** were almost identical in water and 1X PBS for all three analytes, indicating that their binding affinity towards the chemosensor is not affected by salt presence.<sup>248</sup> These promising results show that the mechanical interlocking of the dye moiety in CB8 results in a superior salt tolerance for the chemosensor compared to non-covalent chemosensor designs. A detailed comparison for selected non-covalent chemosensors is further discussed in Section 5.3.4.3. Indole has a larger binding affinity ( $\log K_a \sim 5.4$ ) in water and 1X PBS than Trp and tryptamine. This observation is in good agreement with literature reports for non-covalent CB8•dye complexes and results from the release of high-energy cavity water molecules upon analyte binding in CB8.<sup>103</sup> Indole displaces all remaining cavity water molecules due to its compact size. In contrast, Trp and tryptamine are not fully encapsulated in the CB8 cavity with their bulkier size due to their side chain.<sup>233</sup> In addition, the carboxylate moiety of Trp is located

outside the cavity due to repulsions with the carbonyl (C=O) rims of CB8.<sup>310</sup> Trp as the analyte of interest of this study showed binding affinities in the  $\mu\text{M}$  concentration range ( $\log K_a \sim 4$ ), which is already in the required  $\mu\text{M}$  concentration range for Trp sensing in urine/serum (urine:  $\sim 21 - 93 \mu\text{M}$ , serum:  $\sim 41 - 77 \mu\text{M}$ ).<sup>248</sup> However, a slightly higher  $\log K_a$  would be preferred when trying to reach full sensing capability in the presence of high salt concentrations in biofluids. The binding affinities determined for indole and Trp in diluted urine were slightly lower compared to pure 1X PBS. Urine itself is a complex matrix, containing various bioactive compounds and salts, which act as interferents.<sup>169</sup> The determined binding affinities are shown as  $\log K_a$  values in **Table 6**, and the corresponding emission-based binding isotherms are shown in **Figure 59 - Figure 61**.<sup>248</sup>

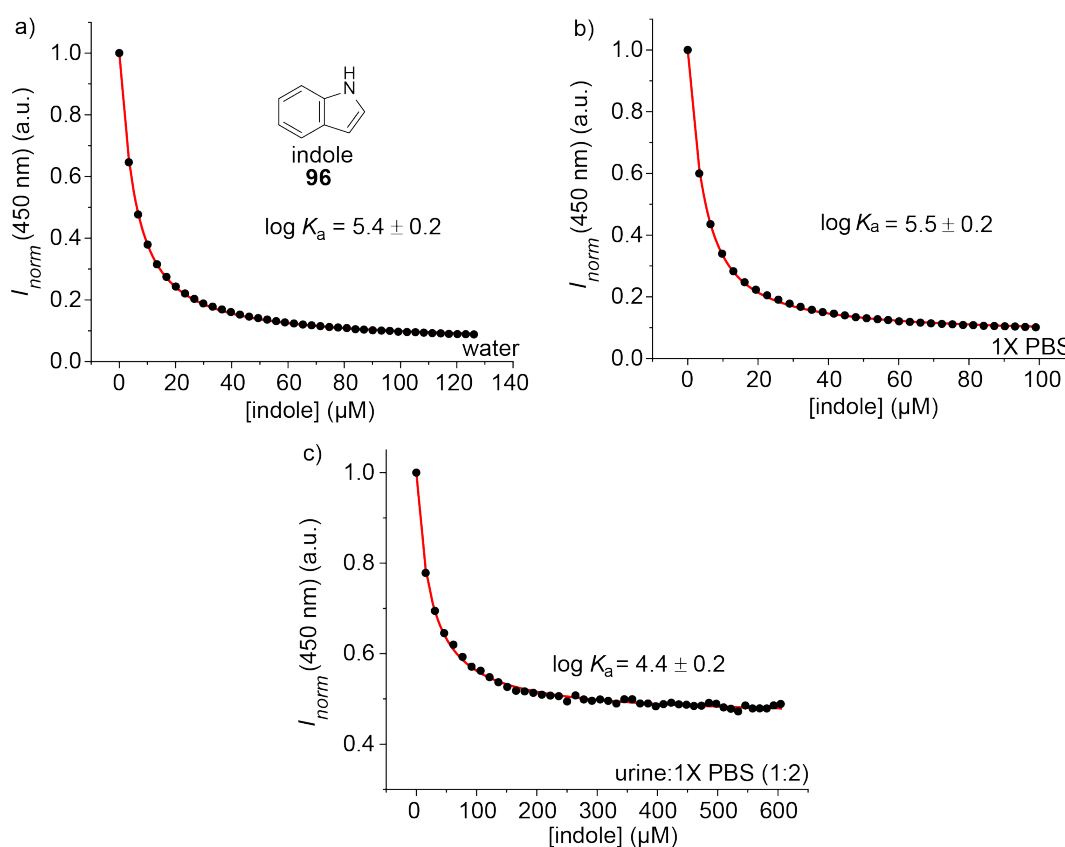


**Figure 59.** Representative binding isotherms determined by emission-based titration measurements of a) rotaxane **95** ( $2.5 \mu\text{M}$ ) with indole **96** ( $0 - 126 \mu\text{M}$ ) in water, b) rotaxane **95** ( $2.5 \mu\text{M}$ ) with indole **96** ( $0 - 100 \mu\text{M}$ ) in 1X PBS, and c) rotaxane **95** ( $1.0 \mu\text{M}$ ) with indole **96** ( $0 - 662 \mu\text{M}$ ) in diluted human urine (1:2 in 1X PBS). Measurements were conducted at  $25^\circ\text{C}$  with  $\lambda_{ex} = 393 \text{ nm}$ ,  $\lambda_{em} = 450 \text{ nm}$ . Acquired data is represented as black dots and fits are shown as red lines. The  $\log K_a$  for the formed rotaxane-guest complex formation is given as an inset in each graph.<sup>248</sup>

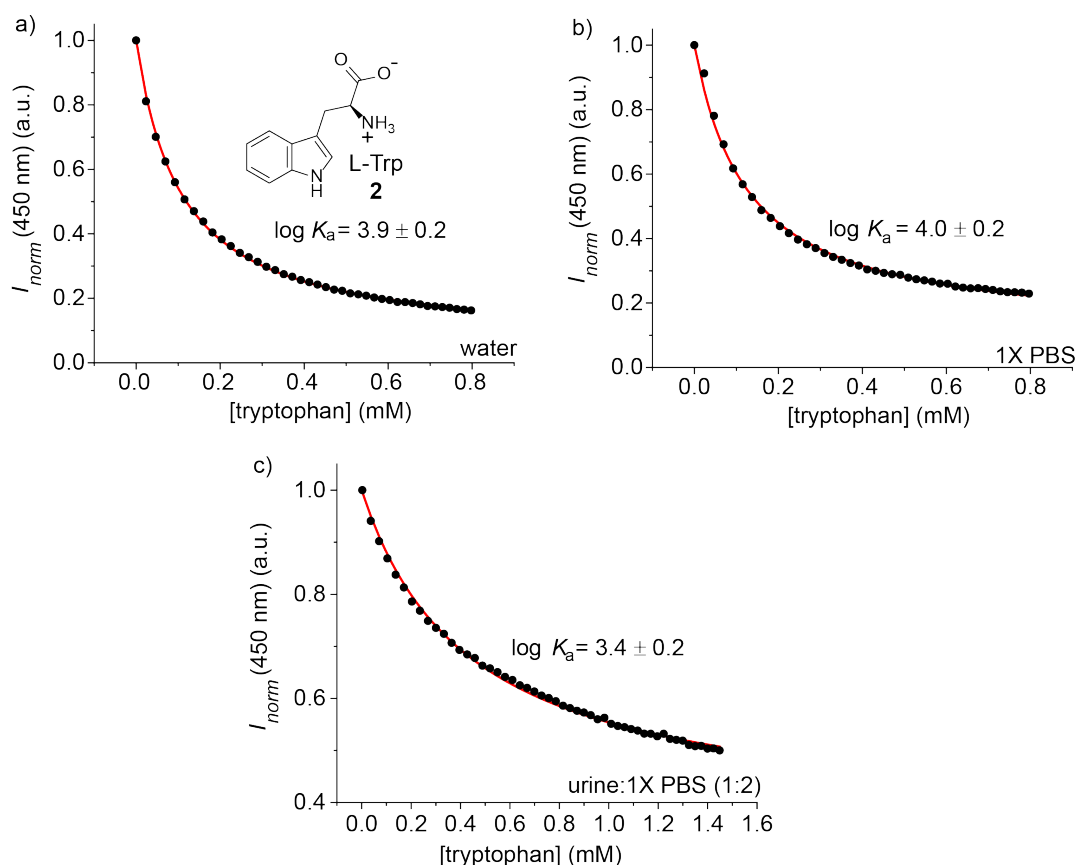


**Figure 60.** Representative binding isotherms determined by emission-based titration measurements of a) rotaxane **95** (2.5  $\mu$ M) with tryptophan **2** (0 - 797  $\mu$ M) in water, b) rotaxane **95** (2.5  $\mu$ M) with tryptophan **2** (0 - 797  $\mu$ M) in 1X PBS, and c) rotaxane **95** (1.0  $\mu$ M) with tryptophan **2** (0 - 1.44 mM) in diluted human urine (1:2 in 1X PBS). Measurements were conducted at 25  $^{\circ}$ C with  $\lambda_{ex} = 393$  nm,  $\lambda_{em} = 450$  nm. Acquired data is represented as black dots and fits are shown as as red lines. The  $\log K_a$  for the formed rotaxane•guest complex formation is given as an inset in each graph.<sup>248</sup>

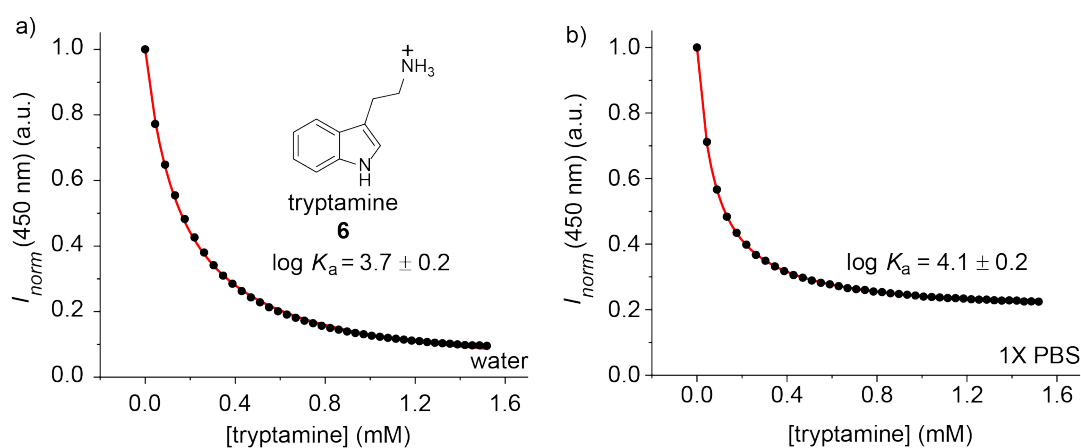


**Figure 61.** Representative binding isotherms determined by emission-based titration measurements of a) rotaxane **95** (2.5  $\mu$ M) with tryptamine **6** (0 - 1.5 mM) in water and b) rotaxane **95** (2.5  $\mu$ M) with tryptamine **6** (0 - 1.5 mM) in 1X PBS. Measurements were conducted at 25  $^{\circ}$ C with  $\lambda_{ex} = 393$  nm,  $\lambda_{em} = 450$  nm. Acquired data is represented as black dots and fits are shown as as red lines. The  $\log K_a$  for the formed rotaxane•guest complex formation is given as an inset in each graph.<sup>248</sup>

Since the in-depth characterization of the rotaxane chemosensor (see Section 5.3.2.3) revealed temperature-induced aggregation, it was necessary to examine the influence of this phenomenon on the chemosensors' sensing capability. Therefore, emission-based titration experiments were performed for the detection of Trp by the rotaxane chemosensor in 1X PBS at 25 °C, 35 °C, and 40 °C. The obtained binding isotherms all showed a similar shape and slope, and the fitted binding constants did not differ significantly within the measured temperature range (see **Table 6**). This proved that the sensing ability of rotaxane is not influenced by its temperature-induced aggregation.

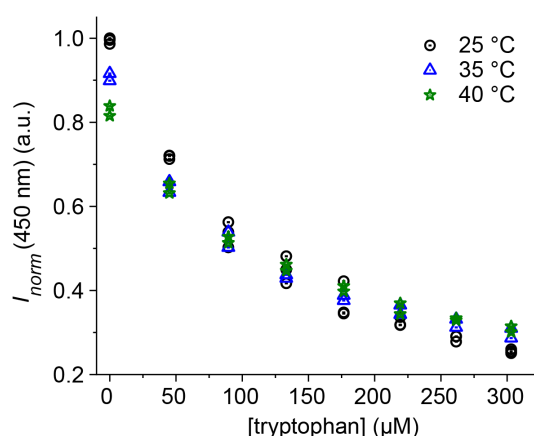


**Figure 62.** Binding curves determined by emission-based titration measurements of the rotaxane **95** (2.0  $\mu\text{M}$ ) with Trp **2** (0 - 303  $\mu\text{M}$ ) in 1X PBS at 25 °C (black dots), 35 °C (blue triangles), and 40 °C (green stars). Measurements were conducted in at least duplicates with  $\lambda_{\text{ex}} = 393 \text{ nm}$ ,  $\lambda_{\text{em}} = 450 \text{ nm}$ . Adapted with permission from ref.<sup>248</sup> Copyright 2023 Springer Nature.

**Table 6.** Overview of binding affinities given as  $\log K_a$  for indoyl-based analytes of the synthesized rotaxane chemosensor **95** in aqueous media at 25 °C. The estimated error of  $\log K_a$  is 0.2 based on at least triplicate measurements for each analyte (n.d. = not determined).

analyte	$\log K_a$ in water	$\log K_a$ in 1X PBS	$\log K_a$ in urine <sup>[e]</sup>
indole ( <b>96</b> )	$5.4 \pm 0.2$	$5.5 \pm 0.2$	$4.4 \pm 0.2$
L-Trp ( <b>2</b> )	$3.9 \pm 0.2$	$4.0 \pm 0.2$ $4.0 \pm 0.2$ <sup>[a]</sup> $4.1 \pm 0.2$ <sup>[b]</sup> $4.0 \pm 0.2$ <sup>[c]</sup> $3.9 \pm 0.2$ <sup>[d]</sup>	$3.4 \pm 0.2$
tryptamine ( <b>6</b> )	$3.7 \pm 0.2$	$4.1 \pm 0.2$	n.d.

<sup>[a]</sup> In the presence of 250  $\mu\text{M}$  cadaverine. <sup>[b]</sup> In the presence of 250  $\mu\text{M}$  L-arginine. <sup>[c]</sup> Measured at 35 °C.

<sup>[d]</sup> Measured at 40 °C. <sup>[e]</sup> Diluted in 1:2 with 1X PBS.

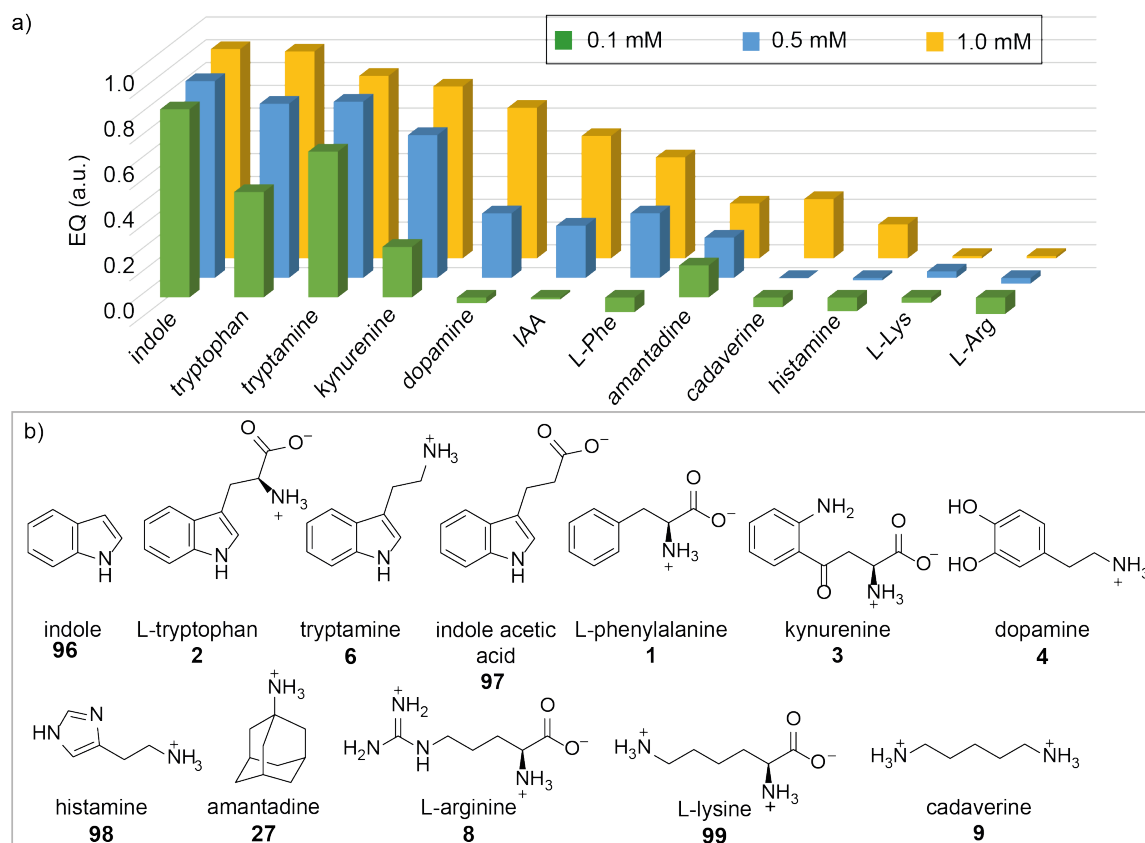


**Figure 63.** a) Overview of the obtained emission quenching values of rotaxane **95** (1.0  $\mu\text{M}$ ) upon the addition of 0.1 mM (green), 0.5 mM (blue), and 1.0 mM (yellow) of the bioactive analytes in 1X PBS. Measurements were conducted at 25  $^{\circ}\text{C}$  with  $\lambda_{\text{ex}} = 393 \text{ nm}$ ,  $\lambda_{\text{em}} = 450 \text{ nm}$ . b) Chemical structure of the examined bioactive analytes. Adapted with permission from ref.<sup>248</sup> Copyright 2023 Springer Nature.

The binding selectivity of the synthesized rotaxane chemosensor **95** was evaluated for various biorelevant analytes in a microwell plate format. For this purpose, 1  $\mu\text{M}$  of the rotaxane **95** in 1X PBS was mixed with 0.1, 0.5, and 1.0 mM of 12 different analytes, such as (aliphatic) amino acids and derivatives as well as polyamines. The emission intensity of the chemosensor was measured before and after the analyte addition. The examined analytes shown in **Figure 63** include zwitterionic, cationic, and anionic analytes. These analytes were selected as they are naturally found in human biofluids and thus could act as potential interferents to the sensing of Trp. In addition to naturally occurring bioanalytes, amantadine was chosen, a commonly administered drug for treating Parkinson's disease.<sup>311</sup> Amantadine, like many other commonly administered drugs (*e.g.*, steroids<sup>200</sup>), has shown a strong binding affinity for CB8 ( $\log K_{\text{a}} = 8.9$ )<sup>312</sup> and, therefore, was chosen as a model drug analyte, which could cause negative interferences with the Trp sensing. The recorded emission intensity of the rotaxane before ( $I_1$ ) and after the analyte addition ( $I_2$ ) was converted into the emission quenching efficiency of each analyte for the rotaxane by using **Eq. 34**.

$$\text{emission quenching (EQ)} = \frac{I_1 - I_2}{I_1} = 1 - \frac{I_2}{I_1} \quad \text{Eq. 34}$$

Aside from Trp the indoyl-type analytes, indole, and tryptamine caused significant emission quenching with increasing concentration of the rotaxane chemosensor in 1X PBS. It may seem unfortunate that they all show similarly strong emission behavior when it comes to using the rotaxane as a Trp sensor in biofluids. However, their concentrations in blood serum and urine are significantly lower ( $< 3 \mu\text{M}$ , see **Table 7**) compared to Trp ( $41 - 77 \mu\text{M}$  in blood serum and  $21 - 93 \mu\text{M}$  in urine, see **Table 7**). Therefore, their interferential effect can be neglected as they are not considered as relevant competitors for Trp sensing in biofluids. Due to its negative charge, the rotaxane **95** showed no response to  $100 \mu\text{M}$  indole-3-acetic acid (IAA, **97**). Emission quenching was only observed in the non-physiological concentration range ( $> 500 \mu\text{M}$ , see **Table 7**). Similar behavior was also observed for the hydrophobic aromatic analytes dopamine (**4**) and phenylalanine (Phe, **1**). Finally, the chemosensor was unresponsive to the amines cadaverine (**9**) and histamine (**98**) as well as to the aliphatic amino acids L-arginine (L-Arg, **8**) and L-Lysine (L-Lys, **99**). An additional displacement assay was conducted with L-Arg and cadaverine to confirm further that they are only weak binders for the rotaxane and, therefore, do not interfere with Trp sensing. A guest displacement assay (GDA)<sup>144</sup> in a microwell plate format was performed by premixing  $250 \mu\text{M}$  of the non-binding analyte (*i.e.*, cadaverine and L-Arg) in 1X PBS with  $2 \mu\text{M}$  of rotaxane. Then, the emission intensity at  $\lambda_{\text{em}} = 450 \text{ nm}$  ( $\lambda_{\text{ex}} = 393 \text{ nm}$ ) was measured before and after the addition of  $0 - 581 \mu\text{M}$  tryptophan. The determined binding affinities using a 1:1 binding model did not differ significantly from those determined by a direct binding assay (DBA) of Trp to rotaxane (see **Table 6**). This shows that neither of the tested analytes negatively affected the sensing abilities of the rotaxane **95** for Trp. **Figure 64** compares the obtained binding isotherms of the rotaxane with Trp in the absence and the presence of L-Arg and cadaverine.<sup>248</sup>

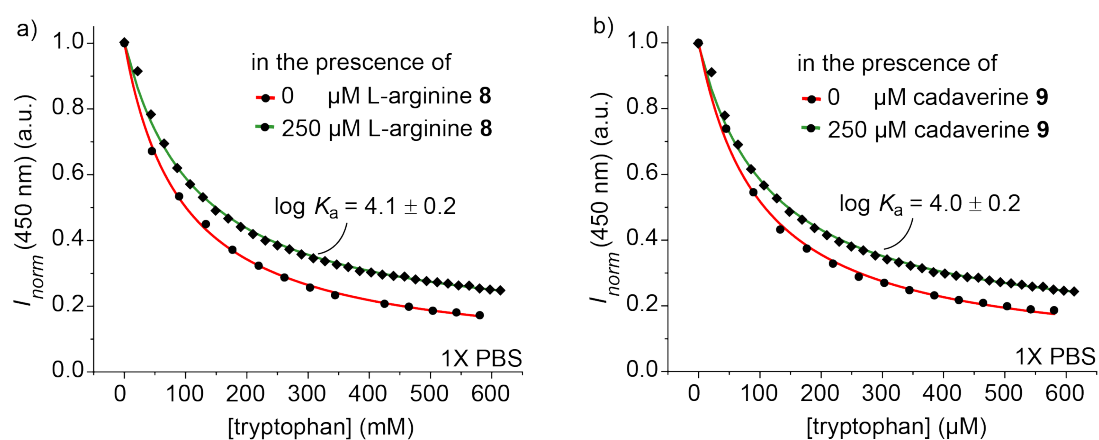


**Figure 64** Representative binding isotherms determined by emission-based titration measurements of rotaxane **95** ( $2.0 \mu\text{M}$ ) with tryptophan ( $0 - 581 \mu\text{M}$ ) in the presence of a)  $250 \mu\text{M}$  L-arginine and b)  $250 \mu\text{M}$  cadaverine in 1X PBS. Measurements were conducted at  $25 \text{ }^\circ\text{C}$  with  $\lambda_{\text{ex}} = 393 \text{ nm}$ ,  $\lambda_{\text{em}} = 450 \text{ nm}$ . Acquired data is represented as black dots, and the fits as red lines. The  $\log K_a$  values for the formed rotaxane•guest complex formation are given in **Table 6**.

**Table 7.** Reported concentration ranges of various tested analytes for healthy adults in blood serum, blood plasma, and urine.<sup>248</sup> (Reported typical creatinine levels in human urine are 97 - 230  $\mu\text{mol kg}^{-1} \text{d}^{-1}$ .<sup>7</sup>)

analyte	conc. ( $\mu\text{M}/\text{mM}$ creatinine) in urine	ref.	conc. ( $\mu\text{M}$ ) in serum	ref.
indole (96)	[a]		[a]	
tryptophan (2)	21.0 - 93.0	168	41 - 77	13,257
kynurenine (3)	0.08 - 1.31	169	0.70 - 3.00	313
tryptamine (6)	0.01 - 0.05	314	0.23	315
indole acetic acid (97)	0.60 - 5.40	169	11.4 - 45.7	316
dopamine (4)	0.20 - 0.70	169	0.0008 - 0.009 <sup>[b]</sup>	317
L-Phe (1)	3.50 - 11.2	169	57.6 - 98.5	168
amantadine (27)	[c]		[c]	
cadaverine (9)	0.051 - 0.065	318	0.25 - 0.39	318
histamine (98)	0.01 - 0.10	169	0.0005 - 0.0018 <sup>[a]</sup>	319
L-lysine (99)	3.6 - 56.1	169	120.4 - 236.8	168
L-arginine (8)	3.2 - 14.6	169	99.0 - 128.2	168

<sup>[a]</sup> Only found in human faeces. <sup>[b]</sup> In human blood plasma. <sup>[c]</sup> Amantadine is a drug used to treat Parkinson's disease and, therefore, does not naturally occur in blood serum or urine.

### 5.3.4. Tryptophan sensing in biofluids

Biofluids contain valuable information about a patient's health status through the accumulation of various metabolites and are, therefore, crucial for the early detection and diagnosis of diseases. However, optical-based chemosensors face a challenge due to the complex biofluid matrix. The salts and other interferents in the matrix reduce the binding constants of the chemosensor, making it difficult to detect the biomarkers at physiologically relevant levels. While chemosensors for the selective detection of specific biomarkers, such as Trp, exist, the complex biofluid matrix

significantly reduces their effectiveness. For example, although some sensor systems already provide sufficient selectivity for an optical Trp detection in complex media, these systems often lack the required sensitivity for Trp as they show small binding affinities ( $\log K_a < 3$ )<sup>320,321</sup> even in low-salinity buffers (red bar graphs in **Figure 65**).<sup>248</sup>

In contrast, others are limited to organic media or aqueous-organic mixtures (violet and dark violet bar graphs in **Figure 65**).<sup>322-326</sup> To date, very few of the developed sensors have overcome the initial hurdle of sufficient selectivity and sensitivity in highly saline buffers and have been studied in simulated or deproteinized and diluted biofluids as media (see chemosensor **100** and **107**).<sup>320,327</sup> The developed rotaxane **95** chemosensor showed no significant attenuation in the binding affinity when transferred from water to 1X PBS, indicating its superior salt-stability. Therefore, I was eager to investigate the performance of rotaxane **95** in complex blood serum and urine biofluids.

**Table 8.** Comparison of representative optical-based chemosensors for tryptophan detection.<sup>248</sup>

sensor	reported medium	$\log K_a$	concentration range	ref.
<b>100</b> <sup>[a]</sup>	saline buffer, simulated serum	2.8	$\mu\text{M}$ range (0 - 200 $\mu\text{M}$ )	320
<b>101</b>	aqueous buffer, pH 7.3	$\sim 2.5$	mM range (0 - 4.0 mM)	321
<b>CB8•40</b>	H <sub>2</sub> O, low saline buffers	2.2	$\mu\text{M}$ range	153
<b>CB8•42</b>	H <sub>2</sub> O, low saline buffers	3.0	$\mu\text{M}$ range	153
<b>102</b>	low saline buffer, ACN	4.2	$\mu\text{M}$ range (50 $\mu\text{M}$ )	324
<b>103</b>	H <sub>2</sub> O:DMSO (7:3)	4.0	$\mu\text{M}$ range (0 - 160 $\mu\text{M}$ )	322
<b>104</b>	EtOH:H <sub>2</sub> O (98:2)	5.7	$\mu\text{M}$ range (0 - 130 $\mu\text{M}$ )	323
<b>105</b>	ACN:MeOH (9:1)	$\sim 3.7$	mM range (0 - 4.5 mM)	325
<b>106</b> <sup>[b]</sup>	chloroform	$\sim 4.0$	$\mu\text{M}$ range ( $\sim 30 \mu\text{M}$ )	328
<b>107</b>	ACN, deproteinized blood serum (serum diluted 2:1 with acid)	9.0	nM - low $\mu\text{M}$ range	327
<b>rotaxane 95 from this work</b>	saline buffers, biofluids	4.0	low $\mu\text{M}$ range	this work

<sup>[a]</sup> Solution of various amino acids. <sup>[b]</sup> TrpOMe binding was investigated.

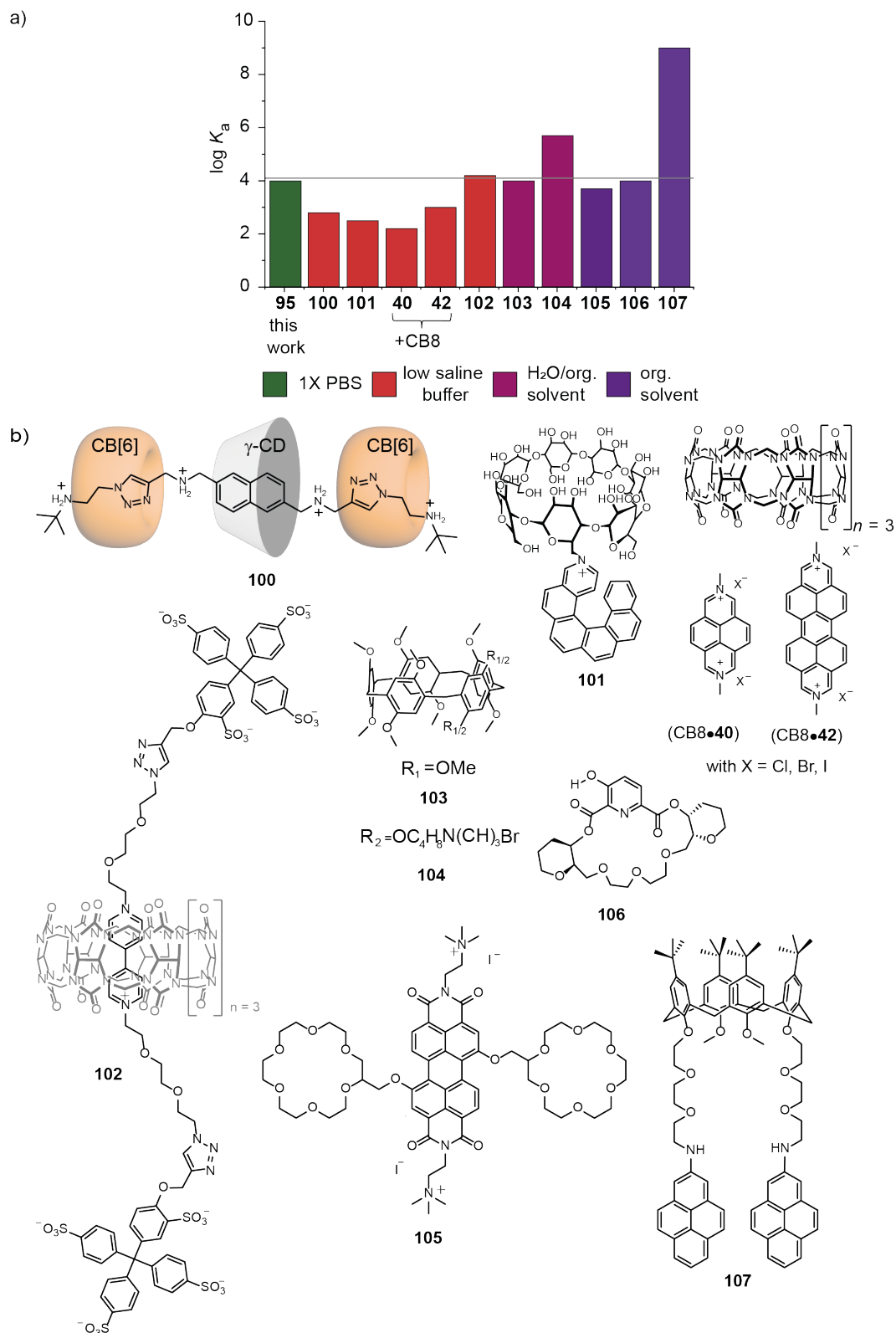


**Figure 65.** a) Binding affinities of the selected chemosensors from b) and the within this work developed and synthesized rotaxane **95**. b) Chemical structures of representative optical-based chemosensors for the detection of Trp.

### 5.3.4.1. Tryptophan sensing in blood serum

The Trp sensing of the rotaxane chemosensor **95** was first investigated in a deproteinized blood serum sample. According to known literature procedures,<sup>257</sup> commercially acquired pooled human and bovine blood serum samples were deproteinized by acid precipitation of serum proteins.<sup>1</sup> The Trp concentration of each serum sample was determined using an HPLC protocol<sup>257</sup> running a calibration with known Trp concentrations from 0 - 100  $\mu\text{M}$  prior to serum sample measurement to compare the performance of the chemosensor to the established HPLC method (see **Figure 66**).<sup>248</sup>

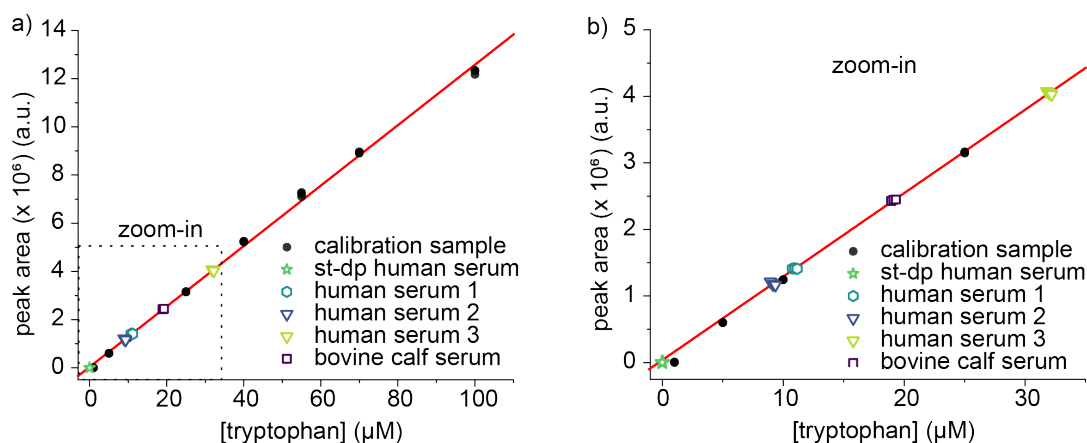


**Figure 66.** a) Plots of the determined Trp concentrations of pooled deproteinized blood serum samples (1:1 diluted with 624 mM perchloric acid) obtained in an HPLC assay with a pre-established calibration curve (data points as black dots and linear fit as red line), measured in triplicates per serum sample and Trp concentration (with  $\lambda_{\text{ex}} = 285 \text{ nm}$ ,  $\lambda_{\text{em}} = 353 \text{ nm}$ ). b) Zoom-in of a). With (st-dp) HS = (steroid-depleted) human serum. Note: Obtained Trp concentrations represent only half of the actual Trp concentration due to dilution. Adapted with permission from ref.<sup>248</sup> Copyright 2023 Springer Nature.

An emission-based calibration curve for Trp was created from the readout of a microplate reader format for the Trp concentration determination with the rotaxane chemosensor. Thus, 0 - 100  $\mu\text{M}$  of Trp were titrated to a known deproteinized human serum matrix from SEQENS (Trp < 1  $\mu\text{M}$ ) with 10  $\mu\text{M}$  rotaxane **95**, and the remaining emission intensity ( $I$ ) of the rotaxane chemosensor was measured. For each Trp concentration, eight independent replicates were measured. Afterward, four different deproteinized (pooled) blood serum samples (human and bovine blood sera) were pipetted into microwell plates. The emission intensity ( $I_1$ ) was recorded upon adding rotaxane **95** in five replicates per serum sample. Emission intensities corrected for autofluorescence emission of each serum ( $I_0$ ) were compared with the established calibration

<sup>1</sup> Please note that there are variations in observed concentration ranges between reported studies. This is likely due to sample preparations, quantification methods and/or other factors such as nutrition, diet, age, weight, sex, and geographical location.

curve and related to the Trp concentrations determined by HPLC (see **Figure 67**).<sup>248</sup> The emission-based measurements using the rotaxane chemosensor gave Trp concentration values and ranges for each unknown blood serum sample that were in good agreement with the HPLC-determined values and are shown in **Table 9**. The deviation between the two measurement methods was less than 15 %, indicating that the rotaxane chemosensor can reliably measure the Trp concentration in the samples. These promising results encouraged me to take the next step by eliminating the time-consuming deproteinization and instead performing the measurement directly in untreated blood serum samples.

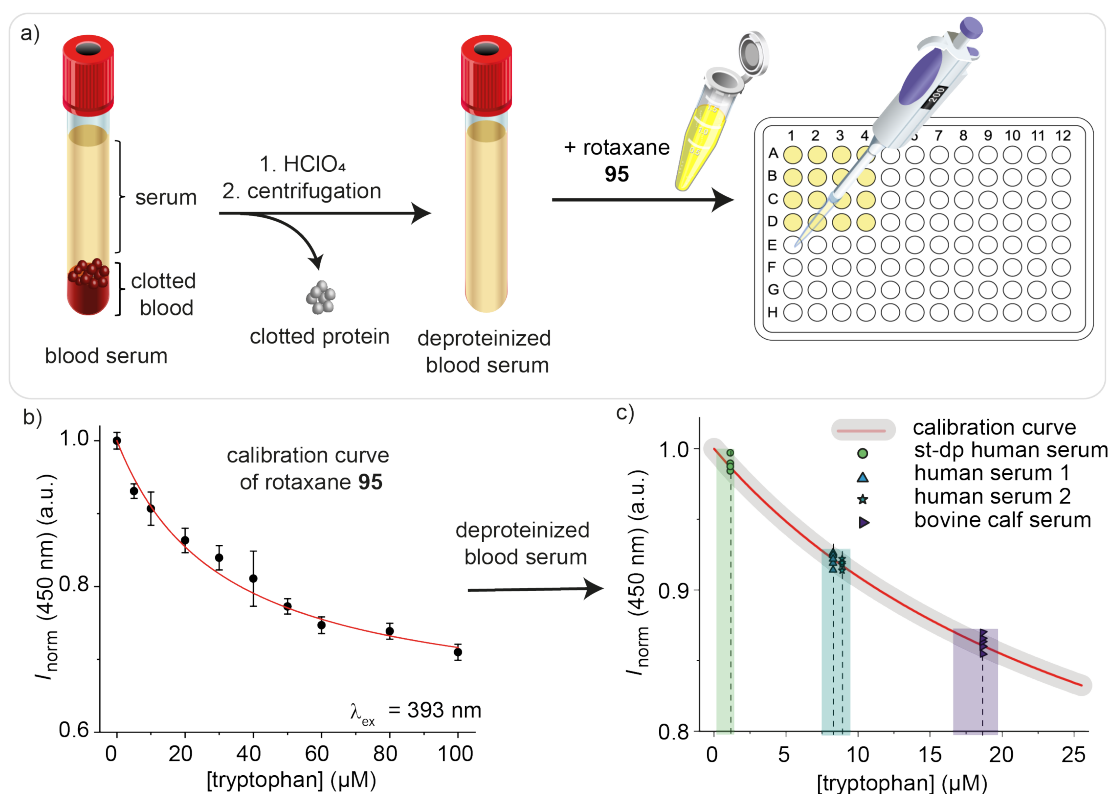


**Figure 67.** a) Schematic representation of the workflow followed for the deproteinization of the pooled blood serum and the subsequent plate reader-based calibration curve for Trp concentration determination with the rotaxane chemosensor. b) Emission-based calibration curve of 10  $\mu\text{M}$  rotaxane upon adding 0 - 100  $\mu\text{M}$  Trp in deproteinized serum matrix. c) Correlated emission intensities of four pooled blood serum samples given as single data points, as Trp concentration ranges (colored boxes), and mean values (dashed lines) for each serum sample ( $\lambda_{\text{ex}} = 393 \text{ nm}$ ,  $\lambda_{\text{em}} = 450 \text{ nm}$ ). With st-dp HS = steroid-depleted human serum, HS = human serum, and BS = bovine calf serum.

**Table 9.** Determined Trp concentrations of different blood serum samples by HPLC with an estimated error of 10 % for repetitive measurements and emission-based microplate reader measurements of the rotaxane at 25 °C.<sup>248</sup> Note that blood serum samples were stored for a minimum period of one month up to one year, which might cause variations in the Trp concentrations.<sup>329,330</sup> n.d. = not determined.

serum sample	HPLC-based	emission-based	
	[Trp] (μM)	[Trp] (μM) <sup>[a]</sup>	[Trp] (μM) <sup>[b]</sup>
steroid-depleted human serum	< 1.0 ± 0.1	2.2	0.6 - 2.8
human serum 1	18.3 ± 0.2	16.6	15.1 - 19.1
human serum 2	21.9 ± 0.2	18.8	16.1 - 19.5
human serum 3	64.0 ± 0.6	n.d.	n.d.
bovine calf serum	38.2 ± 0.4	37.2	32.9 - 39.6

<sup>[a]</sup> Intersect with the calibration curve. <sup>[b]</sup> Concentration range.

In the next step, two pooled serum samples were used in their non-treated form (*i.e.*, serum samples that still contained proteins), and the Trp detection was again performed in a microwell plate format by monitoring the emission intensity at  $\lambda_{em} = 450$  nm utilizing an excitation wavelength of  $\lambda_{ex} = 393$  nm. A schematic depiction of the measurement protocol is shown in **Figure 68**. The experimental setup included the measurement of each serum sample's autofluorescence emission before adding 10 μM rotaxane **95** ( $I_0$ ). Then the emission of rotaxane **95** in the biofluid ( $I_1$ ) and the emission decrease ( $I_2$ ) upon subsequent spiking with quantitative amounts of tryptophan in a range of 5 to 70 μM was recorded. Finally, a complete quenching of the rotaxane **95** was achieved by the addition of an excess of indole ( $I_3$ ). The autofluorescence-corrected emission intensities ( $I_n$  with  $n = 1 - 2$ ) determined were used to calculate each sample's emission quenching (EQ) efficiency to allow a comparison between the different serum samples. The emission intensity of 10 μM rotaxane in water ( $I_{ref}$ ) was used as a reference signal.<sup>248</sup>

$$EQ(\text{serum}) = \frac{(I_n - I_0) - I_{ref}}{I_3 - I_{ref}} \quad \text{Eq. 35}$$

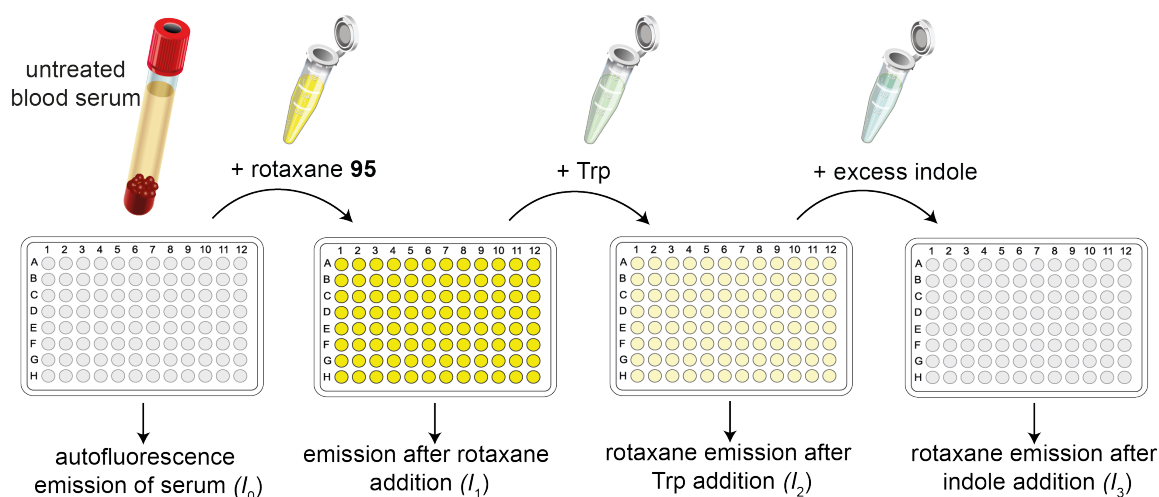


**Figure 68.** Schematic workflow for emission-based Trp sensing with rotaxane **95** in untreated blood serum samples in a microwell plate format and the corresponding signal readouts obtained from each step.

Pleasingly, the results of the rotaxane-based optical assay depicted in **Figure 69a - c** show a trend of increasing quenching efficiency as the Trp concentration in the serum sample increases.<sup>248</sup> This trend corresponds to the semi-quantitative spiking of the serum sample and correlates with the Trp levels derived from HPLC analysis. In addition, it was further possible to distinguish Trp concentrations of spiked blood serum samples from each other within the typical concentration ranges of healthy individuals (approx. 41 - 77  $\mu\text{M}$ ) and diseased patients (approx. 20 - 45  $\mu\text{M}$  for selected diseases).<sup>248</sup> For that purpose, three human serum samples were spiked with an additional 25  $\mu\text{M}$  Trp, mimicking the average concentration differences between healthy and diseased patients, shown in **Figure 69d**. A larger sample set of blood serum with known disease states would be required for a diagnostic tool to distinguish real patient samples.

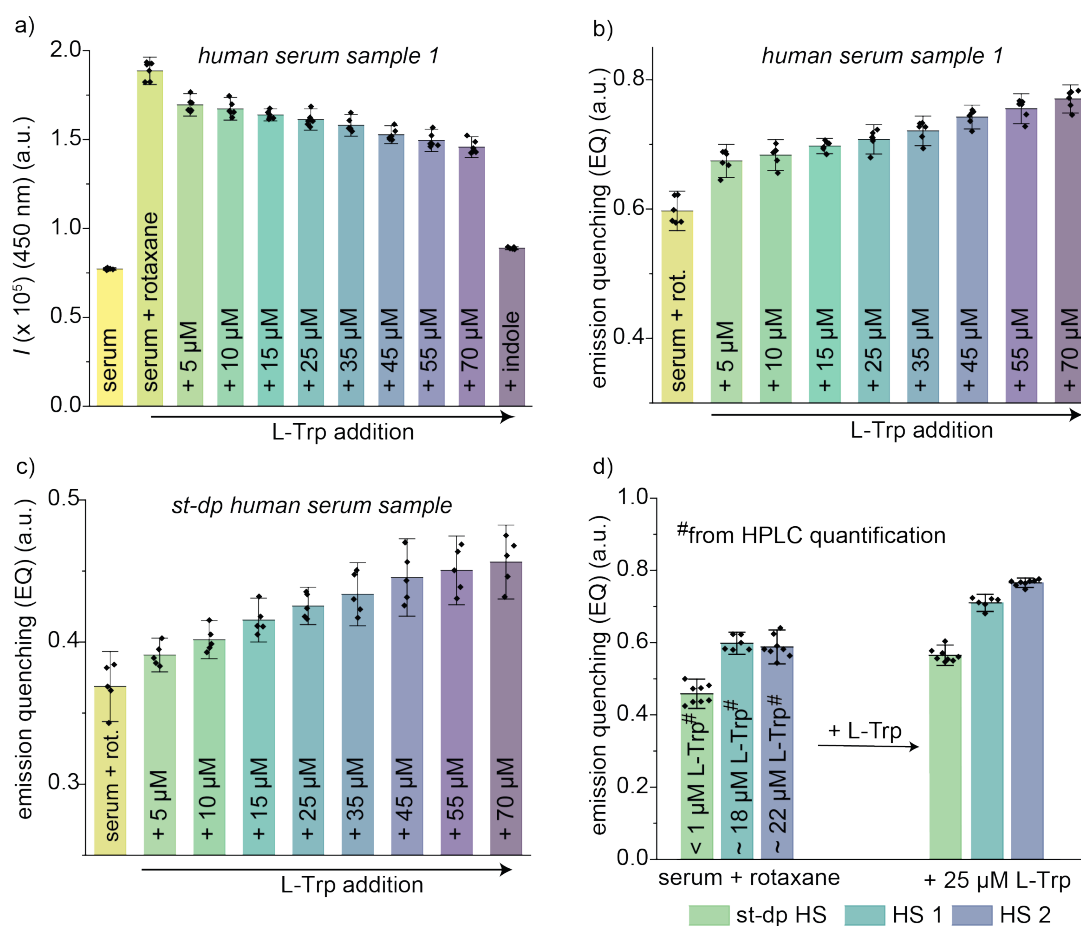


**Figure 69.** a) Bar graphs of the autofluorescence emission of human serum sample 1 ( $I_0$ ), the emission intensity of rotaxane **95** in human serum sample 1 before ( $I_1$ ) and after subsequent spiking with 5 to 70  $\mu\text{M}$  Trp ( $I_2$ ), and after the addition of an excess of indole ( $I_3$ , violet). b) Bar graphs of the emission quenching of rotaxane **95** in human serum sample 1 before and after quantitative spiking with 5 - 70  $\mu\text{M}$  Trp. c) Bar graphs of the emission quenching (EQ) of rotaxane **95** in steroid-depleted human serum sample before and after quantitative spiking with 5 - 70  $\mu\text{M}$  Trp. d) Bar graphs of the emission quenching (EQ) of rotaxane **95** in three different pooled serum samples and after spiking with 25  $\mu\text{M}$  Trp. Initial Trp concentration values were obtained by HPLC and are labeled for better comparison. Measurements were conducted at 25  $^\circ\text{C}$  with  $\lambda_{\text{ex}} = 393 \text{ nm}$ ,  $\lambda_{\text{em}} = 450 \text{ nm}$ . With (st-dp) HS = (steroid-depleted) human serum and BS = bovine calf serum. Adapted with permission from ref.<sup>248</sup> Copyright 2023 Springer Nature.

### 5.3.4.2. Tryptophan sensing in urine samples

The promising results of the Trp sensing in real blood serum encouraged the examination of Trp sensing in human urine as another important biofluid. Compared to blood serum, urine is often preferred as it is easier to collect by the layman and is a non-invasive option for metabolite monitoring. Urine samples were collected from healthy adult volunteers and used as a matrix after pH adjustment (pH 2.0) with 2 M hydrochloric acid and subsequent centrifugation to remove suspended particles. The chemosensor assay was performed in a microwell plate format analogously to the in Section 5.3.4.1 described procedure for the quantitative spiking of pooled blood serum with different concentrations of Trp. The emission quenching obtained for both urine samples in **Figure 70** shows a similar trend with increasing Trp concentration. However, compared to the measurements in blood serum, the received emission response was weaker for

the urine samples despite the same Trp spiking and similar initial Trp concentrations in the serum samples (determined by HPLC; see **Figure 70** and **Table 10**). This indicates that the complexity of the urine matrix is causing a reduced sensitivity of the rotaxane **95**.

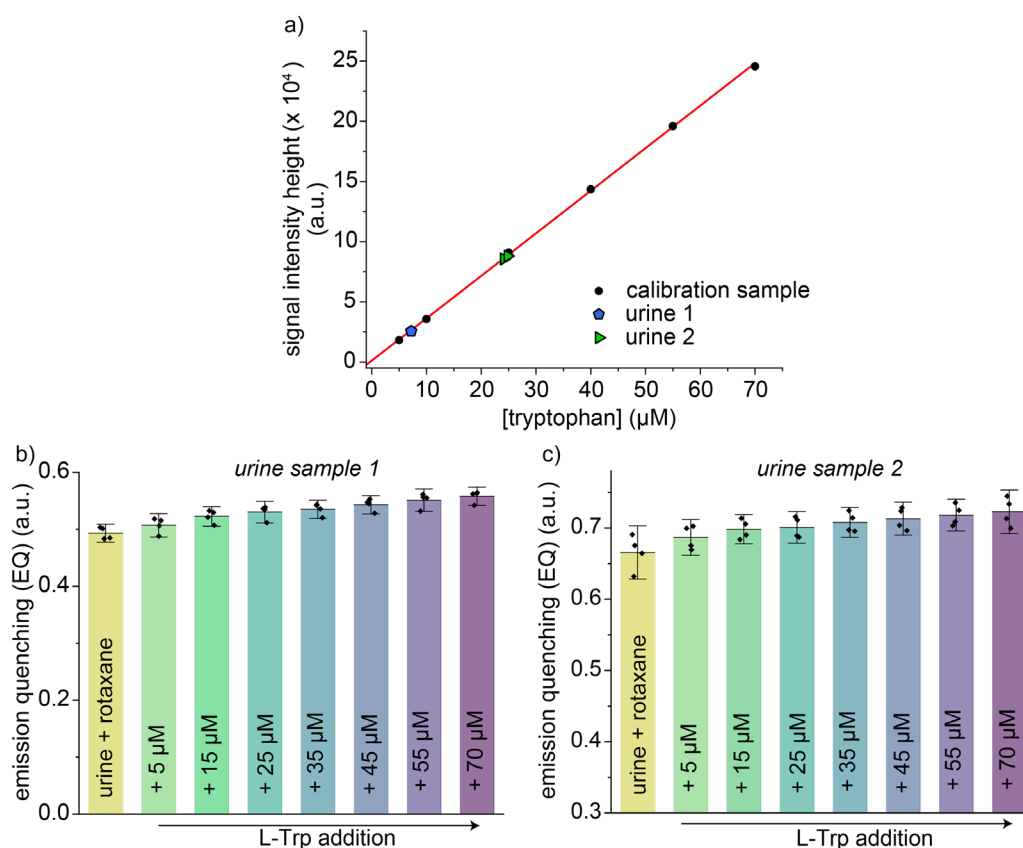


**Figure 70.** a) Plots of the determined Trp concentration levels of used urine samples obtained in an HPLC assay using a pre-established calibration curve (data points shown as black dots and linear fit as red line), measured in triplicates per urine sample and Trp concentration ( $\lambda_{\text{ex}} = 295 \text{ nm}$ ,  $\lambda_{\text{em}} = 340 \text{ nm}$ ). b) and c) Bar graphs of the emission quenching of rotaxane **95** in urine samples 1 and 2 before and after quantitative spiking with 5 - 70  $\mu\text{M}$  Trp. Adapted with permission from ref.<sup>248</sup> Copyright 2023 Springer Nature.

**Table 10.** Trp concentrations of the used urine samples were determined by quantitative HPLC measurement with an estimated error of 10 %.<sup>248</sup> Creatinine concentrations were calculated using a commercially available colorimetric quantification kit from ENZO.

medium	[Trp] ( $\mu\text{M}$ ) in urine	[creatinine] (mg/dL) in urine
urine sample 1	$7.2 \pm 0.7$	59
urine sample 2	$24.3 \pm 2.4$	110

### 5.3.4.3. Comparison of the rotaxane chemosensor to a selection of commonly used non-covalent supramolecular chemosensors

The previous sections focused on the sensing performance of the rotaxane chemosensor in salt-containing (bio)media. However, to obtain a complete picture, it was important to directly compare the rotaxane chemosensor to a selection of commonly used non-covalent supramolecular chemosensors regarding stability and sensing capabilities in aqueous media, saline buffer, and biofluid such as human blood serum. Four different macrocycles and three different indicator dyes were selected to form self-assembled chemosensors, and their chemical structures are shown in **Figure 71**. The selected systems were studied in a microwell plate format at 10  $\mu\text{M}$  by measuring their emission intensity in the selected media at 25  $^{\circ}\text{C}$ .<sup>248</sup>

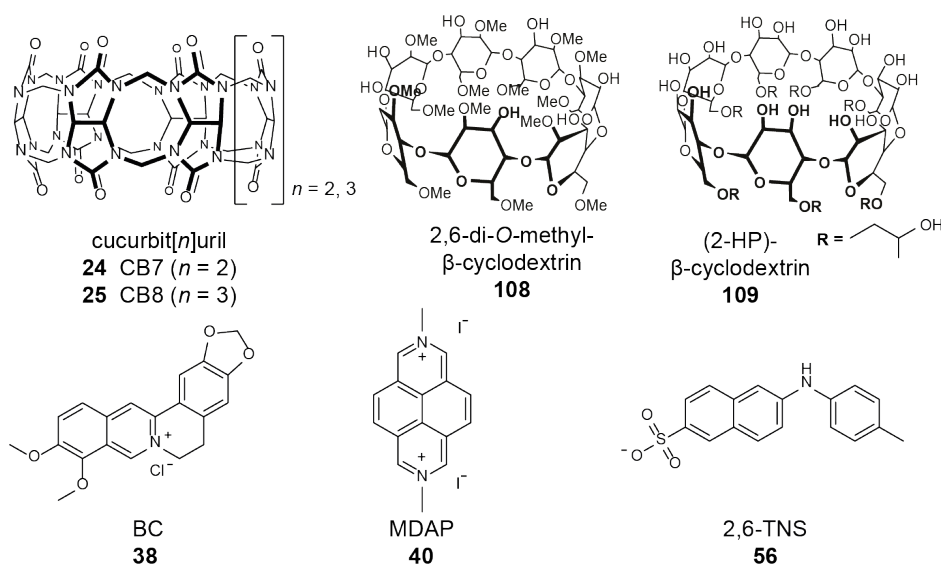


**Figure 71.** Chemical structure of the macrocyclic host (top) and indicator dye (bottom) molecules of the selected supramolecular chemosensor systems.

All dyes tested showed the typical emission turn-on upon complexation by one of the macrocycles.<sup>144,331,332</sup> The self-assembled complex CB7•berberine chloride (CB7•BC) was strongly emissive in water (see black spectra in **Figure 72a**), verifying its stability in water. However, a transfer to the 1X PBS salt buffer system resulted in greatly reduced emission intensity, which was also observed in human blood serum and urine. These results indicate that this supramolecular complex dissociates in the presence of salts due to the competitive binding of metal cations to the CB7 portals.<sup>166</sup> Thus, this chemosensor is unsuitable for measurement in saline media and biofluids.<sup>248</sup> In general, low chemosensor concentrations and high binding affinities of the chemosensor are required for sensing applications in saline buffers or even biological media to overcome the issue of dissociation.  $\beta$ -Cyclodextrins ( $\beta$ -CDs, **108** and **109**) generally show weaker binding (*e.g.*,  $\log K_a \sim 3$ )<sup>144</sup> compared to the CB $n$ , resulting in the necessity of higher host and dye concentrations ( $\sim$  low mM concentration) for a sufficient sensing

experiment. Two different  $\beta$ -CD chemosensors were prepared with 2-*p*-toluidine-6-naphthalene sulfonic acid (2,6-TNS) as the dye (see **Figure 72**). Although the complexation of 2,6-TNS by  $\beta$ -CD and its derivatives usually caused an emission increase in water, no emission enhancement was observed at the used micromolar concentrations of the chemosensor.<sup>333</sup> This was also observed for 1X PBS and human urine. Only in human blood serum was an increase in emission detected, which can be attributed to the complexation of the dye by the protein human serum albumin (HSA).<sup>334,335</sup> These results show that both systems are unsuitable for detecting aqueous or biological media at the selected low chemosensor concentration. Furthermore, the interference of the dye with proteins in human serum further limits its application in biofluids.

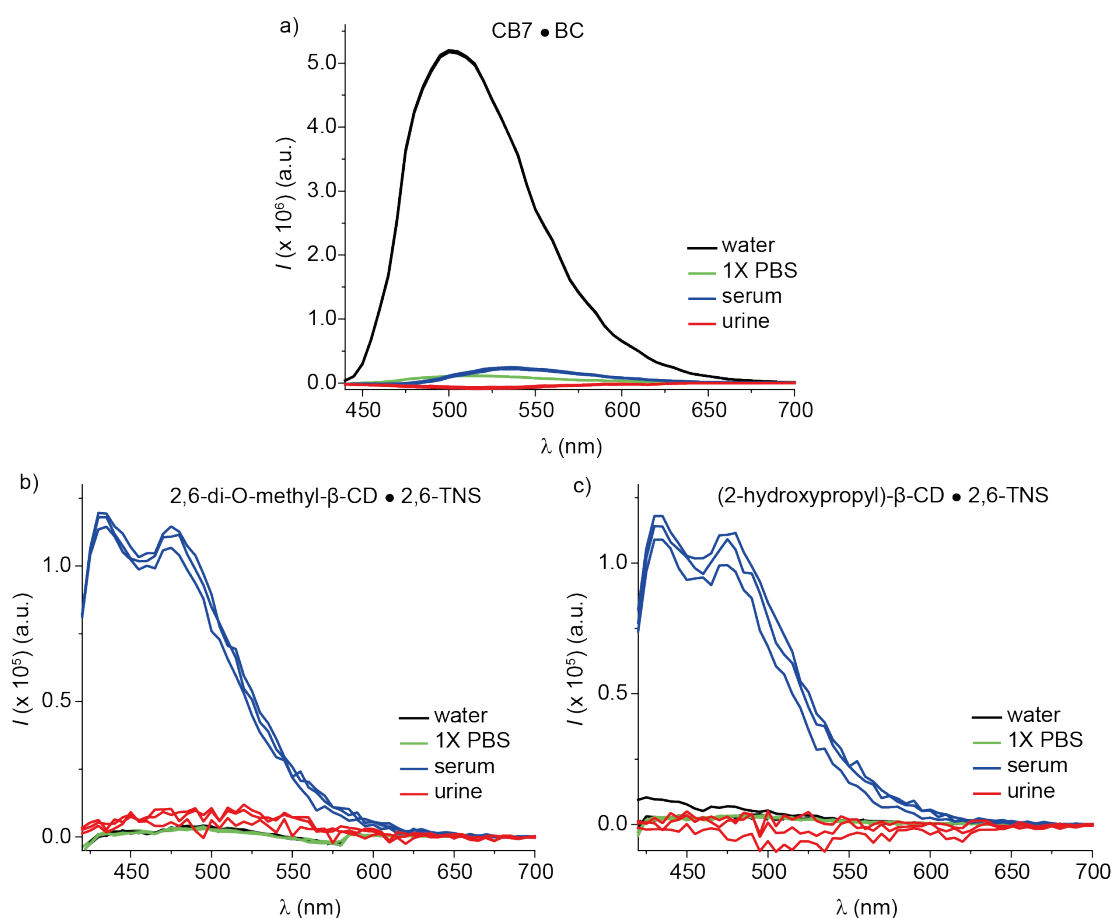


**Figure 72.** Emission spectra of a) CB7•BC (BC: 15  $\mu$ M, CB7: 10  $\mu$ M), b) 2,6-di-O-methyl- $\beta$ -CD•2,6-TNS (2,6-TNS: 15  $\mu$ M,  $\beta$ -CD: 10  $\mu$ M) and c) (2-HP)- $\beta$ -CD•2,6-TNS (2,6-TNS: 15  $\mu$ M,  $\beta$ -CD: 10  $\mu$ M) in water (black line), 1X PBS (green line), pooled human blood serum (blues line), and human urine (red line). All measurements were conducted in triplicates at 25  $^{\circ}$ C with at  $\lambda_{\text{ex}} = 393$  nm. Adapted with permission from ref.<sup>248</sup> Copyright 2023 Springer Nature.

Unlike CB7•BC, the self-assembled CB7•MDAP was less affected by salt cations since CB7 has a larger binding affinity towards the dye 2,7-dimethyl diazapyridinium (MDAP,  $\log K_a = 9.4$ )<sup>144</sup> compared to berberine chloride ( $\log K_a = 7.2$ ).<sup>144</sup> As shown in **Figure 73**, the system was stable in saline buffers, indicated by the similar emission intensity compared to water. A strongly reduced emission intensity in human blood serum compared to water was observed. In addition,

the sensing capability of the system was examined by titration with a Trp solution. The observed emission response was very weak even for high Trp concentrations (66 times excess of Trp to CB7•MDAP). Therefore, the system is unsuitable for measuring low micromolar concentrations of tryptophan ( $\log K_a \sim 3$  for CB7 in water), especially in biofluids, due to numerous competing binders such as biogenic amines, steroids, and proteins. Due to the high binding affinity of the indicator dye for the host, displacement is even more difficult for weaker binding analytes such as Trp. Thus, a dye with lower  $K_a$  would be better. However, one would then encounter the same problems as discussed for CB7•BC.

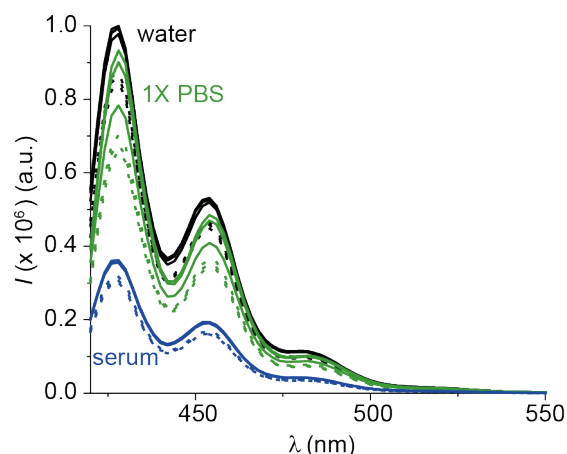


**Figure 73.** Emission spectra of CB7•MDAP (MDAP: 15  $\mu\text{M}$ , CB7: 10  $\mu\text{M}$ ) in water (black), 1X PBS (green), and pooled human blood serum (blue) before (solid line) and after the addition of 655  $\mu\text{M}$  Trp (dashed line). All measurements were conducted in at least duplicates at 25  $^\circ\text{C}$   $\lambda_{\text{ex}} = 393$  nm. Adapted with permission from ref.<sup>248</sup> Copyright 2023 Springer Nature.

Since the synthesized rotaxane consists of a CB8•MDAP moiety as a receptor unit, it was evident to compare the rotaxane **95** with the self-assembled chemosensing system CB8•MDAP. Therefore, titration experiments with Trp (0 - 425  $\mu\text{M}$ ) were conducted for the rotaxane and the CB8•MDAP chemosensor in water, 1X PBS, and human serum at  $\lambda_{\text{em}} = 450$  nm (see **Figure 74a** and **b**). Both systems show a significant emission response upon the addition of tryptophan in water (black dots) and 1X PBS (blue triangles).

In human blood serum, the initial emission intensity of CB8•MDAP was reduced by more than 20 % compared to rotaxane **95**. In addition, the observed emission quenching upon the addition of excess Trp ( $> 400$   $\mu\text{M}$ ) was significantly larger for rotaxane **95** than for CB8•MDAP.<sup>248</sup> Therefore, the synthesized rotaxane chemosensor offers a larger usable detection window, *i.e.*, the partial emission quenching per tryptophan amount, compared to CB8•MDAP, which makes the rotaxane more sensitive for smaller amounts of Trp over a larger concentration range (see **Figure 74c**).<sup>248</sup> In addition, the salt influence ("matrix effect") on the Trp detection of both chemosensor systems was evaluated by measuring the emission intensity quenching of a 25  $\mu\text{M}$

Trp solution in the presence of different amounts of sodium chloride. The results are shown in **Figure 74d**. The coloured boxes show the extent of the interfering influence of an unknown salt concentration on the sensing ability of the corresponding chemosensors. The results show that the rotaxane **95** is less affected by salts than the self-assembled CB8•MDAP chemosensor.

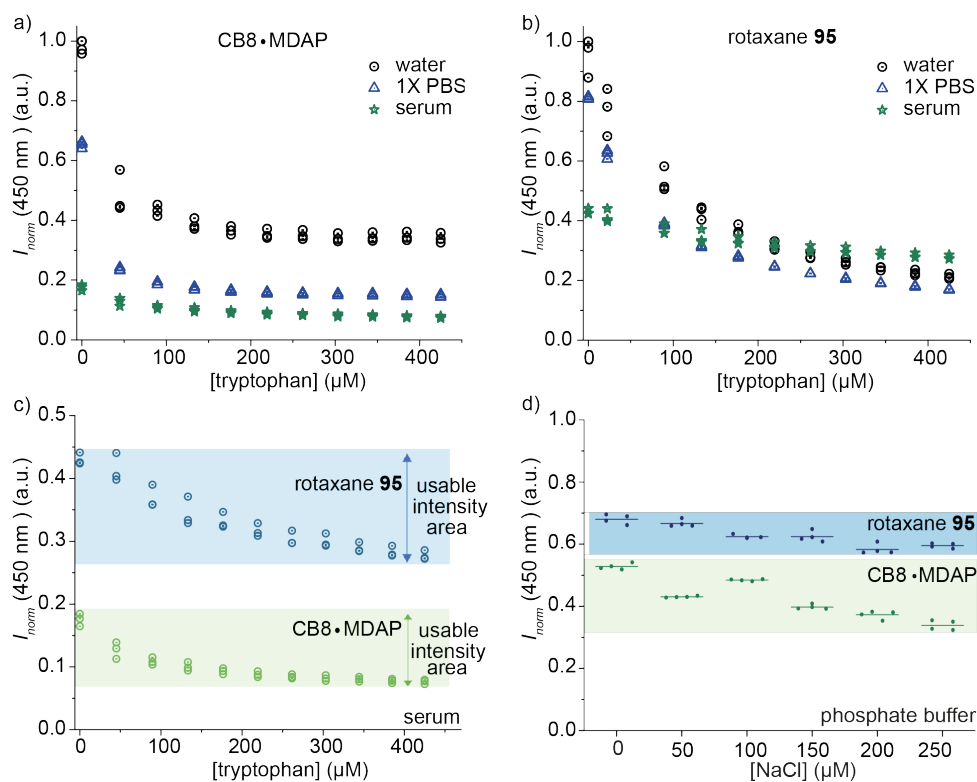


**Figure 74.** Emission-based titration measurements of Trp (0 - 425  $\mu\text{M}$ ) to a) CB8•MDAP (MDAP: 11  $\mu\text{M}$ , CB8: 10  $\mu\text{M}$ ) and b) the synthesized rotaxane **95** (10  $\mu\text{M}$ ) in water (black dots), 1X PBS (blue triangles), and pooled human blood serum (green stars). c) Comparison of the emission-based titration measurements of Trp (0 - 425  $\mu\text{M}$ ) to rotaxane **95** (10  $\mu\text{M}$ , blue dots) and CB8•MDAP (MDAP: 11  $\mu\text{M}$ , CB8: 10  $\mu\text{M}$ , green dots) in human blood serum. The colored boxes indicate the usable intensity area of the corresponding chemosensor for Trp detection. d) Emission intensity of rotaxane **95** (10  $\mu\text{M}$ ) and CB8•MDAP (MDAP: 11  $\mu\text{M}$ , CB8: 10  $\mu\text{M}$ ) after the addition of 25  $\mu\text{M}$  Trp in the presence of various amounts of sodium chloride in 10 mM sodium phosphate buffer at pH 7.7. The colored boxes indicate the intensity reduction due to different amounts of salts. All measurements were conducted in at least triplicates at 25  $^{\circ}\text{C}$  with  $\lambda_{\text{ex}} = 393\text{ nm}$ ). Adapted with permission from ref.<sup>248</sup> Copyright 2023 Springer Nature.

### 5.3.5. Rotaxane microarrays for analyte detection

In addition to the sensing application of the rotaxane chemosensor in bulk solution, the hydroxyl groups of the  $\beta$ -CD stopper groups enable the transition to solid substrates by immobilizing the rotaxane onto functionalized glass surfaces.<sup>336</sup> The immobilization and subsequent sensing measurements were carried out by CHUNTING ZHONG in collaboration with the HIRTZ Group at KIT in Karlsruhe. The obtained results were discussed collectively for analysis. Microchannel cantilever spotting ( $\mu\text{CS}$ ) was chosen as a scanning probe lithography (SPL) method for creating the rotaxane microarrays. In general, SPL methods provide a flexible route to create micro- and even nano-scaled surface patterns of immobilized functional molecules.<sup>337</sup>

Rotaxane **95** was first deposited on an isocyanate-functionalized glass surface by applying small drops of rotaxane ink. In these droplets, an addition reaction occurred between the isocyanate moieties and the OH groups of the  $\beta$ -CD stoppers of the rotaxane, whereby the rotaxane was covalently bound to the surface via a urethane bond.<sup>338,339</sup> After washing with ethanol, the rotaxane microarray (sensor chip) was obtained, which was then usable for the analyte detection experiments (see **Figure 75**).

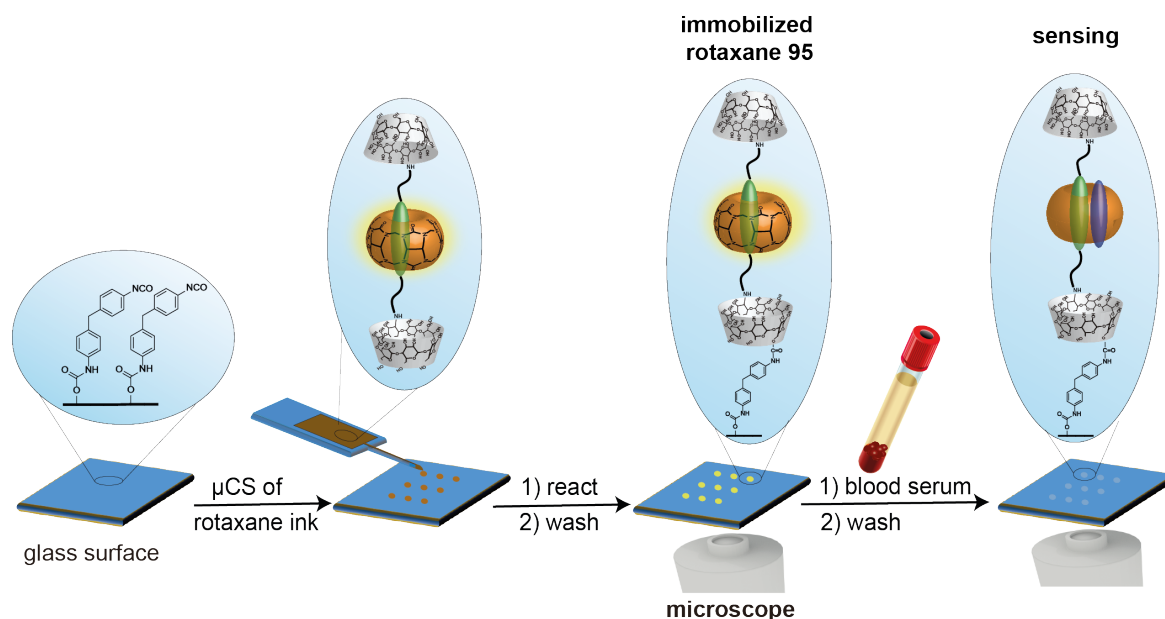


**Figure 75.** Schematic representation of the rotaxane microarray preparation using microchannel cantilever spotting ( $\mu$ CS) on an isocyanate-functionalized surface and analyte detection by microarrays. Adapted with permission from ref.<sup>248</sup> Copyright 2023 Springer Nature.

First, the sensing capability of the created rotaxane array was probed with indole and memantine in HEPES buffer (pH 7.0) and compared to a self-assembled CB8•MDAP microarray. Analogously to the experiments performed in the bulk solution (see Section 5.3.3), the rotaxane **95** only showed an emission quenching upon indole addition. However, for the CB8•MDAP microarray, almost 100 % emission quenching was also observed for incubation with memantine (Mem), suggesting that the MDAP dye is displaced by the larger and stronger binding analyte memantine (see **Figure 89** in Section 8.3).<sup>7,112,200,340</sup> This shows the superior stability of the rotaxane microarray over the self-assembled CB8•dye reporter pairs. Next, the sensitivity of the microarrays for Trp was investigated. The washable microarray was incubated with Trp solutions from micromolar (10  $\mu$ M) down to nanomolar (1 nM) concentration levels in 1X PBS, and the fluorescence microscopy images were compared for their emission quenching. This showed that it was possible to detect tryptophan concentrations down to  $10^{-8}$  M, shown in **Figure 76**.

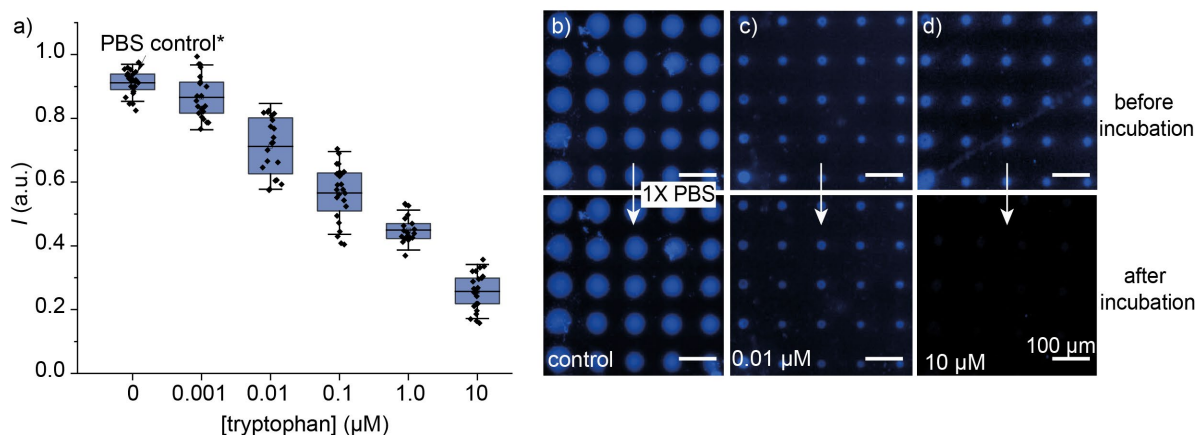


**Figure 76.** a) Box plots of quantifying the fluorescence intensities of the rotaxane microarray spots before and after incubating with Trp solutions of different concentrations and with 1X PBS as control. Box plots show the mean (middle line), 25<sup>th</sup>, 75<sup>th</sup> percentiles (box), and the standard deviation of all data points (single points). b) Fluorescence microscopy images (with DAPI filter,  $\lambda_{\text{ex}} = 395$  nm, 10 seconds exposure time) of the rotaxane microarray before and after incubation with 0.01  $\mu\text{M}$  and 10  $\mu\text{M}$  Trp in 1X PBS. Adapted with permission from ref.<sup>248</sup> Copyright 2023 Springer Nature.

Additionally, the applicability of the microarrays for Trp detection in untreated human blood serum and urine was tested. Therefore, a human serum sample with less than 1  $\mu\text{M}$  initial Trp was spiked with controlled quantities of Trp to obtain serum samples with different Trp concentrations. The incubation of the microarrays with those solutions caused increased emission quenching with increasing Trp concentration (see **Figure 90** in Section 8.3). Furthermore, human serum (containing 58  $\mu\text{M}$  Trp, determined by HPLC, see Section 5.3.4.1) and differently diluted serum (diluted with 1X PBS) were incubated on the rotaxane sensor chip in a reversed approach. In a similar experimental setup, the rotaxane microarray was incubated with human urine ( $c = 60$   $\mu\text{M}$  Trp, determined by HPLC) and its dilutions with 1X PBS. In both cases, a dilution-dependent emission quenching was detected. The observed emission intensities for the various dilutions of human serum and urine are shown in **Figure 77**.

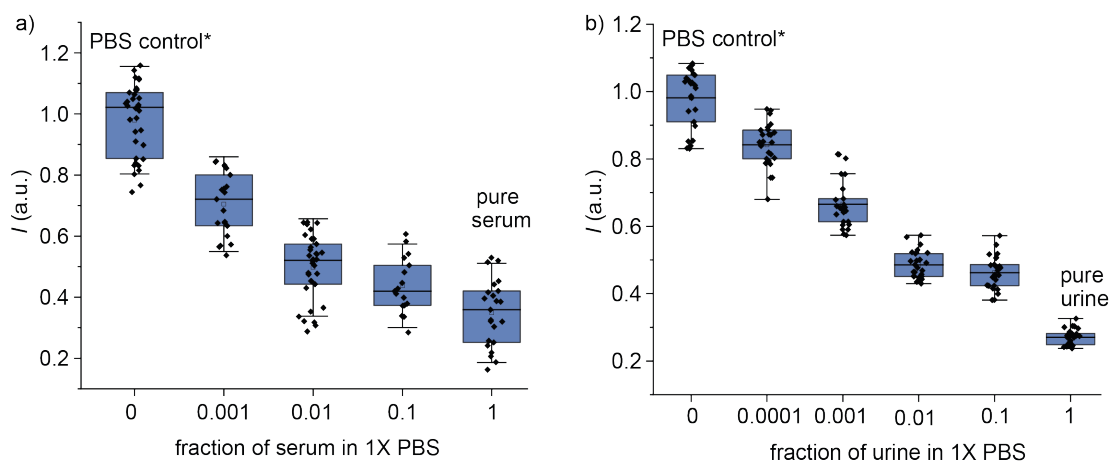


**Figure 77.** Box plots of quantifying the fluorescence intensities of the rotaxane microarray spots for Trp detection in a) human serum and b) human urine at different dilutions with 1X PBS and only 1X PBS as control. Box plots show the mean (middle line), 25<sup>th</sup>, 75<sup>th</sup> percentiles (box), and the standard deviation of all data points (single points). Adapted with permission from ref.<sup>248</sup> Copyright 2023 Springer Nature.

Overall, the findings show that the rotaxane microarrays can reliably detect Trp, even in challenging, complex media like human serum or urine. The operating range of the sensor chips with the immobilized rotaxane was determined to be between 10 nM and 10  $\mu$ M, which is much lower than the possible range in solution-based assays.<sup>248</sup> However, this does not affect the microarray applicability for Trp sensing in biofluids, as biofluid samples with increased Trp concentrations can be diluted before testing. Generally speaking, a practical and low-volume sensing platform can be created by enclosing such sensor devices in microfluidic channels.<sup>340</sup>

### 5.3.6. Label-free enzymatic reaction monitoring

Real-time continuous label-free reaction monitoring is an important tool for elucidating chemical and biochemical reaction mechanisms. Current technologies provide only discontinuous data points within selected time intervals, often requiring time-consuming sample pre- and post-treatment steps. In contrast, analyte-responsive macrocyclic host•dye systems have been shown to enable real-time monitoring of enzymatic reactions and membrane permeation processes.<sup>110,164</sup> However, those systems have been mainly applied in low saline buffers due to their susceptibility to competitors such as salts.<sup>29,38,110</sup> To get a first insight into the behavior of the salt-stable rotaxane chemosensor in a dynamic reaction mixture with more than one compound, real-time monitoring of the enzymatic digestion of bovine serum albumin (BSA, **110**) protein was carried out. Due to the dense structure of BSA in which hydrophobic amino acids such as Phe (**1**) and Trp (**2**) residues are buried inside the protein core,<sup>341</sup> the chemosensor cannot bind to BSA. However, upon digestion (hydrolysis) with endopeptidase pepsin, the protein is broken down into smaller peptides carrying exposed amino acids on the surfaces.<sup>342</sup> Those can then be complexed by the rotaxane **95**, allowing for an optical readout over time. A schematic depiction of the enzymatic assay is shown in **Figure 78**.<sup>248</sup>

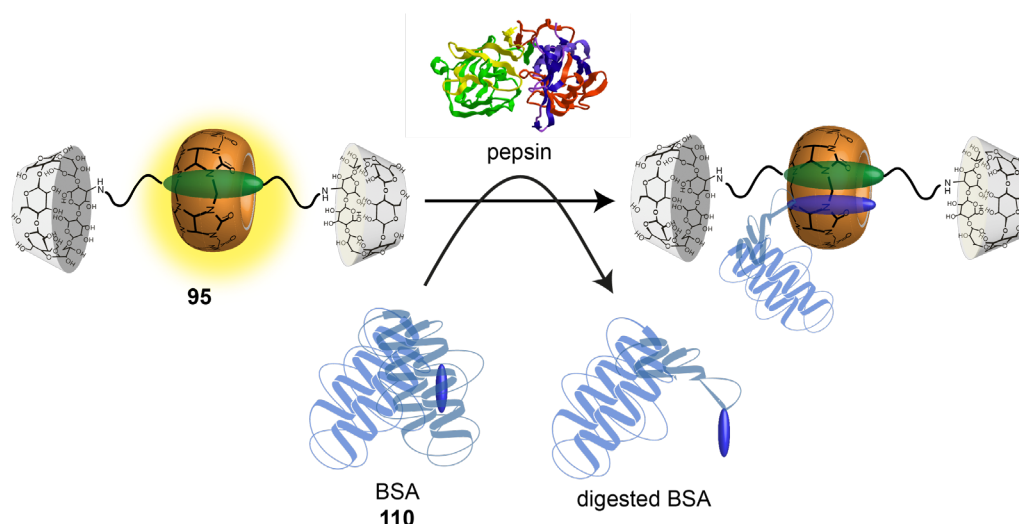


**Figure 78.** Schematic representation of the enzymatic digestion of BSA (**110**). Digestion of BSA by pepsin leads to the exposure of Trp/Phe residues on the peptide surface, which can now be bound by the rotaxane chemosensor **95**, resulting in an emission turn-off. Adapted with permission from ref.<sup>248</sup> Copyright 2023 Springer Nature.

The enzymatic digestion of BSA by pepsin was monitored in real time with the rotaxane chemosensor. Therefore, a mixture of BSA from BIOWEST (100  $\mu\text{g}/\text{mL}$ ) and rotaxane (4.5  $\mu\text{M}$ ) was prepared in 1X PBS at pH 2.0, and the emission intensity was monitored at 450 nm ( $\lambda_{\text{ex}} = 393$  nm) over time at 25  $^{\circ}\text{C}$ , after equilibrating the solution for approximately one hundred seconds, pepsin (in 1X PBS, pH 2.0) was added to the rotaxane-BSA mixture, and the emission decrease was monitored.<sup>248</sup> As expected, faster hydrolysis of a steady BSA concentration was observed with an increasing enzyme concentration. The real-time monitoring of BSA in the presence of the rotaxane **95** without the subsequent addition of pepsin was used as a negative control as well as the addition of pepsin to a 4.5  $\mu\text{M}$  rotaxane solution in the absence of BSA. The obtained kinetic curves of various pepsin concentrations and BSA (in the absence of pepsin) and enzyme (in the absence of BSA) alone are shown in **Figure 78**.

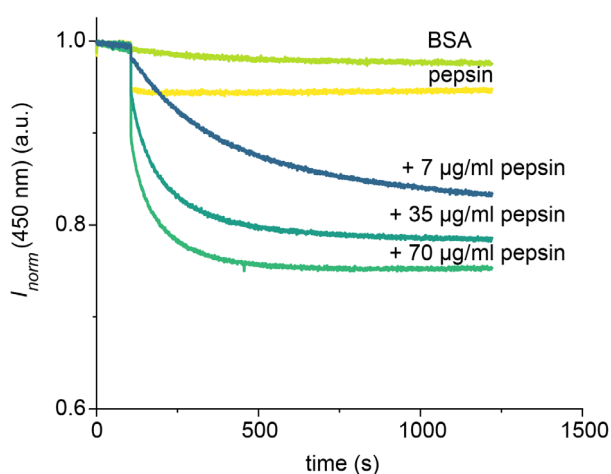


**Figure 79.** Fluorescence kinetic traces for the enzymatic hydrolysis of 100  $\mu\text{g}/\text{mL}$  BSA in the presence of rotaxane **95** (4.5  $\mu\text{M}$ ) by pepsin (0 - 70  $\mu\text{g}/\text{mL}$ ) monitored at  $\lambda_{\text{em}} = 450$  nm ( $\lambda_{\text{ex}} = 393$  nm) in 1X PBS (pH 2.0) at 25  $^{\circ}\text{C}$ . BSA and pepsin were measured as control. Adapted with permission from ref.<sup>248</sup> Copyright 2023 Springer Nature.

Overall, the obtained kinetic traces show that the system is generally operational in complex mixtures, making the chemosensor attractive for application in supramolecular tandem assays<sup>110</sup> and for reaction monitoring of chemical synthesis.

### 5.3.7. Chirality sensing with rotaxane chemosensor

Chirality is an ubiquitous phenomenon in nature, both at the macroscopic level (*e.g.*, snail shells) and at the molecular level (*e.g.*, homochirality of amino acids and sugars). Besides the biological activity of a compound is closely linked to its stereochemical information.<sup>343,344</sup> A deviation from a compound's natural enantiomeric form can already have significant differences in its effect on the organism, *e.g.*, the negative effects of the cancer drug thalidomide.<sup>345</sup> The presence of D-amino acids in living organisms is a valuable indicator of various biological processes, such as aging, diseases, and disorders.<sup>8,346</sup> D-amino acids can provide insight into the underlying causes of these conditions and can be used to develop treatments or therapies.<sup>347</sup> Thus, determining the absolute stereochemical configuration of amino acids and derivatives is essential. However, many small bioactive molecules are spectroscopically challenging to detect or even quantify as they absorb below 280 nm of the electromagnetic spectrum and produce no significant circular dichroism (CD) signal.<sup>348</sup> A common approach for sensing chiral molecules is either the covalent reaction of the analyte with a chiral molecular probe<sup>349,350</sup> or the use of a chiral host or a chiral dye, but the design is often chemically challenging.<sup>351-354</sup> Recently, induced circular dichroism (ICD) has been exploited to detect small chiral molecules with achiral self-assembled CB8•dye complexes.<sup>153,348</sup> As the synthesized rotaxane share the reporter core with those sensors, it was apparent to examine the rotaxane chemosensor's capabilities to differentiate between enantiomeric aromatic amino acids combined with electronic circular dichroism (ECD) spectroscopy.<sup>248</sup>

Phenylalanine (Phe) and tryptophan (Trp) were measured in both of their enantiomeric forms (D and L) with the rotaxane. Therefore, 100  $\mu\text{M}$  of the rotaxane **95** was mixed with 290  $\mu\text{M}$  of the chiral analyte in water at 25 °C, and an ECD spectrum was recorded and compared to the rotaxane **95** and analyte alone (see **Figure 80**). Indeed, the D and L enantiomers of Trp and Phe can be distinguished after complexation with rotaxane **95** by the resulting chiroptic fingerprints in the visible region of the ECD spectrum.<sup>248</sup> For Trp, the CD signals obtained for D and L are almost mirror images of each other, whereas for Phe, a slight spectrum asymmetry can be observed, especially in the region of 360 - 430 nm (see **Figure 80b** and **c**). This asymmetry can be traced back to a chirality induction by the chiral  $\beta$ -cyclodextrin stopper groups due to the rotaxane's

flexible structure. It is suggested that the  $\beta$ -cyclodextrin groups can come in close vicinity to the CB8 dye complex and thereby cause the additional chirality induction.<sup>248</sup> The flexibility of the linker molecules and the associated mobility of the stopper groups is shown in **Figure 80c**. It also explains the remarkable sensing ability of rotaxane **95** in biofluids since the binding pocket of the chemosensor in biofluids is protected from interfering factors.<sup>248</sup>

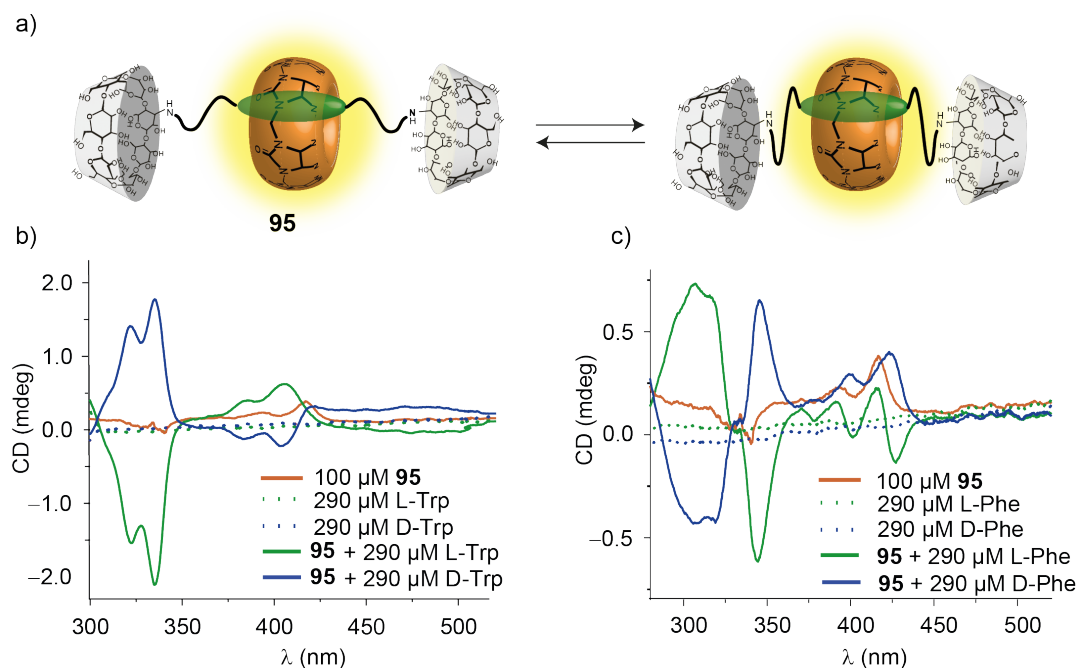


**Figure 80.** a) Schematic depiction of a possible mechanism for chirality induction in the rotaxane **95** through the interaction of the  $\beta$ -CD stopper groups with the DAP reporter dye and the portal areas of CB8. b) and c) electronic circular dichroism (ECD) spectra of rotaxane **95** (100  $\mu$ M, orange line) in the presence b) of L-Trp (green line) or D-Trp (blue line), and c) L-Phe (green line) or D-Phe (blue line). The ECD spectra of the enantiomeric amino acids Phe and Trp are shown as dotted lines. Adapted with permission from ref.<sup>248</sup> Copyright 2023 Springer Nature.

## 6. Conclusion and outlook

The aim of this thesis was the design and development of supramolecular chemosensing systems based on molecular recognition for the optical detection of small biomolecules (biomarkers) and pharmaceutical-relevant agents (illicit drugs) in salt-containing media and complex biofluids.

### 6.1. Fundamental binding studies and assay development for insoluble and weakly binding guest molecules <sup>2</sup>

Existing assays to accurately determine the binding affinity ( $K_a$ ) of a spectroscopically silent host•guest (H•G) system are generally limited to guests soluble in the solvent system used. Therefore, strongly hydrophobic, and thus water-insoluble guests have not been accessible to water-soluble hosts, such as cucurbit[ $n$ ]urils, without the addition of organic co-solvents or salts, resulting in apparent  $K_a$  values. In this work, a novel assay called “**guest displacement assay (GDA)**” was developed to determine the binding affinity of water-insoluble and weakly binding guest molecules. This new method is the mechanistic mirror image of the **indicator displacement assay (IDA)**,<sup>150</sup> in which a guest displaces the dye in a preformed complex of a host and a suitable indicator dye. GDA is a label-free method that exploits the solubility-enhancing effect of macrocyclic hosts<sup>189</sup> such as cucurbit[ $n$ ]urils (CB $n$ ) or cyclodextrins (CD), especially on hydrophobic guests, to form a water-soluble host•guest inclusion complex in a pre-equilibrium state (see **Figure 81**). Titration with a fluorescent dye with similar or stronger binding affinity leads to the spectroscopically observable displacement of the guest, and fitting of the obtained emission-based binding curve allows for the determination of the  $K_a$  values. The new method was first verified by determining and comparing  $K_a$  values for a soluble guest, such as cadaverine, determined in an IDA and a GDA setup. Both assays yielded matching binding affinities, proving the operability of the new guest displacement assay. Binding affinities for water-insoluble or poorly soluble steroids such as estradiol (solubility in water: 9  $\mu$ M) with CB7 were successfully determined in a GDA setup.

In addition, the binding strength of the anti-inflammatory drug phenylbutazone to the protein HSA was investigated as a representative example of drug•protein interactions. The obtained binding affinity ( $\log K_a = 5.83 \pm 0.04$ ) was in good agreement with literature-known values ( $\log K_a = 5.70$ ),<sup>221</sup> showing GDA's applicability to proteins. In addition, binding constants of weakly binding guests (*i.e.*,  $\log K_a \leq 3$ ) such as  $n$ -butanol were successfully determined for both

---

<sup>2</sup> The results of the following chapter have been published in a Chemical Communication article: Sinn, S., Krämer, J. & Biedermann, F. Teaching old indicators even more tricks: Binding affinity measurements with the guest-displacement assay (gda). *Chem. Commun.* **56**, 6620-6623 (2020).

CB7 and  $\beta$ -CD. Weakly binding guests were previously not accessible by titrations, as they required the addition of large amounts of the guest to displace the dye, resulting in poor mathematical fits.

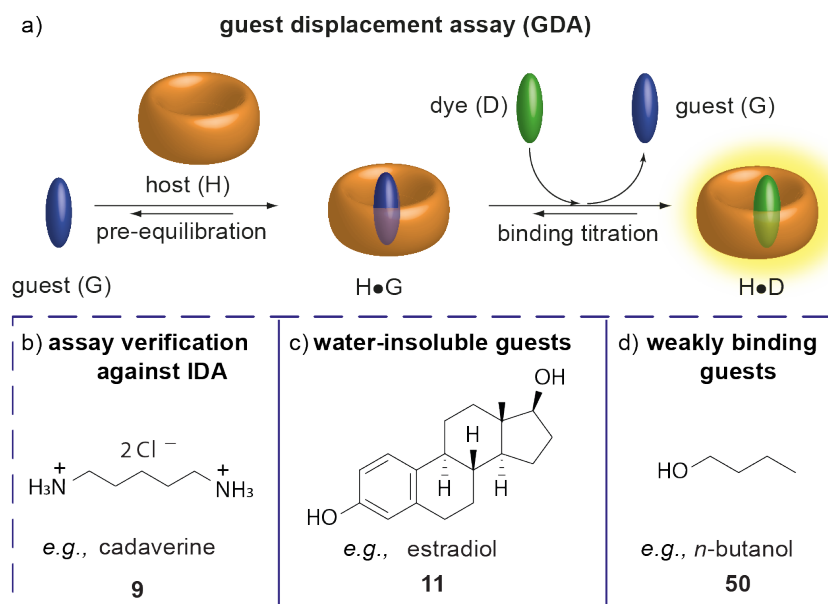


**Figure 81.** a) Schematic depiction of the within this work developed guest displacement assay (GDA) for the binding affinity determination of H•G complexes. b) The assay was first verified by comparing it to the established indicator displacement assay (IDA) with soluble guests. Furthermore, titration experiments for  $K_a$  determination were conducted for c) insoluble ( $< 20 \mu\text{M}$ ) and d) weakly binding ( $\log K_a \leq 3$ ) guests.<sup>144</sup>

Consequently, a performance window for GDA (and IDA) was determined, which can be used to predict whether a dye is suitable as a competitor for a H•G pair and whether the results obtained are trustworthy. On the one hand, a guest can be accurately determined by GDA when the indicator dye does not bind more than a factor of 10 weaker than the guest; otherwise, the obtained titration curve is too flat as the dye cannot displace the guest properly. On the other hand, the indicator dye must not bind more than a factor 100 stronger than the guest, as otherwise, the obtained binding curve is too steep, resulting in a poor fit. Thus, for a reasonable GDA of a H•G pair with, for example, a binding affinity of  $\log K_a = 4$  requires a dye with a binding affinity in the range of  $\log K_a = 3 - 6$ .

GDA is generally superior to IDA for insoluble or weakly binding guests and opens new ways to investigate previously inaccessible guests. Moreover, the extension to other host classes or supramolecular systems will generally deepen the mechanistic understanding of host-guest chemistry since a wider range of guests is now accessible. Besides, this assay setup is also applicable for the determination of the kinetic parameters of a H•G complex.<sup>158</sup>

## 6.2. Conceptual study of a new sensing system for analyte discrimination<sup>3</sup>

A conceptual study of a new chemosensor ensemble was pursued during my research visit at the HOF laboratories at the University of Victoria in Canada. This study aimed to create a new sensing system in a combinatorial approach by assembling multiple chemosensor types with different recognition units to achieve a differential cross-reactive detection of a range of cationic and neutral drugs. Therefore, *p*-sulfonatocalix[*n*]arene-based DimerDye (DD) chemosensors developed in the HOF group, and macrocyclic CB7 and CB8 host molecules were combined. DD are macrocyclic hosts, which carry an intrinsic signaling unit as one of the upper rim sulfonate-groups is substituted with a merocyanine-based dye. These chemosensors form dimers (DD<sub>2</sub>) in an aqueous solution, where the emission of the dye is quenched due to its complexation in the second calix[4]arene cavity.<sup>226</sup> The addition of a cationic guest leads to the disruption of the DD<sub>2</sub> due to the binding of the guest, causing an emission turn-on. Since DDs can successfully detect cationic drugs, the combination with CB*n* was expected to extend the sensing capabilities from smaller cationic to neutral and large (cationic) drugs. The examination of the DD•CB*n* mixtures by <sup>1</sup>H NMR and optical-based spectroscopy indicated the DD•CB*n* hetero-chemosensing complex formation. The complexation of the pendant dye arm by CB*n* disrupted the emission-quenched dimeric DD<sub>2</sub> complex concomitant with a turn-on of the emission of the complexed dye (see **Figure 82**). The subsequent addition of a CB*n* binding analyte (*e.g.*, 1-adamantanol) led to the displacement of the dye from the CB cavity due to the CB*n*•guest interaction. Thus, in the presence of an analyte, the DD reassembled to their dimeric form resulting in an emission turn-off, indicating the sensing capabilities of the sensor system.

The DD•CB*n* sensor combinations were used in an array-based approach to investigate their sensing and discrimination capacities for a selection of cationic and neutral drugs. Using a sensor array allows for the discrimination of structurally closely related compounds which are usually not distinguishable when utilizing only a single chemosensor due to a lack of selectivity.<sup>172</sup> The combination of different unselective chemosensors in a sensor array created a unique fingerprint for each analyte as a result of the cross-reactivity of the chemosensors. Principal component analysis (PCA) was used to reduce the dimensionality of the obtained data and enabled the visual discrimination of the analytes in a 2D score plot.<sup>171</sup> From a pool of fifteen pharmaceutical-relevant agents (*e.g.*, benzodiazepines, opioids) and illicit drugs (*e.g.*, cocaine, THC), as well as common

---

<sup>3</sup> This work was performed during a research stay in the HOF group at the University of Victoria, Canada, as part of a collaboration project. The results discussed in this chapter are the basis of a publication, which is currently in preparation. The here provided data and their analysis is thus similar to the ones in the planned publication.

diluents (*e.g.*, caffeine, Vitamin C), and adulterants (*e.g.*, levamisole, lidocaine), thirteen compounds were selectively detected using a sensor array consisting of four different  $DD_n \cdot CB_n$  sensors and  $CB_8 \cdot BC$ . Only the common diluents caffeine and Vitamin C showed an overlap in the PCA plot. However, they do not pose any serious health repercussions and thus do not restrict the future application of the sensor array.

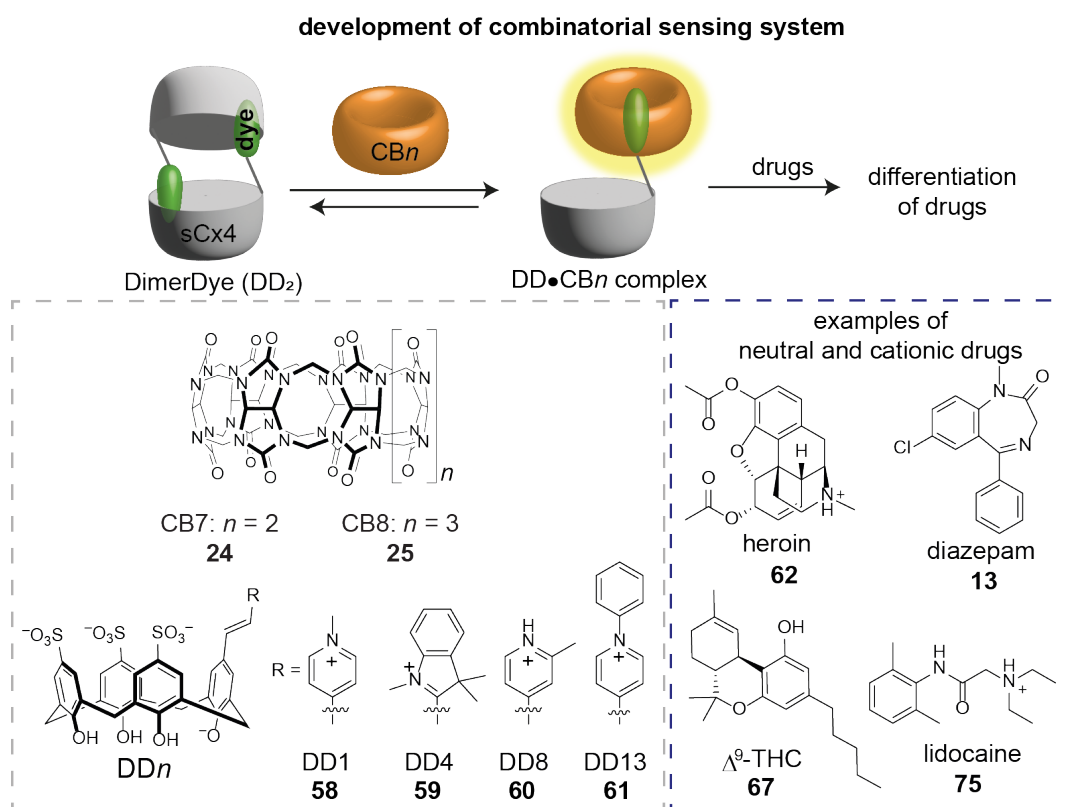


**Figure 82.** Schematic illustration and chemical structures of the developed combinatorial sensing system of hetero complexes of  $CB_7$  and  $CB_8$  with  $sCx_4$ -based DimerDye ( $DD_2$ ) sensors for the differentiation of cationic and neutral pharmaceutically-relevant agents.

In the context of the worldwide opioid-overdose epidemic due to the misuse of opioids, this conceptual study lays the foundation for further investigations and applications of  $DD \cdot CB_n$  sensor arrays in a future identification method of drug mixtures sold on “streets”. Opioids are often associated with diluents (*e.g.*, to increase sample mass) and drug adulterants that enhance the drug effect and pose extreme health risks.<sup>236</sup> Current methods such as mass spectrometry,<sup>234,355</sup> amongst others, are reliable detection methods but have costly and time-consuming due to the need for expensive instrumentation and specialized laboratory sites. Alternatively, fluorometric sensors enable rapid and on-site detection at low costs and are attractive for sensing drugs even by the layperson.<sup>356</sup> Therefore, as a continuation of the collaboration with the HOF group, the discrimination abilities of the sensor array will be tested in actual drug samples from the Vancouver Island Drug Checking Point.<sup>357</sup> It is aimed to establish a so-called “granola bar label”

in the future, which will provide a full readout of the identity and concentrations of active ingredients, solid diluents, and adulterants.

### 6.3. Development of a salt-stable rotaxane chemosensor<sup>4</sup>

Finally, after gaining deeper insights into host-guest chemistry, the main focus of this work was on the development of a new chemosensor that is stable and operational in salt-containing media and biofluids for the detection of the health-relevant biomarker tryptophan (Trp). Self-assembled chemosensors (*e.g.*, CB8•MDAP) are prone to dissociate in the presence of high amounts of salt cations or other competing compounds (*e.g.*, small bioactive compounds or proteins).<sup>7,112,166,281</sup> Preserving the advantages of CB8•dye complexes, *e.g.*, the high binding affinities due to the non-classical hydrophobic effect<sup>233</sup> and the fast signal response due to the close proximity of dye and analyte in the host cavity, a CB8-based rotaxane structure was derived as a general design concept. In the rotaxane-based chemosensing system, the signaling dye unit (*i.e.*, 2,7-diazapyrene (DAP)) was molecularly interlocked into the CB8 host cavity by installing larger stopper groups, preventing the disassembly of the CB8•dye complex (see **Figure 83**). The  $\beta$ -cyclodextrin stopper groups did not only enhance the solubility of the rotaxane but also offered circular dichroism as an additional readout and allowed the immobilization of the rotaxane on sensor chips.

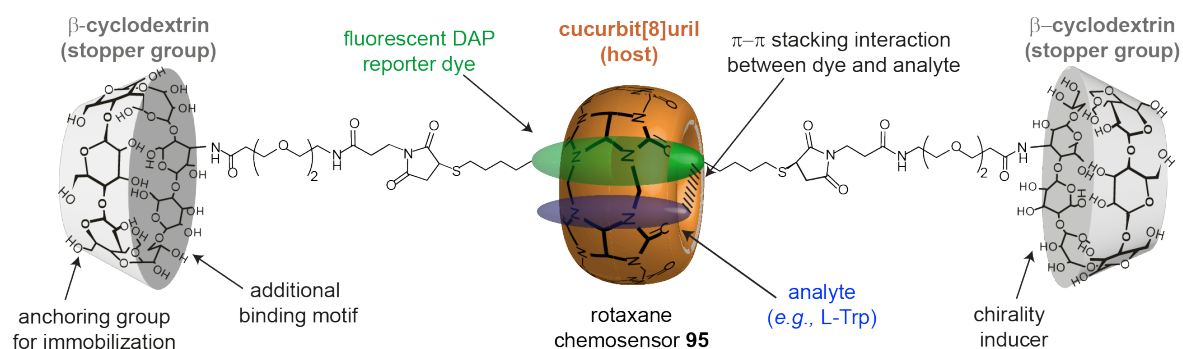


**Figure 83.** Schematic illustration of the design principle of the synthesized rotaxane chemosensor **95**.<sup>248</sup> Adapted with permission from ref. Copyright 2023 Springer Nature.

After successfully synthesizing rotaxane **95** with a CB8•dye receptor-signaling unit, **95** was characterized and tested regarding stability in salt-containing media and its sensitivity and selectivity towards biorelevant molecules. Therefore, emission-based binding studies with Trp and some of its derivatives were conducted in water and 1X PBS. The electron-deficient DAP dye and the electron-rich Trp molecule engage in a  $\pi$ - $\pi$  stacking manner concomitant with charge-

<sup>4</sup> The results have been published in a Nature Communication article: Krämer, J., Grimm, L.M., Zhong, C., Hirtz, M. & Biedermann, F. A supramolecular cucurbit[8]uril-based rotaxane chemosensor for the optical tryptophan detection in human serum and urine. *Nat. Commun.* **14**, 518 (2023).

transfer interactions, which can be observed through an emission quenching. The chemosensor showed high salt stability and remained operational for Trp sensing even in the presence of millimolar salt concentrations, indicated by the almost unchanged binding affinities in 1X PBS compared to water. Besides, the selectivity tests fortunately showed that the chemosensor is irresponsive toward aliphatic amino acids, dopamine, phenylalanine, and polyamines at their typically found concentrations in human blood serum and urine.<sup>248</sup>

Furthermore, qualitative and semi-quantitative sensing of Trp at physiologically relevant concentrations ranges ( $\sim 20 - 70 \mu\text{M}$ ) in untreated pooled blood serum samples and first sensing tests in urine samples was successful (see **Figure 84**). Trp concentrations of spiked blood serum samples in the ranges of healthy ( $\sim 50 - 70 \mu\text{M}$ ) and diseased ( $\sim 20 - 40 \mu\text{M}$ ) individuals were distinguishable from each other. The designed rotaxane chemosensor was further used for label-free enzymatic reaction monitoring, where it was possible to monitor the kinetic traces of the enzymatic digestion of BSA by pepsin in real time under physiological conditions. Real-time monitoring of enzymatic reactions is a practical challenge for existing technologies, which provide only discontinuous data points and often require time-consuming sample pre- and post-processing steps. Furthermore, it was shown that chirality sensing is possible with the rotaxane chemosensor clearly distinguishing D- and L-Trp and D- and L-Phe.<sup>248</sup> At the same time, the cyclodextrin stopper groups caused an additional chirality induction, resulting in an asymmetry of the obtained CD spectra of the enantiomers. Additionally, utilizing the cyclodextrin stopper groups as anchors, the rotaxane chemosensor was successfully immobilized on a sensor chip by our collaboration partners from the HIRTZ group at KIT, allowing the detection of sub- $\mu\text{M}$  Trp concentrations, providing a new platform for biofluid sensing.<sup>248</sup>

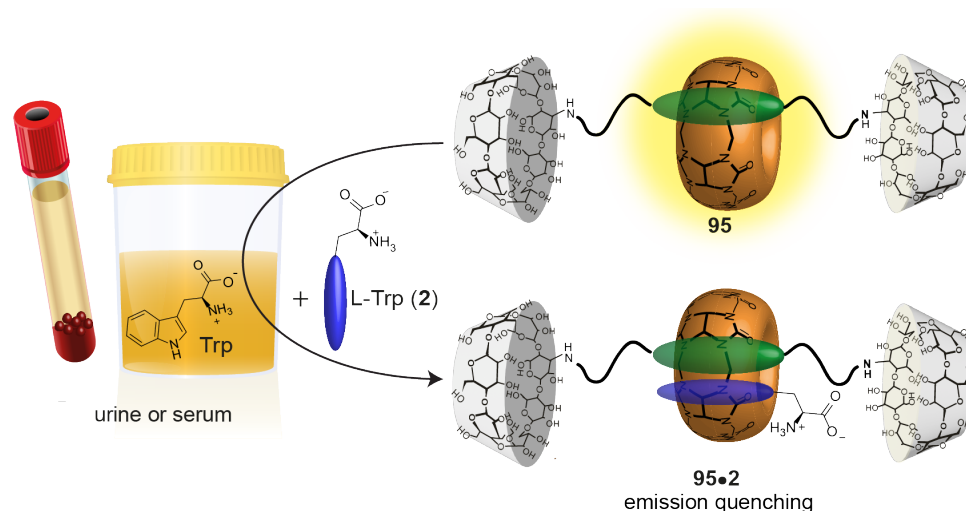


**Figure 84.** Schematic illustration of the sensing principle of tryptophan (**2**) in biofluids with the rotaxane chemosensor **95**.

The supramolecular architecture of the rotaxane solved the issue of disassembly of the non-covalent host•dye chemosensors in the presence of interferents, yielding a superior salt-stability of the rotaxane-chemosensor. In addition, this modular design allows for tuning and improving its sensitivity further towards selected analytes by modifying the dye component and stopper groups. This broadens the potential analyte spectrum of rotaxane chemosensors immensely. For instance, it would be of future interest to expand the spectroscopic range of the chemosensor by utilizing a different dye core, such as DPP, which offers a redshift of the absorbance wavelength. The absorbance shift away from the typical absorbance range of urine and serum will reduce possible interferences by the autoemission of the biofluid. Besides, loading the cyclodextrin stopper groups with an additional indicator dye could allow differential and ratiometric sensing. The second indicator dye could serve as a signal reference or be displaced by a cyclodextrin-binding analyte, expanding the sensing possibilities. The modular concept of different dyes, linkers, and stopper groups generally holds a high potential for tunability. In addition, the immobilization of the rotaxane in polymeric matrices or the development of washable stimuli-responsive hydrogels by inserting additives functionalized with multiple cyclodextrin-binding guests can also be explored in the future. The incorporation into washable hydrogels could improve the sensitivity of the system by erasing signal artifacts from the autoemission of the examined biofluid.

## 7. Experimental Section

### 7.1. Miscellaneous

#### 7.1.1. Materials and equipment<sup>144,248</sup>

##### Nuclear magnetic resonance (NMR) spectroscopy

NMR spectra were collected on a BRUKER Avance 500 and BRUKER Avance Neo 500 spectrometer (<sup>1</sup>H NMR: 500 MHz; <sup>13</sup>C NMR: 126 MHz) at room temperature. The compounds were dissolved in the deuterated solvent and filled into an NMR glass tube. The chemical shift  $\delta$  is stated in parts per million (ppm) with respect to an internal standard. For NMR analysis, the residual signal of the solvent was used as a secondary reference:<sup>358</sup> D<sub>2</sub>O (<sup>1</sup>H:  $\delta$  = 4.90 ppm), CDCl<sub>3</sub> (<sup>1</sup>H:  $\delta$  = 7.26 ppm, <sup>13</sup>C:  $\delta$  = 77.2 ppm). <sup>1</sup>H NMR spectra were analyzed according to first order, <sup>13</sup>C NMR spectra were <sup>1</sup>H-decoupled, and analysis of the <sup>13</sup>C NMR spectra followed the distortion-less enhancement by polarization transfer (DEPT) technique. NMR assignment was achieved by analysis of two-dimensional NMR spectra (COSY, HMBC, and HSQC). For symmetrical signals, the midpoint of the signal is given, whereas, for multiplets, the range of the signal region is provided. The abbreviations for the multiplicities of the signals are given as follows: s = singlet, d = doublet, t = triplet, quart = quartet, quin = quintet, m = multiplet. All coupling constants (J) are stated as modulus in Hertz (Hz).

##### Diffusion-ordered spectroscopy (DOSY)

DOSY data were collected on a BRUKER AM 400 (400 MHz) at 25 °C with the help of JOEL MONTI. Chemical shifts  $\delta$  are stated in parts per million (ppm) and calibrated to D<sub>2</sub>O as an internal standard. DOSY experiments were performed using a LED-bipolar gradient paired with two spoil gradients (ledbpgp2s), with 16 incremental steps in the gradient strength, ramped from 2 % to 98 % of the maximum gradient strength. 16 Scans were recorded per increment step. The gradient pulse length  $\delta/2$  (p30) and diffusion delay  $\Delta$  (d20) were specifically optimized and set to 1.8 ms ( $\delta$  = 3.6 ms) and  $\Delta$  = 79.9 ms, respectively. The spectra were calibrated and phased using TopSpin 3.1. The pseudo-2D DOSY plots were computed using BRUKER Dynamic Center, and the intensity decay was fitted.

### **Mass spectrometry (ESI-MS)**

Electrospray ionization mass spectrometry (ESI-MS) experiments were performed on a BRUKER micrOTOF-Q (208 - 320 Vac, 50/60 Hz, 1800 VA) mass spectrometer, which was equipped with an On-line NanoElectrospray ion source. Interpretation of the spectra was made by molecular peaks  $[M]^{n+}$  or peaks of the protonated molecule  $[M+H]^{n+}$ , which are shown with their mass-to-charge ratio ( $m/z$ ). The following solvents were used for sample preparation: H<sub>2</sub>O, MeOH, and H<sub>2</sub>O:1 % formic acid.

### **Absorbance spectroscopy**

Absorbance spectra were recorded on a JASCO V-730 double-beam UV-Vis spectrophotometer equipped with an automatic stirring unit. Spectra were corrected for baseline using JASCO's Spectra Manager Software Vers. 2 during the measurement.

### **Fluorescence spectroscopy**

Steady-state emission spectra were recorded on an FP-8300 fluorescence spectrometer from JASCO with a 450 W xenon arc lamp, emission monochromators, double-grating excitation, and a temperature-controlled cell holder (STR-812) with an automatic stirring unit. Emission-based titration experiments were carried out manually or by an ATS-827 automatic titration unit at 25 °C if not stated differently, and all cuvettes were equipped with a magnetic stirrer allowing rapid mixing during the titration. Emission spectra were normalized by division with the maximum emission intensity of the spectra. For the determination of binding affinities, the normalized emission intensity was fitted according to a 1:1 binding model using a least square fit.

### **Dynamic light scattering (DLS)**

Dynamic light scattering (DLS) experiments were carried out on a ZetaSizer Nano instrument from MALVERN. The sample solution (150  $\mu$ M in ultrapure water) was heated in 5 °C temperature steps in a temperature range of 20 to 50 °C following the automated heating cycle of the instrument. The wavelength of the laser light used for the light scattering experiments was set to 633 nm, and the light intensity was measured at a fixed angle (173°).

### **Electronic circular dichroism (ECD) spectroscopy**

Electronic circular dichroism (ECD) spectra were recorded on a J-1500 CD spectrometer from JASCO, equipped with a Peltier-thermostated cell holder and an automatic stirring unit. All ECD spectra were corrected for their baseline. All spectra were recorded at 25 °C.

### **Microwell plate reader**

Microwell plate-based measurements were conducted on multimode microplate readers from PERKIN ELMER (EnSight™), BMG LABTECH (CLARIOstar® Plus) and AGILENT, former BIOTEK (Cytation-5). All instruments were equipped with a monochromator for emission measurement (top- and bottom-reading) and filter- and monochromator-based absorbance detection and temperature control.

### **High-performance liquid chromatography (HPLC)**

HPLC experiments were carried out on a JASCO LC-2000Plus HPLC system equipped with a UV-2075 UV-Vis detector, an FP-920 fluorescence detector, and a AS-4050 autosampler for analytical injection volumes. Analytical HPLC experiments were performed on a KROMASIL®100 C18 5 µm LC column (250×4.6 mm, AGELA) with a flow rate of 1.0 mL/min using the autosampler with an injection volume of 20 µL per sample. Preparative HPLC experiments were conducted on a KROMASIL® 100 C18 5 µm LC precolumn (50×20 mm, AGELA) and a KROMASIL® 100 C18 5 µm LC preparative column (250×50 mm, AGELA) with a flow rate of 10 mL/min. Crude samples were dissolved in a water/ACN mixture (v/v = 4/1). HPLC chromatograms were analyzed using ChromNav Ver.2 data analysis software from JASCO. Note: At higher concentrations of the rotaxane, a small peak shoulder in the chromatogram occurred, which can be linked to the formation of aggregates. The re-injection of the main peak fraction to HPLC analysis led to a similar HPLC chromatogram, suggesting that impurities do not cause the small peak shoulder.

### **pH Meter**

The pH of buffer solutions was measured with a FiveEasy Plus pH meter from METTLER TOLEDO. For pH adjustments, hydrochloric acid or sodium hydroxide solution was used.

### **Centrifuge**

A centrifuge by SIGMA, type 2-16KL was used. Centrifugation was carried out at room temperature or 4 °C for the serum deproteinization with a speed of 10 000 rpm.

## Balances

Samples were weighed in mass  $> 1.0$  g at a SARTORIUS TE214S balance as well as METTLER TOLEDO XS204 balance were used. Samples were masses  $< 1.0$  g were needed a SARTORIUS SE2-F balance was used.

## Lyophilization

Aqueous solutions or dispersions were freeze-dried on a ZIRBUS TECHNOLOGY VaCo2 and a CHRIST Alpha 3-4 LSCbasic lyophilization plant.

## Cuvettes and microwell plates

For the emission and absorbance-based measurements, UV transparent disposable cuvettes with four transparent sides by BRAND GMBH with a diameter of 10 mm (Cat No 759128) with a spectroscopic cut-off at 240 nm were utilized. ECD measurements were conducted in Quartz glass cuvettes with a diameter of 10 mm. For the microplate reader, black opaque OptiPlate<sup>TM</sup>-96 polystyrene microwell plates with clear bottoms from PERKIN ELMER and black-walled Thermo Scientific<sup>TM</sup> Nunc 386 microwell plates with clear bottom from THERMOFISHER SCIENTIFIC were used.

## Tip sonicator

Sonication of CB8 solutions and rotaxane chemosensor solutions was carried out with a UP200S tip sonicator (working frequency  $30 \pm 1$  kHz, energy density  $\geq 300$  W cm<sup>-2</sup>) by HIELSCHER.

## Chemicals and solvents

All chemicals used for synthesis and solvents were purchased from ACROS ORGANICS, ALFA AESAR, FLUKA, MERCK, SIGMA ALDRICH, and TCI with the minimum quality label “for synthesis” and were used without further purification. Analytes were purchased from ALFA AESAR, TCI, and SIGMA ALDRICH at the highest grade available and used as received. Illicit drug samples were purchased from SIGMA ALDRICH and received as 1mg/ml solution in methanol or acetonitrile. Cucurbit[*n*]urils were either purchased from STREM CHEMICALS or synthesized following known literature procedures.<sup>359,360</sup> Dry solvents were stored over molecular sieves (3 Å or 4 Å) to ensure their dryness over a long time. Deuterated solvents were purchased from ACROS ORGANICS and VWR CHEMICALS. Buffer solutions were prepared following standard protocols, and adding sodium hydroxide or hydrochloric acid solutions adjusted the pH value. 1X PBS (pH 7.4) was

prepared by dissolving one buffer tablet from CRUZ CHEM in 0.5L ultrapure water. No further pH adjustment was made. Pooled human and bovine blood serum samples were purchased from MERCK, BIOWEST, SEQENS, and CYTIVA. Pepsin (from porcine gastric mucosa powder) was purchased from SIGMA ALDRICH. Bovine serum albumin (BSA) was bought from BIOWEST, and fatty acid-free human serum albumin (HSA) protein was purchased from ALFA AESAR. Surine (synthetic urine) was purchased from CERILLIANT. Ultrapure deionized water was obtained from a SARTORIUS ARIUM® Pro Di water purification system with ASTM Type 1 water quality. All analyte and chemosensor stock solutions were prepared in ultrapure water or 1X PBS and stored at 4 °C for one week. The weekly fresh preparation of analytes and chemosensor stock solutions ensured the reproducibility of the measurements.

### Urine samples

Urine samples were exclusively used as matrices for Trp spiking and collected from voluntary healthy adult donors. Informed consent<sup>361</sup> was obtained from all participants. The sample collection and analysis were performed in blinded experiments (three samples were randomly selected out of five samples), and urine samples were used within one day after excretion. All procedures performed in this study followed the formal statement of ethical principles published by the WORLD MEDICAL ASSOCIATION in the Declaration of Helsinki.<sup>362</sup>

## 7.2. Preparative work<sup>144,248</sup>

### 7.2.1. General procedures and information

#### Concentration determination of cucurbit[*n*]uril stock solutions

The concentrations of CB7 and CB8 stock solutions were determined by emission-based measurements using the complexation of a dye by the macrocycle. The concentration of the CB7 stock solution was determined by fluorescence titration against MDAP by exciting the sample at  $\lambda_{\text{ex}} = 343$  nm and recording the emission intensity at  $\lambda_{\text{em}} = 454$  nm. The concentration of the CB8 stock solution was determined by fluorescence titration against MPCP by exciting the sample at  $\lambda_{\text{ex}} = 368$  nm and collecting the emission intensity at  $\lambda_{\text{em}} = 531$  nm. Host concentrations were obtained from the intersection of the two linearly fitted parts of the signal intensity curve: (i)  $c(\text{host}) < c(\text{dye})$  associated with a steady increase in emission with each titration step as maximum complexation has not yet been reached, (ii)  $c(\text{host}) > c(\text{dye})$  associated with a plateau when

maximum complexation of the dye by the host is reached and further addition of host does not result in any further increase in emission intensity.

### Concentration determination of dye and analyte stock solutions<sup>144</sup>

Dye and analyte stock solutions were prepared in ultrapure water if not stated otherwise and stored in the fridge at 4 °C. The concentration determination of the stock solutions was determined by UV-Vis titration based on their extinction coefficient (see **Table 11**) using Lambert-Beer's law.<sup>363</sup>

**Table 11.** Absorbance maxima ( $\lambda_{\text{abs}}^{\text{max}}$ ) and molar extinction coefficients ( $\epsilon_{\lambda(\text{max})}$ ) of the dyes and analytes used for the concentration determination of their stock solutions by UV-Vis titration measurements.<sup>144</sup>

compound	$\lambda_{\text{abs}}^{\text{max}}$ (nm)	$\epsilon_{\lambda(\text{max})}$ (M <sup>-1</sup> cm <sup>-1</sup> )	ref.
BC (38)	344	22300	364,365
dopamine (4)	280	2670	366
IAA (97)	280	6000	367
indole (96)	278	5670	368
MDAP (40)	393	7800	369
MPCP (111)	335	7111	216
nandrolone (55)	248	17300	this work
L-Phe (1)	257	195	370
2,6-TNS (56)	317	18900	this work
tryptamine (6)	279	5660	371
L-Trp (2)	279	5590	372

### Concentration determination of host•guest complexes by NMR<sup>144</sup>

The concentration determination of the insoluble guests estradiol, cholesterol, and progesterone were carried out *via* <sup>1</sup>H NMR measurements in D<sub>2</sub>O using the dimethyl sulfone singlet signal at 3.14 ppm as an internal standard.

For the measurement, the host•guest stock solution was prepared in D<sub>2</sub>O in a 1:2 ratio and sonicated for 10 min using the tip sonicator. Subsequently, 250 μL of the solution was mixed with 250 μL of a dimethyl sulfone stock solution, of which the concentration was known. The obtained spectra were phase and baseline corrected and calibrated to the solvent peak of D<sub>2</sub>O. The signal of dimethyl sulfone at 3.14 ppm was used as a reference with a total integral of six protons. The integration of host signals and aliphatic guest signals allowed the concentration determination of each compound dissolved in the D<sub>2</sub>O. The by NMR obtained concentrations were used for the fitting of the binding curve.

### Preparation of guest displacement assays

For GDA experiments, information on the solubility of the selected guests and dyes was collected before the preparation of the experiment. **Table 12** gives the absorbance and emission maxima of the used dyes and corresponding host•dye complexes. The solubility of the guests and dyes used for Section 5.1.2 is shown in **Table 13**.

**Table 12:** Photophysical properties of used dyes and corresponding host•dye complexes.<sup>144</sup>

dye	host	$\lambda_{\text{abs}}^{\text{max}}$ (nm) <sup>[a]</sup>	$\lambda_{\text{em}}^{\text{max}}$ (nm) <sup>[b]</sup>
2,6-TNS (56)	–	316	404
	CB7	322	398
	β-CD	316	463
BC (36)	–	432	540 <sup>[c]</sup>
	CB7	430	500
	CB8	425	532
MDAP (40)	–	416	425
	CB7	423	431
warfarin <sup>[d]</sup> (57)	–	308	402
	HSA	308	391

If not stated differently, all measurements were conducted in ultrapure water at 25 °C. <sup>[a]</sup> Maximum of the lowest-energy band. <sup>[b]</sup> Maximum of the highest-energy band. <sup>[c]</sup> Almost no emission signal is detectable. <sup>[d]</sup> Measured in 1X PBS.

**Table 13.** Solubility of selected hosts and guests in water at 25 °C.<sup>144</sup>

<b>compound</b>	<b>solubility in water</b>	<b>ref.</b>
CB7 (24)	~ 20.0 – 30.0 mM	94
CB8 (25)	< 0.02 mM	94
$\beta$ -CD (29)	~ 16.3 mM	300
HSA (47)	~73.0 $\mu$ M (50.0 mg/mL)	SIGMA ALDRICH
ethanol (48)	miscible	-
<i>iso</i> -propanol (49)	miscible	-
<i>n</i> -butanol (50)	miscible	-
<i>tert</i> -butanol (51)	miscible	-
1-AdOH (26)	> 2.00 mM	373
cadaverine (9)	soluble	this work
PBZ (aq. solution) (53)	~ 145 $\mu$ M	374
nortestosterone (55)	~ 810 $\mu$ M	375
estradiol (11)	~ 9.00 $\mu$ M	375
progesterone (12)	~ 33.0 $\mu$ M	375
cholesterol (52)	< 51.7 nM	376
warfarin (aq. solution) (57)	~ 12.8 $\mu$ M	377
BC (38)	~ 13.2 mM	378
MV (54)	~ 2.50 M	379
MDAP (40)	soluble	this work
2,6-TNS (56)	> 4.00 mM	this work

### Examination of DimerDye•CB $n$ complex formation, drug detection and discriminant analysis

The titration experiments of CB7 and CB8 into the different DimerDye (DD) solutions were conducted in 96-well plates with a total volume of 250  $\mu$ L containing 10 - 20  $\mu$ M DD in sodium phosphate buffer (8.4 mM, pH 7.4) and different amounts of CB7 or CB8 (0.5 - 100  $\mu$ M). Full spectra were recorded in triplicates measurements. The measured raw data was blank corrected.

The discriminant analysis of illicit drugs and adulterants was conducted in 384-well plates with a total volume of 70  $\mu$ L for each well. A solution of each DD•CB $n$  combination with 10.5  $\mu$ M DD and 21  $\mu$ M CB $n$  in sodium phosphate buffer (10 mM, pH 7.4) was prepared and subsequently mixed with 105  $\mu$ M of different drugs in water containing 2% MeOH (final buffer concentration: 8.4 mM). For each DD•CB $n$  combination (**M**), each drug of its drug class (**N**) was mixed separately, giving **M x N** mixed samples per experiment. The mixtures were added to a 384-microwell plate with every DD•CB $n$  combination in a separate well, and the absorbance and emission of every DD•CB $n$ •drug combination were measured at a selected wavelength in twelve wells (equals twelve replicates), along with 2 buffer blank measurements. The excitation wavelength was selected at each DD's absorbance maximum and are listed in **Table 14**. The measured raw data was blank-corrected by subtracting the solvent blank from each DD•CB $n$ •drug measurement. Furthermore, the two highest and lowest data values were systematically excluded for further discriminant analysis. The wavelengths of absorbance and fluorescence, which allowed for the differentiation of drugs and adulterants, were carefully chosen to conduct principal component analysis (PCA). The objective was to minimize the number of observations required. PCA correlation plots, accompanied by confidence ellipses (95%) and loading vectors, were skillfully rendered on sample sets comprising eight replicates. This feat was accomplished using OriginPro 2022b. Principal component analysis App (version: 1.50, file name: PCAC.opx).

**Table 14.** The excitation wavelength for each DimerDye.

DimerDye	$\lambda^{\text{ex}}$ (nm)
DD1 (58)	380
DD4 (59)	480
DD8 (60)	380
DD13 (61)	420

**Examination of the selectivity of the rotaxane chemosensor<sup>248</sup>**

The selectivity of the rotaxane chemosensor was determined from the emission response at  $\lambda_{em} = 450$  nm ( $\lambda_{ex} = 393$  nm) of the chemosensor upon adding aliquots of bioorganic analytes in a microplate reader format. Therefore, 96-microwell plates were filled with 100  $\mu$ L of 3.0  $\mu$ M chemosensor in 1X PBS. Then, the analyte stock solutions were added to the microwells and diluted with 1X PBS buffer to achieve a final volume of 300  $\mu$ L per well. Each well was thus equipped with a solution mixture of 1.0  $\mu$ M for rotaxane, and 100  $\mu$ M, 500  $\mu$ M, or 1.0 mM for the tested analyte. The obtained emission intensities were blank corrected, referenced to a 1.0  $\mu$ M rotaxane solution, and averaged over the repetitions performed ( $n \geq 4$ ).

**Influence of aliphatic analytes on Trp binding<sup>248</sup>**

Guest displacement measurements were used to evaluate the influence of non-binding or weakly binding analytes such as L-arginine on the binding interaction of rotaxane chemosensor with Trp.<sup>144</sup> Therefore, microwell plates were equipped with 150  $\mu$ L of a pre-equilibrated mixture of 2.0  $\mu$ M rotaxane and 250  $\mu$ M of the potential interferent in 1X PBS, and the emission intensity was monitored at 393 nm ( $\lambda_{em} = 450$  nm) before and after the addition of 0 - 581  $\mu$ M Trp.

**Deproteinization of blood serum samples<sup>248</sup>**

The commercially purchased blood serum samples with unknown Trp concentrations were deproteinized by adding an equal volume of 624 mM perchloric acid solution, followed by careful mixing. The samples were stored on ice at 0 °C for 10 minutes to complete the precipitation and centrifuged at 10 000 rpm at 4 °C for 10 minutes. Afterward, the supernatant was separated from the precipitated protein and filtrated for HPLC measurements.

**Preparation of urine samples<sup>248</sup>**

Urine samples with unknown Trp concentrations were used within the day of excretion. Therefore, the pH of the samples was adjusted to pH 2.0 with 2.0 M hydrochloric acid. In order to remove suspended particles, the urine samples were centrifuged at 10 000 rpm at 4 °C for 10 min, and the supernatant was separated from the precipitate. Then the urine samples were mixed with an EDTA stock solution to reach 5.0 mM of EDTA in urine (117  $\mu$ L of 128 mM EDTA in 2283  $\mu$ L urine) and subsequently filtrated.

### HPLC-based L-Trp quantification in serum and urine samples<sup>248</sup>

The initial concentration of Trp in different serum samples and urine samples was quantified following literature procedures,<sup>257,380</sup> using standard HPLC methods.

#### *L-Trp in blood serum samples*

Eight different Trp concentrations ( $c_{\text{final}} = 1, 5, 10, 25, 40, 55, 70,$  and  $100 \mu\text{M}$ ) prepared using a  $4.9 \text{ mM}$  standard stock solution of L-tryptophan in  $312 \text{ mM}$  perchloric acid were used to establish a calibration curve.  $10 \%$  Acetonitrile in water was used as a mobile phase with a flow rate of  $1.0 \text{ mL/min}$ , and an injection volume of  $20 \mu\text{L}$  was used for each measurement. Triplicate measurements of each Trp concentration were conducted. The calibration curve was obtained by plotting the integrated peak area of the fluorescence signal at  $353 \text{ nm}$  ( $\lambda_{\text{ex}} = 285 \text{ nm}$ ) against the standard Trp concentrations. The slope and regression parameters were determined by linear fitting of the curve. For the Trp quantification in serum sample,  $20 \mu\text{L}$  of the deproteinized serum sample was injected into the HPLC system for analysis. The integrated peak areas of the chromatograms (fluorescence was recorded for  $\lambda_{\text{ex}} = 285 \text{ nm}$ ,  $\lambda_{\text{em}} = 353 \text{ nm}$ ) were analyzed according to the following equation for concentration determination of Trp in the serum samples.

$$\text{Trp in serum } (\mu\text{M}) = \frac{(\text{peak area of Trp in the serum sample})}{(\text{peak area of Trp in the standard solution})} \times 2 \quad \text{Eq. 36}$$

Each serum sample's triplicate measurements were performed, and the integrated peak areas were averaged.

#### *L-Trp in urine samples*

Six different L-Trp concentrations ( $c_{\text{final}} = 5, 10, 25, 40, 55,$  and  $70 \mu\text{M}$ ) were used for the calibration curve of Trp in synthetic urine (*i.e.*, surine). Triplicate measurements were performed for each Trp concentration using a gradient elution program. The mobile phase consisted of eluent 1 ( $20 \text{ mM}$  sodium acetate,  $30 \text{ mM}$  acetic acid, and  $3 \%$  MeOH) and eluent 2 ( $20 \text{ mM}$  sodium acetate,  $20 \text{ mM}$  acetic acid,  $10 \%$  ACN, and  $10 \%$  MeOH) at a flow rate of  $1.0 \text{ mL/min}$  and an injection volume of  $20 \mu\text{L}$ .<sup>380</sup> The calibration curve was obtained by plotting the intensity height of the received fluorescence signal at  $340 \text{ nm}$  ( $\lambda_{\text{ex}} = 295 \text{ nm}$ ) against the standard concentration and linear fitting given the slope and regression parameters. Three urine samples with unknown Trp concentrations were determined immediately on the day of excretion after pre-treatments (pH adjustment and EDTA). Therefore,  $20 \mu\text{L}$  of the filtrated sample solution was analyzed using HPLC. The obtained signals of each urine sample were used for the concentration determination

of Trp by integrating the peak height of the fluorescence signal at 340 nm according to the following equation.

$$\text{Trp in urine } (\mu\text{M}) = \frac{(\text{peak height of Trp in the urine sample})}{(\text{peak height of Trp in the standard solution})} \quad \text{Eq. 37}$$

At least duplicate measurements were conducted for each urine sample, and the intensity heights of the Trp signal were averaged.

### **Microplate reader assay for L-Trp detection in deproteinized blood serum samples<sup>248</sup>**

Quantitative L-Trp determination of four pooled deproteinized blood serum samples was performed in a microplate reader format. First, a calibration curve was obtained by measuring the quenching intensity of the stepwise addition of Trp aliquots (0 - 100  $\mu\text{M}$ ) to 10  $\mu\text{M}$  of rotaxane **95** in a deproteinized serum sample that initially contained less than 1  $\mu\text{M}$  of Trp (st-dp human serum sample, see HPLC quantification). The measurements were conducted in twelve replicates in total, of which the two highest and two lowest replicates for each addition were systematically excluded for the calibration curve (*i.e.*, analysis with  $n = 8$  replicates). Each deproteinized serum sample was measured in five replicates before (autoemission of serum) and after mixing with 10  $\mu\text{M}$  of the rotaxane chemosensor. The recorded emission intensities ( $I$ ) were corrected for the autofluorescence emission of each serum and the dilution factor. The Trp concentrations of the serum samples were determined by comparing the emission quenching ratio to that of an independently obtained calibration curve.

### **Microplate reader assay for L-Trp detection in untreated blood serum samples<sup>248</sup>**

Semi-quantitative emission quenching (EQ) of the rotaxane chemosensor in the presence of two different untreated pooled blood serum samples (*i.e.*, non-deproteinized serum) was determined using 10  $\mu\text{M}$  of rotaxane in a plate reader format at 450 nm ( $\lambda_{\text{ex}} = 393$  nm). Initially, the wells of a 96-well plate were filled with 150  $\mu\text{L}$  of serum solution per well to obtain the autoemission of the serum ( $I_0$ ). Then, the emission intensity ( $I_1$ ) was obtained by adding 1.95  $\mu\text{L}$  of a 780  $\mu\text{M}$  rotaxane stock solution to each well to reach a concentration of 10  $\mu\text{M}$  of rotaxane **95**. In the next step, the serum-chemosensor samples were spiked eight times with a stock Trp solution to achieve L-Trp concentrations ranging from 5 to 70  $\mu\text{M}$ . After mixing, the emission intensity was acquired for each titration step ( $I_2$ ). Finally, the total emission quenching of rotaxane **95** was obtained by adding an excess of indole (300  $\mu\text{M}$ ) to each well ( $I_3$ ). At least five repetitions were conducted for each serum sample.

**Microplate reader assay for quantitative L-Trp determination in urine samples<sup>248</sup>**

The emission quenching (EQ) of rotaxane **95** in the two different urine samples was determined analogously to the measurements in serum. Six repetitions were conducted for each urine sample. Two values for each sample were systematically excluded from the analysis due to errors in sample preparation.

**Immobilization of rotaxane on glass surfaces<sup>248</sup>**

The immobilization and the subsequent sensing experiments were conducted by CHUNTING ZHONG and will only be briefly explained in the following:

Suitable isocyanate for immobilization was produced by activating a pre-cleaned SiO<sub>2</sub>-glass surface with oxygen plasma (10 sccm O<sub>2</sub>, 0.2 mbar, 100 W, 2 min, ATTO system, DIENER ELECTRONICS, Germany) in order to obtain a hydroxylated SiO<sub>2</sub>-OH layer. Then, the SiO<sub>2</sub>-OH surface was immersed in 1 mg/mL 4,4'-diisocyanato methyldibenzol (MDI) containing 1 μL/mL dibutyltin dilaurate (DBTDL) as a catalyst in anhydrous DMSO at 80 °C for 24 h. Finally, the SiO<sub>2</sub>-NCO-substrate was rinsed with acetone for 2 min and dried with N<sub>2</sub>. Then, 0.5 μL of rotaxane ink (3 mg/mL in DMSO containing 10% (v/v) DBTDL and 10% (v/v) PEG 600) was applied to the reservoir of a microchannel cantilever<sup>381</sup> (SPT-SC10S, BIOFORCE NANOSCIENCES), mounted to the lithography setup (NLP2000, NANOINK), and spotted for defined durations (~0.5 - 1 s) at a controlled humidity of 40%. After printing, the substrate was heated to 80 °C for 24 h, washed with EtOH, and dried with N<sub>2</sub>. Data analysis was performed using NIS-Elements.

**Analyte detection with rotaxane microarrays.<sup>248</sup>**

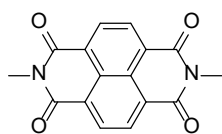
Analyte solutions were prepared in 1X PBS (pH 7.4), st-dp human blood serum (c(Trp) < 1 μM), or in 10 mM HEPES buffer (pH 7.0). The rotaxane-patterned substrates were covered with 20 μL analyte solution for 5 min, washed with water, and dried with N<sub>2</sub>. Fluorescence imaging was performed on a NIKON Eclipse Ti2 inverted fluorescence microscope (NIKON, Germany) equipped with an Intensilight illumination, a NIKON DS Qi2 camera, and a DAPI filter set (DAPI-U HQ, NIKON, Germany) with an excitation filter of 395/25 nm and a barrier filter of 460/50 nm. All data are expressed as mean ± standard deviation of three independent measurements. All concentration-dependent rotaxane microarray printing measurements were done once per concentration or dilution.

**Monitoring of label-free enzymatic reactions in real-time<sup>248</sup>**

The enzymatic digestion of the protein bovine serum albumin (BSA) by the enzyme pepsin was monitored in real-time by intensity signal changes of the chemosensor emission. In 1X PBS (pH 2.0), the stock solutions of BSA and rotaxane chemosensor were mixed to reach a final concentration of 100  $\mu\text{g/mL}$  BSA (**110**) and 4.5  $\mu\text{M}$  of the chemosensor and equilibrated for 100 sec. Then the emission intensity at 450 nm ( $\lambda_{\text{ex}} = 393$  nm) was monitored over time. Various amounts of a pepsin stock solution (in 1X PBS, pH 2.0) were added to achieve pepsin concentrations ranging from 0 to 70  $\mu\text{g/mL}$ , and time-resolved fluorescence traces were monitored for 20 min. A BSA-chemosensor mixture without the enzyme addition and the enzyme addition to the chemosensor solution without BSA were collected as control measurements.

### 7.3. Synthetic procedures<sup>144,248</sup>

#### 2,7-Dimethylbenzo[*lmn*][3,8]phenanthroline-1,3,6,8(2*H*,7*H*)-tetraone<sup>297</sup> (**79**)



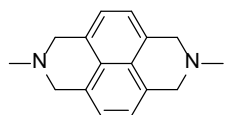
A 250 mL three-neck flask equipped with a reflux condenser was filled with 120 mL aqueous methylamine (40.0 wt%, 1.39 mol, 74.6 eq) and 5.00 g of 1,4,5,8-naphthalene tetracarboxylic dianhydride (**78**) (18.6 mmol, 1.00 eq) was slowly added under vigorous stirring. The orange-brown solution was refluxed for 3 h, cooled to room temperature, and stirred for two days. The formed precipitate was collected by filtration, washed with 100 mL methanol, and dried *in vacuo*. The product was isolated as a nude-colored solid with a yield of 3.09 g (10.5 mmol, 56 %).

<sup>1</sup>H NMR (500 MHz, CDCl<sub>3</sub>, 298 K):  $\delta$  (ppm) = 8.78 (s, 4H, *H*-Ar), 3.61 (s, 6H, CH<sub>3</sub>). — <sup>13</sup>C NMR (126 MHz, CDCl<sub>3</sub>, 298 K):  $\delta$  (ppm) = 163.3 (C<sub>q</sub>), 131.2 (C<sub>q</sub>), 126.8 (C<sub>q</sub>), 126.8 (CH), 27.6 (CH<sub>3</sub>).

#### Chemotion.org:

<https://dx.doi.org/10.14272/reaction/SA-FUHFF-UHFFFADPSC-FERUHHWVLZ-UHFFFADPSC-NUHFF-NUHFF-NUHFF-ZZZ.1>

#### 2,7-Dimethyl-1,2,3,6,7,8-hexahydrobenzo[*lmn*][3,8]phenanthroline<sup>298</sup> (**80**)

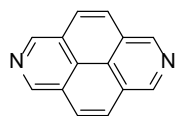


A 250 mL three-neck flask was loaded with 5.30 g of anhydrous AlCl<sub>3</sub> (39.8 mmol, 2.34 eq) which was suspended in 250 mL dry THF. Under ice bath cooling, 4.50 g of LiAlH<sub>4</sub> (120 mmol, 7.05 eq) was added stepwise to the stirring suspension. After the slow addition of 5.00 g of 2,7-dimethylbenzo[*lmn*][3,8]phenanthroline-1,3,6,8(2*H*,7*H*)-tetraone (**79**) (17.0 mmol, 1.00 eq), the solution turned red and was heated to reflux. The reaction mixture changed its color to green after 4 h and was cooled to room temperature. The quenching with 400 mL of ice water caused precipitation of a brown-grey solid, which was filtered off and dried *in vacuo*. The solid was transferred into a soxhlet extractor and extracted with 1.50 L chloroform for one day. The extract was evaporated and recrystallized from 100 mL pyridine, yielding 3.10 g of a yellow solid (12.9 mmol, 76 %).

<sup>1</sup>H NMR (500 MHz, CDCl<sub>3</sub>, 298 K):  $\delta$  (ppm) = 7.12 (s, 4H, *H*-Ar), 3.88 (s, 8H, CH<sub>2</sub>), 2.57 (s, 6H, CH<sub>3</sub>). — <sup>13</sup>C NMR (126 MHz, CDCl<sub>3</sub>, 298 K):  $\delta$  (ppm) = 131.8 (C<sub>q</sub>), 127.4 (C<sub>q</sub>), 121.7 (CH), 58.7 (CH<sub>2</sub>), 45.6 (CH<sub>3</sub>).

#### Chemotion.org:

<https://dx.doi.org/10.14272/reaction/SA-FUHFF-UHFFFADPSC-VHNSKBKZGH-UHFFFADPSC-NUHFF-NUHFF-NUHFF-ZZZ>

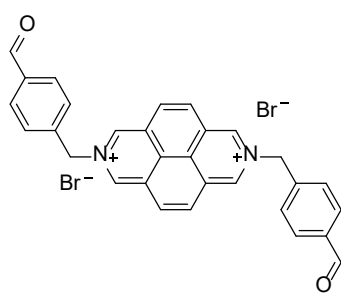
**Benzo[*lmn*][3,8]phenanthroline<sup>298</sup> (DAP) (81)**

In a 250 mL round bottom flask equipped with a mechanical stirring bar, 7.70 g of selenium (97.5 mmol, 19.4 eq) and 1.20 g of 2,7-dimethyl-1,2,3,6,7,8-hexahydrobenzo[*lmn*][3,8]phenanthroline (**80**) (5.04 mmol, 1.00 eq) were stirred at 265 °C for 4 h in an isolated fume hood. The black viscous mixture was heated to 300 °C for 1 h and then cooled to room temperature. Next, 100 mL of 1 M aqueous HCl was added and stirred under reflux for 30 minutes. This procedure was repeated three times in total, and after each boiling, the black solid was filtered off. The filtrates were combined, and aqueous NaOH (5 M) was added until pH 12.0 was reached. The formed yellow precipitate was separated by filtration, dissolved in 1 M HCl, and precipitated again with 1 M NaOH. This procedure was repeated twice. Finally, the obtained precipitate was filtered off and dried *in vacuo*. The product was isolated as a yellow solid with a yield of 720 mg (3.52 mmol, 70 %).

<sup>1</sup>H NMR (500 MHz, CDCl<sub>3</sub>): δ (ppm) = 9.48 (s, 4H, *H*-Ar), 8.17 (s, 4H, *H*-Ar). — <sup>13</sup>C NMR (126 MHz, CDCl<sub>3</sub>): δ (ppm) = 145.5 (CH), 126.5 (C<sub>q</sub>), 126.5 (C<sub>q</sub>), 126.0 (CH).

**Chemotion.org:**

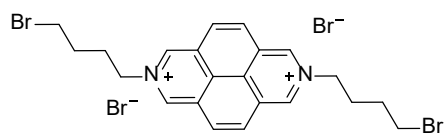
<https://dx.doi.org/10.14272/reaction/SA-FUHFF-UHFFFADPSC-ZPIPUFJBRZ-UHFFFADPSC-NUHFF-NUHFF-NUHFF-ZZZ.1>

**2,7-Dibenzylbenzo[*lmn*][3,8]phenanthroline-2,7-dium dibromide (82)**

Under nitrogen atmosphere, 70.0 mg DAP (**81**) (343 μmol, 1.00 eq) was dissolved in 8.00 mL dry DMF. Subsequently, 220 μL of 4-(bromomethyl) benzaldehyde (218 mg, 1.10 mmol, 3.20 eq) was added, and the reaction solution was stirred at 70 °C for 2 days. The yellow precipitate was filtered off, washed with DMF, and dried under reduced pressure. The product was isolated as a yellow solid with a yield of 113 mg (193 μmol, 55 %).

<sup>1</sup>H NMR (500 MHz, D<sub>2</sub>O, 298 K): δ (ppm) = 10.19 (s, 4H, *H*-Ar), 9.97 (s, 2H, CHO), 8.84 (s, 4H, *H*-Ar), 8.04 (d, <sup>3</sup>*J* = 6.7 Hz, 4H, *H*-Ar), 7.77 (d, <sup>3</sup>*J* = 6.7 Hz, 4H, *H*-Ar), 6.51 (s, 4H, CH<sub>2</sub>). — <sup>13</sup>C NMR (126 MHz, DMSO-*d*<sub>6</sub>, 298 K): δ (ppm) = 165.5 (CH), 133.4 (C<sub>q</sub>), 130.8 (C<sub>q</sub>), 130.7 (CH), 130.5 (C<sub>q</sub>), 130.3 (CH), 130.0 (CH), 127.7 (CH), 67.1 (CH<sub>2</sub>). — HRMS (ESI) (pos., H<sub>2</sub>O/MeOH, 1:1 v/v) (m/z): [M]<sup>+</sup> calc. for C<sub>30</sub>H<sub>22</sub>N<sub>2</sub>O<sub>2</sub><sup>+</sup> CH<sub>3</sub>O<sup>-</sup>, 474.1899; found, 474.1893.

### 2,7-Bis(4-bromobutyl)benzo[*lmn*][3,8]phenanthroline-2,7-diium dibromide (83)



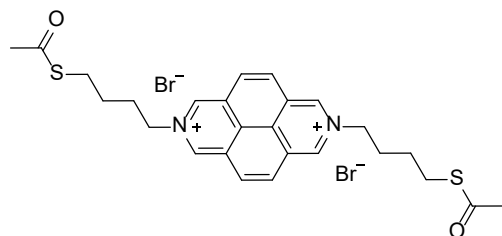
A solution of 50.0 mg DAP (**81**) (245  $\mu\text{mol}$ , 1.00 eq) was prepared in 10.0 mL dry DMF under a nitrogen atmosphere. To the reaction solution, 2.20 mL 1,4-dibromo butane (3.96 g, 18.4 mmol, 75.0 eq) was added, and the reaction mixture was stirred at 75 °C for 48 h. After cooling, the yellow precipitate was filtered off, washed with 25 mL DMF, and dried under reduced pressure. The isolated product was obtained as a yellow solid with a yield of 71.4 mg (112  $\mu\text{mol}$ , 46 %).

$^1\text{H NMR}$  (500 MHz,  $\text{D}_2\text{O}$ ):  $\delta$  (ppm) = 10.11 (s, 4H, *H*-Ar), 8.85 (s, 4H, *H*-Ar), 5.23 (t,  $J = 7.5$  Hz, 4H,  $\text{CH}_2$ ), 3.56 (t,  $J = 6.4$  Hz, 4H,  $\text{CH}_2$ ), 2.54 (quin,  $J = 7.5$  Hz, 4H,  $\text{CH}_2$ ), 2.04 (quin,  $J = 7.5$  Hz, 4H,  $\text{CH}_2$ ). —  $^{13}\text{C NMR}$  (126 MHz,  $\text{D}_2\text{O}$ ):  $\delta$  (ppm) = 141.1 (CH), 130.0 ( $\text{C}_q$ ), 129.9 (CH), 127.0 ( $\text{C}_q$ ), 63.0 ( $\text{CH}_2$ ), 33.0 ( $\text{CH}_2$ ), 30.1 ( $\text{CH}_2$ ), 28.5 ( $\text{CH}_2$ ). — **HRMS (ESI)** (pos.,  $\text{H}_2\text{O}$ ) ( $m/z$ ):  $[\text{M}]^{2+}$  calc. for  $\text{C}_{22}\text{H}_{24}\text{Br}_2\text{N}_2^{2+}$ , 238.0134; found, 238.0134.

#### Chemotion.org:

<https://dx.doi.org/10.14272/reaction/SA-FUHFF-UHFFFADPSC-LHBYXQPXZL-UHFFFADPSC-NUHFF-LUHFF-NUHFF-ZZZ>

### 2,7-Bis(4-(acetylthio)butyl)benzo[*lmn*][3,8]phenanthroline-2,7-diium dibromide (84)

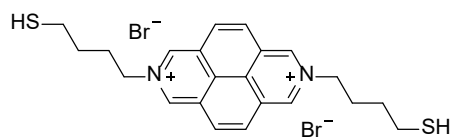


In a vial, 113 mg of 2,7-bis(4-bromobutyl)benzo[*lmn*][3,8]phenanthroline-2,7-diium dibromide (**83**) (178  $\mu\text{mol}$ , 1.00 eq) was dissolved in 10.0 mL ultrapure water and 60.9 mg of potassium thioacetate (533  $\mu\text{mol}$ , 3.00 eq) dissolved in 5.00 mL ultrapure water was added. The reaction solution was stirred for 2 days at room temperature under the exclusion of light. The solvent was removed under reduced pressure. The product was obtained as a brown solid with a yield of  $\geq 99$  % due to residual potassium thioacetate and used as such in the following synthetic step.

$^1\text{H NMR}$  (500 MHz,  $\text{D}_2\text{O}$ ):  $\delta$  (ppm) = 10.10 (s, 4H, *H*-Ar), 8.85 (s, 4H, *H*-Ar), 5.21 (t,  $J = 7.4$  Hz, 4H,  $\text{CH}_2$ ), 2.96 (t,  $J = 7.4$  Hz, 4H,  $\text{CH}_2$ ), 2.35 (quin,  $J = 7.4$  Hz, 4H,  $\text{CH}_2$ ), 2.31 (s, 6H,  $\text{CH}_3$ ), 1.75 (quin,  $J = 7.4$  Hz, 4H,  $\text{CH}_2$ ). —  $^{13}\text{C NMR}$  (126 MHz,  $\text{D}_2\text{O}$ ):  $\delta$  (ppm) = 201.7 (C=O), 141.1 (CH), 130.0 (CH), 129.8 ( $\text{C}_q$ ), 127.0 ( $\text{C}_q$ ), 63.2 ( $\text{CH}_2$ ), 30.2 ( $\text{CH}_2$ ), 30.0 ( $\text{CH}_3$ ), 27.8 ( $\text{CH}_2$ ), 25.5 ( $\text{CH}_2$ ). — **HRMS (ESI)** (pos., MeOH) ( $m/z$ ):  $[\text{M}]^{2+}$  calc. for  $\text{C}_{26}\text{H}_{30}\text{N}_2\text{O}_2\text{S}_2^{2+}$ , 233.0869; found, 233.0867.

**Chemotion.org:**

<https://dx.doi.org/10.14272/reaction/SA-FUHFF-UHFFFADPSC-LNNFMCALYY-UHFFFADPSC-NUHFF-LUHFF-NUHFF-ZZZ>

**2,7-Bis(4-mercaptobutyl)benzo[*lmn*][3,8]phenanthroline-2,7-dium dibromide (85)**

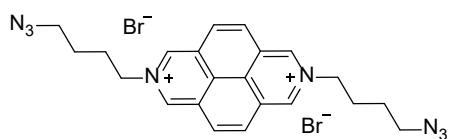
37.2 mg of 2,7-bis(4-(acetylthio)butyl)benzo-[*lmn*][3,8]-phenanthroline-2,7-dium dibromide (**84**) (59.0  $\mu\text{mol}$ , 1.00 eq) was dissolved in 5.00 mL dry MeOH and degassed

with  $\text{N}_2$  for 15 minutes. To the solution, 170  $\mu\text{L}$  acetyl chloride (187 mg, 2.36 mmol, 40.0 eq) was added under a nitrogen atmosphere, and the mixture was stirred for 2.5 days at room temperature. The reaction mixture was quenched by adding water, causing the precipitation of a black solid. The solid was separated by filtration, and the solvent was removed from the filtrate. The product was isolated as a red-brown solid with a yield of 20.9 mg (38.4  $\mu\text{mol}$ , 65 %).

$^1\text{H NMR}$  (500 MHz,  $\text{D}_2\text{O}$ ):  $\delta$  (ppm) = 10.10 (s, 4H, *H*-Ar), 8.86 (s, 4H, *H*-Ar), 5.21 (t, 4H,  $J = 7.4$  Hz,  $\text{CH}_2$ ), 2.63 (t, 4H,  $J = 7.0$  Hz,  $\text{CH}_2$ ), 2.40 (quin, 4H,  $J = 7.4$  Hz,  $\text{CH}_2$ ), 1.77 (quin, 4H,  $J = 7.4$  Hz,  $\text{CH}_2$ ). —  $^{13}\text{C NMR}$  (126 MHz,  $\text{D}_2\text{O}$ ):  $\delta$  (ppm) = 141.1 (CH), 130.0 (CH), 129.8 ( $\text{C}_q$ ), 127.0 ( $\text{C}_q$ ), 63.3 ( $\text{CH}_2$ ), 30.1 ( $\text{CH}_2$ ), 29.5 ( $\text{CH}_2$ ), 23.0 ( $\text{CH}_2$ ). — **HRMS** (ESI) (pos., MeOH) ( $m/z$ ):  $[\text{M}-\text{H}]^+$  calc. for  $\text{C}_{22}\text{H}_{25}\text{N}_2\text{S}_2^+$ , 381.1415; found, 381.1450.

**Chemotion.org:**

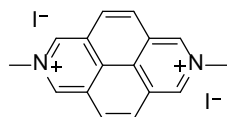
<https://dx.doi.org/10.14272/reaction/SA-FUHFF-UHFFFADPSC-DYWOYJZBS-UHFFFADPSC-NUHFF-NUHFF-NUHFF-ZZZ>

**2,7-Bis(4-azidobutyl)benzo[*lmn*][3,8]phenanthroline-2,7-dium dibromide (86)**

A solution of 25.0 mg of DAP (**81**) (39.4  $\mu\text{mol}$ , 1.00 eq) was prepared in 2.5 mL deionized water and mixed with a solution of sodium azide (17.1 mg, 262  $\mu\text{mol}$ , 6.60 eq) pre-

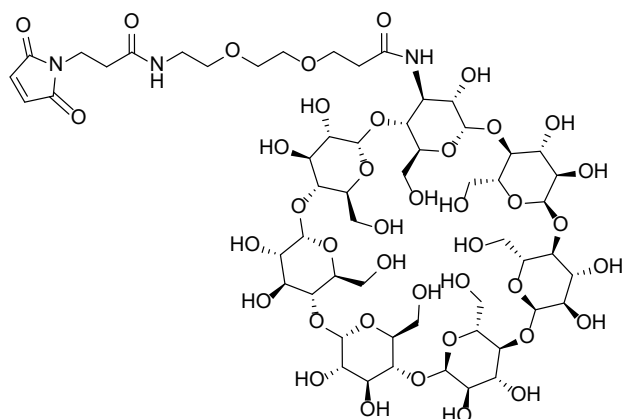
dissolved in 2.5 mL ultrapure water. The reaction mixture was heated at 80  $^\circ\text{C}$  for 3 h before it was concentrated in vacuo. The product was isolated as a yellow solid with a yield of 19.1 mg (34.1  $\mu\text{mol}$ , 87 %).

$^1\text{H NMR}$  (500 MHz,  $\text{D}_2\text{O}$ ):  $\delta$  (ppm) = 10.03 (s, 4H, *H*-Ar), 8.77 (s, 4H, *H*-Ar), 5.14 (t,  $J = 7.4$  Hz, 4H,  $\text{CH}_2$ ), 3.36 (t,  $J = 6.6$  Hz, 4H,  $\text{CH}_2$ ), 2.28 (quin,  $J = 7.4$  Hz, 4H,  $\text{CH}_2$ ), 1.68 (quin,  $J = 7.4$  Hz, 4H,  $\text{CH}_2$ ). —  $^{13}\text{C NMR}$  (126 MHz,  $\text{D}_2\text{O}$ ):  $\delta$  (ppm) = 141.1 (CH), 130.0 ( $\text{C}_q$ ), 129.8 ( $\text{C}_q$ ), 63.3 ( $\text{CH}_2$ ), 50.3 ( $\text{CH}_2$ ), 28.8 ( $\text{CH}_2$ ), 24.9 ( $\text{CH}_2$ ).

**2,7-Dimethylbenzo[*lmn*][3,8]phenanthroline-2,7-diium diiodide<sup>382</sup> (MDAP) (40)**

Under a nitrogen atmosphere, 100 mg of DAP (**81**) (475  $\mu\text{mol}$ , 1.00 eq) was dissolved in 12 mL dry DMF. Subsequently, 1.00 mL methyl iodide (2.28 g, 16.1 mmol, 34.0 eq) was added, and the reaction solution was stirred at room temperature overnight. A second portion of 1.00 mL methyl iodide (2.28 g, 16.1 mmol, 34.0 eq) was added, and the reaction solution was stirred at room temperature for another 24h. The yellow precipitate was filtered off and washed with DMF. The crude product was dissolved in 1 M HCl, overlaid with 10 times the amount of acetone, and stored at 4 °C for three days. The precipitate was filtered off and washed with acetone. The product was isolated as a yellow solid with a yield of 82.2 mg (113  $\mu\text{mol}$ , 34 %).

<sup>1</sup>H NMR (500 MHz, D<sub>2</sub>O, 298 K):  $\delta$  (ppm) = 10.03 (s, 4H, *H*-Ar), 8.85 (s, 4H, *H*-Ar), 4.97 (s, 6H, CH<sub>3</sub>). – <sup>13</sup>C NMR (126 MHz, D<sub>2</sub>O, 298 K):  $\delta$  (ppm) = 141.9 (CH), 129.9 (CH), 129.5 (C<sub>q</sub>), 126.8 (C<sub>q</sub>), 49.9 (CH<sub>3</sub>).

**PEG-maleimide- $\beta$ -CD (94)**

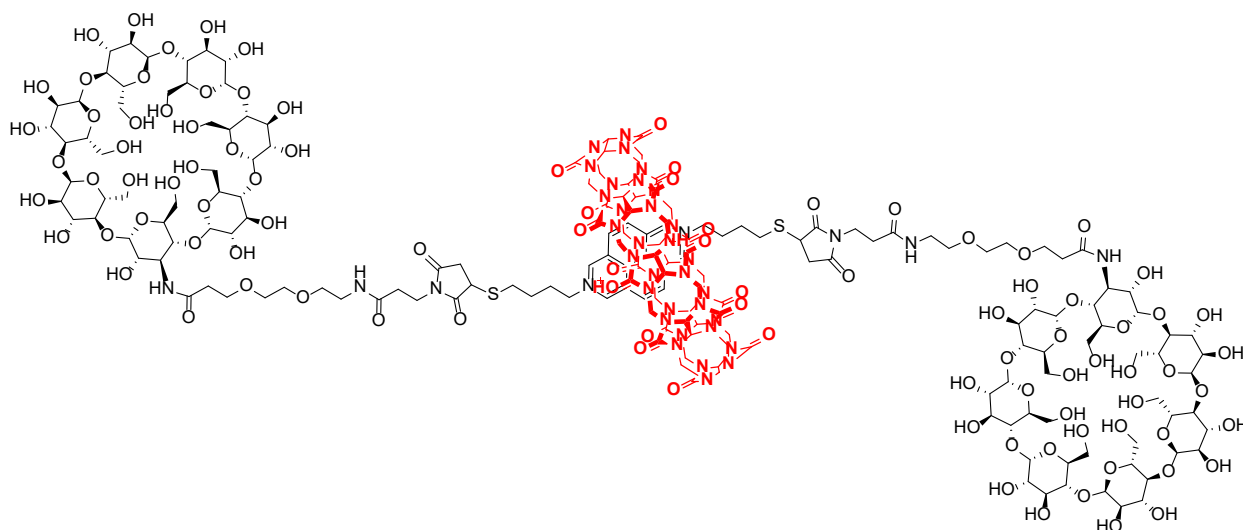
In a vial, 57.1 mg of 3-Amino-3A-deoxy-(2AS, 3AS)- $\beta$ -cyclodextrin hydrate (**93**) (50.0  $\mu$ mol, 1.00 eq) and 23.8 mg of maleimide-PEG<sub>2</sub>-NHS ester (**91**) (56.0  $\mu$ mol, 1.20 eq) were combined and dried in vacuo to remove water from the solids as maleimides are sensitive to hydrolysis. The solids were dissolved in 10 mL dry DMF, and the mixture

was degassed with nitrogen. After adding 100  $\mu$ L of NEt<sub>3</sub> (73.0 mg, 721  $\mu$ mol, 14.4 eq), the reaction solution was stirred overnight at room temperature. The solvent was removed under reduced pressure, and the residue was dissolved in 2.0 mL deionized water and purified by HPLC (gradient: 0-100 % ACN in water, 0.1 % TFA). The product was isolated as a colorless powder with a yield of 61.8 mg (42.7  $\mu$ mol, 85 %).

<sup>1</sup>H NMR (500 MHz, D<sub>2</sub>O):  $\delta$  (ppm) = 6.88 (s, 2H, CH), 5.08-4.99 (m, 6H, CH), 4.94 (d,  $J$  = 5.8 Hz, 1H, CH), 4.28 (s (br), 1H, CH), 3.95-3.53 (m, 52H, CH, CH<sub>2</sub>), 3.34-3.32 (m, 2H, CH<sub>2</sub>), 2.60-2.51 (m, 4H, CH, CH<sub>2</sub>). — <sup>13</sup>C NMR (126 MHz, D<sub>2</sub>O):  $\delta$  (ppm) = 174.3 (C<sub>q</sub>), 172.9 (C<sub>q</sub>), 172.1 (C<sub>q</sub>), 134.5 (CH), 102.0 (CH), 101.9 (CH), 81.3 (CH), 81.1 (CH), 80.9 (CH), 73.2 (CH), 73.1 (CH), 72.7 (CH), 72.3 (CH), 72.0 (CH), 71.9 (CH), 71.8 (CH), 71.4 (CH), 69.5 (CH<sub>2</sub>), 68.9 (CH<sub>2</sub>), 66.7 (CH<sub>2</sub>), 60.2 (CH<sub>2</sub>), 51.0 (CH), 38.9 (CH<sub>2</sub>), 34.7 (CH<sub>2</sub>), 34.5 (CH<sub>2</sub>). — HRMS (ESI) (pos., MeOH) (m/z): [M+H]<sup>+</sup> calc. for C<sub>56</sub>H<sub>89</sub>N<sub>3</sub>O<sub>40</sub>H<sup>+</sup>, 1444.5095; found, 1444.5083.

**Chemotion.org:**

<https://dx.doi.org/10.14272/reaction/SA-FUHFF-UHFFFADPSC-UFNDHZJPQR-UHFFFADPSC-NUHFF-NUOFM-NUHFF-ZZZ>

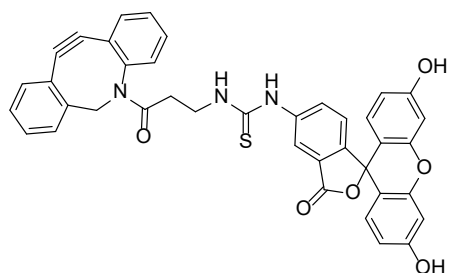
**Rotaxane (95)**

In a vial, 50.0 mg of cucurbit[8]uril (CB8, **25**) (38.0  $\mu\text{mol}$ , 1.10 eq) was dissolved in 50 mL ultrapure water and 14.5 mL of a 2.4 mM aqueous solution of 2,7-bis(4-mercaptobutyl)benzo[1,2,3,4,5,6,7,8]phenanthroline-2,7-dium dibromide (**85**) (18.9 mg, 35.0  $\mu\text{mol}$ , 1.00 eq) were added to the solution. Before synthesis, the thiol concentration (2.00 eq per dye molecule) of **7** was determined through the Ellman test.<sup>305</sup> The mixture was diluted with 8.00 mL of sodium phosphate buffer, pH 7.7, causing a color change from yellow to bright green. After sonication for 15 minutes, 111 mg of TEG-maleimide- $\beta$ -CD (**94**) (77.0  $\mu\text{mol}$ , 2.20 eq) was added. The mixture was stirred at room temperature for 18 h, resulting in a slow color change from green to yellow. After removing the solvent under reduced pressure, the residue was washed with 1:1 EtOH:water three times with subsequent removal of the formed colorless solid by centrifugation. The combined solutions were dried in vacuo, and purification was done by HPLC (mobile phase: 17 % ACN in water (0.1 % TFA) for 45 min, then 100 % ACN for 15 min). The product was obtained as a yellow solid with a yield of 59.4 mg (12.4  $\mu\text{mol}$ , 35 %).

**<sup>1</sup>H NMR** (500 MHz, D<sub>2</sub>O):  $\delta$  (ppm) = 9.67 (br, 4H, CH), 8.11 (br, 4H, CH), 5.67 (d,  $J$  = 14.9 Hz, 16H, CH<sub>2</sub>), 5.44 (s, 16H, CH<sub>2</sub>), 5.27-4.93 (m, 20H, CH, CH<sub>2</sub>), 4.16 (d,  $J$  = 15.4 Hz, 16H, CH<sub>2</sub>), 3.95-3.55 (m, 110H, CH, CH<sub>2</sub>), 3.41-3.36 (m, 4H, CH), 3.30-2.81 (m, 2H, CH<sub>2</sub>), 2.61-2.53 (m, 14H, CH, CH<sub>2</sub>), 2.03 (br, 2H, CH). — **HRMS** (ESI) (pos., 1:1 ACN/H<sub>2</sub>O, 1 % formic acid) (m/z): [M]<sup>2+</sup> calc. for C<sub>182</sub>H<sub>252</sub>N<sub>40</sub>O<sub>96</sub>S<sub>2</sub><sup>2+</sup>, 2299.2765; found, 2299.7039.

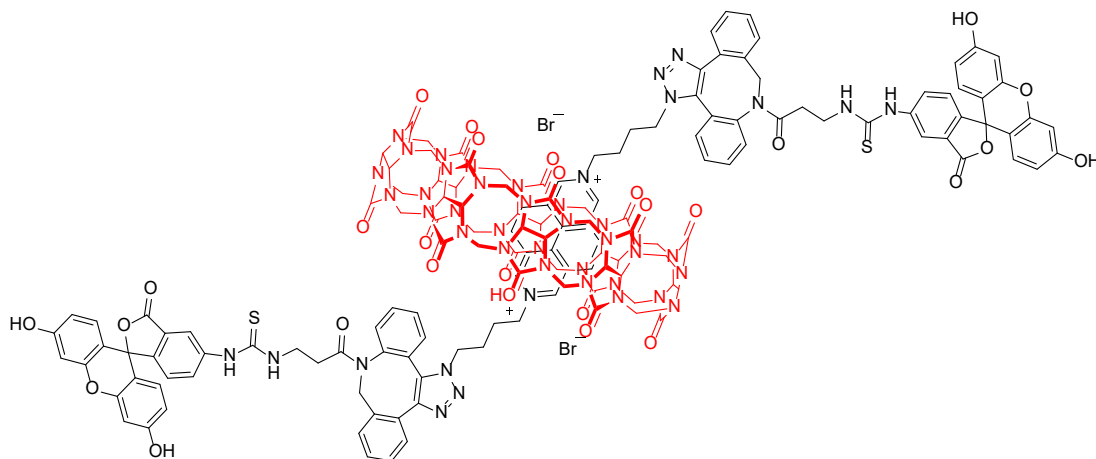
**Chemotion.org:**

<https://dx.doi.org/10.14272/reaction/SA-FUHFF-UHFFFADPSC-YRODUCXAHM-UHFFFADPSC-NUHFF-NDLGW-NUHFF-ZZZ>

**DBCO-fluorescein<sup>383</sup> (87):**

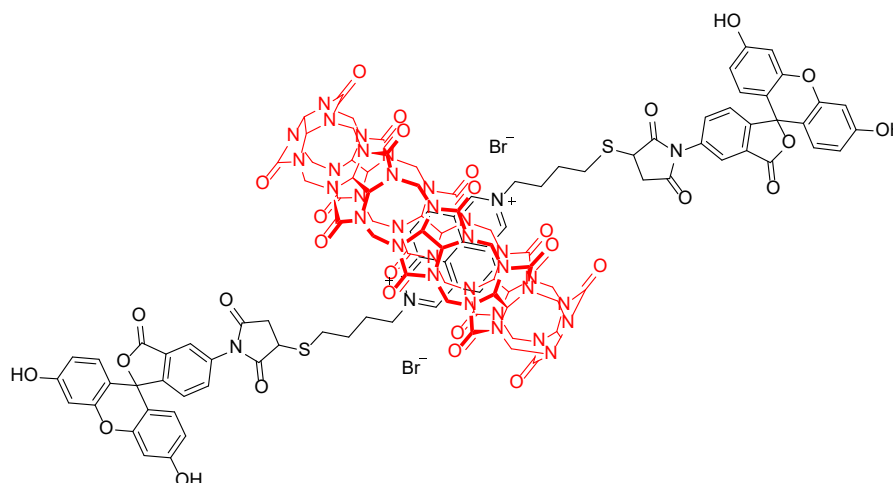
14.8 mg of 5-isothiocyanate fluorescein (39.0  $\mu\text{mol}$ , 1.10 eq) and 9.80 mg of DBCO-amine (35.0  $\mu\text{mol}$ , 1.00 eq) were dissolved in a mixture of acetonitrile and carbonate buffer, pH 10.0 (v:v 3:1). The mixture was stirred for 7 days at room temperature. The reaction progress was controlled via TLC (ethyl acetate as mobile phase, colored with Seebach solution). The reaction solvent was removed under reduced pressure, and the crude product was used without further purification; no NMR spectra were recorded.

**MS (ESI)** (pos., MeOH) (m/z):  $[\text{M}+\text{Na}]^+$  calc. for  $\text{C}_{39}\text{H}_{27}\text{N}_3\text{O}_6\text{SNa}^+$ , 688.1513; found, 688.1647.

**DBCO-fluorescein rotaxane (89)**

In a reaction flask, 3.60 mg of 2,7-bis(4-azidobutyl)benzo[*lmn*][3,8]phenanthroline-2,7-dium dibromide (**86**) (9.00  $\mu\text{mol}$ , 1.00 eq) was dissolved in ultrapure water and 14.3 mg of CB8 (10.8  $\mu\text{mol}$ , 1.20 eq) was added as solid. The reaction mixture was stirred at room temperature for 30 minutes. Subsequently, 18.0 mg DBCO-fluorescein (**87**) (27.0  $\mu\text{mol}$ , 3.00 eq) was added, and the reaction mixture was stirred for 4 days at room temperature. A red precipitate was formed and filtered off. The remaining reaction solution was overlaid with 7.5 mL methanol and stored in the fridge for 1 day. The formed precipitate was filtered off, dried under reduced pressure, and combined with the previously gained red solid. NMR analysis was not possible due to the low solubility of the product.

**MS (ESI)** (neg., DMSO/H<sub>2</sub>O 1:1) (m/z):  $[\text{M}]^{2+}$  calc. for  $\text{C}_{148}\text{H}_{126}\text{N}_{46}\text{O}_{28}\text{S}_2^{2+}$ , 1529.8493; found, 1530.4543.

**FITC-rotaxane (90)**

949  $\mu\text{g}$  of 2,7-*bis*(4-(acetylthio)butyl)benzo[*lmn*][3,8]phenanthroline-2,7-dium dibromide (**85**) (1.75  $\mu\text{mol}$ , 1.00 eq) was dissolved in ultrapure water, and 3.50 mg of CB8 (2.63  $\mu\text{mol}$ , 1.50 eq) was added as solid. The reaction mixture was stirred at room temperature for 30 minutes. Fluorescein-5-maleimide (FITC) was dissolved in dry DMSO with a final concentration of 1 mM. 3.50 mL (equal to 1.50 mg, 3.5  $\mu\text{mol}$ , 2.00 eq) of this 1 mM solution were added to the aqueous reaction mixture, which was stirred for 3 days. The reaction mixture was dried in vacuo, redissolved in water, and lyophilized. Several purification attempts failed, such as normal phase column chromatography and crystallization. HPLC purification was performed by running a gradient from 20 % ACN to 60 % ACN in water containing 0.1 % TFA. NMR analysis was not possible due to the low solubility of the product.

**HRMS (ESI)** (pos., DMSO/H<sub>2</sub>O 3:1) (m/z): [M] calc. for C<sub>118</sub>H<sub>110</sub>N<sub>36</sub>O<sub>30</sub>S<sub>2</sub>, 1282.8432; found, 1282.8538.

## 8. Additional data

### 8.1. Additional data for chapter 5.1

**Table 15.** Simulated slopes for each  $\log K_a^{\text{HD}}$  for a H•G complex with  $\log K_a^{\text{HG}} = 4$ . The slopes are plotted in Figure 30.

$\log K_a^{\text{HD}}$	slope
0	0.0000999
1	0.0000997
2	0.00977
3	0.08189
4	0.35711
4.5	0.54085
5	0.70516
6	0.9086
7	0.97684
8	0.99382
9	0.99818
10	1

## 8.2. Additional data for chapter 5.2

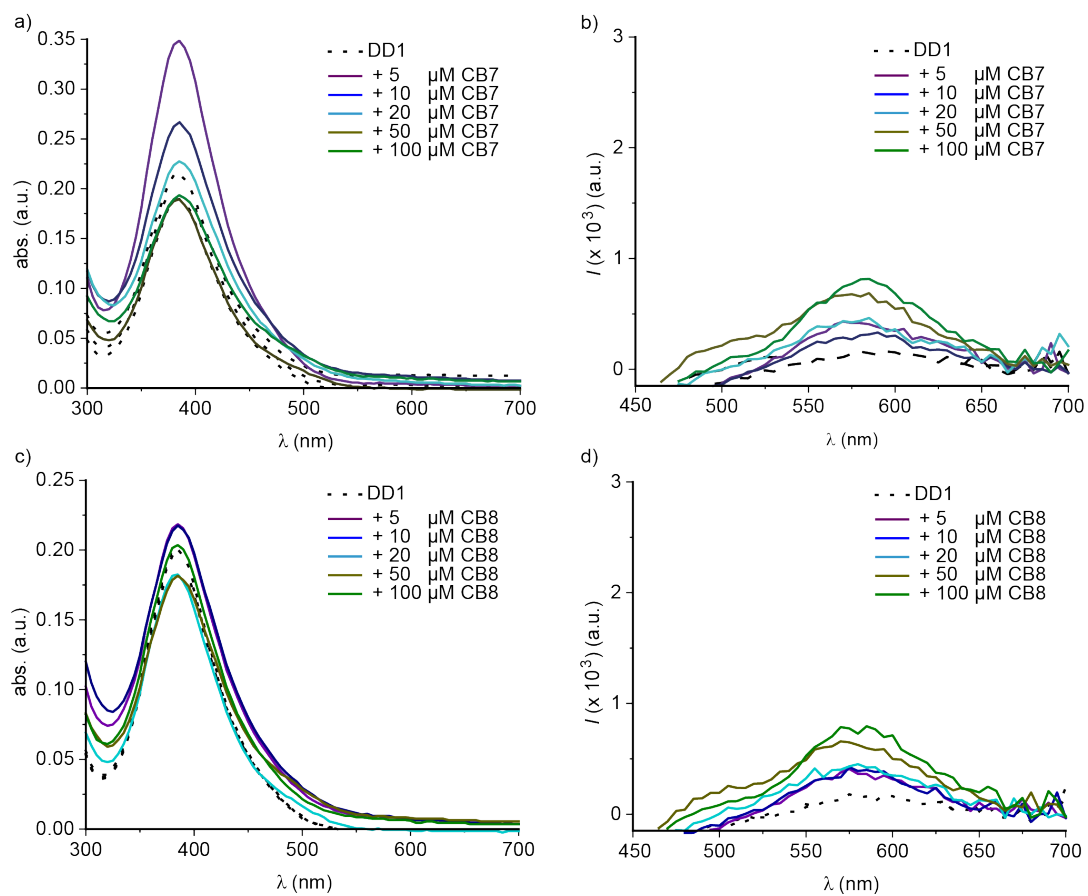


**Figure 85.** Absorbance and emission spectra of selected DD1 with CB7 and CB8. a) absorbance and b) emission spectra of DD1 (10  $\mu\text{M}$ ) upon the addition of CB7 (0 - 100  $\mu\text{M}$ ). c) Absorbance and d) emission spectra of DD1 (10  $\mu\text{M}$ ) upon the addition of CB8 (0 - 100  $\mu\text{M}$ ). All measurements were conducted in triplicates in sodium phosphate buffer (8.4 mM, pH 7.4) at 25  $^{\circ}\text{C}$ .

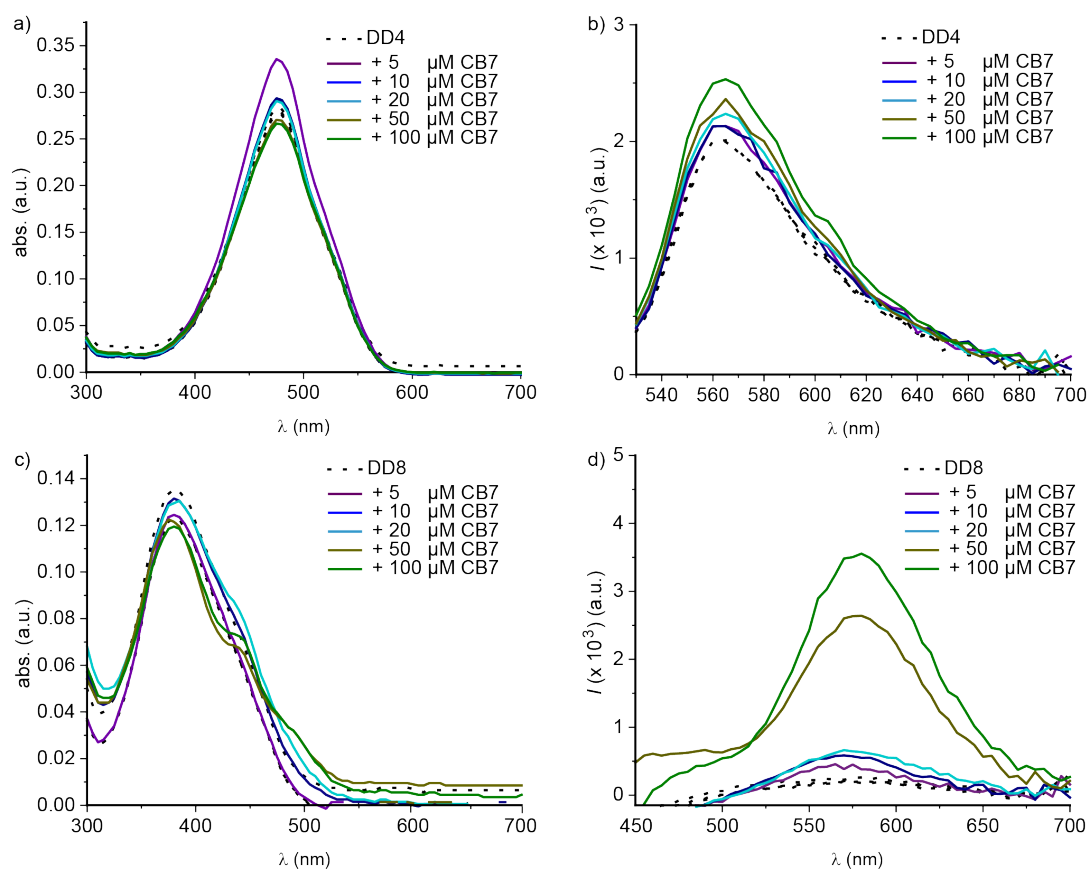


**Figure 86.** Absorbance and emission spectra of selected DDs with CB7 and CB8. a) Absorbance and b) emission spectra of DD4 (10  $\mu\text{M}$ ) upon the addition of CB7 (0 - 100  $\mu\text{M}$ ). c) Absorbance and d) emission spectra of DD8 (10  $\mu\text{M}$ ) upon the addition of CB7 (0 - 100  $\mu\text{M}$ ). All measurements were conducted in triplicates in sodium phosphate buffer (8.4 mM, pH 7.4) at 25  $^{\circ}\text{C}$ .

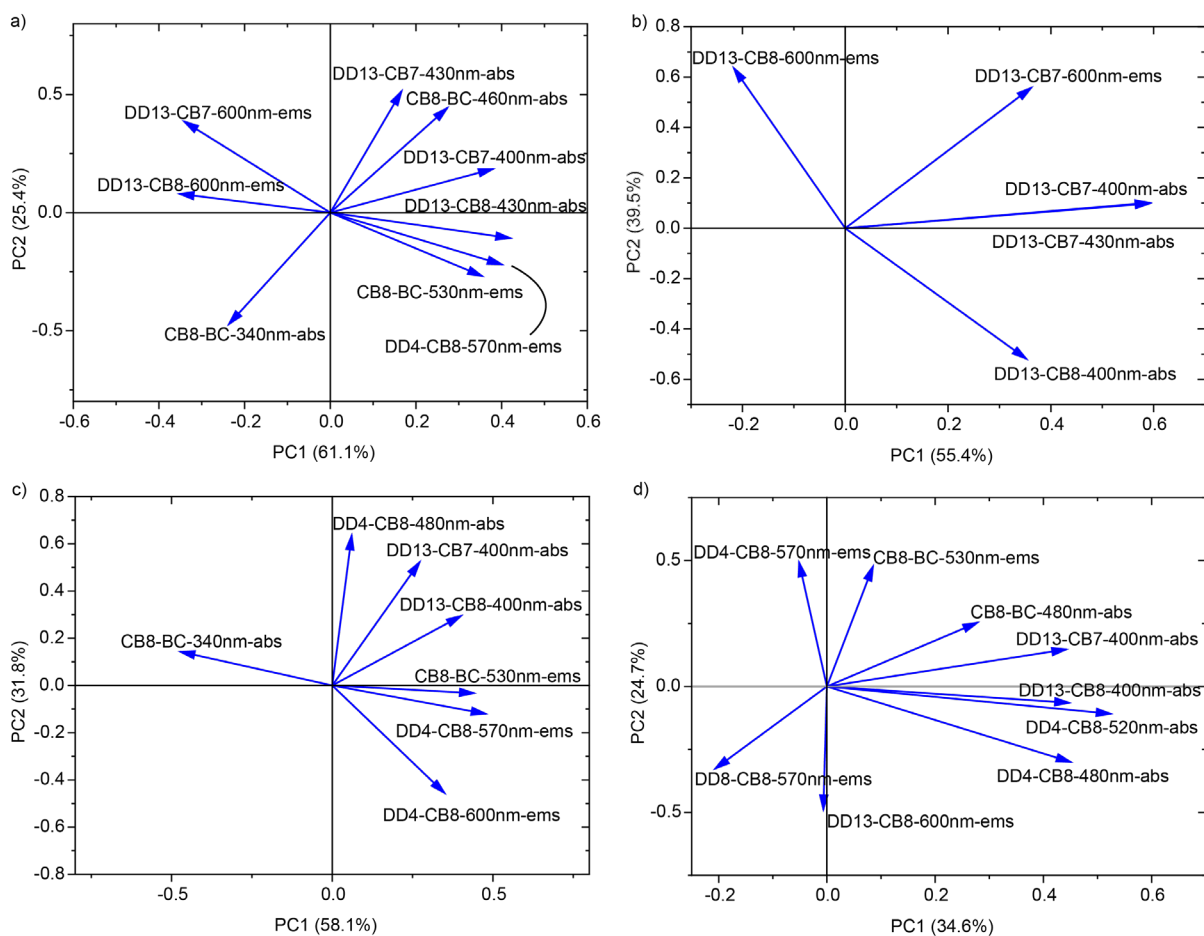


**Figure 87.** Scores plot for the PCA plots in Section 5.2.3 for the discrimination of a) benzodiazepines and opioids, b) THC and derivatives, c) stimulants, adulterants, and diluents, and d) all 15 drugs from a), b), and c).

**Table 16.** Eigenvalues and variance of the PCA plot of benzodiazepines and opioids which is shown in Figure 41.

principal component number	eigenvalue	percentage of variance (%)
1	5.49798	61.08864
2	2.2827	25.36335
3	0.74823	8.31366
4	0.45661	5.07348
5	0.00562	0.06249
6	0.00399	0.04436
7	0.00322	0.03575
8	0.00103	0.01141
9	$6.17421 \times 10^{-4}$	0.00686

**Table 17.** Eigenvalues and variance of the PCA plot of THC and derivatives which is shown in **Figure 42**.

principal component number	eigenvalue	percentage of variance (%)
1	2.7713	55.42604
2	1.97469	39.49376
3	0.21223	4.24468
4	0.04138	0.82755
5	3.99148 x 10 <sup>-4</sup>	0.00798

**Table 18.** Eigenvalues and variance of the PCA plot of stimulants, adulterants, and diluents, which is shown in **Figure 43**.

principal component number	eigenvalue	percentage of variance (%)
1	4.06408	58.05822
2	2.22268	31.75259
3	0.40915	5.84507
4	0.18047	2.57819
5	0.09035	1.29077
6	0.02811	0.40155
7	0.00515	0.07362

**Table 19.** Eigenvalues and variance of the PCA plot of all 15 drugs which is shown in **Figure 44**.

principal component number	eigenvalue	percentage of variance (%)
1	3.11013	34.55704
2	2.22414	24.71264
3	1.68231	18.69236
4	0.84469	9.38544
5	0.55462	6.16246
6	0.43733	4.85927
7	0.08425	0.9361
8	0.04823	0.53584
9	0.0143	0.15886

### 8.3. Additional data for chapter 5.3

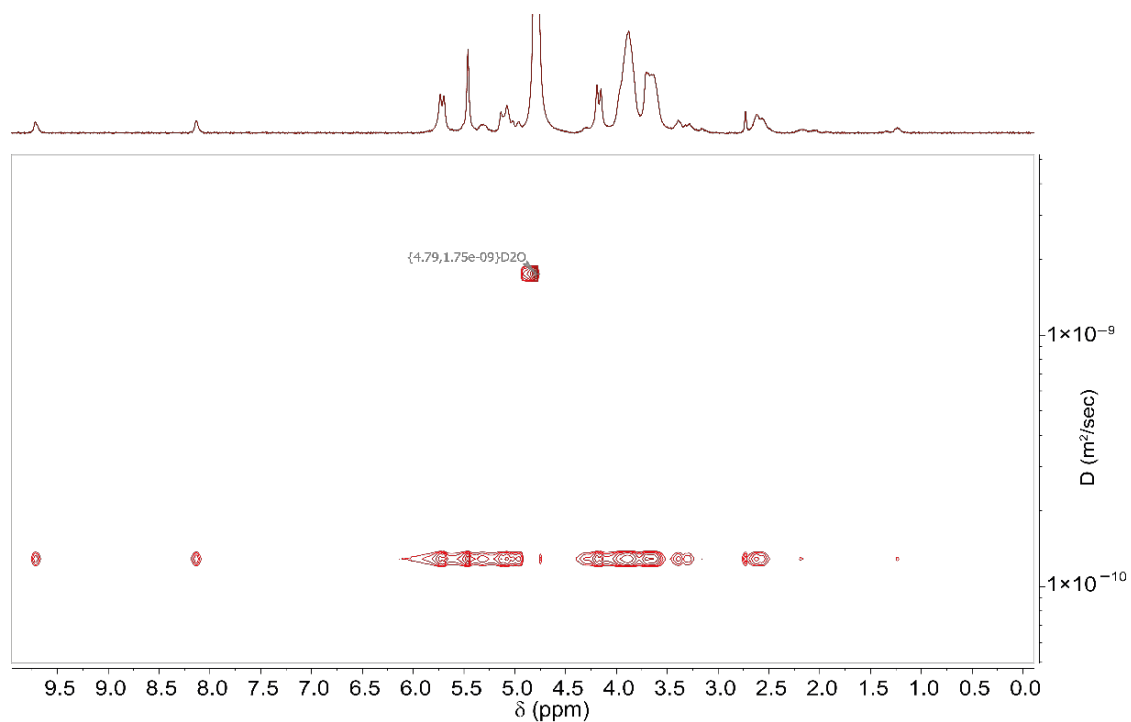


**Figure 88.** 2D DOSY spectrum of rotaxane **95** measured in  $\text{D}_2\text{O}$ . All  $^1\text{H}$  NMR signals show the same diffusion coefficient, which indicates that they correspond to one single molecule, *i.e.*, a rotaxane.<sup>248</sup>

**Table 20.** HPLC recoveries of L-tryptophan concentrations in human blood serum determined for two different types of sample treatment using quantitative HPLC.<sup>248</sup>

sample treatment	[Trp] added ( $\mu\text{M}$ )	[Trp] expected ( $\mu\text{M}$ )	[Trp] found ( $\mu\text{M}$ )	recoveries (%)
1) serum spiked with Trp	10	19.2	18.7	95.7
2) serum deproteinized	25	34.2	33.0	95.3
1) serum deproteinized	10	19.2	20.9	117
2) serum spiked with Trp	25	34.2	37.4	113

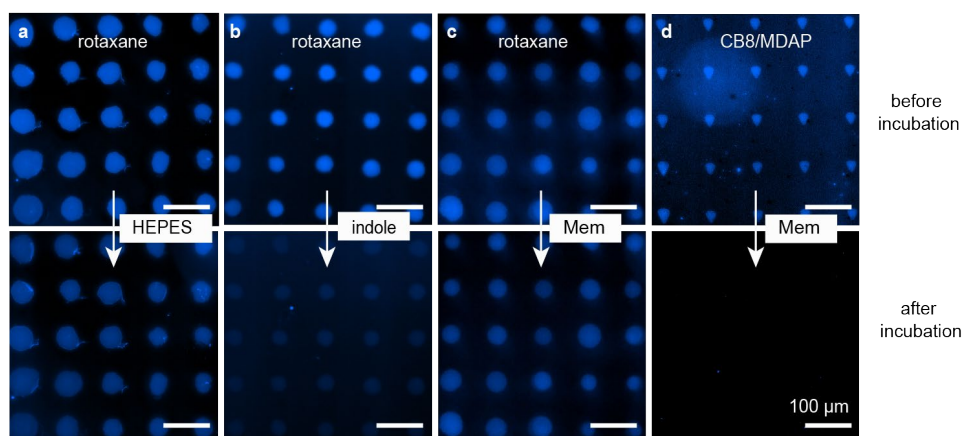


**Figure 89.** Detection of indole and memantine (Mem) with rotaxane **95** and CB8•MDAP microarrays. a)-d) Fluorescence images of the microarrays before and after incubation with an analyte (10 μM) or pure HEPES as control. Images were taken with 10 s exposure time and using a DAPI filter. Scale bars equal 100 μm. Measurements were performed in  $n = 3$  independent replicates per analyte. Adapted with permission from ref.<sup>248</sup> Copyright 2023 Springer Nature.

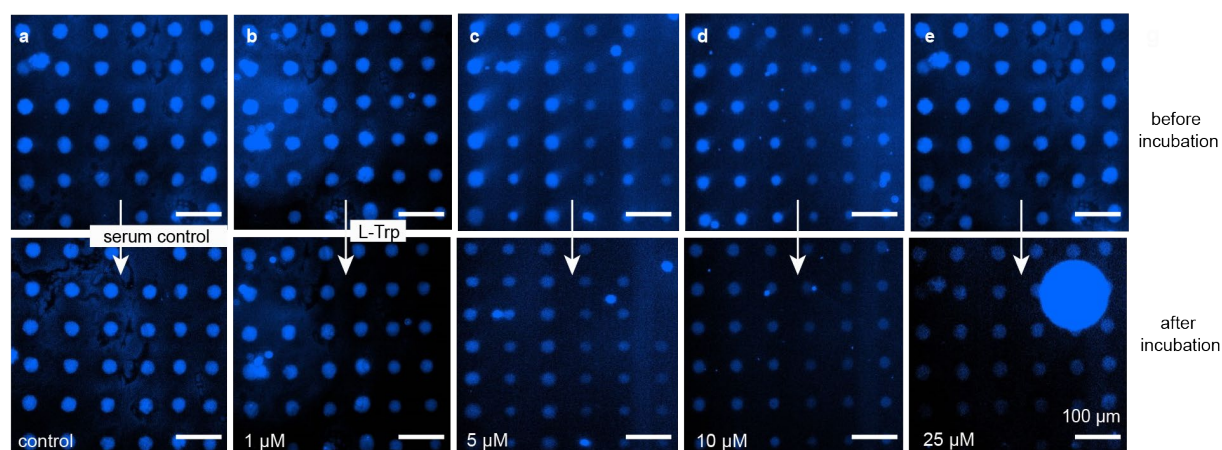


**Figure 90.** Serum experiments with rotaxane microarrays. a)-f) Fluorescence images of rotaxane microarrays before and after incubating with tryptophan solutions of various concentrations. Images were taken with 10 s exposure time and a DAPI filter. Scale bars equal to 100 μm. Images were obtained in  $n = 1$  measurement per Trp concentration. Adapted with permission from ref.<sup>248</sup> Copyright 2023 Springer Nature.

## 9. List of abbreviations

A	Analyte
Å	Angstrom
Abs	Absorbance
ABA	Associative binding assay
ACN	Acetonitrile
AdOH	1-Adamantanol
AdNH <sub>3</sub> <sup>+</sup>	1-Amantadine
Arg	Arginine
BC	Berberine chloride
BSA	Bovine serum albumin
β-CD	β-Cyclodextrin
c	Concentration
CBA	Competitive binding assay
CB <sub>n</sub>	Cucurbit[ <i>n</i> ]uril
CBD	Cannabidiol
CD	Cyclodextrin
CDCl <sub>3</sub>	Deuterated chloroform
CNS	Central nervous system
COSY	Correlation spectroscopy
conc.	Concentration
CTAB	Hexadecyltrimethylammonium bromide
CT	Charge transfer
CU	Chemosensor unit
Cys	Cysteine
d	Doublet
D <sub>2</sub> O	Deuterated water
D	Dye
DAPI	4',6-Diamidino-2-phenylindole
DBA	Direct binding assay
DBTDL	Dibutyltin dilaurate
DD	DimerDye
DD <sub>2</sub>	DimerDye (dimeric form)
DEPT	Distortion-less enhancement by polarization transfer

---

$\Delta G^0$	Free binding energy
DMF	Dimethyl formamide
DMSO	Dimethyl sulfoxide
DNA	Deoxyribonucleic acid
DOSY	Diffusion-ordered NMR spectroscopy
DLS	Dynamic light scattering
$\delta$	Chemical shift
$\varepsilon$	Extinction coefficient
ECD	Electronic circular dichroism
EDTA	Ethylenediamine tetraacetic acid
<i>e.g.</i>	<i>Exempli gratia</i> = 'for example'
Ems	Emission
EN	Electronegativity
EQ	Emission quenching
Eq.	Equation
ESI	Electro spray ionization
ESIPT	Excited-state intramolecular photon transfer
Fl	Fluorescence
FITC	Fluorescein-5-isothiocyanate
g	Gram
G	Guest
GC	Gas chromatography
GDA	Guest displacement assay
H <sub>2</sub> O	Water
H <sub>2</sub> SO <sub>4</sub>	Sulfuric acid
H	Host
HB	Hydrogen bond
hCG	Human chorionic gonadotropin
HCl	Hydrochloric acid
HCys	Homocysteine
H•D complex	Host•dye complex
HEPES	4-(2-Hydroxyethyl)-1-piperazineethanesulfonic acid
H•G	Host•guest complex
HINA	3-Hydroxyisonicotinaldehyde

---

HMBC	Heteronuclear multiple bond correlation
HMBT	2-(2'-Hydroxy-3'-methoxyphenyl) benzothiazole
HPLC	High-performance liquid chromatography
HSA	Human serum albumin
HSQC	Heteronuclear single-quantum coherence
HRMS	High resolution mass spectrometry
Hz	Hertz
IAA	3-Indoleacetic acid
$I_c$	Observable signal change
$I_{norm}$	Normalized signal change
IC	Internal conversion
IDA	Indicator displacement assay
<i>i.e.</i>	<i>Id est</i> = 'that is'
ISC	Intersystem crossing
ITC	Isothermal titration calorimetry
IUPAC	International union of pure and applied chemistry
$J$	Coupling constant
K	Kelvin
$K_a$	Binding affinity constant
$K_a^{HD}$	Binding affinity constant of host•dye complex
$K_a^{HG}$	Binding affinity constant of host•guest complex
$\lambda$	Wavelength
m	Multiplet
M	Molar
MDI	4,4'-Diisocyanato methylenedibenzol
MD simulation	Molecular dynamics simulation
MDAP	2,7-Dimethyl diazapyrene dication
MDMA	3,4-Methylenedioxy- <i>N</i> -methylamphetamine
MDPP	2,7-Dimethyldiazaperoperyleneum dication
Mem	Memantine
MeOH	Methanol
mg	Milligram
min	Minute
MHz	Megahertz

---

MIMs	Mechanically interlocked molecules
mL	Milliliter
mM	Millimolar
mm	Millimeter
$\mu$ L	Microliter
$\mu$ M	Micromolar
$\mu$ mol	Micromole
MPCP	Methylparacyclophane (IUPAC: 1-methyl-4-(5-tricyclo[8.2.2.2 <sup>4,7</sup> ]hexadeca-1(13),4,6,10(14),11,15-hexaenyl)pyridin-1-ium)
MS	Mass spectrometry
MV	Methyl viologen
NEt <sub>3</sub>	Triethylamine
NaH <sub>2</sub> PO <sub>4</sub>	Sodium dihydrogen phosphate
Na <sub>2</sub> HPO <sub>4</sub>	Disodium hydrogen phosphate
NHS	<i>N</i> -Hydroxysuccinimide
NMR	Nuclear magnetic resonance
nm	Nanometer
nM	Nanomolar
N <sub>2</sub>	Nitrogen
P	Phosphorescence
PBS	Phosphate buffered saline
PBZ	Phenylbutazone
PC	Principal component
PCA	Principal component analysis
PCR	Polymerase chain reaction
PDI	Perylene bisdiimide
PET	Photo electron transfer
pH	“Potential of hydrogen” (scale of acidity /basicity)
Phe	Phenylalanine
PKU	Phenylketonuria
ppm	Parts per million
POCT	Point-of-care testing
Pt (II)	Platinum (II)
quart	Quartet

---

quin	Quintet
R	Gas constant
RNA	Ribonucleic acid
Rel <sub>vib</sub>	Non-radiative relaxation
rpm	Pounds per minute
rt	Room temperature
s	Singlet
S <sub>x</sub>	Singlet state
S	Solubility
sCx <sub>n</sub>	2 <i>p</i> -Sulfonatocalix[ <i>n</i> ]arene
S <sub>N</sub> reaction	Nucleophilic substitution reaction
StDev	Standard deviation
t	Triplet
THC	Tetrahydrocannabinol
2,6-TNS	2 <i>p</i> -Toluidinylnaphthalene-6-sulfonate
TFA	Trifluoroacetic acid
TLC	Thin layer chromatography
Trp	Tryptophan
T <sub>x</sub>	Triplet state
T	Temperature
UV-Vis	Ultraviolet-visible
Vol%	Volume percent
%v/v	Volume percent
ZnO <sub>2</sub>	Zinc oxide

## 10. References

1. Vashist, S.K. Point-of-care diagnostics: Recent advances and trends. *Biosensors*. **7**, 62 (2017).
2. Shao, Y., *et al.* Alteration of metabolic profile and potential biomarkers in the plasma of alzheimer's disease. *Aging Dis.* **11**, 1459-1470 (2020).
3. Hyötyläinen, T. Novel methodologies in metabolic profiling with a focus on molecular diagnostic applications. *Expert Rev. Mol. Diagn.* **12**, 527-538 (2012).
4. Zhang, A., Sun, H., Wang, P., Han, Y. & Wang, X. Recent and potential developments of biofluid analyses in metabolomics. *J. Proteomics*. **75**, 1079-1088 (2012).
5. Sanjay, S.T., *et al.* Biomarker detection for disease diagnosis using cost-effective microfluidic platforms. *Analyst*. **140**, 7062-7081 (2015).
6. Nimse, S.B., Sonawane, M.D., Song, K.-S. & Kim, T. Biomarker detection technologies and future directions. *Analyst*. **141**, 740-755 (2016).
7. Krämer, J., Kang, R., Grimm, L.M., De Cola, L., Picchetti, P. & Biedermann, F. Molecular probes, chemosensors, and nanosensors for optical detection of biorelevant molecules and ions in aqueous media and biofluids. *Chem. Rev.* **122**, 3459-3636 (2022).
8. Fuchs, S.A., Berger, R., Klomp, L.W.J. & de Koning, T.J. D-amino acids in the central nervous system in health and disease. *Mol. Genet. Metab.* **85**, 168-180 (2005).
9. Knerr, I. Chapter 21 - amino acid-related diseases. In: *The molecular nutrition of amino acids and proteins*. Academic Press (2016).
10. Hillert, A., *et al.* The genetic landscape and epidemiology of phenylketonuria. *Am. J. Hum. Genet.* **107**, 234-250 (2020).
11. Sorgdrager, F.J.H., Naudé, P.J.W., Kema, I.P., Nollen, E.A. & Deyn, P.P.D. Tryptophan metabolism in inflammaging: From biomarker to therapeutic target. *Front. Immunol.* **10**, (2019).
12. Chen, Y. & Guillemin, G.J. Kynurenine pathway metabolites in humans: Disease and healthy states. *Int. J. Tryptophan Res.* **2**, IJTR.S2097 (2009).
13. Wirleitner, B., *et al.* Immune activation and degradation of tryptophan in coronary heart disease. *Eur. J. Clin. Invest.* **33**, 550-554 (2003).
14. Durant, C., Christmas, D. & Nutt, D. The pharmacology of anxiety. In: *Behavioral neurobiology of anxiety and its treatment*. Springer Berlin Heidelberg (2010).
15. Dulawa, S.C. & Janowsky, D.S. Cholinergic regulation of mood: From basic and clinical studies to emerging therapeutics. *Mol. Psychiatry*. **24**, 694-709 (2019).
16. Cousins, D.A., Butts, K. & Young, A.H. The role of dopamine in bipolar disorder. *Bipolar Disorders*. **11**, 787-806 (2009).
17. Masato, A., Plotegher, N., Boassa, D. & Bubacco, L. Impaired dopamine metabolism in parkinson's disease pathogenesis. *Mol. Neurodegener.* **14**, 35 (2019).
18. Graham, S.F., *et al.* Untargeted metabolomic analysis of human plasma indicates differentially affected polyamine and l-arginine metabolism in mild cognitive impairment subjects converting to alzheimer's disease. *PLOS ONE*. **10**, e0119452 (2015).
19. Bulushi, I.A., Poole, S., Deeth, H.C. & Dykes, G.A. Biogenic amines in fish: Roles in intoxication, spoilage, and nitrosamine formation—a review. *Crit. Rev. Food Sci. Nutr.* **49**, 369-377 (2009).
20. Krentz, A.J. & Hompesch, M. Glucose: Archetypal biomarker in diabetes diagnosis, clinical management and research. *Biomark. Med.* **10**, 1153-1166 (2016).
21. Monnier, L., Colette, C. & Owens, D. Glucose variability and diabetes complications: Risk factor or biomarker? Can we disentangle the “gordian knot”? *Diabetes Metab.* **47**, 101225 (2021).

22. Johnson, R.J., *et al.* Potential role of sugar (fructose) in the epidemic of hypertension, obesity and the metabolic syndrome, diabetes, kidney disease, and cardiovascular disease. *Am. J. Clin. Nut.* **86**, 899-906 (2007).
23. Koire, A., Joffe, H. & Buckley, R. Menopausal hormone therapy and the mind: The role of hormone replacement in the prevention and treatment of cognitive decline, dementia, and cognitive dysfunction of depression. *Harv. Rev. Psychiatry.* **30**, 215-225 (2022).
24. Stevenson, J.C. Type and route of estrogen administration. *Climacteric.* **12**, 86-90 (2009).
25. Short, N.A., Austin, A.E. & Naumann, R.B. Associations between insomnia symptoms and prescription opioid and benzodiazepine misuse in a nationally representative sample. *Addictive Behaviors.* **137**, 107507 (2023).
26. Kienitz, R., *et al.* Benzodiazepines in the management of seizures and status epilepticus: A review of routes of delivery, pharmacokinetics, efficacy, and tolerability. *CNS Drugs.* **36**, 951-975 (2022).
27. Kieffer, B.L. Recent advances in molecular recognition and signal transduction of active peptides: Receptors for opioid peptides. *Cell. Mol. Neurobiol.* **15**, 615-635 (1995).
28. Albrecht, M. Supramolecular chemistry—general principles and selected examples from anion recognition and metallosupramolecular chemistry. *Naturwissenschaften.* **94**, 951-966 (2007).
29. Lehn, J.-M. Perspectives in supramolecular chemistry—from molecular recognition towards molecular information processing and self-organization. *Angew. Chem. Int. Ed.* **29**, 1304-1319 (1990).
30. Borisov, S.M. & Wolfbeis, O.S. Optical biosensors. *Chem. Rev.* **108**, 423-461 (2008).
31. Wu, D., Sedgwick, A.C., Gunlaugsson, T., Akkaya, E.U., Yoon, J. & James, T.D. Fluorescent chemosensors: The past, present and future. *Chem. Soc. Rev.* **46**, 7105-7123 (2017).
32. Liu, W., Yue, F. & Lee, L.P. Integrated point-of-care molecular diagnostic devices for infectious diseases. *Acc. Chem. Res.* **54**, 4107-4119 (2021).
33. Johnson, S. Chapter 2.4 - the home pregnancy test. In: *100 years of human chorionic gonadotropin*. Elsevier (2020).
34. Ranallo, S., Porchetta, A. & Ricci, F. DNA-based scaffolds for sensing applications. *Anal. Chem.* **91**, 44-59 (2019).
35. Rossetti, M., *et al.* Programmable rna-based systems for sensing and diagnostic applications. *Anal. Bioanal. Chem.* **411**, 4293-4302 (2019).
36. Dong, X., *et al.* Rapid pcr powered by microfluidics: A quick review under the background of covid-19 pandemic. *TrAC, Trends Anal. Chem.* **143**, 116377 (2021).
37. Goddard, J.-P. & Reymond, J.-L. Enzyme assays for high-throughput screening. *Curr. Opin. Biotechnol.* **15**, 314-322 (2004).
38. Bisswanger, H. Enzyme assays. *Perspect. Sci.* **1**, 41-55 (2014).
39. Baranwal, J., Barse, B., Gatto, G., Broncova, G. & Kumar, A. Electrochemical sensors and their applications: A review. *Chemosensors.* **10**, 363 (2022).
40. Marie, M., Mandal, S. & Manasreh, O. An electrochemical glucose sensor based on zinc oxide nanorods. *Sensors.* **15**, 18714-18723 (2015).
41. Siddeeg, S.M. Electrochemical detection of neurotransmitter dopamine. *Int. J. Electrochem. Sci.* **15**, 599-612 (2020).
42. Hulanicki, A., Glab, S. & Ingman, F. Chemical sensors: Definitions and classification. *Pure Appl. Chem.* **63**, 1247-1250 (1991).
43. Spichiger-Keller, U.E. Chemical sensors and biosensors for medical and biological applications.) (1998).
44. Spichiger-Keller, U.E. *Chemical sensors and biosensors for medical and biological applications*. John Wiley & Sons (2008).

45. You, L., Zha, D. & Anslyn, E.V. Recent advances in supramolecular analytical chemistry using optical sensing. *Chem. Rev.* **115**, 7840-7892 (2015).
46. Wu, J. & Stoddart, J.F. Mechanical bonds and dynamic covalent bonds. *Mater. Chem. Front.* **4**, 1553-1553 (2020).
47. Rowan, S.J., Cantrill, S.J., Cousins, G.R.L., Sanders, J.K.M. & Stoddart, J.F. Dynamic covalent chemistry. *Angew. Chem. Int. Ed.* **41**, 898-952 (2002).
48. Yemm, E.W., Cocking, E.C. & Ricketts, R.E. The determination of amino-acids with ninhydrin. *Analyst.* **80**, 209-214 (1955).
49. Friedman, M. Applications of the ninhydrin reaction for analysis of amino acids, peptides, and proteins to agricultural and biomedical sciences. *J. Agric. Food. Chem.* **52**, 385-406 (2004).
50. Yang, X., Guo, Y. & Strongin, R.M. Conjugate addition/cyclization sequence enables selective and simultaneous fluorescence detection of cysteine and homocysteine. *Angew. Chem. Int. Ed.* **50**, 10690-10693 (2011).
51. Joshi, H.C. & Antonov, L. Excited-state intramolecular proton transfer: A short introductory review. *Molecules.* **26**, 1475 (2021).
52. Kang, R., *et al.* Discovery of a size-record breaking green-emissive fluorophore: Small, smaller, hina. *Chem. Sci.* **12**, 1392-1397 (2021).
53. Coskun, A. & Akkaya, E.U. Three-point recognition and selective fluorescence sensing of l-dopa. *Org. Lett.* **6**, 3107-3109 (2004).
54. Mortellaro, M. & DeHennis, A. Performance characterization of an abiotic and fluorescent-based continuous glucose monitoring system in patients with type 1 diabetes. *Biosens. Bioelectron.* **61**, 227-231 (2014).
55. Zhang, L., Liu, X.A., Gillis, K.D. & Glass, T.E. A high-affinity fluorescent sensor for catecholamine: Application to monitoring norepinephrine exocytosis. *Angew. Chem. Int. Ed.* **58**, 7611-7614 (2019).
56. Mako, T.L., Racicot, J.M. & Levine, M. Supramolecular luminescent sensors. *Chem. Rev.* **119**, 322-477 (2019).
57. Crane, B.C., *et al.* The development of a continuous intravascular glucose monitoring sensor. *J. Diabetes Sci. Technol.* **9**, 751-761 (2015).
58. Zhai, W., Sun, X., James, T.D. & Fossey, J.S. Boronic acid-based carbohydrate sensing. *Chem. Asian J.* **10**, 1836-1848 (2015).
59. Fang, G., *et al.* Recent development of boronic acid-based fluorescent sensors. *RSC Adv.* **8**, 29400-29427 (2018).
60. Lorand, J.P. & Edwards, J.O. Polyol complexes and structure of the benzenboronate ion. *J. Org. Chem.* **24**, 769-774 (1959).
61. Springsteen, G. & Wang, B. A detailed examination of boronic acid–diol complexation. *Tetrahedron.* **58**, 5291-5300 (2002).
62. Davis, A.P. Synthetic lectins. *Org. Biomol. Chem.* **7**, 3629-3638 (2009).
63. Oshovsky, G.V., Reinhoudt, D.N. & Verboom, W. Supramolecular chemistry in water. *Angew. Chem. Int. Ed.* **46**, 2366-2393 (2007).
64. Bromba, C., Carrie, P., Chui, J.K.W. & Fyles, T.M. Phenyl boronic acid complexes of diols and hydroxyacids. *Supramol. Chem.* **21**, 81-88 (2009).
65. Uhlenheuer, D.A., Petkau, K. & Brunsveld, L. Combining supramolecular chemistry with biology. *Chem. Soc. Rev.* **39**, 2817-2826 (2010).
66. Steed, J.W., Atwood, J.L. Concepts. In: *Supramolecular chemistry*. Wiley-VCH Weinheim (2009).
67. Kubik, S. *Supramolecular chemistry*. De Gruyter (2021).
68. Ke, C., Destecroix, H., Crump, M.P. & Davis, A.P. A simple and accessible synthetic lectin for glucose recognition and sensing. *Nat. Chem.* **4**, 718-723 (2012).

69. Dam, T.K. & Brewer, C.F. Thermodynamic studies of lectin–carbohydrate interactions by isothermal titration calorimetry. *Chem. Rev.* **102**, 387-430 (2002).
70. Lis, H. & Sharon, N. Lectins: Carbohydrate-specific proteins that mediate cellular recognition. *Chem. Rev.* **98**, 637-674 (1998).
71. Ambrosi, M., Cameron, N.R. & Davis, B.G. Lectins: Tools for the molecular understanding of the glycode. *Org. Biomol. Chem.* **3**, 1593-1608 (2005).
72. Silverstein, K.A.T., Haymet, A.D.J. & Dill, K.A. The strength of hydrogen bonds in liquid water and around nonpolar solutes. *J. Am. Chem. Soc.* **122**, 8037-8041 (2000).
73. Nishio, M. The  $ch/\pi$  hydrogen bond in chemistry. Conformation, supramolecules, optical resolution and interactions involving carbohydrates. *PCCP*. **13**, 13873-13900 (2011).
74. Arunan, E., *et al.* Defining the hydrogen bond: An account (iupac technical report). *Pure Appl. Chem.* **83**, 1619-1636 (2011).
75. Takahashi, O.  $Ch\cdots\pi$  interaction in organic molecules. In: *Noncovalent forces*. Springer International Publishing (2015).
76. Mazik, M. Design of lectin mimetics. *ChemBioChem.* **9**, 1015-1017 (2008).
77. Tromans, R.A., *et al.* A biomimetic receptor for glucose. *Nat. Chem.* **11**, 52-56 (2019).
78. Rini, J.M. Lectin structure. *Annu. Rev. Biophys. Biomol. Struct.* **24**, 551-577 (1995).
79. Davis, M.E. & Brewster, M.E. Cyclodextrin-based pharmaceuticals: Past, present and future. *Nat. Rev. Drug Discov.* **3**, 1023 (2004).
80. Chen, G. & Jiang, M. Cyclodextrin-based inclusion complexation bridging supramolecular chemistry and macromolecular self-assembly. *Chem. Soc. Rev.* **40**, 2254-2266 (2011).
81. Guo, D.-S. & Liu, Y. Supramolecular chemistry of p-sulfonatocalix[n]arenes and its biological applications. *Acc. Chem. Res.* **47**, 1925-1934 (2014).
82. Xu, Z., Jia, S., Wang, W., Yuan, Z., Jan Ravoo, B. & Guo, D.-S. Heteromultivalent peptide recognition by co-assembly of cyclodextrin and calixarene amphiphiles enables inhibition of amyloid fibrillation. *Nat. Chem.* **11**, 86-93 (2019).
83. Beatty, M.A., Selinger, A.J., Li, Y. & Hof, F. Parallel synthesis and screening of supramolecular chemosensors that achieve fluorescent turn-on detection of drugs in saliva. *J. Am. Chem. Soc.* **141**, 16763-16771 (2019).
84. Lagona, J., Mukhopadhyay, P., Chakrabarti, S. & Isaacs, L. The cucurbit[n]uril family. *Angew. Chem. Int. Ed.* **44**, 4844-4870 (2005).
85. Behrend, R., Meyer, E. & Rusche, F. I. Ueber condensationsproducte aus glycoluril und formaldehyd. *Justus Liebigs Ann. Chem.* **339**, 1-37 (1905).
86. Mock, W.L., Irra, T.A., Wepsiec, J.P. & Manimaran, T.L. Cycloaddition induced by cucurbituril. A case of pauling principle catalysis. *J. Org. Chem.* **48**, 3619-3620 (1983).
87. Kim, J., *et al.* New cucurbituril homologues: Syntheses, isolation, characterization, and x-ray crystal structures of cucurbit[n]uril ( $n = 5, 7, \text{ and } 8$ ). *J. Am. Chem. Soc.* **122**, 540-541 (2000).
88. Buschmann, H.-J. From small cucurbituril complexes to large ordered networks. *Isr. J. Chem.* **51**, 533-536 (2011).
89. Assaf, K.I. & Nau, W.M. Cucurbiturils: From synthesis to high-affinity binding and catalysis. *Chem. Soc. Rev.* **44**, 394-418 (2015).
90. Barrow, S.J., Kasera, S., Rowland, M.J., del Barrio, J. & Scherman, O.A. Cucurbituril-based molecular recognition. *Chem. Rev.* **115**, 12320-12406 (2015).
91. Hur, M.Y., Murray, J. & Kim, K. Chapter 2 synthesis of the cucurbituril family. In: *Cucurbiturils and related macrocycles*. The Royal Society of Chemistry (2020).
92. Šindelář, V. & Lízal, T. Hemicucurbiturils. In: *Cucurbiturils and related macrocycles*. The Royal Society of Chemistry (2019).
93. Kim, K., Selvapalam, N. & Oh, D.H. Cucurbiturils—a new family of host molecules. *J. Incl. Phenom. Macrocycl. Chem.* **50**, 31-36 (2004).

94. Assaf, K.I. & Nau, W.M. Chapter 4 cucurbituril properties and the thermodynamic basis of host–guest binding. In: *Cucurbiturils and related macrocycles*. The Royal Society of Chemistry (2020).
95. Lee, J.W., Samal, S., Selvapalam, N., Kim, H.-J. & Kim, K. Cucurbituril homologues and derivatives: New opportunities in supramolecular chemistry. *Acc. Chem. Res.* **36**, 621-630 (2003).
96. Assaf, K.I., Alnajjar, M.A. & Nau, W.M. Supramolecular assemblies through host–guest complexation between cucurbiturils and an amphiphilic guest molecule. *Chem. Commun.* **54**, 1734-1737 (2018).
97. Fernandes, R.J., *et al.* Toward light-controlled supramolecular peptide dimerization. *J. Org. Chem.* **86**, 8472-8478 (2021).
98. Li, S., Macartney, D.H. & Wang, R. Host–guest chemistry of the cucurbituril family. In: *Cucurbiturils and related macrocycles*. The Royal Society of Chemistry (2019).
99. Moghaddam, S., *et al.* New ultrahigh affinity host–guest complexes of cucurbit[7]uril with bicyclo[2.2.2]octane and adamantane guests: Thermodynamic analysis and evaluation of m2 affinity calculations. *J. Am. Chem. Soc.* **133**, 3570-3581 (2011).
100. Jeon, W.S., *et al.* Complexation of ferrocene derivatives by the cucurbit[7]uril host: A comparative study of the cucurbituril and cyclodextrin host families. *J. Am. Chem. Soc.* **127**, 12984-12989 (2005).
101. Rekharsky, M.V., *et al.* A synthetic host-guest system achieves avidin-biotin affinity by overcoming enthalpy–entropy compensation. *Proc. Natl. Acad. Sci.* **104**, 20737-20742 (2007).
102. Biedermann, F., Nau, W.M. & Schneider, H.-J. The hydrophobic effect revisited—studies with supramolecular complexes imply high-energy water as a noncovalent driving force. *Angew. Chem. Int. Ed.* **53**, 11158-11171 (2014).
103. Biedermann, F., Uzunova, V.D., Scherman, O.A., Nau, W.M. & De Simone, A. Release of high-energy water as an essential driving force for the high-affinity binding of cucurbit[n]urils. *J. Am. Chem. Soc.* **134**, 15318-15323 (2012).
104. Jon, S.Y., Ko, Y.H., Park, S.H., Kim, H.-J. & Kim, K. A facile, stereoselective [2 + 2] photoreaction mediated by cucurbit[8]uril. *Chem. Commun.*, 1938-1939 (2001).
105. Liu, J., Tan, C.S.Y., Lan, Y. & Scherman, O.A. Aqueous polymer self-assembly based on cucurbit[n]uril-mediated host-guest interactions. *Macromol. Chem. Phys.* **217**, 319-332 (2016).
106. Wiemann, M. & Jonkheijm, P. Cucurbiturils on surfaces. In: *Cucurbiturils and related macrocycles*. The Royal Society of Chemistry (2019).
107. Das, D., Assaf, K.I. & Nau, W.M. Applications of cucurbiturils in medicinal chemistry and chemical biology. *Front. Chem.* **7**, (2019).
108. Day, A.I. & Atthar, A.S. Drug delivery vehicles based on glycoluril oligomers. In: *Cucurbiturils and related macrocycles*. The Royal Society of Chemistry (2019).
109. Biedermann, F., Hathazi, D. & Nau, W.M. Associative chemosensing by fluorescent macrocycle-dye complexes - a versatile enzyme assay platform beyond indicator displacement. *Chem. Commun.* **51**, 4977-4980 (2015).
110. Hennig, A., Bakirci, H. & Nau, W.M. Label-free continuous enzyme assays with macrocycle-fluorescent dye complexes. *Nat. Methods.* **4**, 629-632 (2007).
111. Dsouza, R.N., Hennig, A. & Nau, W.M. Supramolecular tandem enzyme assays. *Chem. Eur. J.* **18**, 3444-3459 (2012).
112. Sinn, S. & Biedermann, F. Chemical sensors based on cucurbit[n]uril macrocycles. *Isr. J. Chem.* **58**, 357-412 (2018).
113. Poulson, B.G., *et al.* Cyclodextrins: Structural, chemical, and physical properties, and applications. *Polysaccharides.* **3**, 1-31 (2022).

114. Loftsson, T., Jarho, P., Másson, M. & Järvinen, T. Cyclodextrins in drug delivery. *Expert Opin. Drug Deliv.* **2**, 335-351 (2005).
115. Saokham, P., Muankaew, C., Jansook, P. & Loftsson, T. Solubility of cyclodextrins and drug/cyclodextrin complexes. *Molecules.* **23**, 1161 (2018).
116. Houk, K.N., Leach, A.G., Kim, S.P. & Zhang, X. Binding affinities of host–guest, protein–ligand, and protein–transition-state complexes. *Angew. Chem. Int. Ed.* **42**, 4872-4897 (2003).
117. Rekharsky, M.V. & Inoue, Y. Complexation thermodynamics of cyclodextrins. *Chem. Rev.* **98**, 1875-1918 (1998).
118. Quaglio, D., *et al.* Calixarene: A versatile scaffold for the development of highly sensitive biosensors. *Supramol. Chem.* **33**, 345-369 (2021).
119. Shinkai, S., Araki, K. & Manabe, O. Does the calixarene cavity recognise the size of guest molecules? On the ‘hole-size selectivity’ in water-soluble calixarenes. *J. Chem. Soc., Chem. Commun.*, 187-189 (1988).
120. Dsouza, R.N., Pischel, U. & Nau, W.M. Fluorescent dyes and their supramolecular host/guest complexes with macrocycles in aqueous solution. *Chem. Rev.* **111**, 7941-7980 (2011).
121. Shinkai, S., Mori, S., Tsubaki, T., Sone, T. & Manabe, O. New water-soluble host molecules derived from calix[6]arene. *Tetrahedron Lett.* **25**, 5315-5318 (1984).
122. Morel, J.-P. & Morel-Desrosiers, N. Binding of monovalent metal cations by the p-sulfonatocalix[4]arene: Experimental evidence for cation– $\pi$  interactions in water. *Org. Biomol. Chem.* **4**, 462-465 (2006).
123. Perret, F., Lazar, A.N. & Coleman, A.W. Biochemistry of the para-sulfonato-calix[n]arenes. *Chem. Commun.*, 2425-2438 (2006).
124. Beatty, M.A. & Hof, F. New technologies powered by protein-binding calixarenes. In: *Calixarenes and beyond*. Springer International Publishing (2016).
125. Coleman, A.W., *et al.* Enhanced detection of the pathogenic prion protein by its supramolecular association with para-sulfonato-calix[n]arene derivatives. *New J. Chem.* **31**, 711-717 (2007).
126. Hanauer, T., *et al.* Selective recognition of the di/trimethylammonium motif by an artificial carboxycalixarene receptor. *Org. Biomol. Chem.* **15**, 1100-1105 (2017).
127. Dougherty, D.A. Cation– $\pi$ ; interactions in chemistry and biology: A new view of benzene, phe, tyr, and trp. *Science.* **271**, 163-168 (1996).
128. Atwood, J.L. & Szumna, A. Cation– $\pi$  interactions in neutral calix[4]resorcinarenes. *J. Supramol. Chem.* **2**, 479-482 (2002).
129. Pan, Y.-C., Hu, X.-Y. & Guo, D.-S. Biomedical applications of calixarenes: State of the art and perspectives. *Angew. Chem. Int. Ed.* **60**, 2768-2794 (2021).
130. Guo, D.-S., Uzunova, V.D., Su, X., Liu, Y. & Nau, W.M. Operational calixarene-based fluorescent sensing systems for choline and acetylcholine and their application to enzymatic reactions. *Chem. Sci.* **2**, 1722-1734 (2011).
131. Thordarson, P. Determining association constants from titration experiments in supramolecular chemistry. *Chem. Soc. Rev.* **40**, 1305-1323 (2011).
132. Haav, K., *et al.* Accurate method to quantify binding in supramolecular chemistry. *J. Org. Chem.* **78**, 7796-7808 (2013).
133. Hargrove, A.E., Zhong, Z., Sessler, J.L. & Anslyn, E.V. Algorithms for the determination of binding constants and enantiomeric excess in complex host : Guest equilibria using optical measurements. *New J. Chem.* **34**, 348-354 (2010).
134. Schmidtchen, F.P. Isothermal titration calorimetry in supramolecular chemistry. In: *Supramolecular chemistry* (2012).

135. Freyer, M.W. & Lewis, E.A. Isothermal titration calorimetry: Experimental design, data analysis, and probing macromolecule/ligand binding and kinetic interactions. In: *Methods in cell biology*. Academic Press (2008).
136. Schalley, C.A. *Analytical methods in supramolecular chemistry*. John Wiley & Sons (2012).
137. Frackowiak, D. The Jablonski diagram. *J. Photochem. Photobiol. B, Biol.* **2**, 399 (1988).
138. Lakowicz, J.R. *Principles of fluorescence spectroscopy*, 3rd edn. Springer (2007).
139. Parkesh, R., Veale, E.B. & Gunnlaugsson, T. Fluorescent detection principles and strategies. In: *Chemosensors* (2011).
140. del Valle, J.C. & Catalán, J. Kasha's rule: A reappraisal. *PCCP*. **21**, 10061-10069 (2019).
141. Lakowicz, J.R. Introduction to fluorescence. In: *Principles of fluorescence spectroscopy*. Springer (2006).
142. Halstead, J.A. Teaching the spin selection rule: An inductive approach. *J. Chem. Educ.* **90**, 70-75 (2013).
143. Lewis, G.N. & Kasha, M. Phosphorescence and the triplet state. *J. Am. Chem. Soc.* **66**, 2100-2116 (1944).
144. Sinn, S., Krämer, J. & Biedermann, F. Teaching old indicators even more tricks: Binding affinity measurements with the guest-displacement assay (gda). *Chem. Commun.* **56**, 6620-6623 (2020).
145. Yu, J.-S., Wei, F.-D., Gao, W. & Zhao, C.-C. Thermodynamic study on the effects of  $\beta$ -cyclodextrin inclusion with berberine. *Spectrochim. Acta Pt. A: Mol. Biomol. Spectrosc.* **58**, 249-256 (2002).
146. Megyesi, M. & Biczók, L. Considerable fluorescence enhancement upon supramolecular complex formation between berberine and p-sulfonated calixarenes. *Chem. Phys. Lett.* **424**, 71-76 (2006).
147. Prabodh, A., *et al.* Teaching indicators to unravel the kinetic features of host-guest inclusion complexes. *Chem. Commun.* **56**, 12327-12330 (2020).
148. Sindelar, V., Cejas, M.A., Raymo, F.M., Chen, W., Parker, S.E. & Kaifer, A.E. Supramolecular assembly of 2,7-dimethyldiazapyrenium and cucurbit[8]uril: A new fluorescent host for detection of catechol and dopamine. *Chem. Eur. J.* **11**, 7054-7059 (2005).
149. Minami, T., Esipenko, N.A., Zhang, B., Isaacs, L. & Anzenbacher, P. "Turn-on" fluorescent sensor array for basic amino acids in water. *Chem. Commun.* **50**, 61-63 (2014).
150. Wiskur, S.L., Ait-Haddou, H., Lavigne, J.J. & Anslyn, E.V. Teaching old indicators new tricks. *Acc. Chem. Res.* **34**, 963-972 (2001).
151. Nguyen, B.T. & Anslyn, E.V. Indicator-displacement assays. *Coord. Chem. Rev.* **250**, 3118-3127 (2006).
152. Nguyen, B.T. & Anslyn, E.V. Indicator-displacement assays. *Coord. Chem. Rev.* **250**, 3118-3127 (2006).
153. Biedermann, F. & Nau, W.M. Noncovalent chirality sensing ensembles for the detection and reaction monitoring of amino acids, peptides, proteins, and aromatic drugs. *Angew. Chem. Int. Ed.* **53**, 5694-5699 (2014).
154. Biedermann, F., Ghale, G., Hennig, A. & Nau, W.M. Fluorescent artificial receptor-based membrane assay (farma) for spatiotemporally resolved monitoring of biomembrane permeability. *Commun. Biol.* **3**, 383 (2020).
155. Biedermann, F. & Scherman, O.A. Cucurbit[8]uril mediated donor-acceptor ternary complexes: A model system for studying charge-transfer interactions. *J. Phys. Chem. B.* **116**, 2842-2849 (2012).
156. Kim, H.-J., *et al.* Selective inclusion of a hetero-guest pair in a molecular host: Formation of stable charge-transfer complexes in cucurbit[8]uril. *Angew. Chem. Int. Ed.* **40**, 1526-1529 (2001).

157. Hirose, K. Quantitative analysis of binding properties. In: *Analytical methods in supramolecular chemistry* (2012).
158. Prabodh, A., *et al.* Teaching indicators to unravel the kinetic features of host–guest inclusion complexes. *Chem. Commun.* **56**, 12327-12330 (2020).
159. Guo, C., Sedgwick, A.C., Hirao, T. & Sessler, J.L. Supramolecular fluorescent sensors: An historical overview and update. *Coord. Chem. Rev.* **427**, 213560 (2021).
160. Lee, J.W., Lee, H.H.L., Ko, Y.H., Kim, K. & Kim, H.I. Deciphering the specific high-affinity binding of cucurbit[7]uril to amino acids in water. *J. Phys. Chem. B.* **119**, 4628-4636 (2015).
161. Urbach, A.R. & Ramalingam, V. Molecular recognition of amino acids, peptides, and proteins by cucurbit[n]uril receptors. *Isr. J. Chem.* **51**, 664-678 (2011).
162. Florea, M., Kudithipudi, S., Rei, A., González-Álvarez, M.J., Jeltsch, A. & Nau, W.M. A fluorescence-based supramolecular tandem assay for monitoring lysine methyltransferase activity in homogeneous solution. *Chem. Eur. J.* **18**, 3521-3528 (2012).
163. Biedermann, F., Hathazi, D. & Nau, W.M. Associative chemosensing by fluorescent macrocycle–dye complexes – a versatile enzyme assay platform beyond indicator displacement. *Chem. Commun.* **51**, 4977-4980 (2015).
164. Bailey, D.M., Hennig, A., Uzunova, V.D. & Nau, W.M. Supramolecular tandem enzyme assays for multiparameter sensor arrays and enantiomeric excess determination of amino acids. *Chem. Eur. J.* **14**, 6069-6077 (2008).
165. Kasera, S., Walsh, Z., del Barrio, J. & Scherman, O.A. A selective supramolecular photochemical sensor for dopamine. *Supramol. Chem.* **26**, 280-285 (2014).
166. Zhang, S., Grimm, L., Miskolczy, Z., Biczók, L., Biedermann, F. & Nau, W.M. Binding affinities of cucurbit[n]urils with cations. *Chem. Commun.* **55**, 14131-14134 (2019).
167. Legg, K.D. & Hercules, D.M. Quenching of lucigenin fluorescence. *J. Phys. Chem.* **74**, 2114-2118 (1970).
168. Psychogios, N., *et al.* The human serum metabolome. *PLOS One.* **6**, e16957 (2011).
169. Bouatra, S., *et al.* The human urine metabolome. *PLOS One.* **8**, e73076 (2013).
170. Wright, A.T. & Anslyn, E.V. Differential receptor arrays and assays for solution-based molecular recognition. *Chem. Soc. Rev.* **35**, 14-28 (2006).
171. Jolliffe, I.T. & Cadima, J. Principal component analysis: A review and recent developments. *Philos. Trans. Royal Soc. A.* **374**, 20150202 (2016).
172. Umali, A.P. & Anslyn, E.V. A general approach to differential sensing using synthetic molecular receptors. *Curr. Opin. Chem. Biol.* **14**, 685-692 (2010).
173. Lavigne, J.J. & Anslyn, E.V. Sensing a paradigm shift in the field of molecular recognition: From selective to differential receptors. *Angew. Chem. Int. Ed.* **40**, 3118-3130 (2001).
174. Geng, Y., Peveler, W.J. & Rotello, V.M. Array-based “chemical nose” sensing in diagnostics and drug discovery. *Angew. Chem. Int. Ed.* **58**, 5190-5200 (2019).
175. Liu, Y., Minami, T., Nishiyabu, R., Wang, Z. & Anzenbacher, P., Jr. Sensing of carboxylate drugs in urine by a supramolecular sensor array. *J. Am. Chem. Soc.* **135**, 7705-7712 (2013).
176. Minami, T., Esipenko, N.A., Akdeniz, A., Zhang, B., Isaacs, L. & Anzenbacher, P., Jr. Multianalyte sensing of addictive over-the-counter (otc) drugs. *J. Am. Chem. Soc.* **135**, 15238-15243 (2013).
177. Tighe, P.J., Ryder, R.R., Todd, I. & Fairclough, L.C. Elisa in the multiplex era: Potentials and pitfalls. *Proteomics Clin. Appl.* **9**, 406-422 (2015).
178. Adams, H., Carver, F.J., Hunter, C.A., Morales, J.C. & Seward, E.M. Chemical double-mutant cycles for the measurement of weak intermolecular interactions: Edge-to-face aromatic interactions. *Angew. Chem. Int. Ed.* **35**, 1542-1544 (1996).

179. Mati, I.K. & Cockroft, S.L. Molecular balances for quantifying non-covalent interactions. *Chem. Soc. Rev.* **39**, 4195-4205 (2010).
180. Wich, P.R. & Schmuck, C. Reversible and noncompetitive inhibition of beta-tryptase by protein surface binding of tetravalent peptide ligands identified from a combinatorial split-mix library. *Angew. Chem. Int. Ed.* **49**, 4113-4116 (2010).
181. Persch, E., Dumele, O. & Diederich, F. Molecular recognition in chemical and biological systems. *Angew. Chem. Int. Ed.* **54**, 3290-3327 (2015).
182. Biedermann, F. & Schneider, H.-J. Experimental binding energies in supramolecular complexes. *Chem. Rev.* **116**, 5216-5300 (2016).
183. Řezáč, J. & Hobza, P. Benchmark calculations of interaction energies in noncovalent complexes and their applications. *Chem. Rev.* **116**, 5038-5071 (2016).
184. He, S., *et al.* Cavitation energies can outperform dispersion interactions. *Nat. Chem.* **10**, 1252-1257 (2018).
185. Jia, F., *et al.* Naphthocage: A flexible yet extremely strong binder for singly charged organic cations. *J. Am. Chem. Soc.* **141**, 4468-4473 (2019).
186. Guo, D.-S., Uzunova, V.D., Assaf, K.I., Lazar, A.I., Liu, Y. & Nau, W.M. Inclusion of neutral guests by water-soluble macrocyclic hosts – a comparative thermodynamic investigation with cyclodextrins, calixarenes and cucurbiturils. *Supramol. Chem.* **28**, 384-395 (2016).
187. Assaf, K.I. & Nau, W.M. The chaotropic effect as an assembly motif in chemistry. *Angew. Chem. Int. Ed.* **57**, 13968-13981 (2018).
188. Remón, P., González, D., Romero, M.A., Basílio, N. & Pischel, U. Chemical signal cascading in a supramolecular network. *Chem. Commun.*, 3737-3740 (2020).
189. Brewster, M.E. & Loftsson, T. Cyclodextrins as pharmaceutical solubilizers. *Adv. Drug Deliv. Rev.* **59**, 645-666 (2007).
190. Ma, D., *et al.* Acyclic cucurbit[n]uril molecular containers enhance the solubility and bioactivity of poorly soluble pharmaceuticals. *Nat. Chem.* **4**, 503-510 (2012).
191. Schneider, H.-J. & Yatsimirsky, A.K. *Principles and methods in supramolecular chemistry*. Wiley (2000).
192. Cram, D.J. & Lein, G.M. Host-guest complexation. 36. Spherand and lithium and sodium ion complexation rates and equilibria. *J. Am. Chem. Soc.* **107**, 3657-3668 (1985).
193. Sommer, F., Marcus, Y. & Kubik, S. Effects of solvent properties on the anion binding of neutral water-soluble bis(cyclopeptides) in water and aqueous solvent mixtures. *ACS Omega*. **2**, 3669-3680 (2017).
194. Dixit, S., Crain, J., Poon, W.C.K., Finney, J.L. & Soper, A.K. Molecular segregation observed in a concentrated alcohol-water solution. *Nature*. **416**, 829-832 (2002).
195. Rosés, M., Ràfols, C., Ortega, J. & Bosch, E. Solute-solvent and solvent-solvent interactions in binary solvent mixtures. Part 1. A comparison of several preferential solvation models for describing  $\epsilon(30)$  polarity of bipolar hydrogen bond acceptor-cosolvent mixtures. *J. Chem. Soc., Perkin trans. II*. 1607-1615 (1995).
196. Marcus, Y. On the preferential solvation of drugs and pahs in binary solvent mixtures. *J. Mol. Liq.* **140**, 61-67 (2008).
197. Francisco, V., Piñeiro, A., Nau, W.M. & García-Río, L. The “true” affinities of metal cations to p-sulfonatocalix[4]arene: A thermodynamic study at neutral ph reveals a pitfall due to salt effects in microcalorimetry. *Chem. Eur. J.* **19**, 17809-17820 (2013).
198. Liu, S., Zavalij, P.Y. & Isaacs, L. Cucurbit[10]uril. *J. Am. Chem. Soc.* **127**, 16798-16799 (2005).
199. Shetty, D., Khedkar, J.K., Park, K.M. & Kim, K. Can we beat the biotin-avidin pair?: Cucurbit[7]uril-based ultrahigh affinity host-guest complexes and their applications. *Chem. Soc. Rev.* **44**, 8747-8761 (2015).

200. Lazar, A.I., Biedermann, F., Mustafina, K.R., Assaf, K.I., Hennig, A. & Nau, W.M. Nanomolar binding of steroids to cucurbit[n]urils: Selectivity and applications. *J. Am. Chem. Soc.* **138**, 13022-13029 (2016).
201. Basílio, N. & Pischel, U. Drug delivery by controlling a supramolecular host-guest assembly with a reversible photoswitch. *Chem. Eur. J.* **22**, 15208-15211 (2016).
202. Lu, X. & Isaacs, L. Uptake of hydrocarbons in aqueous solution by encapsulation in acyclic cucurbit[n]uril-type molecular containers. *Angew. Chem. Int. Ed.* **55**, 8076-8080 (2016).
203. Murray, J., Kim, K., Ogoshi, T., Yao, W. & Gibb, B.C. The aqueous supramolecular chemistry of cucurbit[n]urils, pillar[n]arenes and deep-cavity cavitands. *Chem. Soc. Rev.* **46**, 2479-2496 (2017).
204. Huang, Y., *et al.* Solubility enhancement of kinetin through host-guest interactions with cucurbiturils. *J. Incl. Phenom. Macrocycl. Chem.* **61**, 171-177 (2008).
205. Kimball, J., *et al.* On the origin and correction for inner filter effects in fluorescence part i: Primary inner filter effect-the proper approach for sample absorbance correction. *Methods Appl. Fluoresc.* **8**, 033002 (2020).
206. Weitner, T., Friganović, T. & Šakić, D. Inner filter effect correction for fluorescence measurements in microplates using variable vertical axis focus. *Anal. Chem.* **94**, 7107-7114 (2022).
207. Nau, W.M., Florea, M. & Assaf, K.I. Deep inside cucurbiturils: Physical properties and volumes of their inner cavity determine the hydrophobic driving force for host-guest complexation. *Isr. J. Chem.* **51**, 559-577 (2011).
208. Connors, K.A. Population characteristics of cyclodextrin complex stabilities in aqueous solution. *J. Pharm. Sci.* **84**, 843-848 (1995).
209. Szejtli, J. Introduction and general overview of cyclodextrin chemistry. *Chem. Rev.* **98**, 1743-1754 (1998).
210. Uzunova, V.D., Cullinane, C., Brix, K., Nau, W.M. & Day, A.I. Toxicity of cucurbit[7]uril and cucurbit[8]uril: An exploratory in vitro and in vivo study. *Org. Biomol. Chem.* **8**, 2037-2042 (2010).
211. Park, K.M., *et al.* In situ supramolecular assembly and modular modification of hyaluronic acid hydrogels for 3d cellular engineering. *ACS Nano.* **6**, 2960-2968 (2012).
212. Rowland, M.J., *et al.* An adherent tissue-inspired hydrogel delivery vehicle utilised in primary human glioma models. *Biomaterials.* **179**, 199-208 (2018).
213. Fanali, G., di Masi, A., Trezza, V., Marino, M., Fasano, M. & Ascenzi, P. Human serum albumin: From bench to bedside. *Mol. Aspects Med.* **33**, 209-290 (2012).
214. Frostell-Karlsson, Å., *et al.* Biosensor analysis of the interaction between immobilized human serum albumin and drug compounds for prediction of human serum albumin binding levels. *J. Med. Chem.* **43**, 1986-1992 (2000).
215. Maes, V., Engelborghs, Y., Hoebeke, J., Maras, Y. & Vercrucysse, A. Fluorimetric analysis of the binding of warfarin to human serum albumin. Equilibrium and kinetic study. *Mol. Pharmacol.* **21**, 100-107 (1982).
216. Sinn, S., Spuling, E., Bräse, S. & Biedermann, F. Rational design and implementation of a cucurbit[8]uril-based indicator-displacement assay for application in blood serum. *Chem. Sci.* **10**, 6584-6593 (2019).
217. Dotsikas, Y., Kontopanou, E., Allagiannis, C. & Loukas, Y.L. Interaction of 6-p-toluidinylnaphthalene-2-sulphonate with  $\beta$ -cyclodextrin. *J. Pharm. Biomed. Anal.* **23**, 997-1003 (2000).
218. Hagedoorn, P.-L. Isothermal titration calorimetry in biocatalysis. *Front. Cat.* **2**, (2022).
219. Nývlt, J. Nucleation and growth rate in mass crystallization. *Prog. Cryst. Growth Charact. Mater.* **9**, 335-370 (1984).

220. Tavare, N.S. Characterization of crystallization kinetics from batch experiments. In: *Industrial crystallization: Process simulation analysis and design*. Springer (1995).
221. Elbary, A.A., Vallner, J.J. & Whitworth, C.W. Effect of albumin conformation on the binding of phenylbutazone and oxyphenbutazone to human serum albumin. *J. Pharm. Sci.* **71**, 241-244 (1982).
222. Assaf, K.I., Suckova, O., Al Danaf, N., von Glasenapp, V., Gabel, D. & Nau, W.M. Dodecaborate-functionalized anchor dyes for cyclodextrin-based indicator displacement applications. *Org. Lett.* **18**, 932-935 (2016).
223. Sindelar, V., Cejas, M.A., Raymo, F.M. & Kaifer, A.E. Tight inclusion complexation of 2,7-dimethyldiazapyrenium in cucurbit[7]uril. *New J. Chem.* **29**, 280-282 (2005).
224. Anzenbacher, J.P., Lubal, P., Buček, P., Palacios, M.A. & Kozelkova, M.E. A practical approach to optical cross-reactive sensor arrays. *Chem. Soc. Rev.* **39**, 3954-3979 (2010).
225. Umali, A.P., *et al.* Discrimination of flavonoids and red wine varieties by arrays of differential peptidic sensors. *Chem. Sci.* **2**, 439-445 (2011).
226. Beatty, M.A., Borges-González, J., Sinclair, N.J., Pye, A.T. & Hof, F. Analyte-driven disassembly and turn-on fluorescent sensing in competitive biological media. *J. Am. Chem. Soc.* **140**, 3500-3504 (2018).
227. Lin, R.-G., Long, L.-S., Huang, R.-B. & Zheng, L.-S. Directing role of hydrophobic–hydrophobic and hydrophilic–hydrophilic interactions in the self-assembly of calixarenes/cucurbiturils-based architectures. *Cryst. Growth Des.* **8**, 791-794 (2008).
228. Pessêgo, M., Mendoza, J., da Silva, J.P., Basilio, N. & Garcia-Rio, L. Unveiling the formation 1:2 supramolecular complexes between cucurbit[7]uril and a cationic calix[4]arene derivative. *Chem. Commun.* **55**, 13828-13831 (2019).
229. Tian, X., *et al.* 4-sulfocalix[4]arene/cucurbit[7]uril-based supramolecular assemblies through the outer surface interactions of cucurbit[n]uril. *ACS Omega.* **3**, 6665-6672 (2018).
230. Zhu, J.M., Chen, L.X., Chen, K., Zeng, X. & Tao, Z. Synthesis of a functionalised calix[4]arene and its interactions with hemicucurbit[6,7]urils and cucurbit[8]uril. *Tetrahedron.* **74**, 4095-4099 (2018).
231. Kaifer, A.E., Li, W., Silvi, S. & Sindelar, V. Pronounced pH effects on the kinetics of cucurbit[7]uril-based pseudorotaxane formation and dissociation. *Chem. Commun.* **48**, 6693 (2012).
232. Vincil, G.A. & Urbach, A.R. Effects of the number and placement of positive charges on viologen–cucurbit[n]uril interactions. *Supramol. Chem.* **20**, 681-687 (2008).
233. Biedermann, F., Vendruscolo, M., Scherman, O.A., De Simone, A. & Nau, W.M. Cucurbit[8]uril and blue-box: High-energy water release overwhelms electrostatic interactions. *J. Am. Chem. Soc.* **135**, 14879-14888 (2013).
234. Borden, S.A., Saatchi, A., Vandergrift, G.W., Palaty, J., Lysyshyn, M. & Gill, C.G. A new quantitative drug checking technology for harm reduction: Pilot study in Vancouver, Canada using paper spray mass spectrometry. *Drug Alcohol Rev.* **41**, 410-418 (2022).
235. Fischer, B., Goldman, B., Rehm, J. & Popova, S. Non-medical use of prescription opioids and public health in Canada. *Can. J. Public Health.* **99**, 182-184 (2008).
236. Cole, C., Jones, L., McVeigh, J., Kicman, A., Syed, Q. & Bellis, M. Adulterants in illicit drugs: A review of empirical evidence. *Drug Test. Anal.* **3**, 89-96 (2011).
237. Laposchan, S., Kranenburg, R.F. & van Asten, A.C. Impurities, adulterants and cutting agents in cocaine as potential candidates for retrospective mining of GC-MS data. *Sci. Justice.* **62**, 60-75 (2022).
238. Żubrycka, A., *et al.* Illicit drugs street samples and their cutting agents. The result of the GC-MS based profiling define the guidelines for sensors development. *Talanta.* **237**, 122904 (2022).
239. Origin(Pro), V.O.C., Northampton, MA, USA Version 22b.

240. Gill, A.D., Hickey, B.L., Zhong, W. & Hooley, R.J. Selective sensing of the and related metabolites in biofluids by host:Guest arrays. *Chem. Commun.* **56**, 4352-4355 (2020).
241. Brosh-Nissimov, T., Ingbir, M., Weintal, I., Fried, M. & Porat, R. Central nervous system toxicity following topical skin application of lidocaine. *Eur. J. Clin. Pharmacol.* **60**, 683-684 (2004).
242. Chiang, Y.Y., Tseng, K.F., Lih, Y.W., Tsai, T.C., Liu, C.T. & Leung, H.K. Lidocaine-induced cns toxicity--a case report. *Acta Anaesthesiol. Sin.* **34**, 243-246 (1996).
243. Symoens, J., Veys, E., Mielants, M. & Pinals, R. Adverse reactions to levamisole. *Cancer Treat. Rep.* **62**, 1721-1730 (1978).
244. Larocque, A. & Hoffman, R.S. Levamisole in cocaine: Unexpected news from an old acquaintance. *Clin. Toxicol.* **50**, 231-241 (2012).
245. Manzar, Z., Dutta, T., Koner, A.L. & Mitra, A. Cucurbit[7]uril nanoencapsulation reduces the unpalatability of bitter phytochemicals. *J. Agric. Sci. Technol.* **1**, 117-123 (2021).
246. Scorza, C., Prieto, J.P. & Fabius, S. Caffeine as an active adulterant: Implication for drugs of abuse consumption. In: *Handbook of substance misuse and addictions: From biology to public health*. Springer International Publishing (2022).
247. Harris, M., Scott, J., Wright, T., Brathwaite, R., Ciccarone, D. & Hope, V. Injecting-related health harms and overuse of acidifiers among people who inject heroin and crack cocaine in london: A mixed-methods study. *Harm Reduct. J.* **16**, 60 (2019).
248. Krämer, J., Grimm, L.M., Zhong, C., Hirtz, M. & Biedermann, F. A supramolecular cucurbit[8]uril-based rotaxane chemosensor for the optical tryptophan detection in human serum and urine. *Nat. Commun.* **14**, 518 (2023).
249. Comai, S., Bertazzo, A., Brughera, M. & Crotti, S. Chapter five - tryptophan in health and disease. In: *Advances in clinical chemistry*. Elsevier (2020).
250. Platten, M., Nollen, E.A.A., Röhrig, U.F., Fallarino, F. & Opitz, C.A. Tryptophan metabolism as a common therapeutic target in cancer, neurodegeneration and beyond. *Nat. Rev. Drug Discov.* **18**, 379-401 (2019).
251. van der Goot, A.T. & Nollen, E.A.A. Tryptophan metabolism: Entering the field of aging and age-related pathologies. *Trends Mol. Med.* **19**, 336-344 (2013).
252. Lanari, A., Amenta, F., Silvestrelli, G., Tomassoni, D. & Parnetti, L. Neurotransmitter deficits in behavioural and psychological symptoms of alzheimer's disease. *Mech. Ageing Dev.* **127**, 158-165 (2006).
253. Geisler, S., Mayersbach, P., Becker, K., Schennach, H., Fuchs, D. & Gostner, J.M. Serum tryptophan, kynurenine, phenylalanine, tyrosine and neopterin concentrations in 100 healthy blood donors. *Pteridines.* **26**, 31-36 (2015).
254. Cynober, L.A. Plasma amino acid levels with a note on membrane transport: Characteristics, regulation, and metabolic significance. *Nutrition.* **18**, 761-766 (2002).
255. Strasser, B., *et al.* Probiotic supplements beneficially affect tryptophan-kynurenine metabolism and reduce the incidence of upper respiratory tract infections in trained athletes: A randomized, double-blinded, placebo-controlled trial. *Nutrients.* **8**, (2016).
256. Murr, C., Grammer, T.B., Kleber, M.E., Meinitzer, A., März, W. & Fuchs, D. Low serum tryptophan predicts higher mortality in cardiovascular disease. *Eur. J. Clin. Invest.* **45**, 247-254 (2015).
257. Li, Y., Tang, A.-G. & Mu, S. Hplc-fld determination of serum aromatic amino acids: Application in chronic kidney disease patients. *Clin. Chim. Acta.* **412**, 1032-1035 (2011).
258. Trabado, S., *et al.* The human plasma-metabolome: Reference values in 800 french healthy volunteers; impact of cholesterol, gender and age. *PLOS One.* **12**, e0173615 (2017).
259. Comai, S., Bertazzo, A., Carretti, N., Podfigurna-Stopa, A., Luisi, S. & Costa, C.V.L. Serum levels of tryptophan, 5-hydroxytryptophan and serotonin in patients affected with different forms of amenorrhea. *Int. J. Tryptophan Res.* **3**, IJTR.S3804 (2010).

260. Attenburrow, M.J., *et al.* The effect of a nutritional source of tryptophan on dieting-induced changes in brain 5-ht function. *Psychol. Med.* **33**, 1381-1386 (2003).
261. Ninomiya, S., *et al.* Low levels of serum tryptophan underlie skeletal muscle atrophy. *Nutrients.* **12**, 978 (2020).
262. Nikolaus, S., *et al.* Increased tryptophan metabolism is associated with activity of inflammatory bowel diseases. *Gastroenterology.* **153**, 1504-1516.e1502 (2017).
263. Fonteh, A.N., Harrington, R.J., Tsai, A., Liao, P. & Harrington, M.G. Free amino acid and dipeptide changes in the body fluids from alzheimer's disease subjects. *Amino Acids.* **32**, 213-224 (2007).
264. Konje, V.C., *et al.* Tryptophan levels associate with incident cardiovascular disease in chronic kidney disease. *Clin. Kidney J.* **14**, 1097-1105 (2020).
265. Weiss, G., Schroecksadel, K., Mattle, V., Winkler, C., Konwalinka, G. & Fuchs, D. Possible role of cytokine-induced tryptophan degradation in anaemia of inflammation. *Eur. J. Haematol.* **72**, 130-134 (2004).
266. Herrera-Van Oostdam, A.S., *et al.* Immunometabolic signatures predict risk of progression to sepsis in covid-19. *PLOS One.* **16**, e0256784 (2021).
267. Ploder, M., *et al.* Accelerated tryptophan degradation predicts poor survival in trauma and sepsis patients. *Int. J. Tryptophan Res.* **3**, IJTR.S3983 (2010).
268. Supramolecular systems in biomedical fields. (ed Schneider, H.-J.). Royal Society of Chemistry (2013).
269. Yamamoto, Y., Kanayama, N., Nakayama, Y. & Matsushima, N. Current status, issues and future prospects of personalized medicine for each disease. *J. Pers. Med.* **12**, 444 (2022).
270. Zarei, M. Advances in point-of-care technologies for molecular diagnostics. *Biosens. Bioelectron.* **98**, 494-506 (2017).
271. Wu, J., Dong, M., Rigatto, C., Liu, Y. & Lin, F. Lab-on-chip technology for chronic disease diagnosis. *npj Digital Medicine.* **1**, 7 (2018).
272. Schmerler, D., Neugebauer, S., Ludewig, K., Bremer-Streck, S., Brunkhorst, F.M. & Kiehntopf, M. Targeted metabolomics for discrimination of systemic inflammatory disorders in critically ill patients. *J. Lipid Res.* **53**, 1369-1375 (2012).
273. Trivedi, D.K., Hollywood, K.A. & Goodacre, R. Metabolomics for the masses: The future of metabolomics in a personalized world. *New Horiz. Transl. Med.* **3**, 294-305 (2017).
274. Zhang, A., Sun, H., Wang, P., Han, Y. & Wang, X. Modern analytical techniques in metabolomics analysis. *Analyst.* **137**, 293-300 (2012).
275. Roux, A., Lison, D., Junot, C. & Heilier, J.-F. Applications of liquid chromatography coupled to mass spectrometry-based metabolomics in clinical chemistry and toxicology: A review. *Clin. Biochem.* **44**, 119-135 (2011).
276. Bockus, A.T., *et al.* Cucurbit[7]uril-tetramethylrhodamine conjugate for direct sensing and cellular imaging. *J. Am. Chem. Soc.* **138**, 16549-16552 (2016).
277. Jang, Y., *et al.* Point-of-use detection of amphetamine-type stimulants with host-molecule-functionalized organic transistors. *Chem.* **3**, 641-651 (2017).
278. Nightingale, A.M., *et al.* Monitoring biomolecule concentrations in tissue using a wearable droplet microfluidic-based sensor. *Nat. Commun.* **10**, 2741 (2019).
279. He, H., Mortellaro, M.A., Leiner, M.J.P., Young, S.T., Fraatz, R.J. & Tusa, J.K. A fluorescent chemosensor for sodium based on photoinduced electron transfer. *Anal. Chem.* **75**, 549-555 (2003).
280. Wu, L., *et al.* Aptamer-based detection of circulating targets for precision medicine. *Chem. Rev.* **121**, 12035-12105 (2021).
281. Wolfbeis, O.S. Editorial: Probes, sensors, and labels: Why is real progress slow? *Angew. Chem. Int. Ed.* **52**, 9864-9865 (2013).

282. Schill, G. & Zollenkopf, H. Rotaxanverbindungen. *Justus Liebigs Ann. Chem.* **721**, 53-74 (1969).
283. Safarowsky, O., Windisch, B., Mohry, A. & Vögtle, F. Nomenclature for catenanes, rotaxanes, molecular knots, and assemblies derived from these structural elements. *J. Prakt. Chem.* **342**, 437-444 (2000).
284. Wolf, M., *et al.* Light triggers molecular shuttling in rotaxanes: Control over proximity and charge recombination. *Chem. Sci.* **10**, 3846-3853 (2019).
285. Serreli, V., Lee, C.-F., Kay, E.R. & Leigh, D.A. A molecular information ratchet. *Nature.* **445**, 523-527 (2007).
286. Anelli, P.L., *et al.* Molecular meccano. 1. [2]rotaxanes and a [2]catenane made to order. *J. Am. Chem. Soc.* **114**, 193-218 (1992).
287. Heard, A.W. & Goldup, S.M. Synthesis of a mechanically planar chiral rotaxane ligand for enantioselective catalysis. *Chem.* **6**, 994-1006 (2020).
288. Langton, M.J., Duckworth, L.C. & Beer, P.D. Nitrate anion templated assembly of a [2]rotaxane for selective nitrate recognition in aqueous solvent mixtures. *Chem. Commun.* **49**, 8608-8610 (2013).
289. Arunkumar, E., Forbes, C.C., Noll, B.C. & Smith, B.D. Squaraine-derived rotaxanes: Sterically protected fluorescent near-ir dyes. *J. Am. Chem. Soc.* **127**, 3288-3289 (2005).
290. Neel, A.J., Hilton, M.J., Sigman, M.S. & Toste, F.D. Exploiting non-covalent  $\pi$  interactions for catalyst design. *Nature.* **543**, 637-646 (2017).
291. Huang, Z., *et al.* Highly compressible glass-like supramolecular polymer networks. *Nat. Mater.* **21**, 103-109 (2022).
292. Zhang, Y.-M., Liu, J.-H., Yu, Q., Wen, X. & Liu, Y. Targeted polypeptide-microtubule aggregation with cucurbit[8]uril for enhanced cell apoptosis. *Angew. Chem. Int. Ed.* **58**, 10553-10557 (2019).
293. Wiemann, M., Niebuhr, R., Juan, A., Cavatorta, E., Ravoo, B.J. & Jonkheijm, P. Photo-responsive bioactive surfaces based on cucurbit[8]uril-mediated host-guest interactions of arylazopyrazoles. *Chem. Eur. J.* **24**, 813-817 (2018).
294. Tian, F., Jiao, D., Biedermann, F. & Scherman, O.A. Orthogonal switching of a single supramolecular complex. *Nat. Commun.* **3**, 1207 (2012).
295. Biedermann, F., *et al.* Benzobis(imidazolium)-cucurbit[8]uril complexes for binding and sensing aromatic compounds in aqueous solution. *Chem. Eur. J.* **16**, 13716-13722 (2010).
296. de Vink, P.J., Briels, J.M., Schrader, T., Milroy, L.-G., Brunsveld, L. & Ottmann, C. A binary bivalent supramolecular assembly platform based on cucurbit[8]uril and dimeric adapter protein 14-3-3. *Angew. Chem. Int. Ed.* **56**, 8998-9002 (2017).
297. Stang, P.J., Cao, D.H., Saito, S. & Arif, A.M. Self-assembly of cationic, tetranuclear, pt(ii) and pd(ii) macrocyclic squares. X-ray crystal structure of [pt<sup>2+</sup>(dppp)(4,4'-bipyridyl).Cntdot.2-oso2cf3]<sub>4</sub>. *J. Am. Chem. Soc.* **117**, 6273-6283 (1995).
298. Hünig, S., Groß, J., Lier, E.F. & Quast, H. Über zweistufige redoxsysteme, xii1) synthese und polarographie von quartärsalzen der phenanthroline, des 2,7-diazapyrens sowie der diazoniapentaphene. *Justus Liebigs Ann. Chem.* **1973**, 339-358 (1973).
299. Tewari, N., Nizar, H., Mane, A., George, V. & Prasad, M. Deacetylation of thioacetate using acetyl chloride in methanol. *Synth. Commun.* **36**, 1911-1914 (2006).
300. Loftsson, T., Saokham, P. & Sá Couto, A.R. Self-association of cyclodextrins and cyclodextrin complexes in aqueous solutions. *Int. J. Pharm.* **560**, 228-234 (2019).
301. Bhasikuttan, A.C., Mohanty, J., Nau, W.M. & Pal, H. Efficient fluorescence enhancement and cooperative binding of an organic dye in a supra-biomolecular host-protein assembly. *Angew. Chem. Int. Ed.* **46**, 4120-4122 (2007).
302. Barooah, N., Khurana, R., Bhasikuttan, A.C. & Mohanty, J. Stimuli-responsive supra-biomolecular nanoassemblies of cucurbit[7]uril with bovine serum albumin: Drug delivery and sensor applications. *Isr. J. Chem.* **58**, 276-285 (2018).

303. Plumet, C., *et al.* A  $\beta$ -cyclodextrin-albumin conjugate for enhancing therapeutic efficacy of cytotoxic drugs. *Bioconjugate Chem.* **33**, 1138-1144 (2022).
304. Khan, M.N. Kinetics and mechanism of the alkaline hydrolysis of maleimide. *J. Pharm. Sci.* **73**, 1767-1771 (1984).
305. Ellman, G.L. Tissue sulfhydryl groups. *Arch. Biochem. Biophys.* **82**, 70-77 (1959).
306. Mukherjee, A., *et al.* 2,7-diazapyrenes: A brief review on synthetic strategies and application opportunities. *RSC Adv.* **12**, 9323-9341 (2022).
307. Merz, J., *et al.* Pyrene molecular orbital shuffle—controlling excited state and redox properties by changing the nature of the frontier orbitals. *Chem. Eur. J.* **23**, 13164-13180 (2017).
308. Becker, H.-C., Broo, A. & Nordén, B. Ground- and excited-state properties of molecular complexes between adenine and 2,7-diazapyrene and its n-methylated cations. *J. Phys. Chem. A.* **101**, 8853-8860 (1997).
309. Maciel, A.T., Vitorio, D., Salles, L.D. & Park, M. Sodium concentration in urine greater than in the plasma: Possible biomarker of normal renal function and better outcome in critically ill patients. *Anaesth. Intensive Care.* **42**, 584-591 (2014).
310. El-Barghouthi, M.I., Bodoor, K., Abuhasan, O.M., Assaf, K.I., Al Hourani, B.J. & Rawashdeh, A.M.M. Binary and ternary complexes of cucurbit[8]uril with tryptophan, phenylalanine, and tyrosine: A computational study. *ACS Omega.* **7**, 10729-10737 (2022).
311. Schwab, R.S., England, A.C., Jr., Poskanzer, D.C. & Young, R.R. Amantadine in the treatment of parkinson's disease. *JAMA.* **208**, 1168-1170 (1969).
312. Liu, S., Ruspic, C., Mukhopadhyay, P., Chakrabarti, S., Zavalij, P.Y. & Isaacs, L. The cucurbit[n]uril family: Prime components for self-sorting systems. *J. Am. Chem. Soc.* **127**, 15959-15967 (2005).
313. Hervé, C., Beyne, P., Jamault, H. & Delacoux, E. Determination of tryptophan and its kynurenine pathway metabolites in human serum by high-performance liquid chromatography with simultaneous ultraviolet and fluorimetric detection. *J. Chromatogr. B Biomed. Appl.* **675**, 157-161 (1996).
314. Magos, L. C. Lentner (ed.). Geigy scientific tables, 8th edition. Vol. 1. Units of measurement. Body fluids. Composition of the body. Nutrition. 1981, 298 pp. Vol. 2. Introduction to statistics. Statistical tables. Mathematical formulae. 1982, 241 pp. Vol. 3. Physical chemistry. Composition of the blood. Haematology. Human somatometric data. 1984, 359 pp. Vol. 4. Biochemistry. Metabolism of xenobiotics. Inborn error of metabolism. Pharmacogenetics and ecogenetics. 1986, 330 pp. Ciba-geigy, Distributed by by Farrand press. *J. Appl. Toxicol.* **7**, 413-413 (1987).
315. Borg, J., Warter, J.M., Schlienger, J.L., Imler, M., Marescaux, C. & Mack, G. Neurotransmitter modifications in human cerebrospinal fluid and serum during hepatic encephalopathy. *J. Neurol. Sci.* **57**, 343-356 (1982).
316. Jourde-Chiche, N., *et al.* Levels of circulating endothelial progenitor cells are related to uremic toxins and vascular injury in hemodialysis patients. *J. Thromb. Haemost.* **7**, 1576-1584 (2009).
317. Lambert, G., Naredi, S., Edén, E., Rydenhag, B. & Friberg, P. Monoamine metabolism and sympathetic nervous activation following subarachnoid haemorrhage: Influence of gender and hydrocephalus. *Brain Res Bull.* **58**, 77-82 (2002).
318. Löser, C., Fölsch, U.R., Paprotny, C. & Creutzfeldt, W. Polyamine concentrations in pancreatic tissue, serum, and urine of patients with pancreatic cancer. *Pancreas.* **5**, (1990).
319. Gill, D.S., Fonseca, V.A., Barradas, M.A., Balliod, R., Moorhead, J.F. & Dandona, P. Plasma histamine in patients with chronic renal failure and nephrotic syndrome. *J. Clin. Pathol.* **44**, 243-245 (1991).

320. Yu, X., Liang, W., Huang, Q., Wu, W., Chruma, J.J. & Yang, C. Room-temperature phosphorescent  $\gamma$ -cyclodextrin-cucurbit[6]uril-cowheeled [4]rotaxanes for specific sensing of tryptophan. *Chem. Commun.* **55**, 3156-3159 (2019).
321. Huang, Q., *et al.* Inherently chiral azonia[6]helicene-modified  $\beta$ -cyclodextrin: Synthesis, characterization, and chirality sensing of underivatized amino acids in water. *J. Org. Chem.* **81**, 3430-3434 (2016).
322. Wei, T.-B., *et al.* A novel functionalized pillar[5]arene-based selective amino acid sensor for l-tryptophan. *Org. Chem. Front.* **4**, 210-213 (2017).
323. Zhu, X., *et al.* Selective recognition of tryptophan by a methylpillar[5]arene-based supramolecular fluorescent probe. *Spectrochim. Acta Pt. A: Mol. Biomol. Spectrosc.* **250**, 119381 (2021).
324. Ramalingam, V. & Urbach, A.R. Cucurbit[8]uril rotaxanes. *Org. Lett.* **13**, 4898-4901 (2011).
325. Weißenstein, A., Saha-Möller, C.R. & Würthner, F. Optical sensing of aromatic amino acids and dipeptides by a crown-ether-functionalized perylene bisimide fluorophore. *Chem. Eur. J.* **24**, 8009-8016 (2018).
326. Ghale, G. & Nau, W.M. Dynamically analyte-responsive macrocyclic host-fluorophore systems. *Acc. Chem. Res.* **47**, 2150-2159 (2014).
327. Sutariya, P.G., Pandya, A., Lodha, A. & Menon, S.K. A unique fluorescence biosensor for selective detection of tryptophan and histidine. *Analyst.* **139**, 4794-4798 (2014).
328. Carrillo, R., Feher-Voelger, A. & Martín, T. Enantioselective cooperativity between intrareceptor interactions and guest binding: Quantification of reinforced chiral recognition. *Angew. Chem. Int. Ed.* **50**, 10616-10620 (2011).
329. Kornhuber, M.E., Balabanova, S., Heiligensetzer, G.V., Kornhuber, C., Zettlmeissl, H. & Kornhuber, A.W. Stability of human blood serum aminoacids after storage at different pH and temperature conditions. *Clin. Chim. Acta.* **197**, 189-200 (1991).
330. An, Z., Shi, C., Li, P. & Liu, L. Stability of amino acids and related amines in human serum under different preprocessing and pre-storage conditions based on itraq®-LC-MS/MS. *Biology Open.* **10**, (2021).
331. Miskolczy, Z., Megyesi, M., Biczók, L., Prabodh, A. & Biedermann, F. Kinetics and mechanism of cation-induced guest release from cucurbit[7]uril. *Chem. Eur. J.* **26**, 7433-7441 (2020).
332. Megyesi, M., Biczók, L. & Jablonkai, I. Highly sensitive fluorescence response to inclusion complex formation of berberine alkaloid with cucurbit[7]uril. *J. Phys. Chem. C.* **112**, 3410-3416 (2008).
333. Liu, Y. & You, C.-C. Inclusion complexation of  $\beta$ -cyclodextrin and 6-o- $\alpha$ -maltosyl- and 2-o-(2-hydroxypropyl)- $\beta$ -cyclodextrins -with some fluorescent dyes. *J. Phys. Org. Chem.* **14**, 11-16 (2001).
334. Shaw, A.K. & Pal, S.K. Resonance energy transfer and ligand binding studies on pH-induced folded states of human serum albumin. *J. Photochem. Photobiol. B.* **90**, 187-197 (2008).
335. Haque, N. & Prabhu, N.P. Insights into protein-tns (2-p-toluidinylnaphthalene-6-sulfonate) interaction using molecular dynamics simulation. *J. Mol. Struct.* **1068**, 261-269 (2014).
336. Ludden, M.J.W., *et al.* Assembly of bionanostructures onto  $\beta$ -cyclodextrin molecular printboards for antibody recognition and lymphocyte cell counting. *J. Am. Chem. Soc.* **130**, 6964-6973 (2008).
337. Liu, G., Hirtz, M., Fuchs, H. & Zheng, Z. Development of dip-pen nanolithography (dnp) and its derivatives. *Small.* **15**, 1900564 (2019).

338. Dadfar, S.M.M., Sekula-Neuner, S., Bog, U., Trouillet, V. & Hirtz, M. Site-specific surface functionalization via microchannel cantilever spotting ( $\mu\text{cs}$ ): Comparison between azide–alkyne and thiol–alkyne click chemistry reactions. *Small*. **14**, 1800131 (2018).
339. Atwater, J., *et al.* Combinatorial synthesis of macromolecular arrays by microchannel cantilever spotting ( $\mu\text{cs}$ ). *Adv. Mater.* **30**, 1801632 (2018).
340. Zhong, C., Hu, C., Kumar, R., Trouillet, V., Biedermann, F. & Hirtz, M. Cucurbit[n]uril-immobilized sensor arrays for indicator-displacement assays of small bioactive metabolites. *ACS Appl. Nano Mater.* **4**, 4676-4687 (2021).
341. Zhao, X., Liu, R., Teng, Y. & Liu, X. The interaction between  $\text{ag}^+$  and bovine serum albumin: A spectroscopic investigation. *Sci. Total Environ.* **409**, 892-897 (2011).
342. Rivera del Rio, A., Keppler, J.K., Boom, R.M. & Janssen, A.E.M. Protein acidification and hydrolysis by pepsin ensure efficient trypsin-catalyzed hydrolysis. *Food & Function*. **12**, 4570-4581 (2021).
343. Chen, Y. & Ma, W. The origin of biological homochirality along with the origin of life. *PLoS Comp. Biol.* **16**, e1007592 (2020).
344. Banreti, A., *et al.* Biological effects of the loss of homochirality in a multicellular organism. *Nat. Commun.* **13**, 7059 (2022).
345. Rehman, W., Arfons, L.M. & Lazarus, H.M. The rise, fall and subsequent triumph of thalidomide: Lessons learned in drug development. *Ther. Adv. Hematol.* **2**, 291-308 (2011).
346. Grishin, D.V., Zhdanov, D.D., Pokrovskaya, M.V. & Sokolov, N.N. D-amino acids in nature, agriculture and biomedicine. *All Life*. **13**, 11-22 (2020).
347. Ala-Jaakkola, R., Laitila, A., Ouwehand, A.C. & Lehtoranta, L. Role of d-mannose in urinary tract infections – a narrative review. *Nutr. J.* **21**, 18 (2022).
348. Prabodh, A., *et al.* Fluorescence detected circular dichroism (fdcd) for supramolecular host–guest complexes. *Chem. Sci.* **12**, 9420-9431 (2021).
349. You, L., Berman, J.S. & Anslyn, E.V. Dynamic multi-component covalent assembly for the reversible binding of secondary alcohols and chirality sensing. *Nat. Chem.* **3**, 943-948 (2011).
350. Leung, D., Folmer-Andersen, J.F., Lynch, V.M. & Anslyn, E.V. Using enantioselective indicator displacement assays to determine the enantiomeric excess of  $\alpha$ -amino acids. *J. Am. Chem. Soc.* **130**, 12318-12327 (2008).
351. Galan, A., Andreu, D., Echavarren, A.M., Prados, P. & De Mendoza, J. A receptor for the enantioselective recognition of phenylalanine and tryptophan under neutral conditions. *J. Am. Chem. Soc.* **114**, 1511-1512 (1992).
352. Pagliari, S., *et al.* Enantioselective fluorescence sensing of amino acids by modified cyclodextrins: Role of the cavity and sensing mechanism. *Chem. Eur. J.* **10**, 2749-2758 (2004).
353. Pu, L. Fluorescence of organic molecules in chiral recognition. *Chem. Rev.* **104**, 1687-1716 (2004).
354. Wang, L.-L., Quan, M., Yang, T.-L., Chen, Z. & Jiang, W. A green and wide-scope approach for chiroptical sensing of organic molecules through biomimetic recognition in water. *Angew. Chem. Int. Ed.* **59**, 23817-23824 (2020).
355. Harper, L., Powell, J. & Pijl, E.M. An overview of forensic drug testing methods and their suitability for harm reduction point-of-care services. *Harm Reduct. J.* **14**, 52 (2017).
356. Ebraldize, I.I., Laschuk, N.O., Poisson, J. & Zenkina, O.V. Chapter 1 - colorimetric sensors and sensor arrays. In: *Nanomaterials design for sensing applications*. Elsevier (2019).
357. Victoria, U.o. Substance drug checking (ed <https://substance.uvic.ca/>).

358. Fulmer, G.R., *et al.* Nmr chemical shifts of trace impurities: Common laboratory solvents, organics, and gases in deuterated solvents relevant to the organometallic chemist. *Organometallics*. **29**, 2176-2179 (2010).
359. Marquez, C., Huang, F. & Nau, W. Cucurbiturils: Molecular nanocapsules for time-resolved fluorescence-based assays. *IEEE Trans. Nanobioscience*. **3**, 39-45 (2004).
360. Jiao, D. & Scherman, O.A. Isolation of cucurbit[n]uril homologues with imidazolium salts in a recyclable manner. *Green Chem*. **14**, 2445-2449 (2012).
361. Nijhawan, L., *et al.* Informed consent: Issues and challenges. *J. Adv. Pharm. Technol. Res.* **4**, 134-140 (2013).
362. Association, W.M. World medical association declaration of helsinki: Ethical principles for medical research involving human subjects. *JAMA*. **310**, 2191-2194 (2013).
363. Swinehart, D.F. The beer-lambert law. *J. Chem. Educ.* **39**, 333 (1962).
364. Khan, M.T.H. *Bioactive heterocycles iv*, 1st edn. Springer-Verlag (2007).
365. Díaz, M.S., Freile, M.L. & Gutiérrez, M.I. Solvent effect on the uv/vis absorption and fluorescence spectroscopic properties of berberine. *Photoch. Photobio. Sci.* **8**, 970-974 (2009).
366. Evans, J.P., Ahn, K. & Klinman, J.P. Evidence that dioxygen and substrate activation are tightly coupled in dopamine  $\beta$ -Monooxygenase: Implications for the reactive oxygen species. *J. Biol. Chem.* **278**, 49691-49698 (2003).
367. Raichenok, T.F., Litvinovskaya, R.P., Zhabinskii, V.N., Raiman, M.E., Kurtikova, A.L. & Minin, P.S. Synthesis and spectral and luminescence properties of new conjugates of brassinosteroids for immunofluorescence analysis. *Chem. Nat. Compd.* **48**, 267-271 (2012).
368. Marmorstein, R.Q., Joachimiak, A., Sprinzl, M. & Sigler, P.B. The structural basis for the interaction between l-tryptophan and the escherichia coli trp aporepressor. *J. Biol. Chem.* **262**, 4922-4927 (1987).
369. Prabodh, A., *et al.* Chirality sensing of terpenes, steroids, amino acids, peptides and drugs with acyclic cucurbit[n]urils and molecular tweezers. *Chem. Commun.* **56**, 4652-4655 (2020).
370. *Handbook of biochemistry and molecular biology. Proteins-V. 1-3*, 3rd edn. CRC Press (1976).
371. Vlasova, N.N., Markitan, O.V. & Stukalina, N.G. The adsorption of biogenic amines on the surface of highly dispersed silica from aqueous solutions. *Colloid J.* **68**, 384-386 (2006).
372. Nishino, H., Kosaka, A., Hembury, G.A., Matsushima, K. & Inoue, Y. The ph dependence of the anisotropy factors of essential amino acids. *J. Chem. Soc. Perk. Trans.*, 582-590 (2002).
373. Bendeby, B., Kenne, L. & Sandström, C. <sup>1</sup>H-NMR studies of the inclusion complexes between  $\alpha$ -cyclodextrin and adamantane derivatives using both exchangeable hydroxy protons and non-exchangeable aliphatic protons. *J. Incl. Phenom. Macrocycl. Chem.* **50**, 173-181 (2004).
374. <https://www.drugbank.ca/drugs/DB00812> Pbz.
375. Lazar, A.I., Biedermann, F., Mustafina, K.R., Assaf, K.I., Hennig, A. & Nau, W.M. Nanomolar binding of steroids to cucurbit[n]urils: Selectivity and applications. *J. Am. Chem. Soc.* **138**, 13022-13029 (2016).
376. Barati, F., Yao, Q. & Asa-Awuku, A.A. Insight into the role of water-soluble organic solvents for the cloud condensation nuclei activation of cholesterol. *ACS Earth Space Chem.* **3**, 1697-1705 (2019).
377. Stella, V.J., Mooney, K.G. & Pipkin, J.D. Dissolution and ionization of warfarin. *J. Pharm. Sci.* **73**, 946-948 (1984).

378. Wang, C., Perumalla, S.R., Lu, R., Fang, J. & Sun, C.C. Sweet berberine. *Cryst. Growth Des.* **16**, 933-939 (2016).
379. Janoschka, T., Martin, N., Hager, M.D. & Schubert, U.S. An aqueous redox-flow battery with high capacity and power: The temptma/mv system. *Angew. Chem. Int. Ed.* **55**, 14427-14430 (2016).
380. Zhao, J., *et al.* Simultaneous determination of urinary tryptophan, tryptophan-related metabolites and creatinine by high performance liquid chromatography with ultraviolet and fluorimetric detection. *J. Chromatogr. B.* **879**, 2720-2725 (2011).
381. Xu, J., *et al.* Microfabricated quill-type surface patterning tools for the creation of biological micro/nano arrays. *Biomed. Microdevices.* **6**, 117-123 (2004).
382. Blacker, A.J., Jazwinski, J. & Lehn, J.-M. Molecular anion binding and substrate photooxidation in visible light by 2,7-diazapyrenium cations. *Helv. Chim. Acta.* **70**, 1-12 (1987).
383. Verch, A., Hahn, H., Krause, E., Cölfen, H. & Börner, H.G. A modular approach towards functional decoration of peptide-polymer nanotapes. *Chem. Commun.* **46**, 8938-8940 (2010).

## 11. Appendix

### 11.1. Publications and conference contributions

#### Publications

---

J. Krämer<sup>‡</sup>, A. Selinger<sup>‡</sup>, F. Biedermann & F. Hof. Manuscript in preparation.

<sup>‡</sup>These authors contributed equally.

J. Krämer, L.M. Grimm, C. Zhong, M. Hirtz & F. Biedermann. *Nature Communications*. **14**, 518 (2023). *A supramolecular cucurbit[8]uril-based rotaxane chemosensor for the optical tryptophan detection in human serum and urine.*

J. Krämer<sup>‡</sup>, R. Kang<sup>‡</sup>, L. M. Grimm<sup>‡</sup>, L. De Cola, P. Picchetti & F. Biedermann. *Chemical Reviews*. **122**, 3459-3636 (2022). *Molecular probes, chemosensors, and nanosensors for optical detection of biorelevant molecules and ions in aqueous media and biofluids.*

<sup>‡</sup>These authors contributed equally. This publication was featured as a cover in *Chemical Reviews*.

S. Sinn, J. Krämer & F. Biedermann. *Chemical Communications*. **56**, 6620-6623 (2020). *Teaching old indicators even more tricks: Binding affinity measurements with the guest-displacement assay (gda).*

This publication was featured on the outside front cover of *Chemical Communications*.

#### Conference Contribution-Poster

---

J. Krämer, L.M. Grimm, C. Zhong, M. Hirtz, and F. Biedermann, *1<sup>st</sup> International Supramolecular Chemistry Summer School, Sardinia, Italy, 29<sup>th</sup> May – 02<sup>nd</sup> June 2022. A molecular-engineered rotaxane overcomes longstanding biofluid challenges and enables optical tryptophan detection in human serum.*

J. Krämer, L.M. Grimm, C. Zhong, M. Hirtz, and F. Biedermann, *RSC Macrocyclic and Supramolecular Chemistry, Nottingham, Great Britain, 19<sup>th</sup> – 20<sup>th</sup> December 2022. A supramolecular cucurbit[8]uril-based rotaxane chemosensor for the optical tryptophan detection in human serum and urine.*

## 11.2. Acknowledgements

I would like to take this opportunity to thank everyone who contributed to the success of my PhD thesis. Thank you all for your motivation and support.

First of all, I would like to thank my direct supervisor Dr. Frank Biedermann for giving me the opportunity to work in his group and complete my PhD thesis under his guidance. Thank you not only for the interesting projects, the great opportunity to complete a research visit abroad, but also for the professional support and trust you have placed in me. I would also like to thank Prof. Dr. Stefan Bräse for accepting my PhD proposal in his research group and for giving me scientific freedom and support during this time.

In addition, I would like to thank Prof. PhD Fraser Hof and his group from the University of Victoria, Canada, for the friendly welcome into the group and the great guidance. The research visit has greatly enriched my work and broadened my scientific knowledge.

I would like to express my gratitude towards the Evonik foundation for supporting me financially over the past three years and for the many in-person and online meetings, where I did not only present my work, but also got in contact with other PhD students. The connections that were created during those events are indispensable to me.

I would also like to thank the entire Biedermann group for the warm and friendly welcome into the group and for creating many memorable moments. Thank you for the many informative conversations and discussions about scientific and “non-scientific” topics during meetings, group lunches, and traditional birthday and paper cakes. Thank you all for your effort and help during my time in the group. A special thank you goes to my “lab-and-office partner-in-crime,” Dr. Laura Grimm. Thank you for all the support and motivation over the last few years. I always loved our office vibe, with the long days where too much coffee was consumed, and I am really happy that I was able to share this time with you. In addition, I would like to thank Dr. Stephan Sinn for the many interesting discussions and brainstorming on SupraBank-related questions and more.

Gratitude goes to Chunting Zhong and PD Dr. Michael Hirtz for realizing the immobilization of the rotaxane chemosensor and for the fruitful discussions. I would also like to especially thank Allison Selinger from the Hof lab for supporting me during my time at the Hof lab and for introducing me to the powerful DimerDye chemosensors. I am looking forward to our continued collaboration on this project. Additionally, I want to thank Dr. Papri Chakraborty for measuring ESI-MS, Dr. Joel Monti for helping me with the DOSY measurements, and Eike Hollesen for running last-minute ESI-MS measurements.

A big thank you to all the people at INT who helped and supported me when I had questions, I really appreciated your help. Thank you to Christine Fischer, Patricia Jäger, Felicitas Lauer, Heidi Hagel, and Antje Hase for solving all kinds of administrative matters easily and quickly. Gratitude goes to Dr. Michal Valášek, Dr. Olaf Fuhr, Martin Limbach, and Hagen Sparrenberger for assisting and solving questions about INT devices, chemical waste disposal, and all sorts of technical questions. Thank you to our IT department with Thomas Koch, Daniel Lerch, and Michael Birkel-Suck for your technical support regarding small and big computer and network issues.

I would especially like to thank the proofreaders of this thesis for your time, support, and constructive criticism, I will try to make it up to you.

A big thank you goes to my whole family and friends. Thank you for sharing this period of my life with me and for your constant support and motivation. You made rough times easier.

Lastly, I would particularly like to thank my parents, sister, and partner, who have always supported and motivated me throughout my career. Thank you for your constant love, your patience, and care; without you, I would not be where and who I am today. Thank you for everything!

